Non-modal hydrodynamic stability analysis of ablation flows relative to inertial confinement fusion

Grégoire Varillon

To cite this version:

Grégoire Varillon. Non-modal hydrodynamic stability analysis of ablation flows relative to inertial confinement fusion. High Energy Physics - Theory [hep-th]. Université Paris Saclay (COmUE), 2019. English. NNT : 2019SACLX106 . tel-02489457

HAL Id: tel-02489457
https://theses.hal.science/tel-02489457v1

Submitted on 24 Feb 2020

université
PARIS-SACLAY

ÉCOLE POLYTECHNIQUE
UNIVERSITÉ PARIS-SACLAY

NNT : 2019SACLX106

Non-modal hydrodynamic stability analysis of ablation flows relative to inertial confinement fusion

Thèse de doctorat de l'Université Paris-Saclay
préparée à École polytechnique

École doctorale n°572 Ondes et Matière (EDOM)
Spécialité de doctorat : Physique des plasmas

Thèse présentée et soutenue à Palaiseau, le 13 décembre 2019, par

M. GRÉGOIRE VARILLON

Composition du Jury :

Carlo Cossu Directeur de recherche CNRS, École centrale de Nantes (LHEEA)	Rapporteur
Uwe Ehrenstein Professeur des Universités, Aix-Marseille Université (M2P2)	Rapporteur
Antoine Sellier Professeur, École polytechnique (LadHyx)	Président
Aline Lefebvre-Lepot Chargée de Recherche CNRS, École polytechnique (CMAP)	Examinateur
Arnaud Couairon Directeur de recherche CNRS, École polytechnique (CPHT)	Directeur de thèse
Jean-Marie Clarisse Ingénieur – chercheur, CEA/Bruyères-le-Châtel	Co-directeur de thèse
César Huete Ruiz de Lira Associate Professor, Universidad Carlos III de Madrid	Examinateur
Serge Gauthier Directeur de Recherche CEA (Retraité)	Examinateur

Thèse de doctorat

Acknowledgements

On dit souvent qu'une équation peut remplacer de longues phrases,

$$m\Sigma\mathbb{R} \leqslant i \quad \forall.$$

On dit aussi qu'un mot peut être plus clair que des pages d'équations, alors *merci*. Le remplissage de cette page est l'occasion de remercier ceux qui ont contribué de près ou de loin, de leur plein gré ou non, à la réalisation du travail de thèse présenté ici.

Au commencement il y a tout d'abord Jean-Marie qui m'a proposé ce sujet puis m'a encadré pendant 3 ans en s'impliquant fortement dans ce travail à mes côtés. Il a apporté la rigueur nécessaire et la pertinence, toujours avec bienveillance, et des idées nouvelles pour se sortir des ornières. Il est certain que je n'aurai pas abouti sans son suivi quotidien. Ce fût un plaisir de travailler ensemble, dans la bonne humeur. J'ai appris beaucoup grâce à Jean-Marie, autant que possible, et je pense que cela me sera fortement utile pour la suite.

Il y a ensuite Arnaud qui a dirigé cette thèse depuis le CPHT, avec tout autant de bienveillance. Merci d'avoir accepté cette tâche et d'avoir assuré un suivi régulier. Merci aussi pour les "déblocages" que tu as permis, pour nous avoir fait prendre du recul par moments et pour les nombreuses relectures.

Je tiens ensuite à remercier les membres du jury qui se sont réunis malgré les obstacles, et notamment MM. Cossu et Ehrenstein, rapporteurs de ce manuscrit, pour leurs remarques avisées. D'un point de vue scientifique, un apport déterminant est dû à Aline Lefebvre-Lepot et François Alouges (CMAP, École polytechnique) concernant la formulation du problème adjoint. Un échange avec Stefania Cherubini (Politecnico di Bari) nous a mis sur la voie de la méthode "true gradient" pour l'optimisation, qui nous sera utile dans le futur.

Mais que serait une thèse à la DIF sans les doctorants, post-doctorants et stagiaires du bâtiment qui chaque matin illuminent ce sombre couloir du Rdc ? Une belle équipe qui rend le travail agréable ! Il est important de pouvoir partager ses joies – un premier calcul qui tourne (enfin) ! –, ses peines – la journée noire du 26 juillet 2019... – et ses doutes – mon schéma numérique est-il stable ? – avec ceux qui nous entourent. Merci d'avoir comblé mes lacunes culturelles concernant Top chef, miss France et bien d'autres. Merci aussi pour nos désaccords, scientifiques ou politiques, qui ont permis des discussions passionnées où certains s'emportaient. Une liste s'impose, par ordre d'apparition : Lucile, Alexis, Sophie, Florian, Mathieu, Marie, Jean-Cédric, Cécile, Charles, Antoine, Ronan, Éric, Baptiste, Albretine, Victor, Mathilde, Olivier, Adrien, Clotilde, Vincent, Alexandre, Alexia, Paul, Fanny, Audrey, Léonce, Yoann et Julien. J'accorde une mention particulière à mes compagnons de footing, à mes co-galériens de Cobalt et à mes trois taxis préférés : Mathieu, Marie et Jean-Cédric, ayant pour destination Paris, Briis-sous-Forges et Arpajon. N'hésitez pas à les solliciter. Bruyères c'est bien, mais qu'est-ce que c'est loin ! Je remercie enfin toutes les personnes du centre avec qui j'ai pu échanger durant ces trois années, sans oublier Odile... sans rancune ?

Enfin il y a la vie après le travail, bien que la thèse tourne toujours en "tâche de fond". Je remercie Pauline qui rend cette vie agréable au jour le jour. Et je tâcherai de te donner le courage nécessaire pour cette dernière année de thèse (chacun son tour !).

Bien avant que tout cela ne commence il y a eu mes parents qui m'ont permis d'en arriver là. Ils se sont toujours montrés intéressés par mes choix scolaires puis universitaires, tout en me supportant dans ces choix. Sans oublier de me demander "à quoi ça sert ?", question ô combien importante ! Je pense aussi à mes deux frères qui ont assisté à la soutenance et qui, peut-être, poursuivront eux aussi en thèse.

Pour finir je tiens à remercier chaleureusement tous mes amis, copains, famille, qui se sont enquis de l'avancée du schmilblick ou de mon état – alors tu tiens le coup ? Oui ça va. Un certain nombre d'entre vous était réuni à l'occasion de la soutenance, et pour mon plus grand plaisir !

Contents

Notations

Scalar	x
Vector	$\mathbf{x}$
Matrix	$\mathbf{X}$
Vector coefficient	$\mathbf{x}_i$
Matrix coefficient	$\mathbf{X}_{ij}$
Variable relative to the base-flow	$\bar{\mathbf{x}}$
Fourier-transformed variable relative to linear perturbations	$\widehat{\mathbf{x}}$
Adjoint variable	$\widehat{\mathbf{x}}^\dagger$
Value of $x(y)$ at y_0	$x\|_{y_0}$

Acronyms

ablative Richtmyer–Meshkov instability	ARM
Commissariat à l'Énergie Atomique et aux Énergies Alternatives, France	CEA
Deuterium–Tritium fusible	DT
inertial confinement fusion	ICF
Lawrence Livermore National Laboratory, US	LLNL
Laser Mégajoule, laser facility at CEA, France	LMJ
National Ignition Facility, laser facility at LLNL, US	NIF
laser facility at LLNL, US	NOVA
optimal initial perturbation	OIP
laser facility at Lab. for Laser Energetics, University of Rochester, US	OMEGA
laser facility, China	SG-III

CHAPTER 1

Introduction

Inertial confinement fusion (ICF) is a process designed for achieving thermonuclear fusion ignition between deuterium and tritium nuclei. A deuterium (D) - tritium (T) nuclear fusion reaction emits two fusion products: a fast neutron n and an alpha particle α

$$D \quad + \quad T \quad \rightarrow \quad n \quad + \quad \alpha. \tag{1.1}$$

To carry out such nuclear reaction, a sufficient amount of energy is needed to unbind particles inside the reacting DT nucleus. The most energetically economical way to achieve reaction (1.1) is to cluster DT at sufficiently high temperature and density. Once they are emitted, α particles interacts with electrons and release their energy to the DT mixture over a given range. If the DT cluster is larger than this range, only a few fraction of alpha particles escape and almost all of their energy is released into the DT cluster. The same happens for neutrons, but their mean free path is much larger than that of alpha particles. As a consequence, neutrons release their energy on a much larger range. The rate of change of energy E into the reacting DT cluster evolves as

$$\frac{\mathrm{d}E}{\mathrm{d}t} = P_{\mathrm{fus}} + P_{\mathrm{ext}} + P_{\mathrm{loss}}, \tag{1.2}$$

where P_{fus}, P_{ext} and P_{loss} stands for the power deposited by fusion products, the power provided by an external source and the power losses, respectively. As the DT cluster is heated to a few keV, it forms a plasma that loses its energy mostly *via* electron heat conduction and radiation emitted by electrons (Bremsstrahlung radiation). At temperatures considered here, a few keV, the DT plasma is transparent toward radiation, so radiation escapes from the DT cluster and does not heat the plasma.

Thermonuclear fusion. The self-sustained regime, called thermonuclear fusion, is met when P_{fus} exceeds P_{loss} without external heating P_{ext}. To achieve such an objective, ICF aims at compressing and heating DT fuel into a spherical pellet. The external power P_{ext} corresponds to mechanical work. As it would require too much energy to ignite reactions in the whole pellet, the goal is to create a small region inside the compressed DT fuel sphere where thermonuclear ignition conditions are met. This *hot spot* region is sufficiently large regarding alpha particles range for being heated by alpha particles, but is too small regarding neutron mean free path for neutron energy deposition. Once thermonuclear reactions are ignited, a burn wave will propagate to the surrounding cold fuel.

A criterion for self-heating, based on a minimal value of the parameter

$$\rho_{\mathrm{h}}\, t_{\mathrm{h}}\, T_{\mathrm{h}}, \tag{1.3}$$

is derived from the above mentioned physical phenomenon and known as the Lawson criterion (Atzeni and Meyer-ter-Vehn, 2004, §2.4), where ρ_{h}, t_{h} and T_{h} stand for the hot spot density, confinement time and temperature, respectively. In the case of ICF, the Lawson criterion writes analogously in terms of the areal mass (Atzeni and Meyer-ter-Vehn, 2004, §4.2) as

$$\rho_{\mathrm{h}}\, R_{\mathrm{h}} > f(T_{\mathrm{h}}), \tag{1.4}$$

where R_{h} denotes the hot spot radius. The function f is a threshold depending only on the hot spot temperature. As the self-heating process takes a finite time to set in, the external power source has to confine the DT plasma over a time exceeding this self-heating time. In addition, the hot spot must remain more or less spherical in order to limit energy losses at external surface. In a nutshell, ICF faces the challenge of confining a small amount of DT fuel at sufficiently high temperature, for sufficiently long duration, in a sufficiently spherical volume, surrounded by a denser and colder mantle of fuel. Orders of magnitude of hot spot parameters are given in Tab. 1.1.

Table 1.1: Orders of magnitude of hot spot parameters (Atzeni and Meyer-ter-Vehn, 2004).

Areal mass ($\rho_\mathrm{h} R_\mathrm{h}$)	~ 0.5 g/cm^2
Hot-spot temperature (T_h)	~ 10 keV
Hot-spot confinement time (t_h)	~ 100 ps
Ratio of initial to final shell radius (convergence ratio)	$25 - 45$
Hot-spot pressure (P_h)	250 Gbar

Fuel compression process and hydrodynamic instabilitites. To achieve such a high compression, the DT fuel is placed in a fusion target, an example of which is shown on Fig. 1.1a. The fusion target is composed of a dense outer shell (‘Diamond’on Fig. 1.1a), filled with DT fuel. A fraction of the DT fuel is in solid phase on the inner walls of the shell (‘DT solid’) while the rest of it forms a gaseous phase inside the target (‘DT gas’). The dense and opaque outer part of the shell containing the fuel, called the *ablator* (Fig. 1.1a), is exposed to a strong irradiation flux (Fig. 1.2). This flux is absorbed in the ablator and drives shocks into the target while the external wall of the target is ablated, converted into plasma, and enters in expansion (light orange on Fig. 1.2). In reaction to the plasma outflow, the shell is accelerated inward, driving in the implosion which compresses the fuel. The shell acts as a piston for the fuel. Several approaches exists for shell compression. Here we focus on laser driven compression for which two main alternative approaches have been proposed:

- *Direct-drive ICF*: laser beams illuminate *directly* the target. A large number of overlapping laser beams provide a sufficiently uniform illumination of the target, heating its external surface. Direct-drive ICF experiments are carried out on the OMEGA laser at the Laboratory for Laser Energetics since the mid 90s’.

- *Indirect-drive ICF*: the shell is placed in a cavity ‘holhraum’ whose inner walls are illuminated with laser beams, heating them (Fig. 1.1b). The cavity walls are designed to absorb most of the incident laser energy and to re-emit X-rays. The shell is therefore immersed in a high ambient radiation bath which heats its external surface. This indirect-drive ICF process has been tested on the National Ignition Facility at Lawrence Livermore National Laboratory, US, since 2009 (Lindl et al., 2004). The SG-III, China, is another facility built to achieve indirect-drive ICF (Gu et al., 2018), as well as the Laser Mégajoule which is under completion at CEA, France (Miquel, 2016).

Even though the energy deposition process at the shell surface differs, the expected effect is similar: the heated ablator mass expands outward resulting in a thrust pressure that accelerates the shell walls inward. This *ablative pressure*, which actually drives the implosion, arise in an expansion flow resulting from the shell external irradiation, which falls into the family of *ablation flows*. Such flows are strongly accelerated and highly stratified. They present a situation favourable to the development of Rayleigh–Taylor like instabilities, potentially damaging compression efficiency and hot spot symmetry.

As the efficiency of the fuel compression and its symmetry is crucial to ignition, hydrodynamic instabilities in ICF has been identified as a threat to ignition since the early works of Nuckolls on laboratory DT thermonuclear fusion, in the 1950s (Lindl, 1995). The idea was to ‘create the smallest possible fusion explosion’. Although laser was not yet invented, the principle already relied on achieving thermonuclear ignition conditions by compression. The compression was supposedly driven by radiations. Nuckolls et al. (1972) first predicted ignition with a 1kJ laser

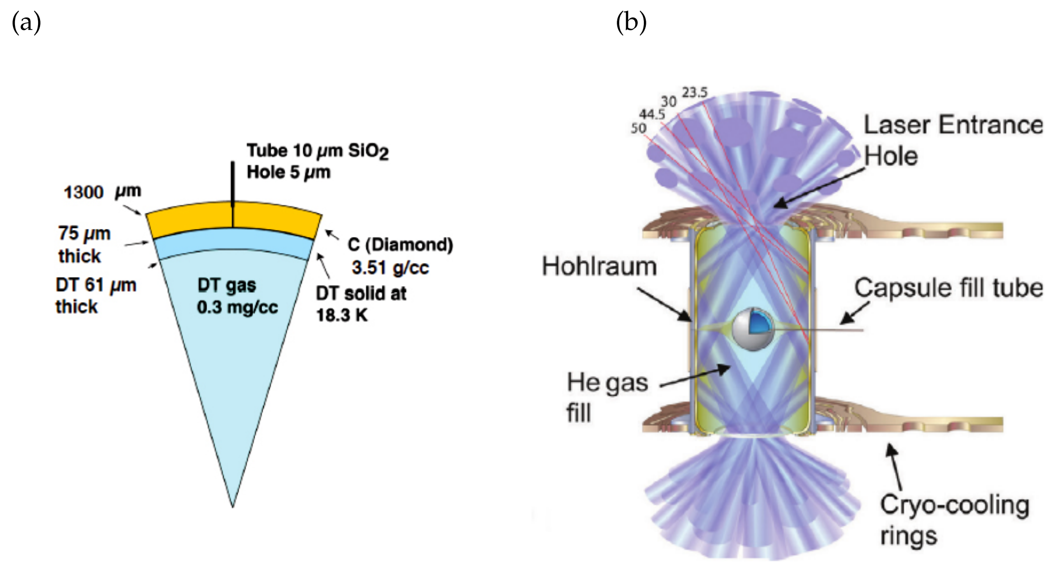

Figure 1.1: (a) Cross section of an ICF target. Orange: ablator, outer light blue: solid DT, inner light blue: gaseous DT. Dimensions and composition of the layers are given on an indicative basis. (b) Setup for indirect-drive ICF (Lindl et al., 2014): laser beam cones (half-transparent) enter the cavity (holhraum) by two laser entrance holes and heat the inner walls (green). The shell is represented at the center of the cavity, which is vacuum or gas filled (as represented here).

energy from a simple Rayleigh–Taylor model with ablation. But the first two–dimensional numerical simulations of these instabilities revised the 1 kJ prediction upwards (Lindl and Mead, 1975). According to these computations, indirect-drive would lead to a weaker growth of Rayleigh–Taylor instabilities, compared to direct-drive, mainly because of a higher ablation rate and smaller illumination asymmetries.

In the 1960s, scientists rapidly took advantage of the novel laser technology and came up with experimental setup to test target implosions in both direct and indirect-drive processes. The first experiments at LLNL (1974) saw the production of neutrons. Following that campaign, the prediction for ignition reached 200kJ of laser energy. Subsequent experiments touched on other limitations such as plasma (parametric) instabilities or hot electrons preheating the target. The NOVA laser built in 1984 at LLNL delivers 100 kJ in 2 to 4 ns laser pulses. Experiments on NOVA allowed a quantitative analysis of Rayleigh–Taylor growth and the improvement of engineering features on targets and cavities. These experiments led to an even larger prediction of laser energy to achieve ignition: ideally 5 to 10 MJ of laser energy would be necessary to reach ignition, but 1 to 2 MJ could be enough provided high implosion velocities are reached. The NIF (1.8 MJ) has been designed according to these predictions. In the mean time, simulation capabilities also greatly developed. However, the National Ignition Campaign (Lindl et al., 2014; Peterson et al., 2015), focused on indirect-drive experiments, failed to reach thermonuclear ignition. Here are a short list of obstacles:

- *Cross beam energy transfers*: laser beams overlap when entering in the laser entrance hole (Fig. 1.1). Some energy transfers take place from one beam to another, resulting in a power imbalance between laser beams (Lindl et al., 2014);

- *Parametric instabilities*: the inner wall of the hohlraum is heated and expands as a plasma progressively filling the hohlraum. Laser beams propagating inside the cavity interact with this plasma which gives rise to parametric scattering instabilities. These instabilities develop as ion sound waves or electron plasma waves over time scales of 0.1 to 10 ps (Lindl et al., 2004, §III). Undesirable effects include laser light reflection, illuminating directly the target, and hot electron preheating the DT fuel and thus reducing its compressibility;

- *Laser filamentation*: in an intense laser beam, the light pressure may not be neglected. Some nonlinear effects become significant and modify the refractive index causing small-scale self-focusing of the laser beam. Filamentation modifies the propagation of laser inside the hohlraum (Lindl et al., 2004, §III);
- *Hydrodynamic instabilities*: flow perturbations develop during the shell implosion from defects at the surfaces of, or inside, the shell, or from pressure or illumination asymmetries of the target. Hydrodynamic instabilities directly endanger the compression of the fuel, regardless of the above mentioned difficulties. These instabilities may result in the breakup of the DT fuel confinement, a loss of the spherical symmetry and the mixing of ablator elements into DT fuel. Each of these consequences reduce the efficiency of the compression, inhibit ignition of degrade the burn.

The above mentioned obstacles were investigated by means of theoretical, experimental and simulation studies. The present works addresses the problem of hydrodynamic instabilities during the shell compression. While the shell is irradiated, the combination of the converging shock fronts with the inward accelerated dense part of the shell and the expanding hot plasma forms a complex flow which is time changing and strongly non-uniform. For a broad study of hydrodynamic instabilities, the flow may not be considered as frozen in time and thus requires an adequate description of time scales that are comparable to the implosion duration (~ 10 ns) and a resolution of a wide range of spatial scales (from one to $10^{-}5$ target radius).

Regarding hydrodynamic instabilities during ICF compression, many works have been devoted to the study of the *acceleration phase* (Fig. 1.2b). During this stage, the converging shock front (red circle on Fig. 1.2b), has already crossed the shell and propagates inside the fuel, and the ablator (orange region) is strongly accelerated. The acceleration phase is therefore highly favourable to a strong amplification of small disturbances. However the acceleration phase follows the *shock transit phase* (Fig. 1.2a), during which the converging shock front, together with the ablation process, compress the ablator and set the ablator into motion. After the first instant of the illumination of the ablator a *deflagration regime* sets up: a subsonic thermal front (green) propagate inversely to the flow direction, following a forerunning shock wave front (red). Any perturbation developing during this shock transit phase will seed the subsequent acceleration phase.

Ablation waves and their stability. Hydrodynamic stability of the shock transit phase is often studied through the intermediary of the following model problem: a semi-infinite, cold, dense and opaque body, in slab symmetry, is suddenly exposed to a growing irradiation flux (Fig. 1.3). Heat is transported thanks to nonlinear heat conduction. After the first instant, a deflagration regime sets up, describing the *ablation flow*, or *ablation wave*, that mimics the shock transit phase. An ablation flow (Fig. 1.4) is composed of a forerunning shock front (sf), propagating inward through the ablator at rest, followed by a subsonic *ablation front* (af) or *ablation layer*, corresponding to the leading edge of an expansion wave and the foot of a thermal front. Ablation flows are non-stationary, compressible, expanding and strongly non-uniform. In the ablation front the material is heated and accelerated before it expands in the conduction region. The acceleration of the heated fluid due to its expansion results in an *ablative pressure* that compresses the target, similarly to the rocket effect.

Over the last decades, the drastic development of computational capabilities has enabled multidimensional simulations coupling the physics of the multiple phenomena at stakes in ICF implosions (laser and plasma physics, hydrodynamics, nuclear physics, etc.). Such simulations are carried out with numerical *multiple physics codes* that

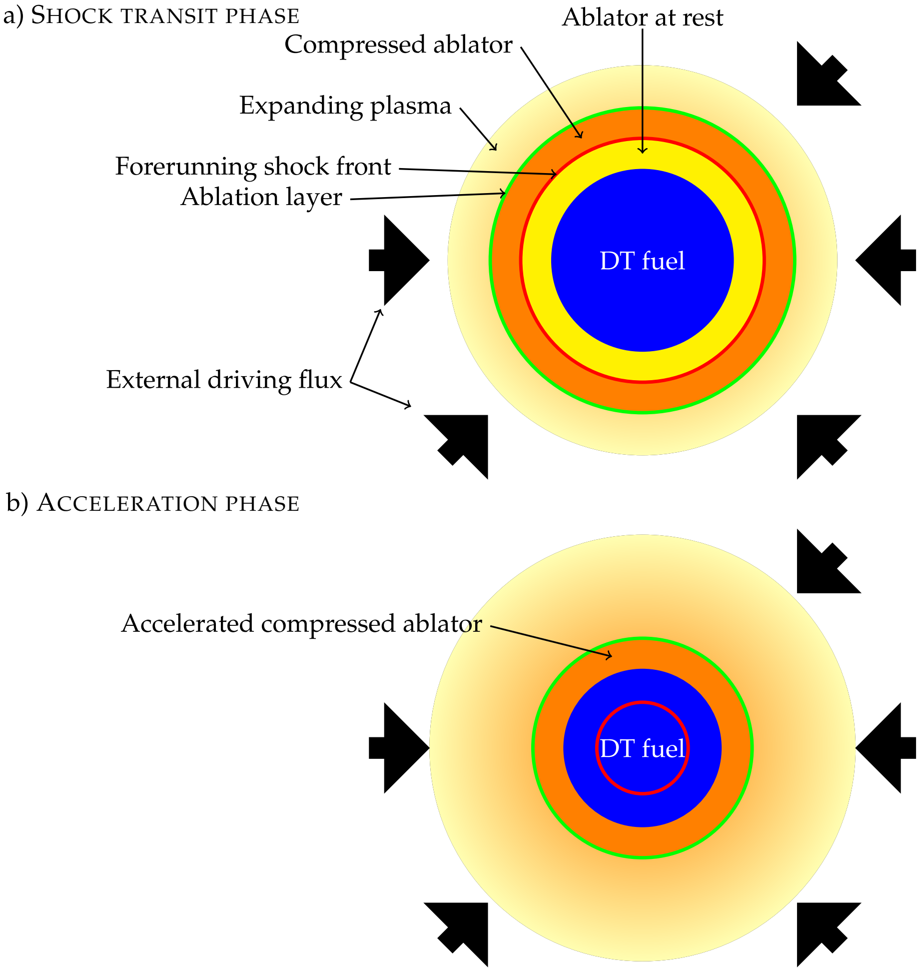

Figure 1.2: Schematic view of the target during (a) the shock transit phase and (b) the acceleration phase.

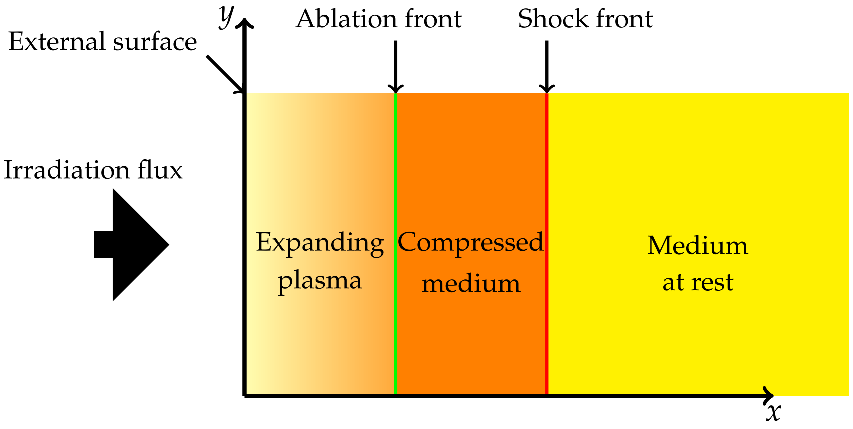

Figure 1.3: Ablation of a semi-infinite slab.

attempt to incorporate all the physical processes which are thought to be influential in these implosions. Being aimed at simulating experimental configurations, these codes have been preferentially used as tools for designing implosion targets and hohlraums rather than investigating the physical mechanisms at stake in ICF implosions. Additionally, these codes are resource intensive which is an important limitation when numerous computations are needed. From the beginning of works on the concept of ICF, dedicated approaches, besides these multiple

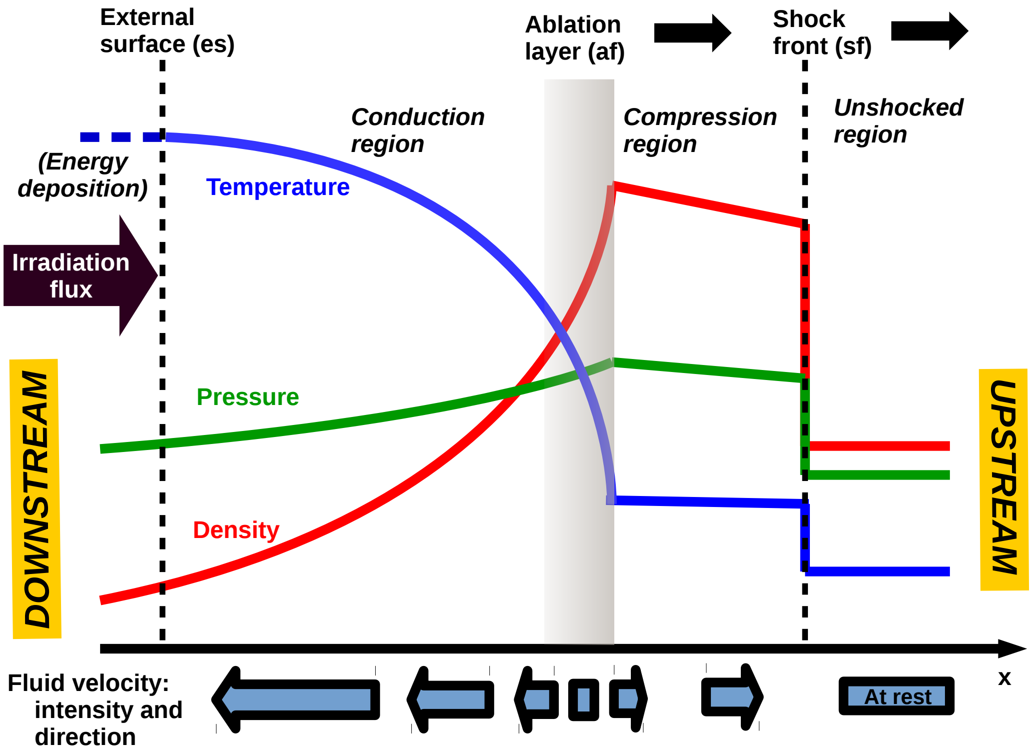

Figure 1.4: Schematic side profile of an ablation flow.

physics codes, have been developed in order to address specific problems that are critical to achieving fusion. Hydrodynamic instabilities are the most emblematic example since a large number of published works has been devoted to the subject since the 1970s.

These works, in their vast majority, have adopted a simplified modeling of ablation flows consisting of the equations of motion for a compressible inviscid fluid (or Euler equations) with nonlinear heat conduction. However progress towards analytical or semi-analytical models could only be made upon using additional *simplifying assumptions*: i.e., flow steadiness, isobaric approximation, discontinuous ablation front, unconfined flow regions, isothermal expansion of the ablated fluid, etc. The recourse to such assumptions has become a standard practice in ablation flow analysis which has led to numerous models, presently designated as *standard models*. These models have undoubtedly helped in getting a better understanding of ablation flows and of their instabilities. When considering ablation waves characteristic of the shock transit phase of a target, this standard model approach leads to the conclusion that, in the linear perturbation regime, ablation and shock front distortions induced by initial surface defects grow linearly with time for wavelengths larger than the depth of the conduction region (Nishihara et al., 1998; Velikovich et al., 1998; Goncharov, 1999; Goncharov et al., 2000). Such a behavior, first inferred from multi-dimensional simulations (Nishihara et al., 1998; Velikovich et al., 1998), was later observed in dedicated experiments (Aglitskiy et al., 2010). However for such rather slow perturbation dynamics, improved quantitative results do require taking into account the base-flow time evolution (Goncharov et al., 2006; Abéguilé et al., 2006). For a self-similar unsteady ablation waves, the growth of long wavelength perturbations thus turns out to be algebraic in time (Abéguilé et al., 2006; Clarisse et al., 2008, 2016) rather than linear as predicted by stationary ablation modeling. Mean flow unsteadiness also induces finite durations of the different regimes of perturbation evolutions and logically leads to the question of short-term perturbation dynamics (Clarisse et al., 2016). From another point of view, a parallel with thermoacoustic instabilities indicates that ablation flows could be prone to non-modal transient growth as a consequence of flow acceleration and non-trivial boundary conditions (Nicoud et al., 2007; Wieczorek et al., 2011). Up to now, short-term perturbation dynamics in ICF ablation flows have never been investigated and the present work aims at changing this fact by performing the first non-modal linear analysis of an ablation flow. This analysis is carried out in the context of the shock transit phase of an ICF target implosion since the possible occurrence of rapid transient growth of perturbations during this phase could change significantly the current understanding of hydrodynamic instabilities in ICF implosions and the methods that are required for their prediction.

The rest of this thesis dissertation is organised as follows. After an overview of the standard models (Chap. 2), we introduce an intermediate approach, between simplified standard models and multiple physics simulations, that uses unsteady self-similar solutions to the Euler equations with non-linear heat conduction as base-flows. Some of these self-similar solutions are well-suited for a stability analysis and are therefore adopted for our study. In Chap. 3 we present the framework of these self-similar solutions in slab symmetry, the evolution equations of their three-dimensional linear perturbations and the numerical methods that have been devised for their computation. Changes in the numerical method for linear perturbations that have been brought for the present goal of a non-modal stability analysis are summarized (§ 3.3.3). Two self-similar ablation waves driven by radiation, relevant to indirect-drive ICF, that are used in the present work are then prensented (§ 3.4): one with a nearly sonic expansion, the other with a supersonic expansion. With the goal of a better understanding of linear perturbation evolutions in ablation flows, a numerical investigation of linear waves propagating in the self-similar ablation wave with a supersonic expansion is carried out and results are analysed in terms of a set of pseudo-characteristic variables (§ 3.5 and App. A). The non-modal analysis of ablation waves is then considered (Chap. 4). After a brief review of non-modal tools for hydrodynamic stability analysis (§ 4.1), we advocate for the use of non-modal analysis for ablation waves (§ 4.2). The question of the perturbation measure, which is central to hydrodynamic stability analyses, is then discussed and objective functionals used in the present work are presented (§ 4.3). A first non-modal local analysis assesses the presence of non-modal effects in ablation flows at small scales (Sec. 4.4) and further justifies to the subsequent global analysis. Dealing with a time dependent mean flow, we have recourse to a direct-adjoint method. We put the emphasis on the derivation of the adjoint problem (Sec. 4.5). Optimal perturbation results are then given for the self similar ablation wave with nearly sonic expansion (§ 4.6). Optimal growth mechanisms are identified on some of the optimal responses with the help of the pseudo-characteristic variables introduced in § 3.5. In addition, optimal responses are compared with perturbation growth in the configuration of an initial surface defect. Finally, we discuss the results that have been obtained, together with computational issues, and conclude on the perspectives that these results open up regarding the stability of ablation waves related ICF.

CHAPTER 2

Ablation waves in inertial confinement fusion (ICF)

Chapter Abstract

Ablation waves form when a dense and optically thick medium is suddenly exposed to an intense irradiation flux. By describing the phenomenology of ICF, we argue that planar ablation waves are representative of the critical stage of an ICF shell implosion. Therefore, studying the linear stability of planar ablation waves provides insights about the stability of ICF induced flows. In that sense, ablation waves are central to the achievement of ICF. After discussing the approximations commonly used to model the physics of ablation flows, we describe the existing models of ablation waves. Finally we present the arguments in favor of the use of self-similar solutions to accurately model realistic ICF ablation waves.

When the external surface of the ablator is being exposed to the growing irradiation flux, a thermal wave starts to run inward. The compression process of ICF relies on the propagation of this thermal wave in the ablator.

A model problem: thermal waves in a cold body. Before presenting the phenomenology of an ICF implosion, we consider the following example case: a cold body is suddenly exposed to a growing temperature T_{es} at its external boundary, following a temporal law $T_{\text{es}} \propto t^q$, $q > 0$, that provokes the inward propagation of a nonlinear heat wave (example taken from Zel'dovich and Raizer (1967), vol. II, §X). Neglecting the motion of the fluid, we only consider the diffusion of temperature

$$\partial_t T = \nabla \cdot \boldsymbol{\varphi}, \quad \text{and} \quad \boldsymbol{\varphi} = -\chi \nabla T \quad \text{with} \quad \chi \propto T^\nu, \quad \nu > 1, \tag{2.1}$$

where $\boldsymbol{\varphi}$ is the heat flux. A supersonic thermal front starts to propagate inward, followed by a shock wave. The heat front moves at the velocity

$$v_{\text{hf}} \propto \left(\frac{\chi}{t}\right)^{\frac{1}{2}} \propto \left(\frac{T^\nu}{t}\right)^{\frac{1}{2}} \propto t^{(\nu q-1)/2}, \tag{2.2}$$

while the shock wave velocity evolves as

$$v_{\text{sf}} \propto \sqrt{T} \propto t^{q/2}. \tag{2.3}$$

Two possibilities arise, illustrating actual situations where the flow motion is considered:

- Supersonic regime: if the rise of the external temperature is fast, i.e. for $q > 1/(\nu-1)$, then $v_{\text{hf}} > v_{\text{sf}}$ and the *supersonic* regime persists (Fig. 2.1a). In the supersonic regime the medium is not set into motion.
- Subsonic or ablation regime: if the rise of the external temperature is sufficiently slow, i.e. $q < 1/(\nu-1)$, then at some time the heat wave becomes subsonic ($v_{\text{hf}} < v_{\text{sf}}$) and a shock wave eventually overtakes the heat front. The cold material is compressed across the shock wave. Downstream in the compressed medium, the heat flux propagates from the external surface. If vacuum is assumed outside of the body in the simplest case, an expansion wave sets up. The leading edge of this expansion wave coincides with the foot of the thermal front and is called the *ablation layer* or *ablation front*. In the ablation regime (Fig. 2.1b), the medium is set into motion.

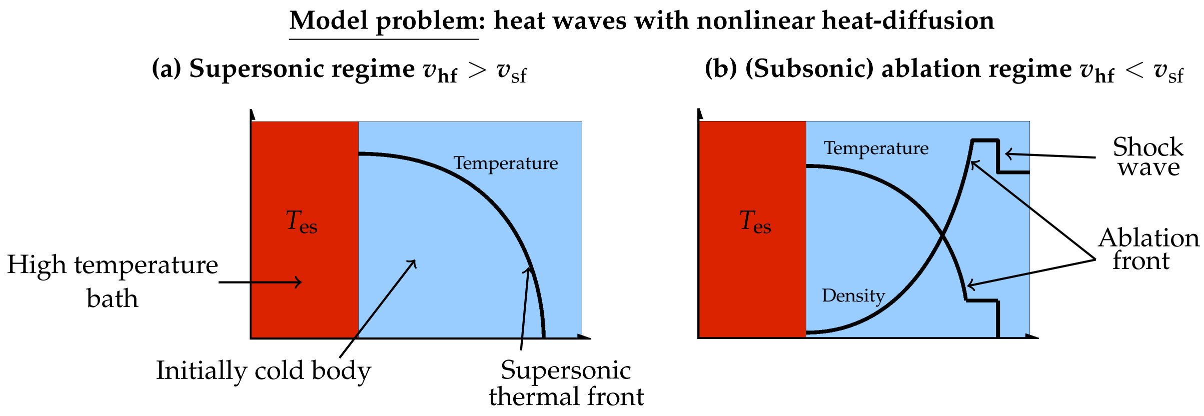

Figure 2.1: A cold body (blue) in contact with a heated medium (red). (a) Temperature profile in the *supersonic* regime. (b) Temperature and density profiles into the *subsonic* regime. Adapted from Dastugue (2013).

Through the ablation layer, the density drops and the fluid expansion velocity strongly increases. Heat conduction dominates in the expansion wave, denominated as the *conduction region*. The ablation layer is the locus where a significant part of the irradiation energy is converted into kinetic energy, thus producing an *ablative pressure* thrusting the shell inward.

Thermal waves in ICF. In the context of ICF, the high temperature bath is replaced by a growing irradiation heat-flux (Fig. 1.4). The supersonic stage is representative of the early illumination of the shell, which is rapidly followed by the subsonic ablation regime. The compression of the ablator material by the forerunning shock front is advantageous as the subsequent ablation and expansion occurs on a denser material, transferring more momentum to the shell. Indeed, for a higher heat flux, the forerunning heat front remains supersonic which inhibits the birth of the shock front compressing the medium. Therefore, compared to the amount of incident irradiation energy, the kinetic acceleration transferred to the shell is higher in the case of a subsonic ablation than in the case of a supersonic regime (see discussion in Atzeni and Meyer-ter-Vehn, 2004, §7.7.3).

2.1 Phenomenology of inertial confinement fusion (ICF) implosions

An ICF target implosion takes place in successive steps (Saillard, 2000):

1. *Shock transit phase* (0 to 12 ns in Fig. 2.3): after the target illumination has started, the subsonic ablation regime, preceded by the supersonic regime, compresses the ablator during the transit of the shock front up to the inner surface of the ablator (Fig. 2.2a).

2. *Acceleration phase* (12 to 21 ns): the ablator is strongly accelerated while rarefaction waves, originating from the forerunning shock interactions with the ablator-fuel interface and the inner solid-fuel surface, travel backward to the external surface, crossing the ablation layer. Some reflected shock fronts may form during that phase (Fig. 2.2b).

3. *Inertial phase* (21 to 24 ns): at some point, the irradiation flux no longer affects the accelerated ablator and the shell enters a phase of inertial motion (Fig. 2.2b),

4. *Deceleration phase* (around 24 ns): the increasing inner pressure and reflected shock waves counterbalance the inertia of the accelerated shell, and decelerate the shell.

5. *Stagnation phase* (around 24 ns): together with the shell compression, multiple inward propagating shock waves converge at the center of the target, heating the DT fuel and creating a hot spot (Fig. 2.2c).

6. *Burn phase* (from 25 ns): if the confinement time, corresponding to the implosion duration, exceeds the fusion charateristic time, then conditions are met for thermonuclear ignition in the hot spot (Lawson criterion), and a burn wave then propagate to the rest of the DT fuel (Fig. 2.2d).

The flows resulting from the different stages of the implosion are strongly stratified and develop instabilities. These instabilities are conceivable in terms of production (or destruction) of vorticity through the baroclinic term, the right hand side of the evolution equation of vorticity $\boldsymbol{\omega}$ (Hirsch, 1988)

$$\partial_t \boldsymbol{\omega} + \nabla \times (\boldsymbol{\omega} \times \boldsymbol{v}) = \frac{1}{\rho^2} \nabla \rho \times \nabla p, \tag{2.4}$$

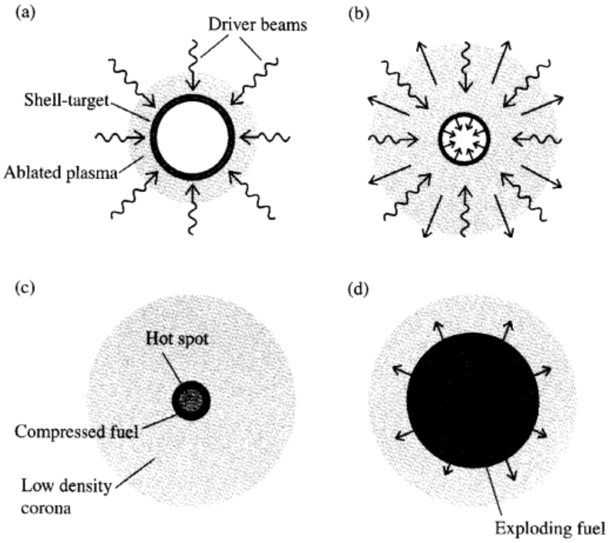

Figure 2.2: Principle of ICF implosion: (a) shock transit and acceleration stages, (b) convergence and deceleration of the shell, (c) stagnation and creation of the hot spot and (d) ignition and propagation of the burn wave (Atzeni and Meyer-ter-Vehn, 2004).

where v, ρ, p denote the velocity, density and pressure, respectively. Vorticity tends to increase, or decrease, the amplitude of the deformations of a layer. Therefore a change in the production of vorticity influences the amplitudes of the deformations.

Rayleigh–Taylor instabilities. During the acceleration phase, the heated light external corona of the ablator is pushed against the denser inner part of the ablator. This situation is favourable to the development of the Rayleigh–Taylor instability which arises in regions where the density gradient and the acceleration are opposite, i.e. for a non-zero baroclinic term in (2.4). Various parameters influence the growth rate of the Rayleigh–Taylor instability (e.g. viscosity, surface tension, heat conduction, stratification, etc., cf. Chandrasekhar, 1961), the main ones being the acceleration and the Atwood number. An example is given by the case of a heavy fluid, density ρ_1, ‘falling’ on a lighter fluid, density ρ_2, due to gravitational or inertial acceleration g. The Atwood number reads

$$\mathrm{At} = \frac{\rho_1 - \rho_2}{\rho_1 + \rho_2}. \tag{2.5}$$

The position of the perturbed interface may initially be described by linear perturbations which correspond to the ‘linear phase’ (Figs. 2.5a-c). In the case of two inviscid and non-conducting fluids, the linear growth rate reads

$$\sigma = \sqrt{g\,\mathrm{At}\,k}, \quad \text{with } k \text{ the wavenumber of the interface deformation.} \tag{2.6}$$

Any small perturbation of the interface will grow in time, forming bubbles and spikes. The perturbation growth is then subject to a saturation phenomenon (Figs. 2.5d-g) which results from nonlinear effects. The ultimate stages of the instability (Figs. 2.5h-l) see the appearance of rolling round resulting ‘mushroom’ patterns and further on, fully turbulent flows. In the case of ablation waves, material flows through the unstable region (ablation layer), which defines the *ablative Rayleigh–Taylor instability*. The earliest analysis of ablation front instabilities (Bodner, 1974) drew the parallel between ablative Rayleigh–Taylor instability and flame front instability, where an expansion

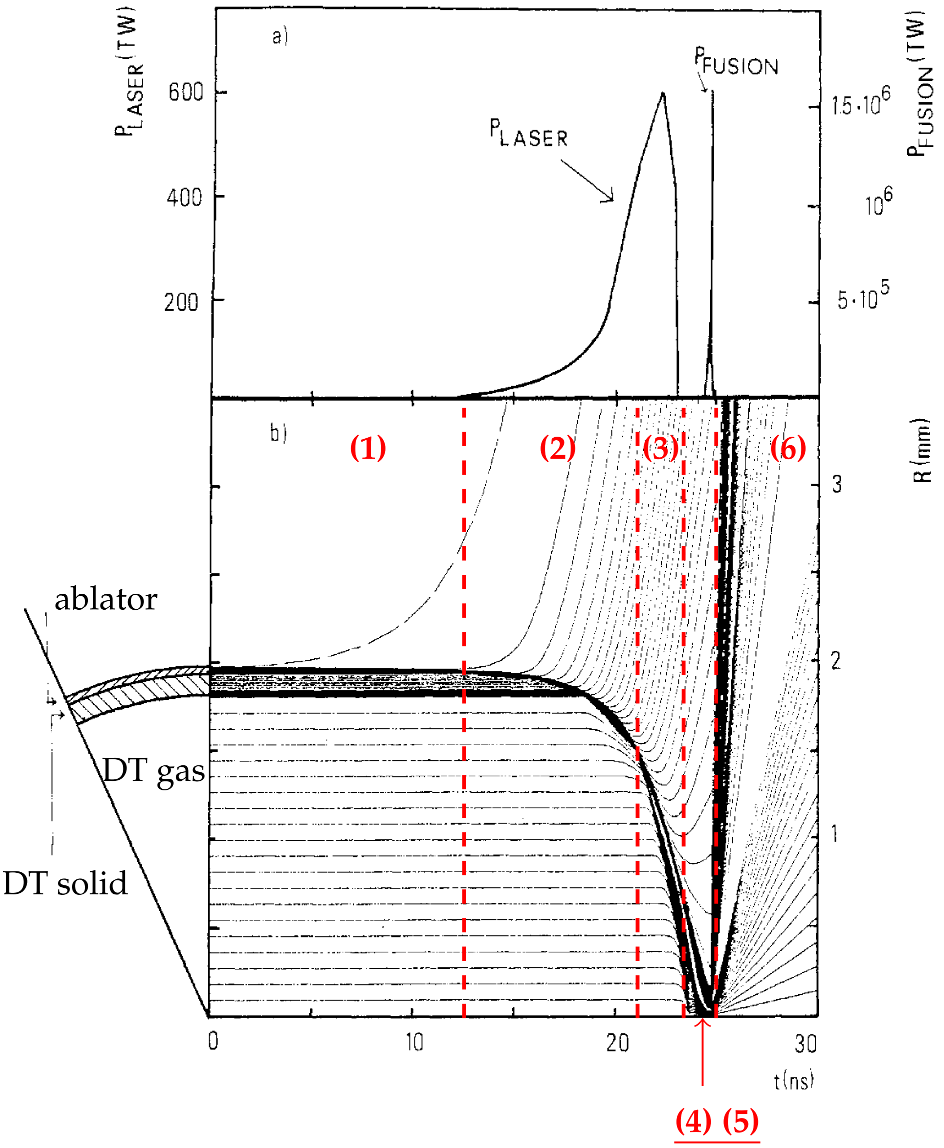

Figure 2.3: Adapted from Atzeni (1987), Fig. 4. Laser power law (P_{LASER}) and fusion power (P_{FUSION}) across time (a) and implosion diagram (b): radial trajectories of fluid elements across time. Clustered lines represent dense regions while spaced lines represent rarefied regions. The 'CH shell' is the ablator, 'frozen D-T' is the fuel in solid phase an d 'D-T vapor' is the gaseous fuel. Red lines and numbering correspond the stages listed in § 2.1.

wave forms from the propagation of a burn wave in a dense and cold medium (see Bychkov et al., 2015 and references therein).

Richtmyer–Meshkov instabilities. Some hydrodynamic instabilities may also arise in stratified flows when a planar (respectively perturbed) shock front crosses a perturbed (resp. planar) strong density gradient zone (e.g. an interface). The shock front delivers a baroclinic impulse to the stratified region which results in an impulsional acceleration of existing deformations of this region. In the limiting case of an interface between two inviscid fluids, small initial perturbations of this interface initially grow linearly in time after the shock front crosses the interface (Chandrasekhar, 1961). This instability was theoretically predicted by Richtmyer (1960) before being experimentally observed by Meshkov (1969), and is named after them: the Richtmyer–Meshkov instability. Any

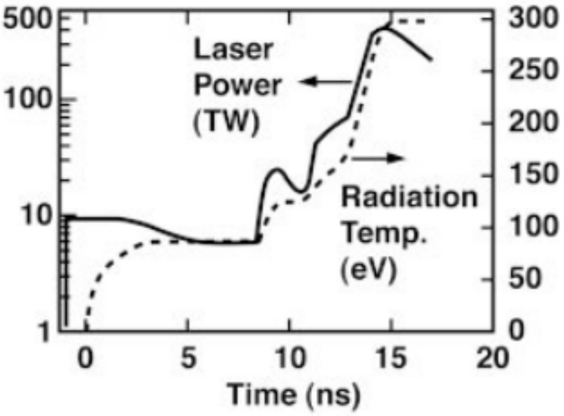

Figure 2.4: Example of laser power law and the resulting radiation temperature at the shell surface for an indirect-drive implosion (Lindl et al., 2004).

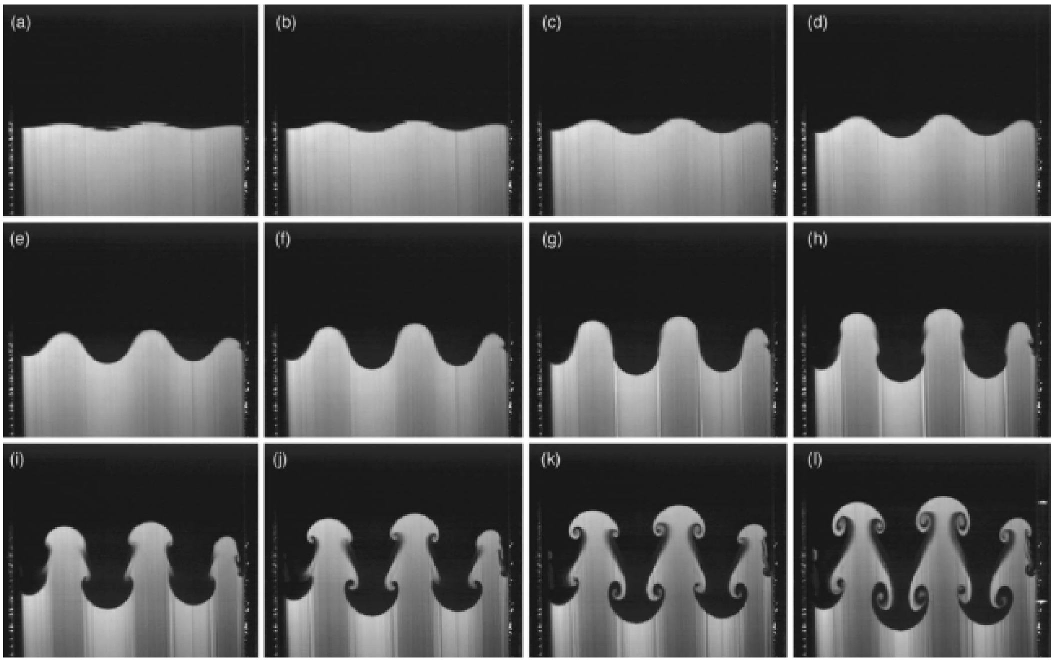

Figure 2.5: Cross-section of a 3D Rayleigh–Taylor instability growth with two miscible fluids in a tank accelerated (13 to 23 $\mathrm{m/s^2}$) observed in a non-inertial frame, At $= 0.15$. Times relative to the beginning of acceleration: (a) 46.7 ms, (b) 80 ms, (c) 113.3 ms, (d) 146.6 ms, (e) 179.9 ms, (f) 213.2 ms, (g) 246.5 ms, (h) 279.8 ms, (i) 313.1 ms, (j) 346.4 ms, (k) 379.7 ms, (l) 413 ms (Wilkinson and Jacobs, 2007).

stratified flow is favourable to this instability, whether it is accelerated or not, as soon as a shock wave goes across the flow. The Richtmyer–Meshkov instability may occur during ICF implosions when a perturbed shock front eventually reaches the inner interface of the shell, or when an unperturbed shock front crosses inhomogeneities inside the shell. Wouchuk (2001b) derived expressions of asymptotic growth rate depending on the shock intensity, in situations of interest for ICF.

Richtmyer–Meshkov like instabilities. An important point to consider is that the ablation layer, the inner and outer interfaces of the shell are coupled due to various waves traveling into the shell thickness and to heat diffusion. For example, a defect on the outer surface of the shell can perturb the forerunning shock front, which will in turn perturb the inner surface of the shell: this is the ‘feedthrough’ mechanism. Alternatively, when one of the converging shock fronts comes out on the inner interface of the target, any defect at this interface will perturb the reflected rarefaction wave travelling back to the external surface, which will, in turn, perturb the ablation layer: this is the ‘feedout’ mechanism (Aglitskiy et al., 2010). Characteristic dimensions, implosion velocity and duration of an ICF implosion are given in Tab. 2.1.

Table 2.1: Charateristic features of an ICF shell implosion (Atzeni and Meyer-ter-Vehn, 2004).

Peak implosion velocity	350 km/s
Implosion duration	25 ns
Shock transit time duration	3–10 ns
Supersonic stage duration	$\sim$ 1 ns
Shell initial radius	2 mm
Ablator initial thickness	0.04 mm
Ablator initial density	1.2 g/cm^3
Surface defect amplitude (Smalyuk et al., 2015)	$\mathcal{O}(10)$ to $\mathcal{O}(100)$ nm

The hydrodynamic stability of shell implosions has been identified as playing a key role in ICF success. During the acceleration phase (Fig. 2.3), ablative Rayleigh–Taylor instabilities strongly develop and form bubbles burning through the ablator. This causes a loss of the confinement. At larger scales, it may result into the loss of symmetry of the implosion. During the deceleration phase (4 in Fig. 2.3b), Rayleigh–Taylor instability forms spikes mixing some ablator material into the fusible, decreasing the burn efficiency. Studying the resulting flows proves to be intricate due to the complexity of the phenomena at stake and the multiplicity of sources of perturbations. Many theoretical and experimental works have focused on the acceleration and deceleration stages (Sakagami and Nishihara, 1990). The present work is focused on the stability of ablation flows presented in Chap. 1, that are representative of the shock transit phase. Although the acceleration (2 in Fig. 2.3b) and the deceleration phases are more subject to instability growth, the ablator undergoes a smaller but still consequent acceleration during the shock transit phase, making it sensitive to ablative Rayleigh–Taylor instabilities. Additionally, the shock transit phase is subject to ablative Richtmyer–Meshkov instabilities (Aglitskiy et al., 2010). Besides, the shock transit phase is crucial to ICF stability as it precedes the acceleration phase: any perturbation developing, even slightly, during the shock transit phase will seed the subsequent acceleration phase.

2.2 Modeling ablation flows and their stability

The first common assumption adopted in ablation wave models is that the flow is close to the thermodynamic equilibrium and is accurately described by a fluid model. As it is impossible to access to the velocity distribution inside the shell, the justification relies on the comparison of the particle mean free path and the characteristic time between collisions (Tab. 2.2) to the characteristic dimensions and durations of the implosion. It follows that a fluid description is adapted to describe dense regions of the ablator plasma. In addition, experimental measures of hydrodynamic quantities, such as shock front velocity in the ablator and ablator velocity, are in satisfactory agreement with results from ICF hydrodynamics codes (Lindl et al., 2014, § V.B.4,6). Needless to say, the compu-

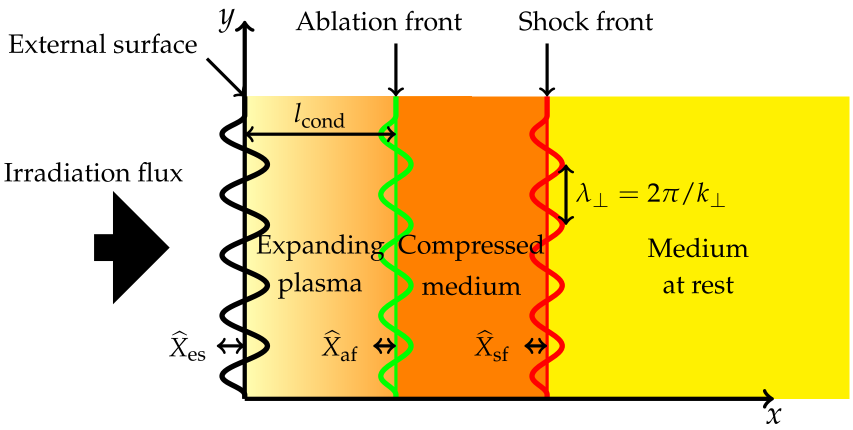

Figure 2.6: Perturbed interfaces in a planar ablation wave. The length of the conduction region is denoted l_{cond}, and $\widehat{X}_{\text{a}}$'s, a=es, af or sf, denote the Fourier coefficients of the perturbation of the external surface (resp. ablation front and shock front) of transverse wavenumer $k_{\perp}$.

tational cost of a kinetic model of ablation flows over durations and dimensions representative of ICF implosions is prohibitive. Radiative temperature at the surface of the shell indicates that the medium forms a plasma and that radiative transport cannot be neglected (Fig. 2.4). Such a situation is described by the equations of radiation hydrodynamics: the motion of a viscous fluid with radiation pressure and energy, supplemented by evolution equations for radiation, electron and ion internal energies, taking into account ion, electron and radiation heat transfer, energy exchanges between electrons and radiation.

Table 2.2: Characteristic collision distance (mean free path l) and time τ of atoms in the ablator cold part (Atzeni and Meyer-ter-Vehn (2004), Tab. 6.1).

l	τ
1 nm	10^{-5} ns

The ablator must be opaque toward the incoming irradiation in order to be set into motion. In the case of direct-drive (Chap. 1), this means that, at some point in the flow, the electron density exceeds the critical density above which laser photons cannot propagate deeper into the ablator. Laser light propagates in the expansion region up to the critical surface (referred to as the *external surface*, es, in Fig. 1.4). The laser energy is transmitted to electrons in the 'energy deposition' region. From the critical surface up to the ablation layer, the irradiation energy is transmitted mainly through electron heat transport ('conduction region'). The fluid model is adapted to describe this second region. Electron and ion temperatures differ in the conduction region away from the ablation layer, but converge when approaching the ablation front (e.g. Takabe et al., 1978). Therefore many models assume that electrons and ions are thermalized, i.e. a single ion–electron temperature is retained in the ablation wave. In addition, laser irradiation is sufficiently high so that electron heat transport dominates other diffusive effects: viscosity effects and radiation conduction. Finally, in the conduction region the electron mean free path is shorter than characteristic lengths of our system so that electron transport is approximated by electron heat conduction (Atzeni and Meyer-ter-Vehn, 2004, §7.2), i.e.

$$\boldsymbol{\varphi} = -\kappa_{\text{elec}}(T)\nabla T, \tag{2.7}$$

where the electron heat conductivity κ_{elec} depends on electron temperature.

In the case of indirect-drive, the driving irradiation is due to thermal radiation. Therefore, indirect-drive ICF is often referred to as radiation-driven ICF. The Rosseland mean free path of photons is small compared to the characteristic size of the ablation wave and local gradient lengths. Therefore radiative transport is approximated by radiation heat conduction (Zel'dovich and Raizer, 1967, §II.10), i.e.

$$\boldsymbol{\varphi} = -\kappa_{\text{rad}}(\rho, T)\nabla T^4, \tag{2.8}$$

where the radiative heat conductivity κ_{rad} depends on the fluid density and radiative temperature. In this case no critical surface is identified as in the direct-drive case, so that the 'external surface' corresponds to the actual external surface of the flow. As a consequence, there is no 'energy deposition' region (Fig. 1.4) in radiation-driven ablation flows. The validity of radiation heat conduction approximation is questionable in the low density tail of the expansion region (*low density corona*) at sufficiently long times because the Rosseland mean free path of photons ceases to be negligible. But our objective is to have an accurate description of the unstable region located close to the ablation front. Temperature at the external surface rises well above many thousands Kelvin (or 0.1 eV) but remains under a few million Kelvin (or a few hundreds eV), cf. Fig. 2.4. As a consequence, radiative energy gradients (radiation flux) dominate viscosity and thermal conduction effects, but radiation energy level and radiation pressure are negligible compared to internal energy and material pressure.

In both direct and indirect-drive cases, the flow dependent variables comprise the density, ρ, the velocity, $\boldsymbol{v}$, a single pressure, p, and temperature, T, defining a specific internal energy, ε. Heat transport is accounted for by means of a nonlinear heat-conduction flux $\boldsymbol{\varphi}$. In a Cartesian system of coordinates (O, x, y, z), motion equations write (Hirsch, 1988)

$$\partial_t \rho + \nabla(\rho \boldsymbol{v}) = 0, \tag{2.9a}$$

$$\partial_t(\rho \boldsymbol{v}) + \nabla \cdot (\rho \boldsymbol{v} \otimes \boldsymbol{v} + p\mathbb{I}) = \mathbf{0} \tag{2.9b}$$

$$\partial_t(\rho e) + \nabla \cdot (\rho \boldsymbol{v} e) = \nabla \cdot [\boldsymbol{\varphi} - p\boldsymbol{v}] + q_H, \tag{2.9c}$$

with the specific total energy

$$e = \varepsilon + \boldsymbol{v}^2/2, \tag{2.9d}$$

the laser photon energy deposition at the critical density surface in the case of direct-drive ICF q_H, and $\mathbb{I}$ the unit tensor. The material is considered to be a polytropic gas obeying the equation of state

$$p = \rho R T, \quad \varepsilon = R T/(\gamma - 1), \tag{2.10}$$

with R the gas constant and γ the adiabatic gas exponent. Finally, most of the models discard the spherical shell curvature effects. This assumption is reasonable in so far as the shell thickness is small compared to its radius, which is the case during the shock transit phase when the ablator has not converged. Additionally, the orthoradial characteristic size of the perturbation considered must be small compared to the shell radius.

The relative amount of acceleration g, due to the ablative pressure, with respect to convection effects is measured by the Froude number,

$$Fr = \frac{u_{\text{a}}}{\sqrt{g\,L}}, \tag{2.11}$$

where u_{a} is the material velocity, with respect to the ablation layer, at the ablation layer, and L a characteristic length. This non-dimensional number is a key parameter for the growth of ablation front instabilities, as explained in the next section. The whole shade of difference lies in the choice of the characteristic length L. Another non-dimensional number important to ablation flow modeling is the Mach number,

$$M = \frac{v_x}{c_\mathrm{s}}, \tag{2.12}$$

with v_x the fluid velocity and c_s the isentropic acoustic velocity at a given location. It measures the importance of compressibility effects. Finally, the Péclet number which measures the relative importance of heat convection over heat diffusion, is defined as

$$Pe = \frac{L v_x}{\chi}, \tag{2.13}$$

with χ the diffusivity.

Various models exist for analysing the stability of ablation waves. In the following section we describe their common foundations and discuss their particularities.

Despite the arrival of numerical simulations taking into account multiple physics couplings, designed to simulate the complete implosion of the target, some models have been derived to model the hydrodynamics of some specific stage of the implosion. These models provide a refined understanding of the key phenomena at stake. In that purpose, the stance is committed to work at the fluid scale and focus on hydrodynamics with nonlinear heat conduction. These models comprise evolution equations for a base flow and linear perturbations around it. The problem of the stability of linear perturbations often boils down to a dispersion relation obtained from a normal mode analysis.

2.2.1 Standard models of ablation flows

Models for steady laser ablation. The first published models of ablation flows and ablation front instabilities, assumed a stationary base flow. Bodner (1974) proposed to model the ablation layer as a rippled surface discontinuity with jump relations. The absence of heat conduction leads to the introduction of a closure relation *ad hoc*. The growth rate of the ripples arises as the classical Rayleigh–Taylor growth rate with a correction term

$$\sigma = \sqrt{g k_\perp} - k_\perp v_a, \tag{2.14}$$

where $k_\perp$ is the ripple wavenumber (Fig. 2.6), g is the external acceleration seen by the ablation layer and v_a the velocity of the fluid through the ablation front. Expression (2.14) displays a damping, relatively to the classical Rayleigh–Taylor growth rate (2.6), and the existence of a cut-off wave number. Kull and Anisimov (1986) introduce heat conduction into a discontinuous model assuming that pressure variations are small compared to temperature variations (quasi-isobaric, or low Mach-number, approximation), in a narrow region about the ablation front. A dispersion relation is obtained for arbitrary heat diffusion rates on each side of the discontinuity. In the limit of strong and negligible diffusions in, respectively, the conduction and compressed-fluid regions, a generalization of (2.14) for arbitrary Atwood number (2.5) is obtained along with a cut-off wavenumber. Due to the introduction of a surface discontinuity, these models are limited to small and moderate Froude numbers (Tab. 2.3). In (Kull, 1989), steady isobaric, yet continuous, ablation flows are considered with variations on the temperature exponent ν of the heat diffusivity (2.1). Linear instability growth rates are obtained as eigenvalues of linear perturbation boundary problems. Kull (1989) relaxes the assumptions, keeping the isobaric one, and investigates the influence of the functional form of heat-diffusion law. Sanz (1996) keeps the isobaric assumption but derives a continuous model of ablation front thanks to a matching of asymptotic expansions. The ablation front is considered as an isotherm, following the flame front analogy (Baker, 1978): as combustion ignites at constant temperature, material ablates at constant temperature. Therefore, a perturbed ablation front element keeps its temperature while moving. A dispersion relation points out the role of heat conduction as a stabilization mechanism: the crest of the rippled ablation front, closer to the heat source, ablates at a higher rate than the trough. This generates a counter pressure that drives the crest back to the mean position of the ablation front. This description is also proposed by Piriz et al. (1997), who derive an evolution equation for the ablation front deformation, z, based on a two fluid model similar to Bodner (1974), but taking into account heat conduction:

$$\frac{\mathrm{d}^2}{\mathrm{d}t^2}z + \eta\frac{\mathrm{d}}{\mathrm{d}t}z + \omega^2 z = 0, \quad \text{where} \quad \omega^2 \propto (k\,v_a^2/g - \beta) \quad \text{and} \quad \eta \propto k\,v_a, \tag{2.15}$$

where β is a coefficient taking into account the density jump across the ablation layer. Equation (2.15) gives another outlook, where the stability of the ablation front depends on the sign of ω which is driven by the dynamical pressure v_a^2, while material convection through the ablation layer acts only as damping. Goncharov et al. (1996b) take into account nonlinear heat-conduction in the isobaric approximation to derive a growth rate in the limit $Fr > 1$. In the opposite case ($Fr \ll 1$, Goncharov et al., 1996a), accounting for compressibility in addition to heat conduction leads to a stabilization wavelength smaller than the ablation layer thickness. Betti et al. (1998) perform a numerical fitting of the growth rate obtained from Goncharov et al. (1996a) with the ablation parameters (Froude number, thermal exponent, ablation front thickness, etc.) to compute expression of the growth rate known as *Takabe formulas*. Clavin and Masse (2004) derive a single model that describes a transition from flame front to ablation layer when varying the Froude from values much smaller to 1 to values close to 1. Based on a two-length-scale model, they found, amongst other results, that thermal relaxation plays a key role in the stabilization.

A key parameter is the characteristic size of the conduction region l_{cond} (Fig. 2.6), between the ablation layer and the surface of energy deposition. In the isobaric approximation of stationary laser-driven ablation flows, Goncharov et al. (2006) find that ablation front modes localized in the conduction region (i.e. of wavelength smaller than l_{cond}) oscillate and are stabilized by a restoring force due to thermal conduction. The longer wavelengths are not stabilized and grow as a result of Richtmyer–Meshkov and Darrieus–Landau mechanisms.

$$k_\perp l_{\text{cond}} > 1 : \quad \textit{damped oscillations} \tag{2.16a}$$

$$k_\perp l_{\text{cond}} < 1 : \quad \textit{growth.} \tag{2.16b}$$

Under the same assumptions, a dispersion relation valid for all wavelengths and accounting for the acceleration regime through the Froude number is derived in (Sanz et al., 2006).

If the base flow is not stationary, an alternative consists in using a frozen time assumption (FTA) of the flow, i.e. assuming that the characteristic evolution time of perturbations is much smaller than the characteristic time of the base flow. Such an assumption allows the consideration of more realistic base flows obtained from multiple physics simulation, frozen at a given time. Takabe et al. (1985) derive and solve an eigenvalue problem from a numerical fitting of flow simulations in spherical symmetry. Bychkov et al. (1991) point out the role of realistic boundary conditions in the derivation of an eigenvalue problem for linear perturbations. They confirm that the primary stabilizing effect is the convection of material through the ablation layer. In addition they show that this mechanism is more effective when the critical surface is close to the ablation layer, the position of the critical surface depending on the laser light wavelength. Bychkov et al. (1994) take into account a laser energy deposition term of finite size at the critical surface. They chose a characteristic length L (2.11) defined as the total thickness of the ablation layer, which is evaluated thanks to an integration of the stationary energy conservation equation across the ablation layer. For wavelengths large with respect to the ablation region, they recover the shape of the dispersion relations obtained with discontinuous models. For small wavelengths with respect to the ablation layer thickness, the stability depends on the Froude number. At moderate acceleration, $Fr < 1$, the 'discontinuous-model' dispersion relation remains valid, while at high acceleration, $Fr \ll 1$, the growth rate is much intricate, and in particular is Froude-dependent. It follows that for wavelengths smaller than the ablation region but larger than the heat-diffusion scale, the growth rate is independent of the thermal conduction. Gardner et al. (1991) perform extensive numerical integrations of perturbations for various ablator materials and laser wavelengths and recover most of the previous results. The growth rate is given by the mass perturbation: the integration of the density across the ablation wave.

Confinement effects. However, the ablation layer cannot be considered in actual ICF configurations as a stratified region between two semi-infinite slabs. The influence of the external or critical surface, downstream, of the forerunning shock front or material interface, upstream, at finite distances, and of travelling waves between these flow 'interfaces' must be taken into account. Such 'confinement effects' are especially important during the shock-transit phase of an implosion (item 1. of § 2.1) where the distances between these interfaces may be much smaller than perturbation transverse wavelengths. Nishihara et al. (1998) derive a model for the temporal evolution of shock front and ablation layer oscillations through a linear wave equation of perturbations in the shock compressed region. They successfully compare their modeled shock front ripples, ablation surface growth rate and areal mass perturbation with experimental data. They also point out that temperature and density perturbations whose wavelengths are larger than l_{cond} are not smoothed by thermal diffusion. Goncharov (1999) defines the 'ablative Richtmyer–Meshkov' instability (ARM) as the result of a distorted shock front created by the ablative pressure at a corrugated ablation front. The main stabilizing mechanism is found to be the dynamic overpressure resulting from thermal conduction. Wouchuk (2001a) derives an analytical model for the asymptotic growth rate of the Richtmyer–Meshkov instability resulting from the shock reflected by an incident planar shock on a corrugated interface, and when a rarefaction wave is reflected in the same conditions (Wouchuk, 2001b). These models accurately take into account the acoustic interactions between the corrugated surface and the reflected wave. Applied to ICF implosions, these works pave the way to the control of velocity perturbations by tuning an initial external pressure perturbation. Using a stationary model composed of two iso-density regions, Goncharov et al. (2000) isolate the effect of the confinement of the flow between the shock front and the ablation layer. This effect dominates over classical Rayleigh–Taylor growth for long distortion wavelengths of the ablation front with respect to the size of the post-shock region. The stretching of the post-shock region (increasing ablation layer – shock front distance) with mass conservation increases the perturbation growth. They recover the classical stabilizing effect of mass convection across the ablation layer, but for large wavelengths, the finite thickness is found to enhance this stabilization.

Compressibility effects. Compressibility effects are rarely taken into account in the above described models, which rely on a low-Mach approximation (Piriz, 2001; Boudesocque-Dubois et al., 2008; Clarisse et al., 2018; Bychkov et al., 2015, § 4.3)

$$\gamma M^2 \ll 1, \quad Fr \gg \sqrt{\gamma M^2}, \quad Pe \gg \gamma M^2. \tag{2.17}$$

Such inequalities are satisfied in the ablation layer, close to the peak density, but are not met at other locations, especially for self-similar flows obtained with growing external heat-flux in the range of ICF-like implosion, as described by Boudesocque-Dubois et al. (2008) and Clarisse et al. (2018).

Table 2.3: Main features of standard models for ablation flows: discontinuous models, ‘base’: base-flow model, ‘pert’: linear perturbation model. Columns: ‘**solutions**’: ‘given’: parameters (i.e. uniform state), ‘ODEs’: solutions to ordinary differential equations, ‘PDEs’: solutions to partial differential equations, ‘IBVP FTA’: Frozen Time Assumption of a base flow simulated through a multiple physics hydrocode, ‘piecewise’: piecewise solution, ‘**self-consistent**’: ‘no’ if necessary to use of an *ad-hoc* closure relation or source term, ‘**acc.** ’: additional term (ext.) for the acceleration or inherent (int.) to the flow description, ‘**perturbation scale**’: domain of validity of perturbations wavelength, ‘**stab.**’: type of stability analysis (for perturbations only), ‘NM’: normal-mode approach. Abbreviations: ‘stat.’: stationary, ‘incomp.’: incompressible, ‘LM’: low-Mach, ‘isoT’: isothermal, ‘isoS’: isentropic, ‘abiab.’: adiabatic.

Model		**solutions**	**self consist.**	**acc.**	**Flow regions**		**perturbation scale**	**stab.**
					cond	**comp.**		
Bodner (1974)	base	given stat.	no	ext.	incomp.	incomp. LM		
	pert	PDEs			LM	incomp.	$l_{\mathrm{af}} \ll \lambda_{\perp} \ll l_{\mathrm{cond}}$	NM
Kull and Anisimov (1986)	base	ODEs stat.	no	ext.	LM	LM		
	pert	PDEs					$l_{\mathrm{af}} \ll \lambda_{\perp}$	NM
Manheimer and Colombant (1984)	base	given stat.	no	ext.	iso T or adiab.	adiab. incomp.		
	pert	PDEs				incomp.	$l_{\mathrm{af}} \ll \lambda_{\perp}$	NM
Bychkov et al. (1994)	base	ODEs stat.	yes	int.	LM	LM		
	pert	PDEs					$l_{\mathrm{af}} \ll \lambda_{\perp}$	NM
Goncharov (1999); Goncharov et al. (2000, 2006)	base	given uniform	yes	int.				
	pert	PDEs piecewise					$l_{\mathrm{af}} \ll \lambda_{\perp}$	NM
Piriz (2001)	base	stat.	yes	ext.	LM	LM		
	pert	PDEs			isoT	isoS	$\lambda_{\perp} < l_{\mathrm{af}}$	NM
Clavin and Masse (2004)	base	ODEs stat.	yes	ext	LM	LM		
	pert	PDEs					$l_{diff,cold} \ll \lambda_{\perp} \ll l_{\mathrm{cond}}$	NM

Models for steady radiation-driven ablation. All the above mentioned models describe laser ablation, representative of direct-drive ICF, where electron heat conduction is the main transport phenomenon. Fewer works are dedicated to radiative ablation (Tab. 2.5). Nozaki and Nishihara (1980) propose a model of stationary radiation-driven ablation in planar symmetry. The ablation flow is decomposed into an undisturbed uniform region, a shock compression, a deflagration region — i.e. the ablation layer, locus of the strongest opposite gradients in density and temperature — and an isothermal expansion region (cf. Fig. 1 in Nozaki and Nishihara, 1980). The point at which the expansion velocity exceeds the isothermal acoustic velocity — isothermal Chapman–Jouguet (CJ) point — defines the boundary between the steady deflagration and the necessarily unsteady isothermal expansion. Two types of ablation waves are distinguished: (1) subcritical deflagrations, characterized by radiation not in thermodynamic equilibrium with the expanding plasma, and (2) supercritical deflagrations for which radiation is in thermodynamic equilibrium throughout the expansion region up to the CJ point. Subcritical deflagrations are found to be more efficient than supercritical ones, in terms of fluid compression. Nishihara (1982) focuses on

Table 2.4: Main features of standard models for ablation flows: continuous models. Terminology similar to Tab. 2.3. Additional abbreviations: ‘assymp.’: solution in an assymptotic limit, ‘isoV’: isochoric, ‘NL’: nonlinear, ‘exp.’: fitted exponential growth rate.

			self		**Flow regions**			**perturbation**	
Model		**solutions**	**consistent**	**acc.**	**cond**	**af**	**comp**	**scale**	**stab.**
Barrero and Sanmartín (1977); Sanmartín and Barrero (1978)	base	ODEs self-sim. piecewise	yes	int.					
Takabe et al. (1985)	base	IBVP FTA	self	int.					
	pert	PDEs						$\lambda \ll l_{\text{cond}}$	NM
Kull (1989)	base	ODEs stat	yes	ext.	LM	LM	LM isoV		
	pert	PDEs piecewise							NM
Bychkov et al. (1991)	base	IBVP FTA	yes	int.					
	pert	PDEs							NM
Gardner et al. (1991)	base	IBVP FTA				yes	int.		
	pert	NL IBVP exp.							NM
Sanz (1996)	base	assymp. stat.	yes	ext.	LM	LM	adiab. LM		
	pert	assymp.						$l_{\text{af}} \ll$	NM
Goncharov et al. (1996b,a); Betti et al. (1998)	base	ODEs stat.	yes	int.	LM	LM	LM		
	pert	PDEs						$l_{\text{af}} \ll$ or $\ll l_{\text{af}}$	NM
Le Métayer and Saurel (2006)	base	ODEs stat.	yes	no					
Clavin and Masse (2004)	base	ODEs stat.	yes	ext	LM		LM		
	pert	PDEs						$l_{diff,cold} \ll \lambda_\perp \ll l_{\text{cond}}$	NM

subcritical deflagrations and obtains scaling laws for the ablation essential parameters. Hatchett (1991) considers the deflagration region as a discontinuity and radiation in thermodynamic equilibrium. The supersonic (detonation) and subsonic (deflagration) regimes are analyzed with scaling laws for the heat wave parameters. Saillard et al. (2010) further refine stationary ablation modeling using the same ablation-wave decomposition as Nozaki and Nishihara (1980) but assuming thermodynamic equilibrium radiation. Approximate analytical expressions are provided for the ablation essential parameters and for the density and temperature spatial profiles in the expansion and deflagration regions, as functions of the radiation drive law.

These models share the same assumptions of planar symmetry and of an isothermal expansion which are necessary to a stationary ablation flow. Stability analysis of such model flows has never been specifically addressed, contrasting with the many works devoted to laser-driven ablation. Rather, the parametrized formulas of Betti et al. (1998) for ablative Rayleigh–Taylor instability, developed in the case of laser-driven ablation, are considered as relevant and directly applicable to radiative ablation (cf. Lindl et al., 2004, § VI.C and Lindl et al., 2014, § V.B.8).

Another approach to the stability of radiation-driven ablation flows builds up from considering self-similar ablation waves.

Table 2.5: Base flow models for radiation driven ablation. Terminology similar to Tab. 2.3.'regularity': continuity of the ablation front, 'jump': jump relations between the conduction region and the compression region.

					Flow regions		
Model	solved	acc.	self consist.	regularity	cond	af	comp
Nozaki and Nishihara (1980)	ODEs stat.	int.	yes	continuous			
Nishihara (1982)	– stat.	int.	yes	jump			
Saillard et al. (2010)	ODEs piecewise stat.	int.	yes	jump	LM. isoT.	LM.	isoS

2.2.2 Self-similar ablation waves

The *standard models* of steady ablation reviewed above rely on assumptions that are not necessarily met in realistic ablation flows. In addition to the unfulfilled low-Mach conditions throughout an ablation wave, the expansion flow is not treated in instability models of laser-driven ablation Bychkov et al. (2015). This truncation of the base flow, or the restriction of the flow modeling to a low-Mach number region, imposes constrains on the perturbation wavelength that are problematic when treating the shock-transit phase of an implosion. Ablation steadiness, and therefore the assumption of an isothermal expansion in the modeling of radiation-driven ablation, is also hardly justified for this early implosion stage for which numerical simulations indicate that the corresponding flows are more akin to self-similar than to steady behaviors (Velikovich et al., 1998). Relaxing such assumptions is possible upon exploiting unsteady self-similar solutions to the Euler equations with nonlinear heat conduction, first identified by Marshak (1958).

The solutions studied by Marshak (1958) correspond to the configuration discussed at the beginning of the present chapter (see Fig. 2.1): a semi-infinite slab of a cold inviscid gas, initially at rest, expands into vacuum under a strong irradiation of its external surface. Self-similarity is obtained provided that the irradiation flux follows some specific time-power laws. This peculiar situation is recovered with the simplified analysis leading to (2.1)–(2.3) for the particular value $q = 1/(\nu - 1)$. The heat-front velocity, driven by heat transport, and shock-front velocity, driven by hydrodynamics, evolve then similarly. The respective positions of these fronts, and therefore the flow regime that they depict, are determined, in this case, by the constant factors that are omitted from (2.2), (2.3) (Zel'dovich and Raizer, 1967, vol. II, § X). This simple example just gives a flavor of the interest presented by Marshak's solutions: the full range of nonlinear heat-wave regimes is covered with the full complexity of the non-viscous compressible fluid equations with nonlinear heat conduction, without any compromise in its description (i.e. without isobaric, steadiness, discontinuous, uniformity, etc. assumptions). Self-similarity is a valuable feature since the base-flow problem boils down to a system of ordinary differential equations (ODEs), rather than of partial differential equations (PDEs).

Building on Marshak's solutions, Bajac (1973) is interested in radiative shock waves in general, more than in the ablation regime. He computes solutions that describe the shock front taking over the supersonic thermal front. Barrero and Sanmartín (1977) derive a two-temperature (electron and ion) model for laser ablation plasma. They compute solutions in the limiting cases of a heating (i) dominated by electron heat conduction, resulting from a very intense external irradiation leading to a supersonic regime, and (ii) dominated by convection, resulting from a moderately intense external irradiation, which gives rise to a forerunning shock front and therefore corresponds to the subsonic ablation regime. In the latter case, electron and ion temperatures are very close.

Through the point explosion problem with nonlinear heat conduction, Reinicke and Meyer-ter-Vehn (1991) compute numerical solutions to the self-similar equations in spherical coordinates. Their solutions describe the early supersonic phase and the later subsonic ablation regime, with a disruption denoting the transition between these two regimes (the shock front overtaking the thermal front). Sanz et al. (1992) propose a model where the expanding plasma is tamped by a wall. Numerical solutions are computed in the asymptotic case of large Pe, i.e. for high ratio of heat convection to heat diffusion, describing the subsonic ablation regime, for the conduction region and the compression region. However these solutions cease to be valid close to the ablation front and do not describe the ablation front.

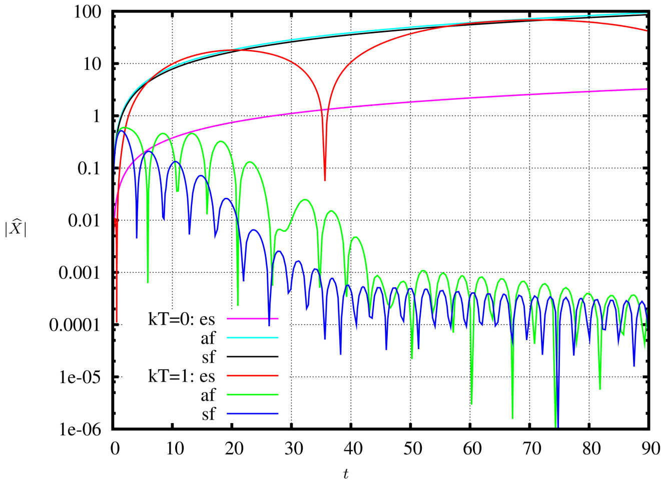

Figure 2.7: External surface (es), ablation front (af) and shock front (sf) perturbations for $k_\perp = 0$ and $k_\perp = 1$ (from Clarisse et al., 2016). External heat flux perturbation starting at $t_0 = 10^{-7}$.

Numerical solutions to self-similar ablation flows, representative of either direct or indirect-drive ablation, with none of the above restrictions, are actually computed in (Boudesocque-Dubois, 2000; Boudesocque-Dubois et al., 2001, 2008; Abéguilé et al., 2006; Clarisse et al., 2018) for wide ranges of heat flux and pressure at the fluid external boundary. These solutions are obtained with the numerical method outlined in § 3.3.2 which is capable of describing accurately the whole flow structure of the ablation, or subsonic heat wave, regime, i.e. from the forerunning shock front up to the external surface. As for all self-similar solutions presented here, they are free of the isobaric, isothermal, low-Mach, stationary, etc. assumptions. But their main benefit is that they are not computed only in asymptotic cases of low heat-conduction and that they describe accurately the ablation layer. A complete hydrodynamic characterization of ICF ablation flows is provided in Boudesocque-Dubois et al. (2008); Clarisse et al. (2018). Dastugue et al. (2012) and Dastugue (2013) pursue this study by computing a series of self-similar solutions describing the transition between the supersonic thermal wave to the subsonic ablation regime.

The numerical quality of these solutions is sufficient to compute the evolution of three-dimensional linear perturbations. Shock front and ablation layer oscillations are in qualitative agreement with *standard models* (Fig. 2.7). However the inherent stretching, or expansion, of ablation flows, accounted for in self-similar solutions, results in an algebraic growth in time of these oscillations (in the growth case) rather than a linear growth and an adaptation of the stability criterion (2.16) (Abéguilé et al., 2006; Clarisse et al., 2008, 2016). Perturbation propagation in the post-shock region is characterized in terms of Kovásznay modes in (Lombard et al., 2008).

The importance of the short term development of perturbations, before the extensively described oscillating behavior sets up, is stressed in (Dastugue, 2013; Clarisse et al., 2016). In the further developments, we make the most of self-similar solutions to conduct the linear stability analysis.

CHAPTER 3

Linear perturbations of self-similar ablation waves

Chapter Abstract

Starting from the Euler equations with nonlinear heat conduction, we recall some useful information about self-similar solutions and the reduced coordinate system (§ 3.1). Governing equations, together with boundary conditions, for three-dimensional linear perturbations are obtained from the Eulerian representation and then formulated in mass coordinate according to the reduced coordinate (§ 3.2). We then illustrate the relations between the three different coordinate systems used.

In § 3.3 we outline the principal numerical methods used for space discretization and time integration. The present work looks upon two different radiation-driven base-flows presented in § 3.4 and illustrated with numerical feature. A new set of pseudo-characteristic variables is finally introduced and allows us to present a first physical analysis of linear perturbation propagation in ablation waves (§ 3.5).

3.1 Self-similar ablation waves

In Chap. 2 we have argued that ablation waves representative of ICF ablation could be adequately described by an inviscid fluid model in slab symmetry (Fig. 1.3), with nonlinear heat-conduction (2.7)–(2.8) and without taking into account radiative, or laser photon, pressure. The fluid obeys the equation of state (2.10) and its motion is described in a Cartesian coordinate system (O, x, y, z), along the x direction. The external surface (es on Fig. 3.1) is a material interface, i.e. it is linked to a given fluid element, unlike the shock front. The evolution of the external surface is easily described in the Lagrangian variable m defined as $\mathrm{d}m = \bar{\rho}\mathrm{d}x$, where $\bar{f}$ stands for the Lagrangian dependent variable corresponding to the Eulerian dependent variable f. A coordinate m corresponds to a given fluid element, therefore the external surface is at fixed $m = m_{\mathrm{es}}$, and we arbitrarily choose $m_{\mathrm{es}} = 0$. At the external surface we assume that the pressure (respectively heat flux) is time dependent and reaches a reference value p_* (resp. φ_*) at some reference time $t_* > 0$. We assume that at $t = 0$ the fluid occupies the half-space $m \geq 0$ and is in a state at rest (Fig. 3.1), given by

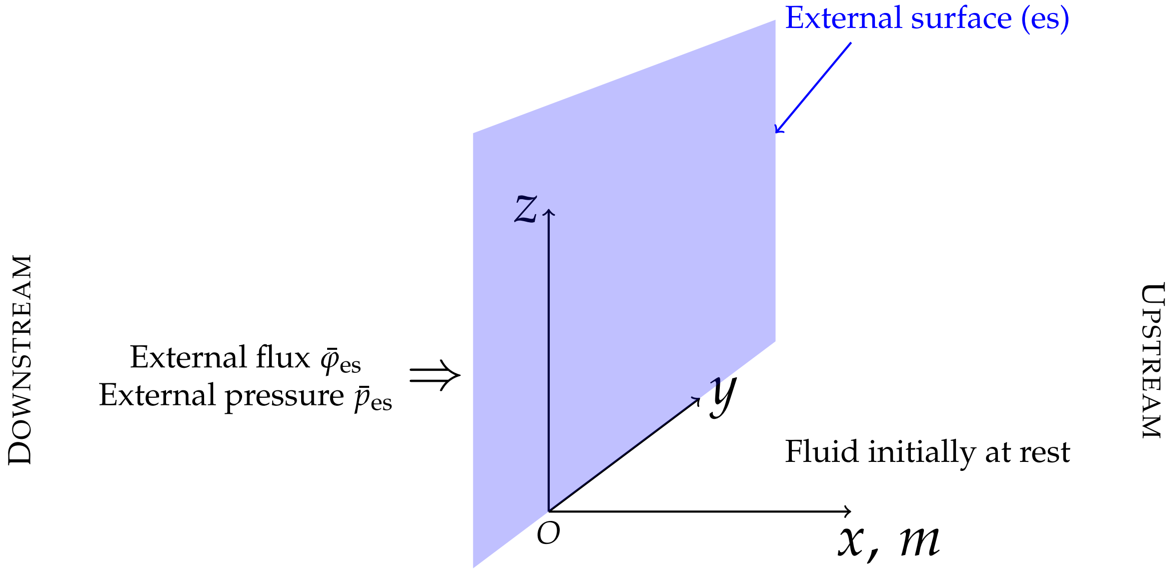

Figure 3.1: Geometry of the problem.

$$\begin{pmatrix} \bar{\rho} \\ \bar{v}_x \\ \bar{T} \end{pmatrix} = \begin{pmatrix} \rho_* \\ 0 \\ 0 \end{pmatrix}, \quad \text{with} \quad \rho_* = \text{const} \geqslant 0. \tag{3.1}$$

The heat flux is assumed to follow a power-law dependency

$$\bar{\varphi}_x \equiv \kappa_* \Psi(\bar{\rho}, \bar{T}, \bar{\rho}\partial_m \bar{T}), \tag{3.2a}$$

$$\Psi(\bar{\rho}, \bar{T}, \bar{\rho}\partial_m \bar{T}) = -\left(\frac{\bar{\rho}}{\rho_*}\right)^{-\mu} \left(\frac{\bar{T}}{T_*}\right)^{\nu} \bar{\rho}\partial_m \bar{T}, \tag{3.2b}$$

where κ_* and T_* are reference values for the heat conduction coefficient and temperature, and μ and ν are constants such that

$$\kappa_* > 0, \quad T_* > 0, \quad \mu \geq 0, \quad \nu > 1. \tag{3.3}$$

3.1.1 Dimensionless formulation

The initial and boundary value problem (2.9), (2.10) depends on seven parameters: ρ_*, p_*, φ_*, γ, κ_*, t_* and the ideal gas constant R. From the Π-theorem (Barenblatt, 1979), we may retain ρ_*, t_*, κ_* and R as reference quantities and define three dimensionless numbers

$$\gamma, \quad \mathcal{B}_\varphi = \varphi_* \sqrt{\rho_* \left(\frac{t_* R}{\kappa_*}\right)^3} \quad \text{and} \quad \mathcal{B}_p = p_* \frac{t_* R}{\kappa_*}. \tag{3.4}$$

The gas exponent γ is fixed in our study. The two remaining parameters, $\mathcal{B}_\varphi$ and $\mathcal{B}_p$ drive the intensity of the heat flux and pressure at the external surface. Let $\bar{f}$ now denote the dimensionless variable of the corresponding dimensional variable. Differentiation operators in Lagrangian coordinate write

$$\partial_t \bar{f} = \partial_t f + v_x \partial_x f \quad \text{and} \quad \bar{\rho} \partial_m \bar{f} = \partial_x f. \tag{3.5}$$

Evolution equations (2.9), with the above conventions, come in dimensionless form (Clarisse et al., 2008) as

$$\partial_t (\frac{1}{\bar{\rho}}) - \partial_m \bar{v}_x = 0, \tag{3.6a}$$

$$\partial_t \bar{v}_x + \partial_m \bar{p} = 0, \tag{3.6b}$$

$$\partial_t \left(\mathrm{C}_v \bar{T} + \bar{v}_x^2/2 \right) + \partial_m (\bar{p} \bar{v}_x + \bar{\varphi}_x) = 0, \quad \text{with} \quad \mathrm{C}_v = \frac{1}{\gamma - 1}, \tag{3.6c}$$

and

$$\bar{\varphi}_x = \Psi(\bar{\rho}, \bar{T}, \bar{\rho} \partial_m \bar{T}). \tag{3.6d}$$

External heat flux and dimensionless boundary conditions at the external surface are taken of the form

$$\bar{p}(0,t) = \mathcal{B}_p t^\beta, \tag{3.7a}$$

$$\bar{\varphi}(0,t) = \mathcal{B}_\varphi t^\delta, \tag{3.7b}$$

and the dimensionless equation of state closes the system

$$\bar{p} = \bar{\rho} \bar{T}. \tag{3.8}$$

Other dimensionless formulations can be chosen (Clarisse et al., 2018). The interest of the present one lie sin the general formulation of the evolution equations which do not depend on the parameters $\mathcal{B}_\varphi$ and $\mathcal{B}_p$. These dimensionless driving parameters are ascribed to the boundary conditions (3.7).

3.1.2 Self-similar solutions

The set of self-similar solutions that we consider for modeling shock-transit phase flows, proceeds from the family of density invariant solutions to (3.6) detailed in (Boudesocque-Dubois et al., 2008). These solutions depend on a single reduced independent variable

$$\xi = \frac{m}{t^\alpha}, \quad \text{where} \quad \alpha = (2\nu - 1)/(2\nu - 2). \tag{3.9}$$

Dimensionless dependent variables $\bar{\rho},\ \bar{v}_x,\ \bar{T},\ \bar{p}$ and $\bar{\varphi}_x$, corresponding to this set of solutions, are related to the reduced variables $\bar{\mathbf{U}} = (\bar{G} \quad \bar{V}_x \quad \bar{\Theta} \quad \bar{\Phi})^\top$ and $\bar{P}$ through the relations

$$\bar{\rho}(m,t) = \bar{G}(\xi), \tag{3.10a}$$

$$\bar{v}_x(m,t) = t^{\alpha-1}\bar{V}_x(\xi), \tag{3.10b}$$

$$\bar{T}(m,t) = t^{2(\alpha-1)}\bar{\Theta}(\xi), \tag{3.10c}$$

$$\bar{p}(m,t) = t^{2(\alpha-1)}\bar{P}(\xi), \tag{3.10d}$$

$$\bar{\varphi}_x(m,t) = t^{3(\alpha-1)}\bar{\Phi}(\xi). \tag{3.10e}$$

The reduced variables $\bar{\mathbf{U}}$ are solutions to the nonlinear differential equation

$$\mathrm{d}_\xi \bar{\mathbf{U}} = \mathcal{F}(\xi, \bar{\mathbf{U}}), \tag{3.11}$$

where the function $\mathcal{F}$ is given in (Boudesocque-Dubois et al., 2008), Eq. (2.18). The reduced variables satisfy the dimensionless equation of state

$$\bar{P} = \bar{G}\bar{\Theta}, \tag{3.12}$$

and the reduced heat flux come as

$$\bar{\Phi} = \Psi(\bar{G}, \bar{\Theta}, \bar{G}\mathrm{d}_\xi\bar{\Theta}), \quad \text{with} \quad \Psi(\bar{G}, \bar{\Theta}, \bar{G}\mathrm{d}_\xi\bar{\Theta}) = -\bar{G}^{-\mu}\bar{\Theta}^{\nu}\bar{G}\mathrm{d}_\xi\bar{\Theta}. \tag{3.13}$$

Boundary conditions are given by

$$\bar{P}(\xi = 0) = \mathcal{B}_p, \quad \bar{\Phi}(\xi = 0) = \mathcal{B}_\varphi, \tag{3.14a}$$

$$\bar{G}(\xi \to +\infty) = 1, \quad \bar{V}_x(\xi \to +\infty) = \bar{\Theta}(\xi \to +\infty) = 0. \tag{3.14b}$$

The ordinary differential equation (3.11) presents three kinds of singularities, each of them representing a particular feature of the propagation of a thermal wave (Reinicke and Meyer-ter-Vehn, 1991; Boudesocque-Dubois et al., 2008; Clarisse et al., 2018):

- an isothermal sonic point at $\xi_{\mathrm{sp}} = \bar{G}^2\bar{\Theta}/\alpha$,

- a thermal-wave front at ξ_{th} where $\bar{G}(\xi) \to 1^+$, $\bar{V}(\xi) \to 0^+$, $\bar{\Theta}(\xi) \to 0^+$ and $\bar{\Phi}(\xi) \to 0^+$, as $\xi \to \xi_{\mathrm{th}}^-$,

- an ablation front in an infinitely dense medium at ξ_{ρ_∞}, where $\bar{G}(\xi) \to \infty$, $\bar{\Theta}(\xi) \to 0^+$, $\bar{G}\bar{\Theta} < \infty$ and $\bar{\Phi}(\xi) \to 0^+$ as $\xi \to \xi_{\rho_\infty}^-$.

The isothermal sonic point and the thermal-wave are the singularities relevant to the modeling of our problem. Marshak (1958) noted that both singularities may exist: the sonic point corresponds to an isothermal shock front at ξ_{sp} and the compressed fluid radiates through the latter, so that an 'infinitesimal radiation wavelet' (Marshak, 1958) precedes the isothermal shock front at ξ_{th} and preheats the unshocked cold fluid. This 'Marshak wavelet' when negligible, as it is the case for not too high values of the heat flux parameter $\mathcal{B}_\varphi$, may be combined with the isothermal shock front into a non-isothermal shock front at $\xi_{\mathrm{sf}} \approx \xi_{\mathrm{sp}} \approx \xi_{\mathrm{th}}$ (Marshak, 1958; Boudesocque-Dubois et al., 2008; Clarisse et al., 2018). Boundary conditions at $\xi \to +\infty$ (3.14b) are therefore replaced by non-isothermal

Rankine–Hugoniot relations at ξ_{sf}, in the strong shock approximation, between the unshocked region

$$\left(\bar{G}_u \quad \bar{V}_{x_u} \quad \bar{\Theta}_u\right) = \left(1 \quad 0 \quad 0\right), \quad \text{for} \quad \xi \geqslant \xi_{\mathrm{sf}}, \tag{3.15}$$

and the shocked fluid domain $\xi < \xi_{\mathrm{sf}}$ (3.16). These non-isothermal Rankine–Hugoniot relations are given by (Boudesocque-Dubois et al., 2008, Eq. A2)

$$\bar{G}|_{\mathrm{sf}^-} = \frac{(\gamma+1)\bar{W}}{\gamma\bar{W}^2 - \mathcal{R}}, \quad \bar{V}_x|_{\mathrm{sf}^-} = \frac{\bar{W}^2+\mathcal{R}}{(\gamma+1)\bar{W}}, \quad \bar{P}|_{\mathrm{sf}^-} = \frac{\bar{W}^2+\mathcal{R}}{\gamma+1}. \tag{3.16a}$$

with

$$\mathcal{R} = \sqrt{\bar{W}^4 - 2(\gamma-1)(\gamma+1)\bar{W}\bar{\Phi}(\xi_{\mathrm{sf}}^-)} \tag{3.16b}$$

where $\bar{W}$ is the shock front reduced velocity, defined as

$$\bar{W} \equiv t^{1-\alpha}\left(\partial_t x(m,t)\right)|_{\xi_{\mathrm{sf}}} = \left(\frac{\alpha\xi_{\mathrm{sf}}}{\bar{G}(\xi_{\mathrm{sf}})} + \bar{V}_x(\xi_{\mathrm{sf}})\right).$$

The only heat flux at the shock front, $\Phi|_{\mathrm{sf}^-}$, is not given by Rankine-Hugoniot jump relations.

Second law of thermodynamics at the shock front. The radiation transport has a strong impact on the structure of the shock front. For a sufficiently high temperature of the compressed fluid $\bar{T}_{\mathrm{comp}}$, the unshocked fluid is heated by the radiation wavelet up to $\bar{T}_-$ and jumps to a peak temperature $\bar{T}_+$ as a result of compression. The compressed fluid then cools down by the emission of radiation energy over a few photon mean free path to reach $\bar{T}_{\mathrm{comp}}$. Although $\bar{T}_-$ increases with the strength of the compression, $\bar{T}_-$ can at most reach $\bar{T}_{\mathrm{comp}}$ but never exceed it. Indeed, the case $\bar{T}_- > \bar{T}_{\mathrm{comp}}$ implies a spontaneous energy transfer from a region of low temperature to a region of high temperature, which contradicts the second law of thermodynamics (Zel'dovich and Raizer, 1967, VII, §14).

In our case, radiation heat transfer is considered under the radiation heat conduction approximation, which is valid in the compression region close to the shock front. In such a case, phenomena occurring at distances less than the scale of photon mean free path are not considered, which results in a "cut off" of the peak temperature $\bar{T}_+$. The temperature profile corresponds to that of an isothermal shock front, i.e. continuity of the temperature through the front, preceded by the preheating wavelet. The entropy distribution reaches a peak value in the shock front, but its downstream value is higher thant its value upstream from the shock front (Zel'dovich and Raizer, 1967, VII, §3).

Coordinate systems

The corresponding abscissa x of a fluid element m^* is given by

$$x(m^*,t) = t^\alpha\left(\frac{\xi^*}{\bar{G}(\xi^*)} + \frac{\bar{V}_x(\xi)}{\alpha}\right) + x(0,0) = t^\alpha\bar{X}(\xi^*) + x(0,0), \quad \xi = m^*/t^\alpha, \tag{3.17}$$

with $\bar{X}$ the reduced position in the reference frame. Equation (3.17) indicates that lengths scale as $l(t) = t^\alpha L$, where L is a reduced length. Self-similar ablation waves develops at $t = 0$ from a point located at $\xi = 0$, or $m = 0$, or $x = x(0,0)$ (Fig. 3.2). In the Eulerian coordinate (x,t), the shock front (sf) and the ablation layer propagate upstream (growing x), while the external surface (es) may propagate inward or outward depending on the external pressure strength. The trajectories of a fluid element located at m^* are represented in the three different coordinate systems on Fig. 3.2: $x = x(m^*, t)$, $m = m^*$ and $\xi = m^*/t^\alpha$. Each of these coordinate system has its own interest:

- *Cartesian coordinate system* (x, y, z, t): it is the natural coordinate system to obtain the evolution equations for the base flow and the linear perturbations (§ 3.2).

- *Lagrange coordinate system* (m, y, z, t): or 'mass variable', such that $\mathrm{d}m = \bar{\rho}\mathrm{d}x$. The coordinate transformation $(x, t) \rightarrow (m, t)$ incorporates the fluid motion, meaning that fluid particles move at constant m, i.e. describe vertical lines in the (m, t) diagram (Fig. 3.2). This point is of interest in order to characterize the advection of perturbations at the fluid velocity, which describes vertical lines in the (m, t) diagram (i.e. constant m). The mass coordinate is the natural independent variable for describing the motion of a material interface such as the external surface.

- *Self-similar coordinate system* (ξ, y, z, t): the coordinate system for which base flow profiles are time homothetic. The external surface, shock front and ablation layer velocities follow the same time dependency. This property is inscribed into the definition of the reduced coordinate $\xi = m/t^\alpha$, $\alpha > 1$, which takes into account the expanding nature of the ablation wave and is exemplified by the fact that trajectories of the flow external surface, ablation front and shock front are vertical lines in a (ξ, t) diagram. The ablation front is defined as the location of the minimum of the temperature gradient length, located in the ablation layer.

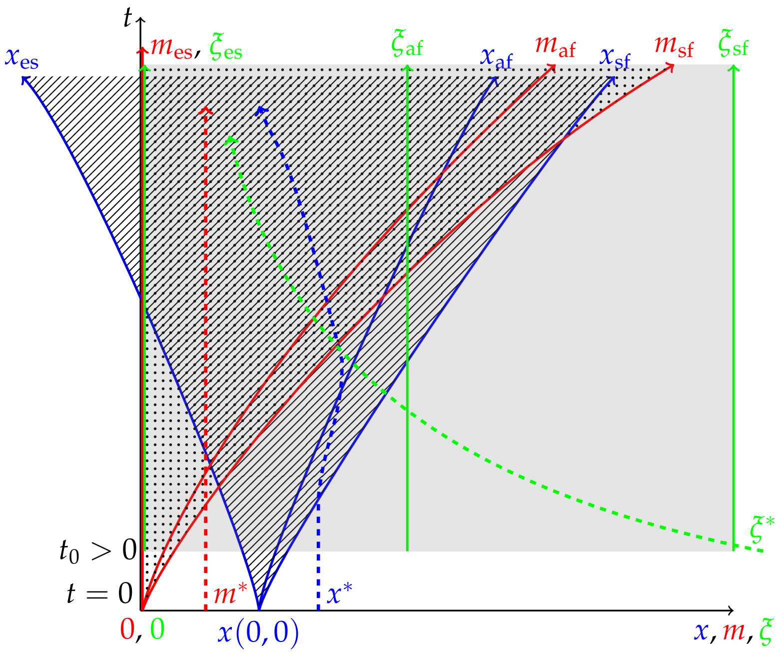

Figure 3.2: Representation of the ablation wave extents in the three coordinate systems that are used: hatched for the coordinate system (x, t), dotted for (m, t) and in gray for (ξ, t). Plain lines: trajectories of the external surface (es), ablation front (af) and shock front (sf) in the coordinate system (x, t), (m, t) and (ξ, t) in blue, red and green, respectively. Dashed lines: trajectories of a fluid particles m^* in the three coordinate system, same color code.

3.2 Linear perturbations of a self-similar ablation wave

The linear stability analysis starts by obtaining the evolution equations of first-order perturbations of base flow variables. Any Eulerian dependent variable now write

$$f(x,y,z,t) = f^{(0)}(x,t) + \epsilon f^{(1)}(x,y,z,t) + \mathcal{O}(\epsilon^2), \tag{3.18}$$

where $f^{(0)}$ is the Eulerian dependent variable corresponding to the solution to (3.6), (3.7), and $f^{(1)}$ denotes its three-dimensional linear perturbation. The linear perturbation $f^{(1)}$ is a good approximation of small fluctuations of f around $f^{(0)}$, i.e. for infinitesimal values of the parameter ϵ.

Linear perturbations in the coordinate system (m,y,z,t)**.** Assuming that $\bar{f}$ is solution to (3.6), the Euler equations with nonlinear heat conduction for f leads to evolution equations for the linear perturbations in Lagrangian variable, $\widetilde{f}$, which write

$$\partial_t\widetilde{\rho} + \bar{\rho}\big(\partial_m\bar{\rho}\,\widetilde{v}_x + \bar{\rho}\,\partial_m\widetilde{v}_x + \partial_m\bar{v}_x\,\widetilde{\rho} + \nabla_\perp\cdot\widetilde{\boldsymbol{v}}_\perp\big) = 0, \tag{3.19a}$$

$$\partial_t\widetilde{v}_x + \bar{\rho}\,\partial_m\bar{v}_x\,\widetilde{v}_x + \partial_m\widetilde{p} - \partial_m p\,\widetilde{\rho}/\bar{\rho} = 0, \tag{3.19b}$$

$$\partial_t\widetilde{\boldsymbol{v}}_\perp + \frac{1}{\bar{\rho}}\nabla_\perp\widetilde{p} = \mathbf{0}, \tag{3.19c}$$

$$\begin{aligned} &C_v\big(\partial_t\widetilde{T} + \bar{\rho}\,\partial_m\bar{T}\,\widetilde{v}_x\big) + \bar{\rho}\,\partial_m\bar{v}_x\,\widetilde{T} + \bar{p}\,\partial_m\widetilde{v}_x + \partial_m\widetilde{\varphi}_x \\ &\qquad - \partial_m\bar{\varphi}_x\,\widetilde{\rho}/\bar{\rho} + \big(\bar{p}\,\nabla_\perp\cdot\widetilde{\boldsymbol{v}}_\perp + \nabla_\perp\cdot\widetilde{\boldsymbol{\varphi}}_\perp\big)/\bar{\rho} = 0, \end{aligned} \tag{3.19d}$$

where $\widetilde{\boldsymbol{v}}_\perp$ denotes the transverse component (i.e. in the (O,y,z) plane) of the velocity linear perturbation. The longitudinal component of the heat-flux perturbation $\widetilde{\varphi}$ expands as

$$\widetilde{\varphi}_x = \widetilde{\rho}\,\Psi_\rho + \widetilde{T}\,\Psi_T + \bar{\rho}\Psi_{T'}\partial_m\,\widetilde{T} \tag{3.20}$$

where Ψ_ρ, Ψ_T and $\Psi_{T'}$ stand for the partial derivatives of Ψ (3.2a) with respect to density, temperature and temperature gradient. The equation of state (2.10) yields its linearized form as

$$\widetilde{p} = \widetilde{\rho}\bar{p} + \bar{\rho}\widetilde{p}. \tag{3.21}$$

The transverse component of the heat-flux linear perturbation is defined by

$$\widetilde{\boldsymbol{\varphi}}_\perp = \Psi_{T'}\nabla_\perp\widetilde{T}. \tag{3.22}$$

In (3.19) we have used the transverse gradient, $\nabla_\perp = \big(\partial_y\;\partial_z\big)^\top$, and the transverse divergence, $\nabla_\perp\cdot$. Following a Helmholtz decomposition of the transverse velocity field $\widetilde{\boldsymbol{v}}_\perp$, the rotational part is conserved according to the conservation equation

$$\partial_t\nabla_\perp\times\widetilde{\boldsymbol{v}}_\perp = \mathbf{0}, \tag{3.23}$$

and (3.19c) is replaced by

$$\partial_t\nabla_\perp\cdot\widetilde{v}_\perp + \frac{1}{\bar{\rho}}\Delta_\perp\widetilde{p} = 0, \quad \text{where} \quad \Delta_\perp = \nabla_\perp\cdot\nabla_\perp. \tag{3.24}$$

(O, y, z)-Fourier transformation of linear perturbations. Equations (3.19) are Fourier transformed in the (O, y, z) plane as the base flow dependent variables do not depend on (y, z) coordinates. The Fourier component $\widehat{f}$ of the linear perturbation $\widetilde{f}$ depends on the transverse wave number $k_\perp = \sqrt{k_y^2 + k_z^2}$. We introduce the Fourier component $\widehat{d}_\perp$ of the transverse divergence of the transverse velocity $\nabla_\perp \cdot \widetilde{\boldsymbol{v}}_\perp$. Evolution equations for Fourier components read

$$\partial_t \widehat{\rho} + \bar{\rho}\big(\partial_m \bar{\rho}\, \widehat{v}_x + \bar{\rho}\, \partial_m \widehat{v}_x + \partial_m \bar{v}_x\, \widehat{\rho} + \nabla_\perp \cdot \widehat{\boldsymbol{v}}_\perp\big) = 0, \tag{3.25a}$$

$$\partial_t \widehat{v}_x + \bar{\rho}\, \partial_m \bar{v}_x\, \widehat{v}_x + \partial_m \widehat{p} - \partial_m p\, \widehat{\rho}/\bar{\rho} = 0, \tag{3.25b}$$

$$\partial_t \widehat{d}_\perp + k_\perp^2 \frac{1}{\bar{\rho}^2} \widehat{p} = 0, \tag{3.25c}$$

$$\begin{aligned} C_v\big(\partial_t \widehat{T} + \bar{\rho}\, \partial_m \bar{T}\, \widehat{v}_x\big) + \bar{\rho}\, \partial_m \bar{v}_x\, \widehat{T} + \bar{p}\, \partial_m \widehat{v}_x + \partial_m \widehat{\varphi}_x \\ - \partial_m \bar{\varphi}_x\, \widehat{\rho}/\bar{\rho} + \big(\bar{p}\, \nabla_\perp \cdot \widehat{\boldsymbol{v}}_\perp + \nabla_\perp \cdot \widehat{\boldsymbol{\varphi}}_\perp\big)/\bar{\rho} = 0, \end{aligned} \tag{3.25d}$$

Equation (3.25c) represents the evolution of the irrotational part of the transverse velocity field.

Linear perturbations in the coordinate system (ξ, t). Linear perturbations are now rewritten in (ξ, t) variables using the following definitions

$$\widehat{G}(\xi, t) = \widehat{\rho}(m, t), \tag{3.26a}$$

$$\widehat{V}_x(\xi, t) = \widehat{v}_x(m, t), \tag{3.26b}$$

$$\widehat{D}_\perp(\xi, t) = \widehat{d}_\perp(m, t), \tag{3.26c}$$

$$\widehat{\Theta}(\xi, t) = \widehat{T}(m, t), \tag{3.26d}$$

$$\widehat{P}(\xi, t) = \widehat{p}(m, t). \tag{3.26e}$$

With the definition (3.9) of the reduced coordinate ξ, partial derivatives of the dependent variable $\widehat{f}(m, t, k_\perp)$ are transformed into partial derivatives of the dependent variable $\widehat{F}(\xi, t, k_\perp)$ as

$$\partial_t \widehat{f}(m, t, k_\perp) = \partial_t \widehat{F}(\xi, t, k_\perp) - \frac{\alpha \xi}{t} \partial_\xi \widehat{F}(\xi, t, k_\perp), \quad \text{and} \quad \partial_m \widehat{f}(m, t, k_\perp) = t^{-\alpha} \partial_\xi \widehat{F}(\xi, t, k_\perp). \tag{3.27}$$

The evolution equation for $\widehat{\mathbf{U}} = \begin{pmatrix} \widehat{G} & \widehat{V}_x & \widehat{D}_\perp & \widehat{\Theta} \end{pmatrix}^\top$ reads then as

$$\partial_t \widehat{\mathbf{U}} + \mathbf{A} \partial_\xi^2 \widehat{\mathbf{U}} + \mathbf{B} \partial_\xi \widehat{\mathbf{U}} + \mathbf{C} \widehat{\mathbf{U}} = \mathbf{0} \quad \Leftrightarrow \quad \partial_t \widehat{\mathbf{U}} = \mathbf{L}(\xi, t) \widehat{\mathbf{U}}, \tag{3.28a}$$

where

$$\mathbf{A} = \begin{pmatrix} 0 & 0 & 0 & 0 \\ 0 & 0 & 0 & 0 \\ 0 & 0 & 0 & 0 \\ 0 & 0 & 0 & t^{-1} C_v^{-1}\, \bar{G}\, \bar{\Psi}_{\Theta'} \end{pmatrix}, \tag{3.28b}$$

$$\mathsf{B} = \begin{pmatrix} -\alpha\xi/t & t^{-\alpha}\,\bar{G}^2 & 0 & 0 \\ t^{\alpha-2}\,\bar{\Theta} & -\alpha\xi/t & 0 & t^{-\alpha}\,\bar{G} \\ 0 & 0 & -\alpha\xi/t & 0 \\ t^{2\alpha-3}\,C_v^{-1}\,\bar{\Psi}_G & t^{\alpha-2}\,C_v^{-1}\,\bar{P} & 0 & t^{-1}\,\left(-\alpha\xi + C_v^{-1}\left[\mathrm{d}_\xi(\bar{G}\bar{\Psi}_{\Theta'}) + \bar{\Psi}_\Theta\right]\right) \end{pmatrix}, \tag{3.28c}$$

$$\mathsf{C} = \begin{pmatrix} t^{-1}\,\bar{G}\mathrm{d}_\xi\bar{V}_x & t^{-\alpha}\,\bar{G}\mathrm{d}_\xi\bar{G} & \bar{G} & 0 \\ -t^{\alpha-2}\,\bar{\Theta}\mathrm{d}_\xi\bar{G}/\bar{G} & \bar{G}\mathrm{d}_\xi\bar{V}_x/t & 0 & t^{-\alpha}\,\mathrm{d}_\xi\bar{G} \\ -t^{2(\alpha-1)}\,k_\perp^2\,\bar{\Theta}/\bar{G} & 0 & 0 & -k_\perp^2 \\ C_{41} & t^{\alpha-2}\bar{G}\mathrm{d}_\xi\bar{\Theta} & t^{2(\alpha-1)}\,C_v^{-1}\,\bar{\Theta} & C_{44}^{\parallel} + k_\perp^2\,C_{44}^{\perp} \end{pmatrix}, \tag{3.28d}$$

$$C_{41} = t^{2\alpha-3}\,C_v^{-1}\left(\mathrm{d}_\xi\bar{\Psi}_G - \bar{G}^{-1}\,\mathrm{d}_\xi\bar{\Psi}\right), \quad C_{44}^{\parallel} = t^{-1}\,C_v^{-1}\,\left[\bar{G}\mathrm{d}_\xi\bar{V}_x + \mathrm{d}_\xi\bar{\Psi}_\Theta\right], \quad C_{44}^{\perp} = -t^{2\alpha-1}\,\bar{G}^{-1}\,\bar{\Psi}_{\Theta'}.$$

We define the matrices $\mathsf{C}^{\perp}$ and $\mathsf{C}^{\parallel}$ such that

$$\mathsf{C}^{\parallel} = \mathsf{C}|_{k_\perp=0}, \quad \text{and} \quad \mathsf{C} = \mathsf{C}^{\parallel} + k_\perp^2\mathsf{C}^{\perp}. \tag{3.28e}$$

In (3.28) we have used the linearized equation of state (3.21) in the variables (3.26), namely

$$\widehat{P} = \bar{G}\widehat{\Theta} + t^{2\alpha-2}\widehat{G}\bar{\Theta}. \tag{3.29}$$

System (3.28) forms a linear *reaction-advection-diffusion* equation. The partial derivatives of the heat flux (3.13) with respect to $\bar{G}$, $\bar{\Theta}$ and $\bar{G}\mathrm{d}_\xi\bar{\Theta}$ are denoted $\bar{\Psi}_G$, $\bar{\Psi}_\Theta$ and $\bar{\Psi}_{\Theta'}$. The transformation (3.27) used in (3.28) introduces an advection velocity

$$v_{\mathrm{adv}} = -\alpha\xi/t,$$

in (3.27) and consequently in the definition (3.28c) of the matrix B. Accordingly, a fluid element initially located at (ξ_0, t_0) will follow a trajectory $\xi(t) = \xi_0(t/t_0)^{-\alpha}$ in a (ξ, t) diagram (green dashed line in Fig. 3.2).

Equations (2.9) can be written in a quasi linear formulation where quadratic terms in spatial first derivatives are present. As a consequence, (3.28) contains products between base-flow and perturbation spatial derivatives: cf. the coefficients $(\mathsf{B})_{41}$ and $(\mathsf{B})_{44}$.

3.2.1 Mathematical properties of the perturbation evolution equation

System (3.28) rewrites as

$$\partial_t \begin{pmatrix} \widehat{\mathbf{U}}_{\mathrm{I}} \\ \widehat{\mathbf{U}}_{\mathrm{II}} \end{pmatrix} + \begin{pmatrix} \mathbf{0} & \mathbf{0} \\ \mathbf{0} & \mathsf{A}_{22} \end{pmatrix} \partial_\xi^2 \begin{pmatrix} \widehat{\mathbf{U}}_{\mathrm{I}} \\ \widehat{\mathbf{U}}_{\mathrm{II}} \end{pmatrix} + \begin{pmatrix} \mathsf{B}_{11} & \mathsf{B}_{12} \\ \mathsf{B}_{21} & \mathsf{B}_{22} \end{pmatrix} \partial_\xi \begin{pmatrix} \widehat{\mathbf{U}}_{\mathrm{I}} \\ \widehat{\mathbf{U}}_{\mathrm{II}} \end{pmatrix} + \begin{pmatrix} \mathsf{C}_{11} & \mathsf{C}_{12} \\ \mathsf{C}_{21} & \mathsf{C}_{22} \end{pmatrix} \begin{pmatrix} \widehat{\mathbf{U}}_{\mathrm{I}} \\ \widehat{\mathbf{U}}_{\mathrm{II}} \end{pmatrix} = \mathbf{0}, \tag{3.30}$$

where $\widehat{\mathbf{U}}_{\mathrm{I}} = \begin{pmatrix} \widehat{G} & \widehat{V}_x & \widehat{D}_\perp \end{pmatrix}^\top$ and $\widehat{\mathbf{U}}_{\mathrm{II}} = \widehat{\Theta}$. The submatrices A_{ij}, B_{ij} and C_{ij} are conformal to the subvectors $\widehat{\mathbf{U}}_{\mathrm{I}}$, $\widehat{\mathbf{U}}_{\mathrm{II}}$. This system is composed of:

- a parabolic scalar subequation since $\mathsf{A}_{22} = (\mathsf{A})_{44}$, with $(\mathsf{A})_{44} < 0$ as a consequence of (3.13). This equation corresponds to a diffusion equation along the longitudinal direction of the temperature linear perturbation $\widehat{\Theta}$.

$$\partial_t \widehat{\mathbf{U}}_{\mathrm{II}} + \mathsf{A}_{22}\partial^2_{\xi^2}\widehat{\mathbf{U}}_{\mathrm{II}} = 0, \tag{3.31}$$

- a hyperbolic subsystem for which a Kreiss symmetrizer exists Kreiss (1970), of size 3 × 3, and corresponding to isothermal gas dynamics,

$$\partial_t \widehat{\mathbf{U}}_{\mathrm{I}} + \mathsf{B}_{11}\partial_\xi \widehat{\mathbf{U}}_{\mathrm{I}} = 0. \tag{3.32}$$

The existence of the hyperbolic subsystem is tightly linked to the compressible aspect of the model.

The eigenvalues of the matrix B_{11} are indeed real and come as

$$\lambda_1 = \frac{\bar{G}C_T - \alpha\xi}{t}, \tag{3.33a}$$

$$\lambda_2 = -\frac{\alpha\xi}{t}, \tag{3.33b}$$

$$\lambda_3 = -\frac{\bar{G}C_T + \alpha\xi}{t}. \tag{3.33c}$$

with $C_T = \sqrt{\bar{\Theta}}$, the isothermal sound velocity. The diaginal form D of B_{11} is then given by

$$\mathsf{B}_{11} = \mathsf{R}_{11}\mathsf{D}_{11}{\mathsf{R}_{11}}^{-1}, \quad \text{with} \quad \mathsf{D}_{11} = \mathrm{diag}\{\lambda_i, i = 1..3\}. \tag{3.33d}$$

where R_{11} is the matrix of right eigenvectors. The eigenvalues λ_i are associated to characteristics along which conserved quantities are advected:

$$({\mathsf{R}_{11}}^{-1})_{ij}\mathrm{d}\widehat{\mathbf{U}}_{\mathrm{I}j} = 0 \quad \text{along} \quad \mathrm{d}\xi/\mathrm{d}t = \lambda_i, \quad \text{for} \quad i = 1, 2, 3. \tag{3.34}$$

At $\xi = 0$ (respectively ξ_{sf}), the incoming characteristics are those along which the conserved quantity enters the domain, i.e. of positive (resp. negative) eigenvalues, and the outgoing characteristics are those of negative (resp. positive) eigenvalues. We define the projectors on the incoming characteristics of the hyperbolic subsystem

$$\mathcal{P}^{\mathrm{in}}_{11\mathrm{es}} = \mathsf{B}^{\mathrm{in}}_{11_{\mathrm{es}}} = \mathsf{R}_{11}|_{\mathrm{es}}\mathsf{D}^{+}_{11}|_{\mathrm{es}}\mathsf{R}^{-1}_{11}|_{\mathrm{es}}, \quad \mathsf{D}^{+}_{11} = \mathrm{diag}\{\max(\lambda_i, 0)\}, \tag{3.35a}$$

at the free surface, and

$$\mathcal{P}^{\mathrm{in}}_{11\mathrm{sf}} = \mathsf{B}^{\mathrm{in}}_{11_{\mathrm{sf}}} = \mathsf{R}_{11}|_{\mathrm{sf}}\mathsf{D}^{-}_{11}|_{\mathrm{sf}}\mathsf{R}^{-1}_{11}|_{\mathrm{sf}}, \quad \mathsf{D}^{-}_{11} = \mathrm{diag}\{\min(\lambda_i, 0)\}, \tag{3.35b}$$

at the shock front. Consequently the system

$$\partial_t \begin{pmatrix} \widehat{\mathbf{U}}_{\mathrm{I}} \\ \widehat{\mathbf{U}}_{\mathrm{II}} \end{pmatrix} + \begin{pmatrix} \mathbf{0} & \mathbf{0} \\ \mathbf{0} & \mathsf{A}_{22} \end{pmatrix} \partial^2_{\xi} \begin{pmatrix} \widehat{\mathbf{U}}_{\mathrm{I}} \\ \widehat{\mathbf{U}}_{\mathrm{II}} \end{pmatrix} + \begin{pmatrix} \mathsf{B}_{11} & \mathsf{B}_{12} \\ \mathsf{B}_{21} & \mathsf{B}_{22} \end{pmatrix} \partial_\xi \begin{pmatrix} \widehat{\mathbf{U}}_{\mathrm{I}} \\ \widehat{\mathbf{U}}_{\mathrm{II}} \end{pmatrix} = \mathbf{0}, \tag{3.36}$$

constitutes an incompletely parabolic system (Strikwerda, 1977). A boundary value problem for this system is well posed if, at each boundary (Strikwerda, 1977; Gustafsson and Sundström, 1978):

1. one condition is enforced on each parabolic subequations,

2. one condition is enforced on each incoming characteristic waves of the hyperbolic subsystem and outgoing characteristics are left free from any constraint.

System (3.30) differs from the strictly incompletely parabolic system (3.36) as it includes reaction terms through the matrix C. These terms do not affect advection velocities or the heat-diffusion process. They only introduce couplings between dependent variables and do not change the properties of the incoming and outgoing characteristics. We assume that the well-posedness result of Strikwerda (1977) remains valid in such conditions. This has been empirically verified along the computations we carried out. The numerical method chosen to enforce boundary conditions needs to comply with the above mentioned well-posedness properties.

To our knowledge there exists no analytical expressions for the eigenvalues ϖ_i of the matrix B, which are therefore determined numerically. However, for all the different ablation flows treated, we have always found real-valued eigenvalues for B. Therefore we may define at any location

$$\mathsf{B} = \mathsf{R}\mathsf{D}\mathsf{R}^{-1}, \quad \mathsf{D} = \mathrm{diag}\{\varpi_i, i = 1..4\}, \tag{3.37a}$$

and

$$\mathsf{B}^{\pm} = \mathsf{R}\mathsf{D}^{\pm}\mathsf{R}^{-1}, \quad \mathsf{D}^{+} = \mathrm{diag}\{\max\{\varpi_i, 0\}\}, \quad \mathsf{D}^{-} = \mathrm{diag}\{\min\{\varpi_i, 0\}\} \tag{3.37b}$$

with R the matrix of right eigenvectors of B. We also define the projectors

$$\mathcal{P}^{\mathrm{in}}_{\mathrm{es}} = \mathsf{B}^{\mathrm{in}}_{\mathrm{es}} = \mathsf{B}^{+}|_{\mathrm{es}}, \tag{3.37c}$$

and

$$\mathcal{P}^{\mathrm{in}}_{\mathrm{sf}} = \mathsf{B}^{\mathrm{in}}_{\mathrm{sf}} = \mathsf{B}^{-}|_{\mathrm{sf}}, \tag{3.37d}$$

at the external surface (es) and shock front (sf).

3.2.2 Boundary conditions

Both the external surface and the shock front are perturbed about their mean base-flow positions. The value $\widehat{f}_{\mathrm{es}}$ of a Lagrangian dependent variable $\widehat{f}$ at the external surface is related to the value at the base-flow position through the linear expansion

$$\widehat{f}_{\mathrm{es}}(t) = \widehat{f}(0,t) + \widehat{X}_{\mathrm{es}}(t)\bar{\rho}(0,t)\partial_m \bar{f}(0,t), \tag{3.38}$$

where $\widehat{X}_{\mathrm{es}}$ denotes the amplitude of the linear deformation of the external surface $\widehat{X}_{\mathrm{es}}(t)e^{i(k_y y+k_z z)}$: see Fig. 2.6. Cases of an external density perturbation, i.e.

$$\widehat{\rho}_{\mathrm{es}} = \widehat{\rho}(0,t) + \widehat{X}_{\mathrm{es}}(t)\bar{\rho}(0,t)\partial_m \bar{\rho}(0,t), \tag{3.39a}$$

or of an external pressure perturbation, i.e.

$$\widehat{p}_{\mathrm{es}} = \widehat{p}(0,t) + \widehat{X}_{\mathrm{es}}(t)\bar{\rho}(0,t)\partial_m \bar{p}(0,t), \tag{3.39b}$$

are considered, while the continuity of the heat flux leads to

$$\widehat{\varphi}_{\mathrm{es}} = \widehat{\varphi}(0,t) + \widehat{X}_{\mathrm{es}}(t)\bar{\rho}(0,t)\partial_m\bar{\varphi}_x(0,t). \tag{3.39c}$$

As the external surface is a material surface, the following kinematic relation holds

$$\dot{\widehat{X}}_{\mathrm{es}}(t) = \widehat{v}_{x_{\mathrm{es}}} = \widehat{v}_x(0,t) + \widehat{X}_{\mathrm{es}}(t)\bar{\rho}(0,t)\partial_m\bar{v}_x(0,t). \tag{3.39d}$$

The position of the shock front is also disturbed around its base position $m_{\mathrm{sf}}(t)$, with an amplitude $\widehat{X}_{\mathrm{sf}}$ (Fig. 2.6). Similarly to the base flow, the linear perturbations are discontinuous at the shock front. Jump relations are obtained from a linear perturbation of Rankine–Hugoniot relations (see 3.42) which link perturbations 'upstream' (m_{sf}^{+}) and 'downstream' (m_{sf}^{-}) to the shock front. It must be noted that perturbed Rankine–Hugoniot relations inherently includes an evolution equation for the shock front deformation $\widehat{X}_{\mathrm{sf}}$, similarly to (3.39d). Boundary conditions are expressed in (ξ, t) coordinates using the variable reductions (3.10) and (3.26) under the generic form

$$\widehat{\mathbf{B}}_{\mathrm{a}}(\widehat{\mathbf{U}}, \widehat{X}_{\mathrm{a}}) = \mathbf{N}^{\mathrm{a}}\partial_\xi\widehat{\mathbf{U}}|_{\mathrm{a}} + \mathbf{M}^{\mathrm{a}}\widehat{\mathbf{U}}(\mathrm{a},t) + \mathbf{S}^{\mathrm{a},0}\widehat{X}_{\mathrm{a}} + \mathbf{S}^{\mathrm{a},1}\dot{\widehat{X}}_{\mathrm{a}} - \widehat{F}_{\mathrm{a}}(t) = \mathbf{0} \quad \text{with} \quad \mathrm{a} = \mathrm{es}, \mathrm{sf}, \tag{3.40}$$

where $\widehat{F}_{\mathrm{es}}(t) = (\widehat{\rho}_{\mathrm{es}}(t) \quad 0 \quad \widehat{\varphi}_{\mathrm{es}}(t))^{\top}$ or $(\widehat{p}_{\mathrm{es}}(t) \quad 0 \quad \widehat{\varphi}_{\mathrm{es}}(t))^{\top}$ depending on whether an external density or pressure disturbance is applied, and $\widehat{F}_{\mathrm{sf}}(t)$ represents the contribution of an upstream perturbation in the unshocked region. The matrices $\mathbf{N}^{\mathrm{a}}$, $\mathbf{M}^{\mathrm{a}}$ and the vectors $\mathbf{S}^{\mathrm{a},0}$, $\mathbf{S}^{\mathrm{a},1}$ are defined for the external surface and the shock front as follows:

At the external surface (es), we have

$$\mathbf{M}^{\mathrm{es}} = \begin{pmatrix} \mathbf{M}^{\mathrm{es}}_{11} & \mathbf{M}^{\mathrm{es}}_{12} \\ \mathbf{M}^{\mathrm{es}}_{21} & \mathbf{M}^{\mathrm{es}}_{22} \end{pmatrix}, \quad \mathbf{M}^{\mathrm{es}}_{\mathrm{par}} = \begin{pmatrix} \mathbf{M}^{\mathrm{es}}_{21} & \mathbf{M}^{\mathrm{es}}_{22} \end{pmatrix}, \quad \mathbf{S}^{\mathrm{es},0} = \begin{pmatrix} \mathbf{S}^{\mathrm{es},0}_{\mathrm{I}} \\ \mathbf{S}^{\mathrm{es},0}_{\mathrm{II}} \end{pmatrix}, \tag{3.41a}$$

with

$$\mathbf{M}^{\mathrm{es}}_{11} = \left.\begin{pmatrix} t^{2\alpha-2}\bar{\Theta} & 0 & 0 \\ 0 & 1 & 0 \\ 0 & 0 & 1 \end{pmatrix}\right|_{\mathrm{es}}, \quad \mathbf{M}^{\mathrm{es}}_{12} = \left.\begin{pmatrix} \bar{G} \\ 0 \\ 0 \end{pmatrix}\right|_{\mathrm{es}}, \quad \mathbf{S}^{\mathrm{es},0}_{\mathrm{I}} = \left.\begin{pmatrix} t^{-\alpha}\bar{G}\mathrm{d}_\xi\bar{P} \\ t^{-1}\bar{G}\mathrm{d}_\xi\bar{V} \\ 0 \end{pmatrix}\right|_{\mathrm{es}} \tag{3.41b}$$

in the case of an external pressure disturbance, and

$$\mathbf{M}^{\mathrm{es}}_{11} = \left.\begin{pmatrix} 1 & 0 & 0 \\ 0 & 1 & 0 \\ 0 & 0 & 1 \end{pmatrix}\right|_{\mathrm{es}}, \quad \mathbf{M}^{\mathrm{es}}_{12} = \left.\begin{pmatrix} 0 \\ 0 \\ 0 \end{pmatrix}\right|_{\mathrm{es}}, \quad \mathbf{S}^{\mathrm{es},0}_{\mathrm{I}} = \left.\begin{pmatrix} t^{-\alpha}\bar{G}\mathrm{d}_\xi\bar{G} \\ t^{-1}\bar{G}\mathrm{d}_\xi\bar{V} \\ 0 \end{pmatrix}\right|_{\mathrm{es}} \tag{3.41c}$$

in the case of an external density disturbance. Heat conduction related terms write, whatever the case,

$$\mathbf{M}^{\mathrm{es}}_{21} = \left.\begin{pmatrix} t^{3\alpha-3}\Psi_G & 0 & 0 \end{pmatrix}\right|_{\mathrm{es}}, \quad \mathbf{M}^{\mathrm{es}}_{22} = t^{\alpha-1}\Psi_\Theta|_{\mathrm{es}}, \quad \mathbf{S}^{\mathrm{es},0}_{\mathrm{II}} = t^{2\alpha-3}\bar{G}\mathrm{d}_\xi\bar{\Phi}|_{\mathrm{es}} \tag{3.41d}$$

$$\mathbf{S}^{\mathrm{es},1} = \left.(0 \quad -1 \quad 0 \quad 0)^{\top}\right|_{\mathrm{es}}, \tag{3.41e}$$

and

$$\mathbf{N}^{\text{es}} = \left.\begin{pmatrix} 0 & 0 & 0 & 0 \\ 0 & 0 & 0 & 0 \\ 0 & 0 & 0 & t^{\alpha-1}\bar{G}\Psi_{\Theta'} \end{pmatrix}\right|_{\text{es}} . \tag{3.41f}$$

At the shock front (sf): the linear perturbation of the Rankine–Hugoniot relations (3.16), including a perturbation of the shock front position $\widehat{X}_{\text{sf}}$, is obtained in (Lombard, 2008). The corresponding vectors and matrices are given by

$$\mathbf{M}^{\text{sf}} = \begin{pmatrix} \mathbf{M}^{\text{sf}}_{11} & \mathbf{M}^{\text{sf}}_{12} \\ \mathbf{M}^{\text{sf}}_{21} & \mathbf{M}^{\text{sf}}_{22} \end{pmatrix}, \quad \mathbf{M}^{\text{sf}}_{\text{par}} = \begin{pmatrix} \mathbf{M}^{\text{sf}}_{21} & \mathbf{M}^{\text{sf}}_{22} \end{pmatrix}, \quad \mathbf{S}^{\text{sf},0} = \begin{pmatrix} \mathbf{S}^{\text{sf},0}_{\text{I}} \\ \mathbf{S}^{\text{sf},0}_{\text{II}} \end{pmatrix}, \quad \mathbf{S}^{\text{sf},1} = \begin{pmatrix} \mathbf{S}^{\text{sf},1}_{\text{I}} \\ \mathbf{S}^{\text{sf},1}_{\text{II}} \end{pmatrix} \tag{3.42a}$$

with

$$\mathbf{M}^{\text{sf}}_{11} = \left.\begin{pmatrix} t^{\alpha-1}\bar{U}_x & -\bar{G} & 0 \\ t^{2\alpha-2}(\bar{U}_x\bar{V}_x - \bar{\Theta}) & t^{\alpha-1}\bar{G}(\bar{U}_x - \bar{V}_x) & 0 \\ 0 & 0 & 1 \end{pmatrix}\right|_{\text{sf}}, \quad \mathbf{M}^{\text{sf}}_{12} = \left.\begin{pmatrix} 0 \\ -\bar{G} \\ 0 \end{pmatrix}\right|_{\text{sf}}, \tag{3.42b}$$

$$\mathbf{S}^{\text{sf},0}_{\text{I}} = \left.\begin{pmatrix} t^{-1}\bar{G}d_{\xi}(\bar{G}\bar{U}_x)|_d \\ t^{\alpha-2}\bar{G}d_{\xi}(\bar{G}\bar{V}_x\bar{U}_x - \bar{P})|_d \\ t^{\alpha-1}k_{\perp}^2\,[\bar{V}_x]_d^u \end{pmatrix}\right|_{\text{sf}}, \quad \mathbf{S}^{\text{sf},1}_{\text{I}} = \left.\begin{pmatrix} [\bar{G}]_d^u \\ t^{\alpha-1}\,[\bar{G}\bar{V}_x]_d^u \\ 0 \end{pmatrix}\right|_{\text{sf}}, \tag{3.42c}$$

(3.42d)

$$\mathbf{M}^{\text{sf}}_{21} = \left.\begin{pmatrix} (\gamma-1)(\bar{W}-\gamma\bar{V}_x)\bar{\Theta} + \bar{U}_x\bar{V}_x^2/2 - \Psi_G \\ \bar{G}\bar{V}_x(\bar{U}_x - \bar{V}_x/2) - C_P\bar{P} \\ 0 \end{pmatrix}^{\top}\right|_{\text{sf}}, \tag{3.42e}$$

$$\mathbf{S}^{\text{sf},0}_{\text{II}} = \left.\left(t^{2\alpha-3}\bar{G}d_{\xi}\left[((\gamma-1)\bar{P} + \bar{G}\bar{V}_x^2/2)\bar{U}_x - \bar{P}\bar{V}_x - \bar{\Phi}\right]_d\right)\right|_{\text{sf}}, \tag{3.42f}$$

$$\mathbf{S}^{\text{sf},1}_{\text{II}} = \left.\left(t^{2\alpha-2}\left[(\gamma-1)\bar{P} + \bar{G}\bar{V}_x^2/2\right]_d^u\right)\right|_{\text{sf}}, \tag{3.42g}$$

and

$$\mathbf{N}^{\text{sf}} = \left.\begin{pmatrix} 0 & 0 & 0 & 0 \\ 0 & 0 & 0 & 0 \\ 0 & 0 & 0 & 0 \\ 0 & 0 & 0 & -t^{\alpha-1}\bar{G}\Psi_{\Theta'} \end{pmatrix}\right|_{\text{sf}},$$

where $\bar{W}$ is the shock front velocity in the reference frame and $\bar{V} = \bar{W} - \bar{V}_x$ is the shock front velocity with respect to the the fluid.

3.2.3 Domains of resolution

Sections 3.1.2 and 3.2 define two problems. The first one is the Cauchy problem (3.11)–(3.14b)–(3.16), for ξ in $\Omega = [0, \xi_{\mathrm{sf}})$, which defines the base-flow solutions. In the unshocked region, the solution is uniform. As a consequence, the boundary conditions at $\xi \to \infty$ (3.14b) are taken into account together with Rankine–Hugoniot relations (3.16). The solution is smooth over Ω.

The second problem is the initial and boundary value problem (IBVP) (3.28)–(3.40) together with initial perturbations, for (ξ, t) in $\Omega \times [t_0, \infty)$ with $t_0 > 0$ (gray area on Fig. 3.2). The solution to this problem describes the evolution of linear perturbations of a given base flow.

In the general case, which we are interested in, no analytical solution are known for the base-flow boundary problem and for the perturbation IBVP. As a consequence, numerical methods are needed to obtain solutions. Base-flow solutions obtained numerically have to be sufficiently accurate for a proper computation of perturbations. In particular these solutions exhibit steep gradients in the ablation layer, owing to the heat conduction nonlinearity, thus requiring a suitable description.

3.3 Methods of solution

Numerical methods employed to solve the boundary value problem (3.11), (3.14a), (3.16) relative to the base flow and the IBVP (3.28), (3.40) together with initial conditions, relative to the linear perturbations, have been developed in preceeding works. The self-adaptative domain decomposition method with a pseudo-spectral discretization solving to compute the base flow has been developed in (Gauthier et al., 2005; Boudesocque-Dubois et al., 2013). Outlines of this procedure are given in § 3.3.2. Boudesocque-Dubois (2000); Boudesocque-Dubois et al. (2003); Lombard (2008) and Dastugue (2013) devised the method for solving linear perturbations of the above mentioned base flow. The current section only emphasize key information the existing methods to focus on the modifications brought to the linear perturbation code. These changes affect the boundary condition handling (§ 3.3.3), the time integration (§ 3.3.3) and require an adjustment of the critical time step (§ C.2). The new numerical method is verified on test-cases (App. D).

Why spectral methods? Ordinary or partial differential equations that possess solutions with steep variations are often classified as *stiff equations* (Gear, 1971, §11). Solutions to such equations are subject to instabilities if the numerical method is not adapted. An elementary improvement consists in refining the spatial discretization in the regions of steep gradients. However, in addition to increasing the number of points, a finer spatial resolution could lead to a smaller time step for time dependent solutions, as it is the case for the numerical schemes used in this thesis. When dealing with ablation waves representative of ICF implosions, the spatial resolutions needed by a first-order finite difference scheme to describe accurately a stiff solution would lead to a prohibitively small time step for computing time dependent perturbations. An alternative possibility is to use high order numerical schemes able to describe stiff solutions with a relatively low spatial resolution compared to lower order schemes. The choice to use pseudo-spectral methods for the spatial discretization is motivated by the fact that these methods have an exponential spatial convergence and that they are characterized by low dissipations and low dispersions. As (3.28) contains advection terms, low levels of dissipation and dispersion are a necessity in order to have a high fidelity description of perturbations. For these reasons, among others, spectral methods has been widely used for hydrodynamic stability analysis.

3.3.1 Spectral methods

Spectral methods fall within the scope of *weighted residual* methods (Canuto et al., 1988). We consider an ordinary differential equation under the general form

$$\mathcal{A}\left(F(\zeta)\right) = g(\zeta), \quad \text{for} \quad \zeta \in \Omega, \tag{3.43}$$

where $\mathcal{A}$ contains derivatives in ζ, g is a given right hand side and F is the solution. We define $\mathcal{P}_N$, a projection operator

$$F_N(\zeta) = \mathcal{P}_N F(\zeta) = \sum_{i=0}^{N} a_n \Phi_n(\zeta), \tag{3.44}$$

which projects any function F on the finite dimension space $\underset{n=0..N}{\operatorname{span}} \{\Phi_n\}$, where $\{\Phi_n\}_{0 \leqslant n \leqslant N}$ is a set of expansion functions and $(a_n)_{0 \leqslant n \leqslant N}$ some expansion coefficients. Finally, we define the inner product

$$\langle F^1, F^2 \rangle = \int_{\Omega} F^1(\zeta) F^2(\zeta) p(\zeta) \mathrm{d}\zeta, \quad \text{for} \quad \zeta \in \Omega, \tag{3.45}$$

where $p(\zeta)$ is a weight function. A weighted residual method amounts to finding an approximation F_N in $\underset{n=0..N}{\operatorname{span}} \{\Phi_n\}$ for which the residual $R_N = \mathcal{A}(F_N) - g$ vanishes on average, i.e.

$$\langle R_N, \psi_n \rangle = 0, \quad 0 \leqslant n \leqslant N,$$

where $\{\psi_n\}_{0 \leqslant n \leqslant N}$ is a set of test functions.

Collocation methods

The expansion functions can be chosen as Chebyshev polynomials $\Phi_n(\zeta) = T_n(\zeta)$, which form an orthogonal set relatively to the inner product (3.45) with the weight function $p(\zeta) = 1/\sqrt{1-\zeta^2}$. The Chebyshev polynomial of order n is defined by

$$\begin{aligned} T_n : [-1, 1] &\to \mathbb{R} \\ \zeta &\to \cos(n \arccos(\zeta)). \end{aligned}$$

A 'collocation method' combines polynomials as expansion functions and test functions being Dirac functions centred on 'collocation points'. In the present work we use a Chebyshev collocation method, for which the Gauss-Lobatto collocation points ζ_i are the extrema of the largest order polynomial T_N, i.e.

$$\zeta_i = \cos\left(\frac{i\pi}{N}\right), \quad i = 0..N. \tag{3.46}$$

Boundary conditions are enforced at ζ_0 and ζ_N collocations points.

Computing derivatives

Chebyshev polynomials satisfy a relation between derivatives (Canuto et al., 1988)

$$T_n(\zeta) = \frac{1}{4}\left(\frac{T'_{n+1}(\zeta)}{n+1} - \frac{T'_{n-1}(\zeta)}{n-1}\right), \quad n > 1, \tag{3.47}$$

whereupon computing the derivative $\mathrm{d}_\zeta F_N$ at collocation points conveniently comes down to a matrix product

$$\mathrm{d}_\zeta F_N|_{\zeta_i} = \sum_{j=0}^{N} \mathsf{D}^N_{ij}\, F_N(\zeta_j). \tag{3.48}$$

Entries of the matrix D^N follow from the combination of the relation (3.47) and the expansion (3.44) and are given in (Canuto et al., 1987, § 2.4).

As mentioned at the beginning of the present section, spectral methods present many advantages over other numerical schemes. The other side of the coin is that the matrix $\boldsymbol{D}^N$ is not sparse, as for the above mentioned methods, but full and is ill-conditioned. Such drawbacks are of importance when performing an implicit resolution for time dependent problems and are detailed later.

Coordinate transformation and dynamical adaptation

Chebyshev polynomials are defined on the interval $[-1, 1]$ and the density of collocation points ζ_i is higher close to the endpoints of this interval, leaving the region close to $\zeta = 0$ with a poor resolution. These two limitations are overcome by a coordinate transformation, such as the one proposed in (Renaud, 1996; Renaud and Gauthier, 1997) depending on a parameter L

$$\begin{aligned} h :\ [-1,1] &\to \left[\xi_{\mathrm{inf}}, \xi_{\mathrm{sup}}\right] \\ \zeta \to \xi &= \frac{\xi_{\mathrm{inf}} + \xi_{\mathrm{sup}}}{2} + \frac{L\,\zeta}{\sqrt{1 + \left(\dfrac{2\,L}{\xi_{\mathrm{sup}} - \xi_{\mathrm{inf}}}\right)^2 - \zeta^2}}. \end{aligned} \tag{3.49}$$

This coordinate transformation presents the advantage of changing the length of the domain, from $[-1, 1]$ to $\left[\xi_{\mathrm{inf}}, \xi_{\mathrm{sup}}\right]$, and adapting the distribution of collocation points, i.e. the mapping, inside the domain to the needs of the resolution.

Multiple domain method. The present work uses a multiple domain method where several subdomains Ω_i are juxtaposed, such that

$$\Omega = \bigcup_{i=1}^{N_{\mathrm{dom}}} \Omega_i, \tag{3.50}$$

each $\Omega_i = \left[\xi^i_{\mathrm{inf}}, \xi^i_{\mathrm{sup}}\right]$ with its own coordinate transformation. The dynamical adaptive method (Renaud, 1996; Renaud and Gauthier, 1997; Peyret, 2002) takes advantage of the flexibility provided by the coordinate transformation and the multiple domain method to build a grid that minimizes a functional J_{proj} measuring the projection error (Bayliss and Turkel, 1992). This dynamical adaptive method is performed during the resolution of the base flow problem and computes an optimal grid dedicated to a given base flow. A new grid has to be computed for any new base flow. We here give the outlines of the dynamical adaptative method, computing an optimal grid composed of N_{dom} subdomains (Boudesocque-Dubois et al., 2013)

1. The interface $\xi^i_{\text{sup}} = \xi^{i+1}_{\text{inf}}$ between subdomains Ω_i and Ω_{i+1} is tested for a set of predefined positions $\{z_k\}$,
    (a) For each position z_k, the optimal parameters L_i and L_{i+1} are found by computing the projection error J_{proj}.
2. The position z_{k^*} of the interface ξ^i_{sup} minimizing the projection error J_{proj} is selected,
3. The interface ξ^{i+1}_{sup} is dealt with similarly.

As each interface is adapted independently from the others, this procedure is repeated several times until the positions of the interfaces reach convergence.

3.3.2 Numerical computation of the base flow

The nonlinear ODE (3.11), together with boundary conditions (3.14a)–(3.16), has to be numerically integrated. The solution needs to be sufficiently smooth as its first and second derivatives enter as coefficients in the perturbation evolution equation (3.28). The operator $\mathcal{F}$ in (3.11) is approximated thanks to the Chebyshev collocation method described in § 3.3.1 on a N_{dom} subdomain grid, containing N_{cheb} collocation points each. The $4N_{\text{cheb}} \times 4N_{\text{cheb}}$ resulting matrix is block defined with full blocks and is ill conditioned due to the presence of the spectral approximation of a first-order differential operator: the ratio of its largest to its smallest eigenvalue is very large. The resolution uses an iterative algorithm until convergence is reached (Orszag, 1980), see (Boudesocque-Dubois et al., 2013) for details.

A sophisticated precedure has been developed to (i) find an initial guess to initiate the iterative relaxation method mentioned above, and (ii) run the multiple domain dynamical adaptive method outlined in § 3.3.1 to provide an optimal grid (Gauthier et al., 2005; Boudesocque-Dubois et al., 2013).

3.3.3 Numerical integration of perturbations

Once the base flow is computed, the IVBP (3.28), (3.40) is ready to be integrated in time from initial conditions $\widehat{\mathbf{U}}(\xi, t_0)$, $t_0 > 0$. In § 3.2.1 we have characterized the numerical properties of this system, i.e. an incompletely parabolic system, and relevant boundary conditions ensuring the well-posedness of the IBVP. Knowing these information, we present the numerical procedures complying with these conditions, namely the matching conditions between subdomains and the boundary conditions. The critical time step of the new temporal integration scheme is obtained in App. C.2.

Matching conditions between subdomains

Equation (3.28) is solved on each subdomain. Suitable matching conditions are applied at interfaces between each subdomain to transmit the relevant information:

- for the parabolic subequation, the continuity and differentiability of $\widehat{\mathbf{U}}_{\text{II}}$ is enforced,
- for the advection part, matching conditions has to ensure that information travelling along characteristics, upstream and downstream are moved across subdomain interfaces appropriately. Therefore, at each subdomain interface the advection term is split and the following equations are integrated (Kopriva, 1986;

Boudesocque-Dubois et al., 2003)

$$\partial_t \widehat{\mathbf{U}}^i\Big|_{\xi^i_{\text{sup}}} + \left(\mathsf{A}^i \partial^2_{\xi^2} \widehat{\mathbf{U}}^i\right)\Big|_{\xi^i_{\text{sup}}} + \left(\mathsf{B}^{+^i} \partial_\xi \widehat{\mathbf{U}}^i\right)\Big|_{\xi^i_{\text{sup}}} + \mathsf{B}^{-^i}\Big|_{\xi^i_{\text{sup}}} \partial_\xi \widehat{\mathbf{U}}^{i+1}\Big|_{\xi^{i+1}_{\text{inf}}} + \left(\mathsf{C}^i \widehat{\mathbf{U}}^i\right)\Big|_{\xi^i_{\text{sup}}} = \mathbf{0},$$

$$\partial_t \widehat{\mathbf{U}}^{i+1}\Big|_{\xi^{i+1}_{\text{inf}}} + \left(\mathsf{A}^{i+1} \partial^2_{\xi^2} \widehat{\mathbf{U}}^{i+1}\right)\Big|_{\xi^{i+1}_{\text{inf}}} + \mathsf{B}^{+^{i+1}}\Big|_{\xi^{i+1}_{\text{inf}}} \partial_\xi \widehat{\mathbf{U}}^i\Big|_{\xi^i_{\text{sup}}} + \left(\mathsf{B}^{-^{i+1}} \partial_\xi \widehat{\mathbf{U}}^{i+1}\right)\Big|_{\xi^{i+1}_{\text{inf}}} + \left(\mathsf{C}^{i+1} \widehat{\mathbf{U}}^{i+1}\right)\Big|_{\xi^{i+1}_{\text{inf}}} = \mathbf{0},$$

where $\mathsf{B}^{\pm}$ are defined in (3.37), and the uperscript i denotes the approximation over the domain Ω_i of the corresponding matrices and dependent variables.

Penalized boundary conditions for the hyperbolic subsystem

The above described method is also suited to enforce boundary conditions. Such a method is known as Thompson's method (1987; 1990) and has been previously used to solve (3.28) (Lombard et al., 2008). However, this requires computing time derivatives of dependent variables in (3.40). This is a cumbersome task, especially for the heat flux φ_{es}, which implies computing cross derivatives, in space and time, of the temperature.

Penalty methods make the enforcement of boundary conditions systematic, whatever the type of boundary equations to which they are applied (e.g. density, pressure, heat flux, or combinations of the three) and do not require the computation of time derivatives. For this reason, and having in mind the fact that we will also have to compute another linear system of a form similar to (3.30), with its own boundary conditions, we have chosen to apply such a method to our problem. The principle of penalized boundary conditions is to enforce the evolution equation at boundary nodes — in addition to internal nodes — rather than boundary relations. Such a scheme is admissible provided the evolution equation is modified to include a term accounting for the residual error between the value of the solution at the boundary and the boundary set point. The solution does not strictly match boundary conditions. However the norm of the boundary error decays in time, and Funaro et al. (1988) showed that, for hyperbolic problems solved with a spectral method, the penalty method preserves the exponential decay of the global projection error with respect to the number of polynomials. Finally, the projection error in the case of penalized boundary conditions could be lower than the projection error resulting from a strict enforcement of boundary conditions at boundary nodes.

In order to comply with the requirement that boundary conditions for the hyperbolic part of the system § 3.2.1 should only be applied on the incoming characteristics of this system (§ 3.2.1), the boundary condition obtained from (3.40) are projected on the subspace spanned by the eigenvectors corresponding to the incoming characteristics. Care needs to be taken to leave the subspace spanned by the eigenvectors of the outgoing characteristics free from any constraints, unless the problem becomes ill-posed. Let us build

$$\widehat{\mathbf{\Pi}}^{\text{a}} = \tau_{\text{a}} \mathcal{P}^{\text{in}}_{\text{a}} \left(\widehat{\mathbf{U}} - \widehat{\mathbf{U}}_{\text{a}}(t)\right), \quad \text{a} = \text{es, sf}, \tag{3.52a}$$

which takes into account the boundary residual error. The vector $\widehat{\mathbf{U}}_{\text{es}}(t)$ (respectively $\widehat{\mathbf{U}}_{\text{sf}}(t)$) is the set point obtained from (3.40), $\mathcal{P}^{\text{in}}_{\text{es}}$ (resp. $\mathcal{P}^{\text{in}}_{\text{sf}}$) a projector on the incoming characteristics (3.37) and τ_{es} (resp. τ_{sf}) a penalty weights to be determined for stability. The evolution equation (3.28) is modified to include the above defined terms

$$\partial_t \widehat{\mathbf{U}} = \mathbf{L}\widehat{\mathbf{U}} + \sum_{\mathrm{a=es,sf}} \delta_{\mathrm{a}} \widehat{\mathbf{\Pi}}^{\mathrm{a}} = \mathbf{L}_{\pi}(\widehat{\mathbf{U}}), \tag{3.53}$$

with δ_{es} and δ_{sf} are Dirac functions centred on 0 and ξ_{sf}. The method ensures the stability if the penalty weights are chosen such that

$$\tau_{\mathrm{a}} \geq \pi_{\mathrm{a}} N_{\mathrm{cheb}}(N_{\mathrm{cheb}}+1) \quad \text{for} \quad \mathrm{a} = \mathrm{es,\ sf}, \tag{3.54}$$

where π_{a} depends on the coordinate transformation (3.49). A derivation of this result and values of π_{a} are given in App. C.1.

Boundary conditions for the parabolic subequation

Following the second requirement of § 3.2.1, one boundary condition needs to be applied at each boundary on the parabolic subequation which corresponds to the linear perturbation of the energy conservation equation. These boundary relations arise, at the external surface, from heat-flux continuity (3.40), and at the shock front, from the total energy conservation component of perturbed Rankine–Hugoniot relations (3.42). In both cases, these boundary conditions are of mixed — or Robin — type.

Penalty method has been tried to enforce boundary conditions on the parabolic subequation. However, numerical tests presented in App. D.2 show that the penalty method for the parabolic subequation gives poor results compared to the exact enforcement of boundary conditions on the 0th and N_{cheb}th points of the domain. As a consequence, boundary conditions are applied on the parabolic subequation *via* an exact enforcement at each boundary node.

Implicit-explicit time integration

Perturbations are integrated in time using a low-storage three-steps Runge-Kutta (RK3) scheme (Williamson, 1980; Renaud, 1996). With (3.28) under the form

$$\partial_t \widehat{\mathbf{U}} = \mathbf{L}_{\pi}(\widehat{\mathbf{U}}) = \widehat{\mathbf{F}} + \widehat{\mathbf{G}}, \tag{3.55}$$

this RK3 scheme integrates $\widehat{\mathbf{U}}$ from t to $t + \Delta t$ as

$$\widehat{\mathrm{Q}}^{r+1} = \Delta t\, \widehat{\mathbf{F}}^{r} - c_{r+1} \widehat{\mathrm{Q}}^{r} \tag{3.56a}$$

$$\widehat{\mathbf{U}}^{r+1} = \widehat{\mathbf{U}}^{r} + a_{r+1} \widehat{\mathrm{Q}}^{r+1} + b_{r+1} \Delta t \left(\widehat{\mathbf{G}}^{r} + \widehat{\mathbf{G}}^{r+1} \right), \tag{3.56b}$$

for $r = 0, 1, 2$, $\widehat{\mathrm{Q}}^0 = \mathbf{0}$ and $\widehat{\mathbf{U}}^r$ stands for $\widehat{\mathbf{U}}(\xi, t^r)$. Coefficients a_r, b_r, c_r are given in Dastugue (2013). This temporal scheme is semi-implicit of second order. Its purely explicit part is of third order.

The previous works have used a temporal splitting between the equations of gas dynamics and the heat-diffusion equation. This temporal splitting is devised in (Lombard, 2008; Dastugue, 2013) and has furnished the results presented in (Abéguilé et al., 2006; Clarisse et al., 2008; Lombard et al., 2008; Clarisse et al., 2016). The gas dynamics system was integrated purely explicitly (i.e. $\widehat{\mathbf{G}} = \mathbf{0}$), while the heat conduction equation was integrated with a semi-implicit part (i.e. $\widehat{\mathbf{G}} \neq \mathbf{0}$) The necessity of the temporal splitting followed from the use of Thompson's method for boundary conditions (§ 3.3.3) but is no longer relevant when using of a penalty method. Therefore the full system (3.25) is integrated in time simultaneously with the following definitions of $\widehat{\mathbf{F}}$ and $\widehat{\mathbf{G}}$. For stability purpose, the longitudinal and transverse diffusion related terms of the total energy perturbation equation constitutes the semi-implicit part, so that

$$\widehat{\mathbf{G}}(\xi, t) = -\begin{pmatrix} \mathbf{0} & \mathbf{0} \\ \mathbf{0} & \mathbf{A}_{22} \end{pmatrix} \partial^2_\xi \widehat{\mathbf{U}} - \begin{pmatrix} \mathbf{0} & \mathbf{0} \\ \mathbf{0} & k_\perp^2 C_{44}^\perp \end{pmatrix} \widehat{\mathbf{U}}, \tag{3.57}$$

The remaining terms, which form a hyperbolic system, are integrated explicitly:

$$\widehat{\mathbf{F}}(\xi, t) = \mathbf{L}_\pi(\widehat{\mathbf{U}}) - \widehat{\mathbf{G}}(\xi, t). \tag{3.58}$$

The withdrawal of temporal splitting allows to improve the convergence in time of the scheme from being of order one in time with the splitting to second order.

The presence of an explicit integration step requires the time step to remain under a critical value Δt_c. It is a consequence of the following heuristic stability requirement: when dealing with advection phenomena, the time step needs to be lower than the time required by a fluctuation to travel from a grid point to its neighbour (MacCormack, 1971). Boudesocque-Dubois et al. (2003) derive a critical time step based on the gas dynamics system. Dastugue (2013) improve that stability criterion by adding a correction term taking into account the advection term of the internal energy perturbation equation (3.26a). In App. C.2 we derive a stability criterion based on actual advection velocities (i.e. eigenvalues of matrix $\mathbf{B}$), which are determined numerically, and the eigenvalues of Chebyshev first-order differential operator modified by penalty terms.

The semi-implicit part (3.56b) of the RK3 scheme requires solving an implicit equation, which only affects $\widehat{\mathbf{U}}_{\mathrm{II}} = \widehat{\Theta}$, by definition of $\widehat{\mathbf{G}}$. The corresponding equation is reformulated under the general form of the Helmholtz-type equation (Dastugue, 2013)

$$\left(\partial^2_\xi - \sigma^{r+1}(k_\perp)\right) \widehat{\Theta}^{r+1} = f^r(\widehat{\Theta}^r, \widehat{Q}_4^{r+1}). \tag{3.59}$$

The multi-domain discretization perfectly combines with the influence matrix method (M. G. Macaraeg, 1986; Pulicani, 1988) for an efficient inversion, taking into account boundary conditions including first-order space derivatives, such as heat-flux continuity (3.39c). The implementation of the influence matrix method is described in Lombard (2008); Dastugue (2013). In particular, it employs a relaxation method similar to that used for the base flow (Boudesocque-Dubois et al., 2013).

The numerical code solving the perturbations performs computations over each subdomain in parallel using the MPI paradigm with a single process per subdomain (Perron, 2015). The computation of perturbations has been verified on a series of test cases listed in Tab. 3.1 and detailed in App. D.

3.4 Base flows

We present two radiation driven ablation flows solution to (3.11) and their characteristics. The base-flow profiles are displayed in Fig. 3.4. In the approximation of the non-isothermal shock front, i.e. combined infinitesimal preheating tongue and isothermal shock front at sf, the ablation flow is uniquely defined by the ablation front and shock front positions ($\xi_{\mathrm{af}}, \xi_{\mathrm{sf}}$), or the external heat flux and pressure parameters ($\mathcal{B}_\varphi, \mathcal{B}_p$). These parameters, $\mathcal{B}_\varphi$ and $\mathcal{B}_p$, define the external pressure and heat flux laws driving the ablation wave. The resulting ablation flow is analysed in terms of Mach number M and Froude number Fr, which are defined as (Boudesocque-Dubois et al., 2008):

Name	Base flow	Portion tested
Acoustic periodic	Uniform & stationary	Explicit part $\partial_t \widehat{\mathbf{U}} = \widehat{\mathbf{F}}$
Acoustic forced	Uniform & stationary	Explicit part $\partial_t \widehat{\mathbf{U}} = \widehat{\mathbf{F}}$ & penalty method
Heat conduction	Uniform & stationary	Semi-implicit part $\partial_t \widehat{\mathbf{U}} = \widehat{\mathbf{G}}$
Thermoacoustic periodic	Uniform & stationary	Full part $\partial_t \widehat{\mathbf{U}} = \widehat{\mathbf{F}} + \widehat{\mathbf{G}}$
Munro's rippled shock	Uniform & stationary	Perturbed RH relations and $\widehat{X}_{\text{sf}}$ with $\widehat{\mathbf{U}}_u = (1 \quad 0 \quad 0 \quad 0)^\top$ and penalty method
Translation	Ablation wave RC-1	Full system, for $k_\perp = 0$, $\widehat{\varphi}_{\text{es}} = \widehat{p}_{\text{es}} = 0$ and $\widehat{\mathbf{U}}_u = \mathbf{0}$.

Table 3.1: Test cases carried out to verify the numerical methods. These test cases are detailed in App. D.

- $M(\xi) = \dfrac{|\bar{V}_x(\xi) - \bar{V}_x(\xi_{\text{af}})|}{\sqrt{\gamma\bar{\Theta}(\xi)}}$: ratio of the fluid velocity relatively to the ablation front, to the isentropic sound velocity,
- $Fr(\xi) = \dfrac{|\bar{V}_x(\xi)|}{\sqrt{\bar{a}(\xi) L_{\nabla_T}(\xi)}}$, where $\bar{a}$ is the ablation front acceleration and $L_{\nabla_T} = \dfrac{\bar{\Theta}}{\bar{G} \mathrm{d}_\xi \bar{\Theta}}$ is the local temperature gradient length.

Subsonic ablation flows necessarily implies $M(\xi_{\text{af}}) < 1$. Ablation flows representative of ICF implosion are characterized by a low external pressure, which induces a high expansion velocity as the fluid expands in a quasi-vacuum. A Chapman–Jouguet point may form in the expansion wave, which is the case for the RC-3 ablation flow (Tab. 3.2), while the RC-1 ablation flow is close to be sonic at the end of the conduction region. As a consequence of the rather low external pressure, the ablation front is steeper, i.e. presents high base-flow gradients. These steeper gradients results in a larger range of characteristic lengths to be described, from the total length of the flow L_{tot} to the smallest gradient length $\min L_{\nabla_T}$. The ratio of these two lengths defines the stiffness of the ablation flow.

Table 3.2: Characteristics of the base flows considered in this present work: values of the boundary parameters $(\mathcal{B}_\varphi, \mathcal{B}_p)$, positions of the ablation front ξ_{af} and shock front ξ_{sf}, heat conduction exponents (μ, ν), stiffness of the ablation front, values at the ablation front and maximum value of the Mach number (M) and Froude number (Fr) at the ablation front (Dastugue, 2013). Numerical parameters: number of subdomains N_{dom}, number of points N_{cheb} per subdomain, and critical time-step Δt_c.

	$(\mathcal{B}_\varphi, \mathcal{B}_p)$	$(\xi_{\text{af}}, \xi_{\text{sf}})$	(μ, ν)	L_{cond}	$\min \frac{L_{\nabla_T}}{L_{\text{tot}}}$	$M\|_{\xi_{\text{af}}}$	$\max M$	$Fr\|_{\xi_{\text{af}}}$	N_{dom}	N_{cheb}	Δt_c
RC-1	(3.33, 1.15)	(1.06, 1.5)	$(2, \frac{13}{2})$	1.15	$4.0\ 10^{-3}$	0.32	0.95	12.2	189	50	$1.3\,10^{-7}$
RC-3	(0.8, 0.31)	(0.51, 1)	$(2, \frac{13}{2})$	1.29	$2.74\ 10^{-5}$	0.22	1.12	80.3	39	50	$9.\,10^{-9}$
EC	(0.12, 0.12)	(0.118, 0.3)	$(0, \frac{5}{2})$	0.26	$7.3\ 10^{-3}$	0.13	0.45	2.0	4	50	$3.34\,10^{-5}$

A stiff ablation wave requires a spatial resolution sufficiently fine to describe the whole range of characteristic lengths. This constraint is adequately handled with the adaptive multidomain method. Subdomains are refined in the the ablation layer to describe the steep gradients, and become larger in the conduction region and the post shock region where gradients are smoother (Fig. 3.3). However, the size of two adjacent subdomains cannot differs

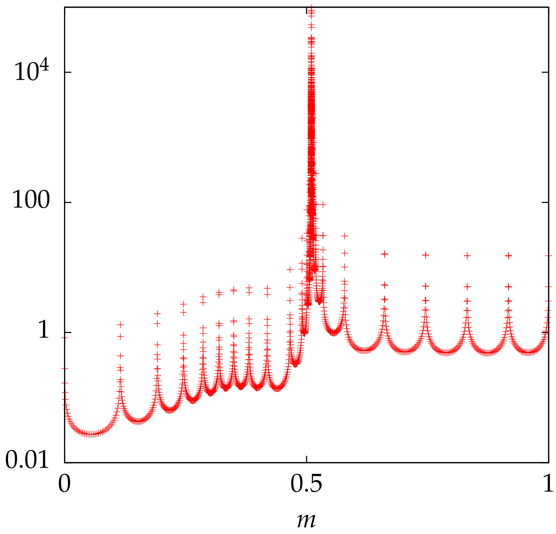

Figure 3.3: Ablation wave RC-1. Density of collocation points across the computational domain at $t = 1$, with a grid $(N_{\text{cheb}}, N_{\text{dom}}) = (50, 39)$.

by orders of magnitude. Indeed, a perturbation, well described on a given subdomain, and propagating into an adjacent coarser subdomain, may become under-resolved if the ratio of the coarser to the finer domain sizes is too large. From the spectral-method point of view, the higher modes existing on the refined subdomain are not described by the polynomial basis of the coarser subdomain. Therefore, the refinement has to be gradual. In practice the ratio of the sizes between two adjacent subdomains is constrained to be within the range $[1/2, 2]$.

The critical time step Δt_c (App. C.2) explicitly depends on the grid refinement: a locally finer grid results in a locally lower Δt_c. Penalty coefficients (§ 3.3.3 and App. C.1) also tend to lower the local the value of Δt_c in the boundary subdomains. The value retained is the lowest Δt_c over the whole grid, which is usually attained in the ablation layer, close to the location of the minimum gradient length where collocation points density is the highest (Fig. 3.3). The limitation in handling ablation waves with faster expansion – i.e. more realistic – is therefore constrained, on the one hand, by the ability to construct a grid correctly describing the stiffness of the ablation wave, and on the other hand, by the smallness of Δt_c.

The ablation wave RC-3 is used in § 3.5 and § 4.4. For computational issues, the ablation wave RC-1 is used instead of RC-3 in § 4.5. The ablation wave EC, with electron heat conduction, has served to test the numerical tools. This base flow is also used in App. B to produce a first global non-modal analysis.

3.5 Linear wave propagation

The present section summarizes the main results of an article submitted to *Physical Review E* (App. A). Wave propagation is influential in the cases of ablative Richtmyer–Meshkov instabilities (ARM) and irradiation asymmetries (Goncharov et al., 2006; Lombard et al., 2008; Aglitskiy et al., 2010). This propagation of waves is classically analysed in terms of Kovásznay modes (Chu and Kovásznay, 1958), namely pressure, vorticity and entropy perturbations. However, these modes prove to be not suited for analyzing wave propagation in a stratified flow, and particularly in the conduction region (Lombard et al., 2008). In the conduction region, the standard models of radiative ablation, because of an isothermal assumption, ascribe wave propagation to isothermal acoustic waves, while temperature perturbations are only diffused (Nozaki and Nishihara, 1980; Nishihara, 1982; Saillard et al.,

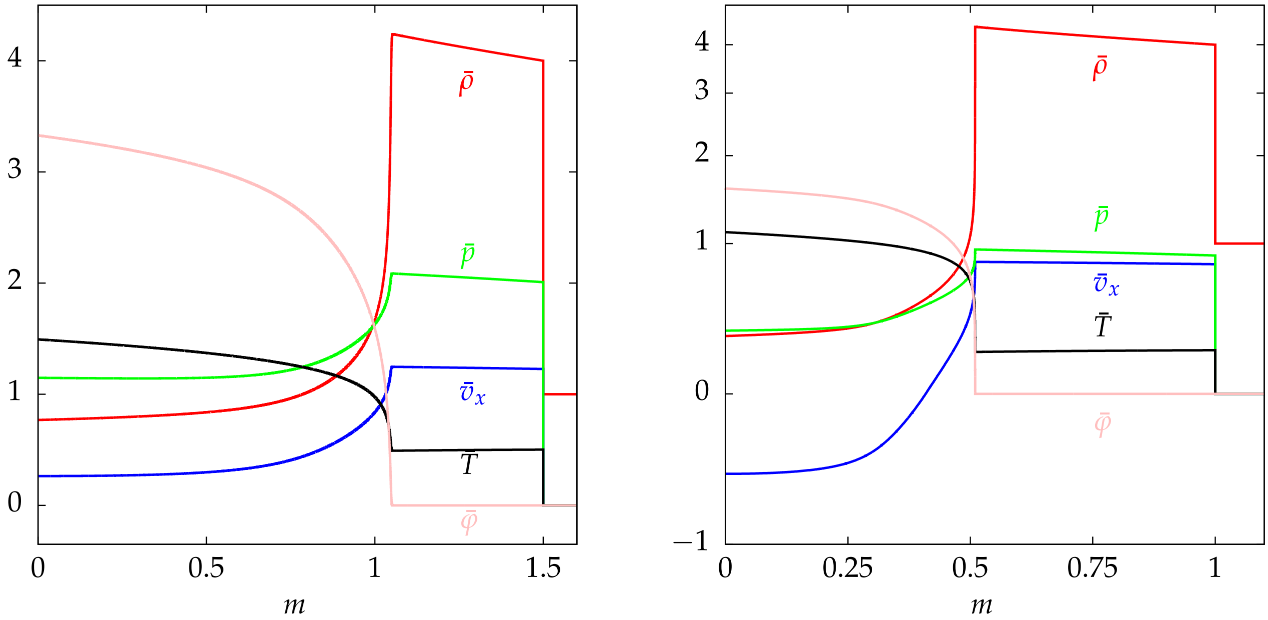

Figure 3.4: Base flow variables of the ablation waves (a) RC-1and (b) RC-3 in coordinate m at $t = 1$.

Table 3.3: Identification of the characteristic waves in the conduction region and the post-shock region of an ablation flow (adapted from Tab. 6 in Clarisse et al., 2018).

	Conduction region	Post-shock region
$\mathcal{C}_1$	*Heat conductivity*	*Upstream quasi-isentropic acoustic*
$\mathcal{C}_2$	*Upstream quasi-isothermal acoustic*	*Quasi-entropy*
$\mathcal{C}_3$	*Transverse velocity*	*Transverse velocity*
$\mathcal{C}_4$	*Downstream quasi-isothermal acoustic*	*Downstream quasi-isentropic acoustic*

2010). However, a one-dimensional local analysis of linear wave propagation in radiation driven ablation waves has identified the existence, in the conduction region, of supersonic upstream propagating wave, termed *heat conductivity* waves (Clarisse et al., 2018). These linear waves carry fluctuations of the heat flux perturbation. They are a direct consequence of nonlinear conduction, together with temperature stratification in the conduction region. As a consequence, heat conductivity waves cannot be describe by the standard models of radiative ablation.

Here we investigate linear wave propagation in the radiation-driven ablation wave RC-3 (Tab. 3.2) by computing linear perturbations responses to external pressure or heat flux perturbations. In other words we examine the feedthrough, or 'transmission mechanism' described in § 2.2. This analysis confirms the existence of heat conductivity waves for perturbations whose longitudinal characteristic lengths are of the order of — or larger than — the conduction region size l_{cond} and transverse wavelengths exceeding this size. For this range of wavelengths, advection is the dominant propagation mechanism over diffusion and couplings, which are exactly taken into account. The advection velocity of the heat conductivity wave is supersonic (see λ_1 on Fig. 3.6). The direct consequence is that any hydrodynamic perturbation at the external surface may be advected through the conduction region, beyond a potential Chapman–Jouguet point, up to the ablation front. Therefore, consequences of acoustic-like events taking place outside an ICF target may not be omitted when studying ablation front perturbations, even in the case of supersonic expansion flows. Heat conductivity waves consist in an additional feedthrough mechanism. In particular, the presence of heat-conductivity waves explains how the feedthrough may be modified by the history of external disturbances *after* the formation of the ablation flow.

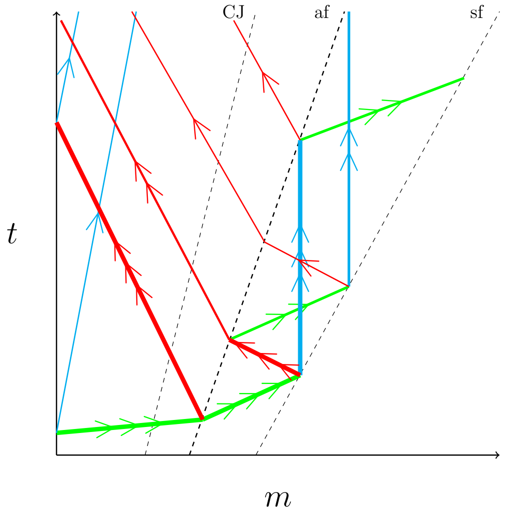

Figure 3.5: Schematic representation of perturbation propagation in the (m, t) plane originating from a heat flux perturbation at the external surface. Perturbation trajectories are sketched as colored lines: $\mathcal{C}_1$ (green), $\mathcal{C}_2$ (cyan) and $\mathcal{C}_4$ (red). Arrows indicate the propagation direction. The thickness and number of arrows render the intensity of the corresponding signal. Trajectories of CJ point, ablation front ('af') and shock front ('sf') are also indicated.

From a broader point of view, heat conductivity waves take part into a set of four pseudo-characteristic variables, (see App. A). These pseudo-characteristics furnish a relevant set of variables to describe perturbation propagation in ablation waves, an example of which is given in Fig. 3.5 for an impulse external perturbation in heat flux. The nature of these pseudo-characteristics is identified in Tab. 3.3. Pseudo-characteristic variables $\widehat{\mathcal{W}}_1$, $\widehat{\mathcal{W}}_2$ and $\widehat{\mathcal{W}}_4$, supplemented by vorticity perturbations $\widehat{\omega}$, will be used in Chap. 4 to analyze *optimal responses* of (3.28).

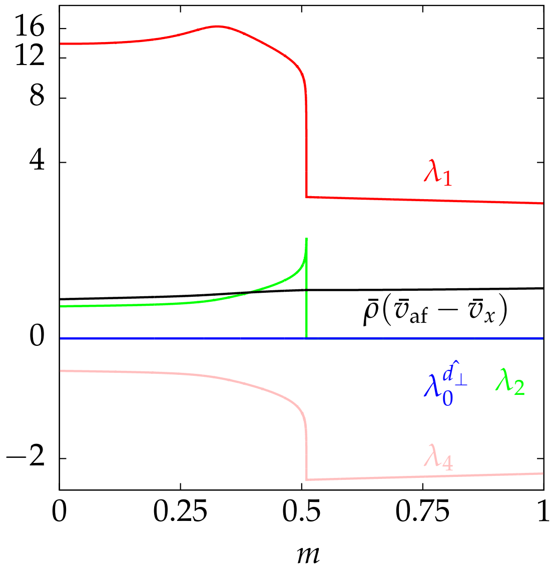

Figure 3.6: Eigenvalues of the matrix $\mathbf{B}$ for the RC-3 base flow and fluid expansion momentum relatively to the ablation layer ($\bar{v}_{\mathrm{af}}$ is the ablation front velocity).

CHAPTER 4

Non-modal effects in ablation flows

Chapter Abstract

In this chapter we advocate for the necessity for a non-modal analysis of perturbations in ablation waves, the major argument being the multiplicity of perturbation sources. We then determine the initial conditions leading to the maximum growth rate of perturbations, from a local non-modal analysis (§ 4.4), and to the maximum amplification of perturbations, from a global non-modal analysis (§ 4.5). The latter result follows from an iterative direct adjoint resolution. The adjoint problem is derived using the Lagrange multipliers technique (§ 4.5.1). We stress the correct inclusion of boundary conditions (3.40) in the Lagrange functional. This point is linked to the compressibility and the presence of deformations of the external surface and shock front. Optimal initial perturbation (OIP) are computed for various terminal times, transverse wavenumbers and initial distributions of the perturbation. The analysis unveils two different optimal amplification mechanisms depending on the terminal time.

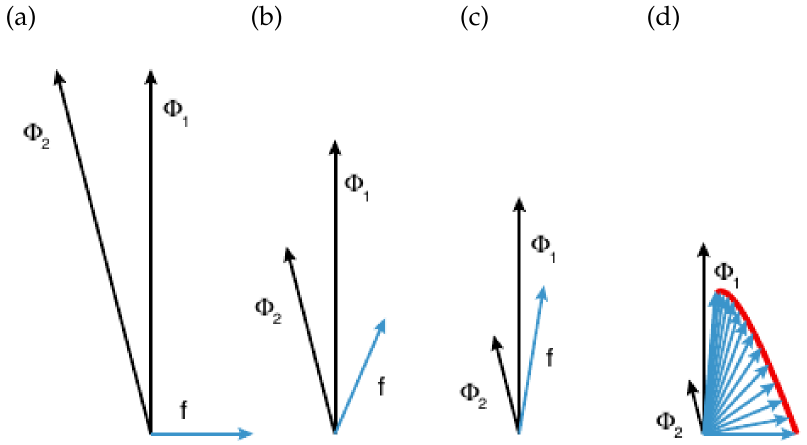

Figure 4.1: Vector example of transient growth, from Schmid (2007), Fig. 2. From (a) to (d), the length of the linear combination $f = \Phi_1 - \Phi_2$ increases transiently although it is the superposition of two vectors Φ_1 and Φ_2 whose length monotonously decays.

4.1 A brief review of non-modal tools for stability analysis

In the field of hydrodynamic stability, the term ‘non-modal’, or ‘non-normal’, analysis is used in reference to ‘modal’, or ‘spectral’, analysis. Modal stability analysis focuses on the eigenspectrum of the evolution operator of flow perturbations, in order to assess the stability of a given flow. Eigenvalues and eigenfunctions are considered separately without considering interactions between them. This classical approach has been widely used to predict the stability of flows (Drazin and Reid, 1981; Trefethen et al., 1993). For a dynamical system described by a (vector) state variable $\widehat{\mathbf{U}}$ and obeying the linear equation

$$\partial_t \widehat{\mathbf{U}} = \mathbf{L}\widehat{\mathbf{U}}, \tag{4.1}$$

the evolution operator $\mathbf{L}$ is *normal* if it commutes with its adjoint, i.e.

$$\mathbf{L}\mathbf{L}^\dagger = \mathbf{L}^\dagger\mathbf{L}, \tag{4.2}$$

where the adjoint $\mathbf{L}^\dagger$ is properly defined (e.g. the transconjugate in finite dimension). In such a case, the set of eigenfunctions of $\mathbf{L}$ forms an orthogonal basis of the space of solutions and the knowledge of the least stable eigenvalue and its associated eigenfunction is sufficient to assess the potential instability mechanisms. However, if $\mathbf{L}$ is non-normal, its eigenfunctions are not orthogonal. In such a case, the linear combination of two decaying (i.e. stable) eigensolutions may yield an initially amplified solution, as it is illustrated in Fig. 4.1, i.e. the operator is not monotonously stable (Schmid and Henningson, 2001, def. 4). This transient amplification cannot be predicted by a spectral analysis as interactions between eigenfunctions are not considered. In the context of hydrodynamic stability analysis, transient amplifications can lead to an earlier onset of nonlinear evolution than that inferred from the sole knowledge of the eigenvalues. In short, the spectrum provides us with information about the asymptotic behavior at long times, while information driving short-term dynamics is additionally contained in the set of eigenfunctions (Trefethen et al., 1993; Reddy et al., 1993). The principle of non-modal analysis is precisely to combine the information of eigenvalues and eigenfunctions to investigate the amplification of solutions at all time horizons. These methods have been successfully applied to many hydrodynamic stability problems (see Schmid, 2007 and references therein).

Non-normality indicates the sensitivity of an operator to small perturbations. Let E be a random perturbation of $\mathbf{L}$, such as $\|E\| \leqslant \epsilon$ for a given norm $\|\cdot\|$. Each eigenvalue λ_i of $\mathbf{L}$ is shifted by a quantity $\delta\lambda_i$ (Schmid and Henningson, 2001, §3.3) such that

$$|\delta\lambda_i| \leqslant \varrho\epsilon, \quad \text{where } \varrho \text{ is a constant.} \tag{4.3}$$

For a normal operator $\mathbf{L}$, ϱ tends to 1^+ as ϵ tends to 0. If $\mathbf{L}$ is non-normal, ϱ is as large as $\mathbf{L}$ is sensitive to perturbations. In the context of hydrodynamics, the evolution operator represents the structure of the flow and its non-normality indicates if the flow is prone to fast growth of small disturbances, i.e. faster than predicted by the eigenvalues. Some *scalar measures* of the non-normality of an operator have been proposed in (Henrici, 1962; Trefethen, 1999). These measures can be refined to reflect the sensitivity of each eigenvalue to a perturbation of the operator (Reddy et al., 1993; Trefethen, 1999). Still, these scalar measures only reveal a *potential* for transient growth. Another indicator is the numerical range of an operator $\mathbf{L}$, which is defined in the complex plane as the set of Rayleigh quotients

$$\mathfrak{d}(\mathbf{L}) = \left\{ \left\langle \widehat{\mathbf{U}}, \mathbf{L}\widehat{\mathbf{U}} \right\rangle \Big/ \left\langle \widehat{\mathbf{U}}, \widehat{\mathbf{U}} \right\rangle \quad : \quad \widehat{\mathbf{U}} \neq \mathbf{0} \right\}, \quad \text{with} \quad \langle \cdot, \cdot \rangle \quad \text{a scalar product.} \tag{4.4}$$

If $\mathbf{L}$ is normal, then $\mathfrak{d}(\mathbf{L})$ is the convex envelope of the spectrum in the complex plane (Horn and Johnson, 1990). If $\mathbf{L}$ is non-normal, then $\mathfrak{d}(\mathbf{L})$ is larger than the convex envelope of the spectrum. In the case of a dynamical system, the numerical range $\mathfrak{d}(\mathbf{L})$ may protrude in an unstable region of the complex plane while the spectrum is confined in a stable region. In that case, the *numerical abscissa*

$$\max \left\{ \Re \left(\mathfrak{d}(\mathbf{L}) \right) \right\}, \tag{4.5}$$

gives the maximum attainable growth rate of $\langle \widehat{\mathbf{U}}, \widehat{\mathbf{U}} \rangle$. The *maximum initial growth rate* of perturbations in an ablation wave is studied in § 4.4.

The *optimal initial perturbation* (OIP) is the initial (non zero) perturbation $\widehat{\mathbf{U}}|_{t_0}$ maximizing the *gain*

$$\mathcal{G}(T) = \frac{\left\| \widehat{\mathbf{U}}|_T \right\|}{\left\| \widehat{\mathbf{U}}|_{t_0} \right\|} \tag{4.6}$$

at a given terminal time T. To address the OIP problem, we consider the fundamental solution operator defined by (Schmid and Henningson, 2001, § 6.4.2)

$$\widehat{\mathbf{U}}|_T = \mathbf{M}(T) \widehat{\mathbf{U}}|_{t_0}. \tag{4.7}$$

If $\mathbf{L}$ does not depends on time then $\mathbf{M}$ corresponds to the operator exponential

$$\mathbf{M}(T) = \exp(\mathbf{L}T). \tag{4.8}$$

In such a case, the OIP is the principal singular vector of $\mathbf{M}(T)$ and the gain is its associated principal singular value (Schmid and Henningson, 2001, § 4.4). However, if $\mathbf{L}$ is time dependent then the computation of a satisfactory numerical approximation of $\mathbf{M}(T)$ is intricate. Rather than working with the operator $\mathbf{M}$ itself, an alternative approach uses iterative solutions to converge to the OIP. Such a method is called *direct-adjoint* (see § 4.5).

Another application of non-modal analysis is the *receptivity* problem, which aims at determining an optimal external forcing maximizing (or minimizing) a quantity (Cossu, 2014), e.g. air blowing or suction on a wing profile to delay the loss of lift. Receptivity problems may also have recourse to direct-adjoint looping for determining the optimal forcing.

4.2 Why non-modal analysis for ablation waves?

Nicoud et al. (2007) and Wieczorek et al. (2011) noticed that the non-modal behavior of thermoacoustic instabilities is favoured in accelerated flows or in flows with complex boundary conditions. Ablation flows present these particularities because of pressure gradient and the deformed external surface and shock front. Although ablation flow perturbations do not exactly correspond to thermoacoustic perturbations, they are somewhat similar to them: a superposition of acoustic, vorticity and nonlinear heat-flux perturbations. As a consequence we can expect some non-modal behaviors of ablation flow perturbations.

In ICF implosions, sources of perturbations are multiple. The target may present surface defects, density inhomogeneities of the ablator material or some defects at the inner interfaces of the target. Moreover the target is immersed in an uncontrolled environment (the hohlraum cavity in the case of indirect-drive ICF, Fig. 1.1). The external pressure applied to the target can be inhomogeneous and driving irradiation can display asymmetries.

In practice ICF codes furnish computations of the amplification of some initial perturbations. Due to the multiplicity of perturbation sources, experiments and ICF code simulations have often focused on studying a specific source of perturbation (e.g. internal density inhomogeneities or surface defects) for a given wavelength. In dedicated experiments, an initial perturbation is artificially introduced in the shell to control its shape and size. In such cases ICF code simulations have been found in good agreement with experiments (Raman et al., 2014; Peterson et al., 2015). However, implosion simulations of ‘native roughness’ shells still fail to produce satisfactory agreements with experiments (Raman et al., 2014; Smalyuk et al., 2017). Native roughness shells are designed to achieve ignition. The spectrum of each kind of defect has to comply with specifications derived from experiments and simulations. For such shells, initial defects, individually considered as acceptable regarding the implosion process, may interact and lead to an amplification level not predicted by experiments and simulations. Additionally, some sources of perturbations not considered in experiments and simulations have turned out to be significant (Haan et al., 2015; Smalyuk et al., 2017). It appears that current limitations of studies on ICF implosion instabilities come predominantly from the omission of certain sources of perturbations and of the interactions between shell surface defects and material inhomogeneities.

Hoping to remedy to such limitations by sampling the entire range of admissible initial condition and terminal time T by a sufficiently large number of amplification computations is simply unrealistic. Sensitivity analysis regarding initial conditions has never been performed for ablation ICF implosions. Non-modal analysis is able to face the challenge of the multiplicity of perturbation sources: *not missing out the most dangerous initial perturbations*.

The other approach that has been used to study the stability of particular phases of implosion flows (see Fig. 2.3) is normal-mode analysis. The linear stability of ablation waves has extensively been studied by means of the normal-mode approach (cf. Tabs. 2.3-2.5). In addition to assumptions on mean flow unsteadiness, uniformity and compressibility, these works focus on the least stable eigensolutions, omitting possible transient growth phenomena proper to non-normal operators. In that context, non-modal analysis provides us with a systematic tool to determine the OIPs, unobtainable by modal methods or by simple amplification computations from simulations.

4.3 Perturbation measure

Measuring the ‘size’ of perturbations requires the use of a metric. For convenience, we have used the norm symbol $\|\cdot\|$ to denote this measure. To gain in generality, this metric is now designated by a functional $\mathcal{J}$. On the one hand $\mathcal{J}$ has to respect some mathematical properties and on the other hand it is desirable for this functional to be physically meaningful. The early non-modal stability analyses dealt with incompressible flows for which perturbation kinetic energy furnishes a relevant measure (Schmid and Henningson, 2001, § 1.2). Analyses taking into account compressibility have incorporated the acoustic energy in addition to the kinetic one (Cantrell and Hart, 1964). For more complex flows presenting sources of entropy it is necessary to adapt the measure in order to account for entropy (Chu, 1965; Myers, 1991). The choice of a functional $\mathcal{J}$ rendering faithfully the non-normality of a flow, and not "spurious growth" due to the choice of $\mathcal{J}$ rather than intrinsic to the flow, has been a matter of discussions (Hanifi et al., 1996; George and Sujith, 2012). To the question of whether transient growth is due to the choice of $\mathcal{J}$ or to the flow, Blumenthal et al. (2017) answer that although different functionals display non-normality differently, the non-modal dynamics is not affected by the choice of $\mathcal{J}$. These authors propose a "system" point of view, in which non-normality is not considered with respect to the sole evolution operator of the flow, but relatively to an observation tool which is the functional $\mathcal{J}$. This framework follows from Foures et al. (2012): it is sufficient that $\mathcal{J}$ (i) is a norm, or a semi-norm, for the state variable, and (ii) the set of control parameters is normalized by a sum of semi-norms $\sum_k \mathcal{I}_k$ defined so that the direct sum of the kernels of the semi-norms $\mathcal{I}_k$ may span the whole space of control parameters, i.e. the sum$\sum_k \mathcal{I}_k$ is a full norm.

Following these considerations, other stability problems were addressed, where $\mathcal{J}$ is not an ‘energy’ built as an integral of an energy density over the flow domain, or over a period of periodic disturbances, but rather a localized measure in the flow (Foures et al., 2013). For example in the case of flame front stability, the quantity of interest is localized in the region of the highest reaction rate (Lemke et al., 2014). Similarly, in the case of ablation flows one of the quantities of interest is the distortion of the ablation layer, locus of the highest variation of specific total energy. The different objective functionals considered in the present work are as follows (see Tab. 4.1).

Table 4.1: Objective functionals $\mathcal{J}$ considered here and their complementary semi-norms $\mathcal{J}^*$. The integration windows q_{af} and q^*_{af} are defined in App. E.3.

Name	$\mathcal{J}$	$\mathcal{J}^*$
L_2-norm	$\frac{1}{2}\left(\int_0^{\xi_{\mathrm{sf}}} \mathrm{j}_2 \mathrm{d}\xi + \widehat{X}_{\mathrm{es}}^2 + \widehat{X}_{\mathrm{sf}}^2\right)$	
Chu’s energy	$\frac{1}{2}\int_0^{\xi_{\mathrm{sf}}} \mathrm{j}_C \mathrm{d}\xi$	$\frac{\widehat{X}_{\mathrm{es}}^2 + \widehat{X}_{\mathrm{sf}}^2}{2}$
Myers’ energy	$\frac{1}{2}\int_0^{\xi_{\mathrm{sf}}} \mathrm{j}_M \mathrm{d}\xi$	$\frac{\widehat{X}_{\mathrm{es}}^2 + \widehat{X}_{\mathrm{sf}}^2}{2}$
Ablation layer deformation	$\frac{1}{2}\int_0^{\xi_{\mathrm{sf}}} q_{\mathrm{af}}(\xi)\widehat{X}_T^2 \mathrm{d}\xi$	$\frac{\widehat{X}_{\mathrm{es}}^2 + \widehat{X}_{\mathrm{sf}}^2}{2}$ $+ \frac{1}{2}\int_0^{\xi_{\mathrm{sf}}} \left(\widehat{G}^2 + \widehat{V}_x^2 + \widehat{D}_\perp^2 + q^*_{\mathrm{af}}(\xi)\widehat{\Theta}\right) \mathrm{d}\xi$

- **L_2-norm** constitutes the most simple objective functional but bears little physical meaning. However the L_2-norm remains interesting to account for an amplification of the solution to (3.25) from a mathematical point of view. The L_2-norm of the state variable $\widehat{\mathbf{U}}$ is defined by the L_2-norm density

$$\mathrm{j}_2 = \widehat{\rho}^2 + \widehat{v}_x^2 + \widehat{d}_\perp^2 + \widehat{T}^2 = \widehat{\mathbf{U}}^\top \mathbf{W}_2 \widehat{\mathbf{U}}, \quad \text{with } \mathbf{W}_2 \text{ the } 4 \times 4 \text{ identity matrix,} \tag{4.9}$$

supplemented by the squares of the boundary deformations.

- **Chu's energy.** The energy of Chu (1965) is derived from conservation equations and corresponds to the energy density

$$\bar{\rho}\left(\widehat{v}_x^2 + \widehat{d}_\perp^2/k_\perp^2\right) + \widehat{p}^2/(\bar{\rho}\bar{c}_s) + \frac{(\gamma-1)}{\gamma}\bar{\rho}\bar{T}\widehat{s}^2$$

or

$$\mathrm{j}_C = \widehat{\mathbf{U}}^\top \mathbf{W}_C \widehat{\mathbf{U}}, \quad \text{with} \quad \mathbf{W}_C = t^\alpha \bar{G}^{-1} \begin{pmatrix} t^{2\alpha-2}\bar{\Theta}/\bar{G} & 0 & 0 & 0 \\ 0 & \bar{G} & 0 & 0 \\ 0 & 0 & \bar{G}/k_\perp^2 & 0 \\ 0 & 0 & 0 & t^{2-2\alpha}C_p\bar{G}/\bar{\Theta} \end{pmatrix}, \quad \text{for} \quad k_\perp > 0. \tag{4.10}$$

Chu's energy is conserved for a uniform base flow without external source of perturbations. This energy includes terms accounting for kinetic energy, acoustic energy and entropy (entropy perturbation reads $\widehat{s} = C_v(\widehat{T}/\bar{T} - (\gamma-1)\widehat{\rho}/\bar{\rho})$). This norm has been classically used in thermoacoustics. Chu's energy is a full norm over the computation domain $[0, \xi_{\mathrm{sf}}]$ but does not account for deformations $\widehat{X}_\mathrm{a}$. Therefore, if Chu's energy is used for normalization it needs to be supplemented by a complementary norm $\mathcal{J}^*$ measuring the boundary deformations.

- **Myers' energy.** The energy of Myers (1991) is given by the density

$$\bar{\rho}\left(\widehat{v}_x^2 + \widehat{d}_\perp^2/k_\perp^2\right) + 2\widehat{\rho}\bar{v}_x\widehat{v}_x + \widehat{p}^2/(\bar{\rho}\bar{c}_s) + \frac{(\gamma-1)}{\gamma}\bar{\rho}\bar{T}\widehat{s}^2$$

or

$$\mathrm{j}_M = \widehat{\mathbf{U}}^\top \mathbf{W}_M \widehat{\mathbf{U}}, \quad \text{with} \quad \mathbf{W}_M = t^\alpha \bar{G}^{-1} \begin{pmatrix} t^{2\alpha-2}\bar{\Theta}/\bar{G} & t^{\alpha-1}\bar{V}_x & 0 & 0 \\ t^{\alpha-1}\bar{V}_x & \bar{G} & 0 & 0 \\ 0 & 0 & \bar{G}/k_\perp^2 & 0 \\ 0 & 0 & 0 & t^{2-2\alpha}C_v\bar{G}/\bar{\Theta} \end{pmatrix}, \quad \text{for} \quad k_\perp > 0. \tag{4.11}$$

This energy is also conserved for uniform base flows without external source of perturbations, but may take negative values in case of negative base-flow velocities $\bar{v}_x$. Myers' energy also loses its positiveness in the case of a supersonic mean flow (George and Sujith, 2012). Similarly to Chu's energy, if used for normalization, Myers' energy needs to be augmented by a complementary norm $\mathfrak{J}^*$ measuring the boundary deformations.

- **'Ablation layer deformation' .** This is defined as the integral of the deformation of the isotherm lines in the ablation layer. The function $q_{\mathrm{af}}(m)$ is an integration window $\left[m_{\mathrm{af}}^-, m_{\mathrm{af}}^+\right]$ encompassing the maximum of the specific total energy variation rate $\bar{q}_0$ with smooth matching at its boundaries (see App. E.3 for a complete definition). This objective functional is inspired by flame front stability analysis (Lemke et al., 2014). Ablation layer deformation is defined as

$$\widehat{X}_T = -\frac{\widehat{T}}{\bar{\rho}\partial_m \bar{T}} = -t^{\alpha-2}\frac{\widehat{\Theta}}{\bar{G}\mathrm{d}_\xi\bar{\Theta}}, \quad \text{for} \quad \mathrm{d}_\xi\bar{\Theta} \neq 0. \tag{4.12}$$

For normalization purpose, the ablation layer deformation needs to be supplemented by a norm of boundary deformations, a norm on $\widehat{T}$ outside $\left[m_{\mathrm{af}}^-, m_{\mathrm{af}}^+\right]$ and a norm on $(\widehat{\rho} \quad \widehat{v}_x \quad \widehat{d}_\perp)$ over the whole domain.

Link with experimental diagnostics. Measurements of Chu's and Myers' energies, as well as of the L_2-norm, are not accessible by experimental means. Although these quantities provide us with interesting insights about hydrodynamics, it is necessary to consider some outputs that model experimentally measurable quantities. Radiography measurements carried out on ablation waves, either planar or in spherical symmetry, enable to track the forerunning shock front and ablation layer. These measurements are based on the areal mass perturbation (Aglitskiy et al., 2010). Face-on radiography records the two-dimensional distribution of areal mass perturbation and side-on radiography records the trajectories and geometries of the shock front and ablation layer. A common experimental diagnostic used to detect hydrodynamic perturbations in imploding shells is the *optical depth*, defined as the integral of the opacity κ over the shell radial thickness (Raman et al., 2014). In the case of radiation heat conduction (2.8), the opacity writes $\kappa = 4\,\bar{\rho}^{\mu}\bar{T}^{3-\nu}$ (Mihalas and Mihalas, 1984). As the medium upstream to the leading shock front is undisturbed, the optical depth linear perturbation writes

$$\widehat{OD} = \int_{x_{\mathrm{es}}}^{x_{\mathrm{sf}}} (\widehat{\rho}\kappa_\rho + \widehat{T}\kappa_T)\,\mathrm{d}x = \int_0^{m_{\mathrm{sf}}} (\widehat{\rho}\kappa_\rho + \widehat{T}\kappa_T)\frac{\mathrm{d}m}{\bar{\rho}} + \widehat{X}_{\mathrm{es}}\kappa + \widehat{X}_{\mathrm{sf}}\kappa, \tag{4.13}$$

where κ_ρ and κ_T stands for the partial derivatives of κ with respect to the density and the temperature. Although $\widehat{OD}$ is an integral quantity as the norms presented in Tab. 4.1, it is not positive definite, i.e. $\widehat{OD}$ can display positive and negative variations, or vanish for non-zero perturbations.

4.4 A local analysis

In the following article prepared for *Physical Review Letters* we conduct a local analysis to assess the presence of non-modal effects at small scales in the ablation wave RC-3, i.e. for perturbations of characteristic wavelengths much smaller than the gradient lengths of the base flow. Such an analysis has never been carried out on ablation flows. This study allows us to have a first glimpse at the non-normality of the evolution operator. This insight is necessarily partial but useful to decide on the necessity to set up a more complex global analysis.

Our goal is to maximize the *initial growth rate* of the L_2-norm. To do so, we perform a Fourier transform in the longitudinal direction and analyze the non-normality of the resulting evolution operator. The numerical range of this operator is computed for several longitudinal and transverse wavelengths. We observe that the numerical abscissa is positive in large regions of the flow, including the conduction region classically considered as stable, and for a wide range of longitudinal and transverse wavelengths.

This measure of non-normality is verified by an amplification computation of perturbations initialized as a Fourier mode, locally, in the conduction region. This computation indeed displays an initial transient growth of the L_2-norm. This growth rate is in agreement with the one predictied by the numerical abscissa of the longitudinal Fourier transformed evolution operator. Moreover, the amplification of the L_2-norm is not visible on the optical depth perturbation. These results encourages us to perform a global non-modal analysis.

Stability of ablation flow in inertial confinement fusion: non-modal optimal growth

G. Varillon,[1, 2] J.-M. Clarisse,[1] and A. Couairon[2]
[1]*CEA, DAM, DIF, F-91297 Arpajon, France*
[2]*CPHT, CNRS, Ecole Polytechnique, Institut Polytechnique de Paris, Route de Saclay, 91128 Palaiseau, France**

(Dated: July 18, 2019)

Ablation flows relevant to inertial confinement fusion (ICF) are found to display transient amplification of linear hydrodynamic perturbations thanks to a nonmodal analysis, the first of its kind on ablation flows. These transient amplifications result from constructive interactions of in-phase acoustic and vorticity waves in the conduction region. Non-modal growth of perturbations may lead to a precocious transition to nonlinear behaviour during ICF implosion stages considered as stable, thus accelerating the phenomena degrading the ICF pellet implosion. We finally notice the optical depth measurements does bring useful information to detect non-modal growth.

PACS numbers:

Inertial confinement fusion (ICF) aims at achieving thermonuclear burn by imploding a spherical pellet filled with a fusible mixture under the action of an intense irradiation [1]. Such implosions are strongly nonuniform and unsteady flows, prone to hydrodynamic instabilities which, by degrading the desired compression and heating of the fuel, may ruin the whole process. Early and recent experiments have confirmed that hydrodynamic instabilities are, among others, crucial to ICF achievement [2]. In particular, the subsonic heat-wave flow, or "ablation flow", that prevails throughout the irradiation of the outer dense shell of the pellet, is highly sensitive to instabilities of its heat front—"ablation front". Linear stability analyses of ablation fronts have been conducted using the method of normal modes, *modal stability analysis*, for idealized ablation flows (e.g. steady, quasi-isobaric, discontinuous, etc. [cf. 3]) or more realistic, i.e. simulated, flows under the frozen-time assumption (FTA). Such analyses yield asymptotic stability results and are therefore of limited relevance for the rapidly evolving flows of ICF implosions. An alternative method that is free from such limitations, consists in computing perturbation amplification about a base flow that results from initial and boundary values, as a response to selected initial and/or boundary perturbations. This approach, sometimes called "amplification theory" (AT), has been favored in ICF when treating realistic configurations, either with dedicated numerical codes in the case of simplified physics flows, either with multi-physics hydrodynamic codes when simulating experiments, including pellet implosions. Good agreements between AT simulations and specifically designed experiments where a dominant, "most dangerous", perturbation source is selected by a careful control of experimental conditions, have helped building confidence in the ability of multi-physics hydrocodes to reproduce instability dynamics [e.g. 4, 5]. However such simulations, carried out with these very codes, still display unexplained discrepancies with pellet implosions at standard specifications for fusion [6]. In such experiments, many perturbation sources are competing, without a clear dominance of one on the others, and the characterization of their initial or temporal contributions is unsufficient for setting up representative enough AT simulations. The matter is further complicated by the fact that even individually decaying perturbations, thus held innocuous, can induce, through their interaction, perturbation transient growth [7]. In principle, AT computations could capture such growth provided that they are started from (driven by) appropriate initial (resp., boundary) conditions. However, performing computations for a sufficiently large set of eligible initial or boundary conditions so as to identify which of them lead to perturbation amplification, and, above all, to the *maximum amplification*, is unfeasible.

Non-modal stability analysis which exploits the fact that the short-time dynamics of a system is not only driven by the eigenvalues of its evolution operator, which are only indicative of the system long-time behavior, but also by this operator eigenfunctions, might yield useful information. This approach, formalized in [8], has been successfully applied to many hydrodynamic problems (see [9] and references therein) but not yet to the hydrodynamic stability of ablation flows. This Letter performs the first non-modal analysis of an ablation flow and aims at exhibiting possible non-modal effects in such flows.

For a dynamical system, in space and time variables (m, t), ruled by

$$\partial_t \widehat{U} = \mathcal{A}(m, t, \partial_m \cdot)\widehat{U}, \quad t \geq t_0, \tag{1}$$

where $\widehat{U}$ is the vector of state variables, $\mathcal{A}$ is a linear differential operator, and given a scalar product $\langle \cdot, \cdot \rangle$ of associated norm $\| \cdot \|$, over some spatial domain, the instantaneous growth rate of $\|\widehat{U}\|^2$ at time $t^* \geq t_0$ is given by [7]

$$\sigma(t^*) \equiv \left(\frac{1}{\|\widehat{U}\|^2} \frac{\mathrm{d}\|\widehat{U}\|^2}{\mathrm{d}t} \right)\Bigg|_{t^*} = 2\mathrm{Re}\left(\frac{\langle \widehat{U}, \mathcal{A}\widehat{U} \rangle}{\langle \widehat{U}, \widehat{U} \rangle} \right)\Bigg|_{t^*}. \tag{2}$$

The above ratio of scalar products defines the numerical range of the operator $\mathcal{A}$. In the general case of a non-normal operator $\mathcal{A}$, the numerical range is wider than the convex envelope of the spectrum of $\mathcal{A}$ (relevant for a normal operator [10]) in the complex plane. In particular, this numerical range may protrude into the unstable half-plane (Re > 0) even though the spectrum of $\mathcal{A}$ may be confined to the stable half-plane (Re < 0). In such a case *non-modal growth* occurs, i.e. an initial amplification of $\widehat{U}$ although all eigenvalues are stable. The maximum of $\sigma(t^*)$, or numerical abscissa of $\mathcal{A}|_{t^*}$, corresponds to the largest eigenvalue of the normal operator $(\mathcal{A}+\mathcal{A}^\dagger)|_{t^*}$, where † denotes the transconjugate, and is achieved for the principal eigensolution of $(\mathcal{A}+\mathcal{A}^\dagger)|_{t^*}$ [9]. Here we focus on finding the *optimal-growth initial condition* $\widehat{U}_0^{\text{opt}}$ which maximizes the initial growth rate $\sigma(t_0)$.

Following previous investigations [11, 12] of linear perturbation dynamics in ablation flows relevant to the shock-transit stage of an ICF target irradiation, the chosen base flow is a self-similar ablation wave driven by nonlinear heat conduction in slab symmetry for a compressible inviscid fluid [13]. Such waves present essential features of shock-transit ablation flows (compressibility, stratification, unsteadiness) as well as describe their complete structure [Fig. 1]: (i) leading shock front, (ii) quasi-isentropic compression ('post-shock') region, (iii) ablation layer and (iv) expansion wave where heat condution dominates (the 'conduction region'). For one-dimensional motion in the direction x of a Cartesian coordinate system (O,x,y,z), the equations of motion, written in dimensionless form and in the Lagrangian coordinate m where $\mathrm{d}m=\rho\mathrm{d}x$, come as [14]

$$\begin{gathered}\partial_t(1/\rho)-\partial_m v_x=0,\quad \partial_t v_x+\partial_m p=0,\\ \partial_t(\mathrm{C}_v T+v_x^2/2)+\partial_m(p v_x+\varphi_x)=0,\end{gathered} \tag{3}$$

where ρ, v_x, p, T, φ_x denote, respectively, the fluid density, velocity, pressure, temperature and heat flux as functions of (m,t). This system is closed by the dimensionless equation of state $p=\rho T$, $\mathrm{C}_v=1/(\gamma-1)$, and the nonlinear heat-flux expression

$$\varphi_x=-\rho^{-\mu}T^{\nu}\rho\partial_m T,\quad \mu\geq 0,\quad \nu>1. \tag{4}$$

Self-similar reductions of Eqs. (3), (4) arise when a semi-infinite slab ($m\geq 0$), initially such that $(\rho,\,v_x,\,T)=(1,\,0,\,0)$, is subject to the boundary conditions at the material surface $m=0$: $\varphi_x(0,t)=\mathcal{B}_\phi t^{3\alpha-3}$, $p(0,t)=\mathcal{B}_p t^{2\alpha-2}$, for $t>0$, with $\alpha=(2\nu-1)/(2\nu-2)$. For the choice $\gamma=5/3$, $(\mu,\nu)=(2,13/2)$, Eqs. (3) and (4) describe the motion of a monatomic gas with the radiative conduction model of Kramers for a fully ionized gas [15]. This modelling is relevant to the ablation of an opaque material, remaining at local thermodynamic equilibrium, in the radiation heat-conduction approximation and for material temperatures ranging between a few thousands and a few millions of Kelvin degrees, in which case radiation diffusive effects dominate those of thermal conduction and viscosity, and radiation pressure and energy are negligible in front of material pressure and internal energy. These conditions comply rather well with those of fusion-pellet ablation driven by hohlraum X-rays in current ICF laser facilities, except for non-grey irradiation effects which cannot be rendered by Eqs. (3), (4). Nevertheless these equations contain the basic nonlinear diffusion mechanism which is at stake, at the hydrodynamic scale, in such ablation process. The particular solution $(\mathcal{B}_\phi,\mathcal{B}_p)=(0.8,0.31)$ is chosen for its features that are representative of shock-transit ablation flows [16]: subsonic ablation Mach number, high (>80) ablation front Froude number, steep ablation front, and fast expansion flow with Chapman–Jouguet point. This solution is computed using an adaptive multidomain Chebyshev method, providing a high accuracy description of the flow down to its finest scales [17].

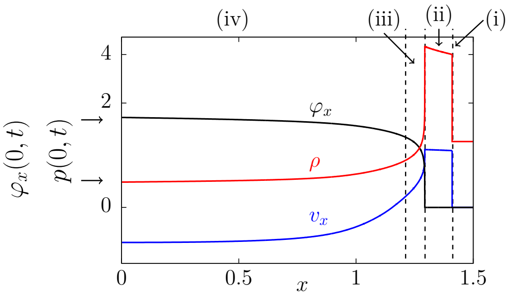

FIG. 1: Radiation driven self-similar ablation wave for boundary condition parameters $(\mathcal{B}_\phi,\mathcal{B}_p)=(0.8,0.31)$ of (3). Spatial profiles in the coordinate x at time $t_0=1$ of the fluid density ρ, longitudinal velocity v_x and heat flux φ_x.

The linear stability of flows solution to Eqs. (3), (4) is studied using an Eulerian description of the flow three-dimensional perturbations in the coordinate system (m,y,z). The corresponding system of partial differential equations, once Fourier transformed in the variables (y,z), comes down to [12]

$$\begin{aligned}&\partial_t\widehat{\rho}+\rho\big(\partial_m\rho\,\widehat{v}_x+\rho\,\partial_m\widehat{v}_x+\partial_m v_x\,\widehat{\rho}+\widehat{d}_\perp\big)=0,\\ &\partial_t\widehat{v}_x+\rho\,\partial_m v_x\,\widehat{v}_x+\partial_m\widehat{p}-\partial_m p\,\widehat{\rho}/\rho=0,\\ &\partial_t\widehat{d}_\perp-k_\perp^2\,\widehat{p}/\rho=0,\\ &\mathrm{C}_v\big(\partial_t\widehat{T}+\rho\,\partial_m T\,\widehat{v}_x\big)+\rho\,\partial_m v_x\,\widehat{T}+p\,\partial_m\widehat{v}_x+\partial_m\widehat{\varphi}_x\\ &\qquad\qquad-\partial_m\varphi_x\,\widehat{\rho}/\rho+\big(p\,\widehat{d}_\perp+k_\perp^2\,\rho^{-\mu}\,T^{\nu}\,\widehat{T}\big)/\rho=0,\end{aligned}$$

or, equivalently,

$$\partial_t\widehat{U}=\mathcal{A}(m,t,\partial_m\cdot,k_\perp)\,\widehat{U},\ \text{with}\ \widehat{U}=\big(\widehat{\rho}\ \widehat{v}_x\ \widehat{d}_\perp\ \widehat{T}\big)^\top, \tag{5}$$

with $\widehat{f}$ the yz-Fourier component of the linear perturbation of the base flow quantity f; $\widehat{d}_\perp$ the Fourier component of the transverse divergence of the transverse velocity perturbation; and $k_\perp=\sqrt{k_y^2+k_z^2}$ the transverse wavenumber. This system is supplemented by linear perturbation boundary conditions at the perturbed external surface $m = 0$ and leading shock front $m = m_{\rm sf}$ [12]. Solutions to (5) are computed thanks to the same adaptive multidomain Chebyshev method as for the base flow.

The non-normality of the operator $\mathcal{A}(m, t_0, \partial_m\cdot, k_\perp)$ is assessed locally by considering perturbations of longitudinal characteristic lengths that are smaller than the local gradient lengths of the base flow, l_∇, and the Euclidean norm of $\widehat{U}$. In effect, the numerical abscissa of the operator $\mathcal{A}(m, t_0, ik_m, k_\perp)$, or $\max \sigma(t_0)$, is computed [18] at various flow locations m spanning the whole ablation wave, $0 \leq m \leq m_{\rm sf}$, for values of the longitudinal wavenumber k_m satisfying the conditions $\varkappa_x(m) \equiv k_m\, \rho(m)\, l_\nabla(m) \geq 10$, and for given $k_\perp$: see Fig. 2. The numerical abscissa $\sigma(t_0)$ displays positive values in regions of stable eigenvalues, which means that non-modal growth is expected. In black areas (Fig. 2), there exist at least an unstable eigenvalue so that initial growth is predicted by a standard modal, or spectral, analysis. The numerical abscissa is at least as unstable as the least stable eigenvalue. The transverse wavenumber $k_\perp$ tends to widen the region of non-modal growth in the conduction region together with the initial growth rate. In the post shock region, non-modal growth growth occurs for a limited range of $\varkappa_x$, about ≈ 500, vanishing at the shock front (Fig. 2). At $k_\perp = 0$, (low transverse modes) the upper bound of this $\varkappa_x$ range extends up to large values.

The evolution operator $\mathcal{A}$ is locally non-modal everywhere. This is the first assessment of non-modal effects in the ablation flow considered. Therefore, (transient) growth is expected at any location, for all longitudinal wavelength $\varkappa_x$ represented on Fig. 2. Actual transient growth is further tested by performing AT computations of $\widehat{U}$ satisfying Eq. (5) for initial conditions deduced from the above local analysis of non-modal effects at a given abscissa, $m_* = 0.25$ ($x_* = 0.71$), located in a zone of non-modal growth.

In effect non-zero initial conditions are defined over a small domain S_0 of the flow conduction region, centered about m_*, according to the expression

$$\widehat{U}(m, t_0, k_\perp) = \mathrm{Re}\big(\widehat{U}_0^{\rm opt}(m_*)\, e^{ik_m m}\big), \text{ for } m \text{ in } S_0, \quad (6)$$

where $\widehat{U}_0^{\rm opt}(m_*)$ is the principal eigenvector of the operator $(\mathcal{A} + \mathcal{A}^\dagger)(m_*, t_0, ik_m, k_\perp)$. Applying this initial condition to the perturbation evolution operator $\mathcal{A}$ (Eq. 5) leaves the latter in a Fourier approximation – say $\mathcal{A}_0$ – depending on space-dependent base flow variables, plus two control parameters: $\varkappa_x(x)$ and $\varkappa_\perp(x) = k_\perp l_\nabla(x)$.

We keep $\varkappa_x(x_*) \gg 1$ and $S_0/l_{\rm cond} \ll 1$ to ensure the local approximation. Noticing that $U_0^{\rm opt}(x)$ does not vary significantly for x in S_0, as S_0 is small, we compute $U_0^{\rm opt}(x_*)$ with (2) and extend it for all x in S_0.

Although the optimal initial condition (Eq. 6) have been determined by means of a local analysis, the numerical integration of Eq. (5) from this initial condition is free from any assumptions on steadiness, uniformity and characteristic scales. The amplification of perturbations is measured according to the global L_2 norm

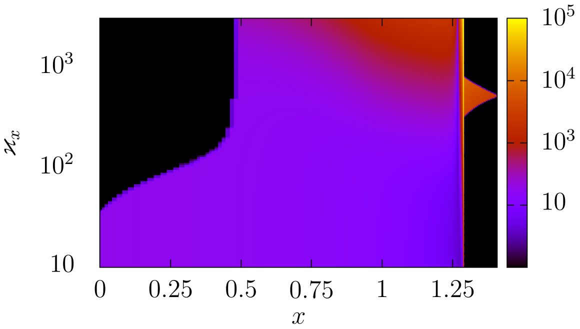

FIG. 2: Coloured region: Numerical range of $\mathcal{A}_0$ depending on $\varkappa_x$ and the location x for $k_\perp = 10$, in the case of negative eigenvalues. Black region: correspond to the case where a positive eigenvalue exists.

$$\|\widehat{U}\|^2 = \int_0^{x_{\rm sf}} \frac{1}{2} \widehat{U}^\top \widehat{U} \mathrm{d}x.$$

An initial amplification of the norm is identified in all three cases (Fig. 3), confirming the effectiveness of non-modal effects in ablation flows. However the initial growth rate differs with $\varkappa_x$ and $\varkappa_\perp$. Furthermore, the initial growth rates $\max(\sigma(t_0))$ (Eq. 2) predicted thanks to the local analysis, i.e. $\mathcal{A}_0$, are in good agreement with the values postprocessed from the AT ($\sigma_{\rm AT}$ in Tab. I). We note that the FTA is valid for the chosen values $(\varkappa_x, \varkappa_\perp)$, as $\sigma_{\rm AT}^{-1} \ll t \sim 1$, t being the characteristic time of the base flow.

TABLE I: Values of $\max(\sigma(t_0))$ 'predicted' *via* Eq. (2), $\sigma_{\rm AT}$ postprocessed from solutions to Eq. (5), characteristic growth time $\sigma_{\rm AT}^{-1}$ and pseudo period of oscillations.

$(\varkappa_x, \varkappa_\perp)$	$\max(\sigma(t_0))$	$\sigma_{\rm AT}$	$\sigma_{\rm AT}^{-1}$	pseudo-period
$(515, 0)$	93	91	$1.1\,10^{-2}$	$7.5\,10^{-2}$
$(515, 23.4)$	308	300	$3.2\,10^{-3}$	$7.5\,10^{-2}$
$(2575, 0)$	455	450	$2.2\,10^{-3}$	$1.7\,10^{-2}$

For the present ablation flow, the duration of the shock transit phase is $t_{\rm st} \approx 10$. As $\sigma_{\rm AT}^{-1} \ll t_{\rm st}$ the initial growth of perturbation is an *actual fast transient* with respect the shock transit duration. Such a behaviour is not predicted by a standard *modal stability* analysis, i.e. based solely on eigenvalues, which would predict an initial decay of perturbations.

Solution to (5) for $(\varkappa_x, \varkappa_\perp) = (515, 23.4)$ is projected in the (m, t) plane on upstream and downstream longitudinal acoustic modes (Fig. 4a and b) and the transverse divergence of the transverse velocity, $\widehat{d}_\perp$ (Fig. 4c). The initial optimal perturbation is a superposition of both acoustic modes and a vorticity mode propagating at fluid velocity (i.e. constant m), whose track emerges on $\widehat{d}_\perp$. Fig. 3 displays an initial growth of the L_2 norm followed by oscillations around a mean value. Peak values result from constructive interactions between in-phase acoustic and vorticity fields (Fig. 4d). The transient growth is therefore a consequence of local interactions between travelling waves. These oscillations are fast compared to base-flow characteristic time, t, and the shock transit duration, t_{st}, and obey the acoustic dispersion relation.

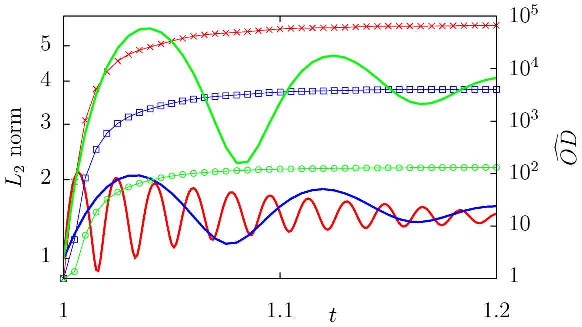

FIG. 3: Normalized L_2 norm of the perturbations (solid) and optical depth perturbation (symbol) for the case $(\varkappa_x, \varkappa_\perp) = (515, 0)$ (blue), $(515, 23.4)$ (green) and $(2.5\,10^3, 0)$ (red).

Optical depth, defined as the integral of the opacity κ over the shell thickness, is a common experimental diagnostic used to detect hydrodynamic perturbations in imploding shells [5]. In the case of radiation heat conduction (4), the opacity writes $\kappa = 4\,\rho^\mu T^{3-\nu}$ [19]. As the medium upstream to the leading shock front is undisturbed, the optical depth linear perturbation writes

$$\widehat{OD} = \int_0^{x_{\mathrm{sf}}} (\widehat{\rho}\kappa_\rho + \widehat{T}\kappa_T)\,\mathrm{d}x, \tag{7}$$

where κ_ρ and κ_T stands for the partial derivatives of κ with respect to the density and the temperature. Even though the optical depth perturbation increases with time, it does not render, at all, the oscillations observed on the norm (Fig. 3). This fact is rather intuitive, as the optimal growth initial condition as been shown to be mainly the superposition of isothermal acoustic and vorticity waves, which spatial fluctuations may balance one another when integrated in space. The initial growth rate of $\widehat{OD}$ does not scale as the initial growth rate of $\|\widehat{U}\|$ either, nor 'long' time values of $\widehat{OD}$ are representative of the initial growth rate or mean values of $\|\widehat{U}\|$. In particular, the presence of vorticity tends to lower the initial growth and long time values of $\widehat{OD}$ while it results in an increased initial growth and mean value of $\|\widehat{U}\|$. The velocity perturbation is not accounted for in $\widehat{OD}$ while it is in $\|\widehat{U}\|$. The consequence is that non-modal effects cannot be deduced from optical depth measurements.

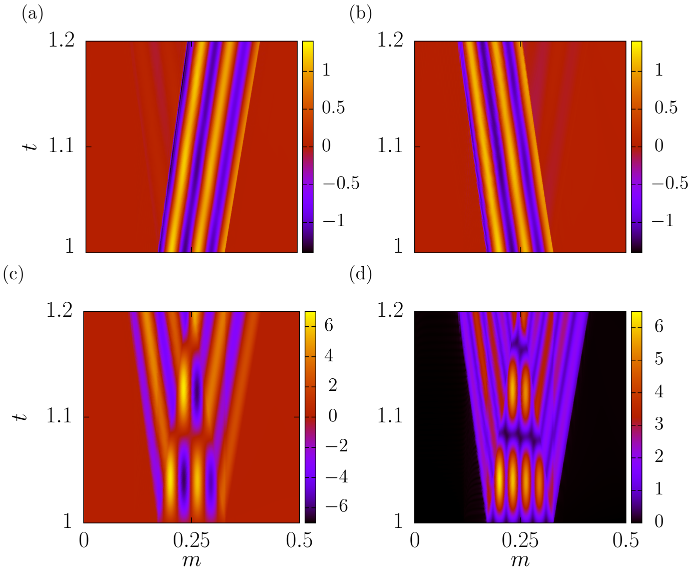

FIG. 4: Projection of the response to Eq. (5), for initial conditions given by Eq. (6), in the case $(\varkappa_x, \varkappa_\perp) = (515, 23.4)$, on (a) upstream and (b) downstream quasi-isothermal longitudinal acoustic waves and (c) transverse divergence of the transverse velocity, in the conduction region. (d) Local Euclidean norm.

The present analysis brings to light transient growth of linear perturbations in an ablation flow representative of a radiation driven ICF implosion. The evolution operator is locally non-modal every where for a wide range of longitudinal and transverse characteristic lengths, which paves the way to transient growth of the norm of perturbations. The operator represents hydrodynamic mechanisms of an ablation flow: advection, nonlinear heat diffusion, acceleration, unsteadiness and nonuniformity. The presence of non-modal behaviour in thermoacoustic systems has been raised in the case of accelerated flows [20], as it is the case in ablation waves. Transient growth of the global L_2 norm of perturbations is actually observed, with characteristic times short with respect to the shock transit duration, followed by oscillations. This behaviour results from constructive interactions of in-phase acoustic and vorticity waves. Perturbations of the optical depth are of no use to detect non-modal growth. This is a first assessment of non-modal effects in ablation flows. Transient growth resulting from non-modal effects may lead to a transition to nonlinear behaviour more precocious than predicted thanks to a standard modal analysis. These results open up a new perspective for studying ablation flows stability. A global analysis is now necessary to get a complete picture of non-modal phenomena without any restriction on the characteristic scale of initial perturbations and taking into account couplings between the perturbed boundaries and the ablation layer. In particular, a global non-modal analysis may find out perturbation amplifications in ICF implosion stages that are considered as stable.

---

[*] `gregoire.varillon@polytechnique.edu`

[1] S. Atzeni and J. Meyer-ter-Vehn, *The physics of inertial fusion* (Oxford University Press, Oxford, U.K., 2004).

[2] J. Lindl et al., Phys. Plasmas **21**, 020501 (2014).

[3] V. Bychkov et al., Prog. Energy Combust. Sci. **47**, 32 (2015).

[4] Y. Aglitskiy et al., Phil. Trans. R. Soc. A **368**, 1739 (2010).

[5] K. S. Raman et al., Phys. Plasmas **21** (2014).

[6] V. A. Smalyuk et al., Phys. Plasmas **24**, 042706 (2017).

[7] P. J. Schmid and D. S. Henningson, *Stability and transition in shear flows* (Springer, 2001).

[8] L. N. Trefethen et al., Science **261**, 578 (1993).

[9] P. J. Schmid, Annu. Rev. Fluid Mech. **39**, 129 (2007).

[10] R. A. Horn and C. R. Johnson, *Matrix Analysis* (Cambridge University Press, 1990).

[11] F. Abéguilé et al., Phys. Rev. Lett. **97**, 035002 (2006).

[12] J.-M. Clarisse et al., J. Fluid Mech. **609**, 1 (2008).

[13] R. Marshak, Phys. Fluids **1**, 24 (1958).

[14] C. Boudesocque-Dubois et al., J. Fluid Mech. **603**, 151 (2008).

[15] Y. B. Zel'dovich and Y. P. Raizer, *Physics of shock waves and high-temperature hydrodynamic phenomena* (Academic Press, New York, 1967).

[16] J.-M. Clarisse et al., J. Fluid Mech. **848**, 219 (2018).

[17] C. Boudesocque-Dubois et al., J. Comput. Phys. **235**, 723 (2013).

[18] C. C. Cowen and E. Harel, *An effective algorithm for calculating the numerical range* (1995).

[19] D. Mihalas and B. W. Mihalas, *Foundations of radiation hydrodynamics* (Oxford University Press, Oxford, 1984).

[20] K. Wieczorek et al., Phys. Fluids **23** (2011).

4.5 Global analysis

We are now interested in the solutions to the following OIP problem:

$$\textit{Find the initial state} \quad (\widehat{\mathbf{U}}, \widehat{X}_{\mathrm{es}}, \widehat{X}_{\mathrm{sf}})|_{t_0} \quad \textit{that maximizes} \quad \mathcal{J}(T), \tag{4.14}$$

where $\mathcal{J}(T)$ depends only on the final state $(\widehat{\mathbf{U}}, \widehat{X}_{\mathrm{es}}, \widehat{X}_{\mathrm{sf}})|_T$, and $(\widehat{\mathbf{U}}, \widehat{X}_{\mathrm{es}}, \widehat{X}_{\mathrm{sf}})$ are solutions to (3.28), (3.40), for zero external forcing (i.e. $\widehat{\mathbf{F}}_{\mathrm{es}} = \mathbf{0}$ and $\widehat{\mathbf{U}}_u = \mathbf{0}$ in 3.40). Ablation flows are nonuniform, therefore it is necessary to use a global method. In our case the base flow is time dependent, which leads to a time dependent evolution operator L for perturbations. As explained in § 4.1, it is cumbersome to work with the fundamental solution operator M for time dependent evolution operators L. As an alternative we have recourse to a direct-adjoint method: the set of equations (3.28), (3.40), along with initial conditions, constitutes the *direct* problem and its *adjoint* problem is derived. Solving both the direct and adjoint problems simultaneously yields the optimal perturbation. Adjoint problems have been widely used in the field of hydrodynamic stability analysis (see Luchini and Bottaro, 2014 and references therein). Here we chose to derive the adjoint problem from the Lagrange multiplier technique taken from optimal control theory (Gunzburger, 1997), but there exists other methods to do so, e.g. *via* the derivation of a dual problem (Giles and Pierce, 1997, 2000; Luchini and Bottaro, 1998) or the projection on a set of test functions (Schmid and Henningson, 2001). The Lagrange multiplier technique presents the advantage of furnishing optimality conditions and a gradient direction suitable for a use in a gradient descent algorithm (Guégan et al., 2006).

Since its introduction in the field (Corbett and Bottaro, 2001), this technique has gained popularity in hydrodynamic stability studies, due to its versatility. However the majority of stability analyses deal with incompressible fluids and applications of this technique to compressible flows are still rather scarce. In the compressible flow community, the use of adjoint problems emerged in the late 1980s as a convenient tool for solving optimal design problems in computational fluid dynamics (CFD): see (Jameson, 1988). Early works derived adjoint problems straight from duality considerations (e.g. Jameson, 1988) and this method has remained favored by some people (Giles and Pierce, 1997, 2000). The Lagrange multiplier technique came later on (e.g. Jameson, 1995) and became widespread in aeronautical CFD due to its connection with constrained optimization and optimal control theory. However, the issue of adjoint boundary conditions for hyperbolic systems of equations was treated by Giles and Pierce (1997) within the dual problem approach and, to our knowledge, no equivalent analysis has been produced within the context of the Lagrange multiplier technique. In fact, the dominant practice is by far to exclude boundary conditions — unless they are part of the control variables — from the Lagrange multiplier formulation. The optimization is then performed in a solution space that is constrained by the desired boundary conditions and the proper adjoint boundary conditions are deduced from considering boundary contributions. In that respect, this way of proceeding shows little difference with the dual problem approach. The fact that, in our case, boundary conditions are applied on moving boundaries that are subject to their own dynamics and must be found as part of the solution to the problem, brings in an additional complication. An adjoint-based optimization of a steady and incompressible flow with free boundaries is treated in (Volkov et al., 2009) with a Lagrange multiplier formulation. But having to deal presently with both a compressible flow and unsteady free boundaries has required us to identify a suitable formulation of the Lagrange functional with limited insights from previous works.

4.5.1 Building the Lagrange functional

The Lagrange functional is built in the following way: the constraints (evolution equation, boundary and initial conditions) that the state variable must verify are added to the objective functional (Gunzburger, 1997). The Lagrange functional we ended up with is the result of trials and errors. This formulation obeys the following principle: the constraints enforced for boundary conditions have to be such that the direct problem inferred from the Lagrange functional is well-posed. What is clear for a scalar advection equation requires, in the case of a hyperbolic system, to include constraints only on the incoming characteristics and leave the outgoing characteristics free from constraints. As a consequence, there are as many Lagrange multipliers as there are incoming waves at each boundary ($\widehat{\boldsymbol{\nu}}_{\mathrm{a}}$, a=es,sf).

However (3.28) is an incompletely parabolic system. The hyperbolic subsystem is treated as for the hyperbolic system explained above but two boundary conditions need to be added on the parabolic subequation, which adds two Lagrange multipliers ($\widehat{\eta}^{\dagger}_{\mathrm{a}}$, a=es,sf).

The additional complication is that the boundaries are deformed, as we describe perturbations of the base flow variables but also of the external surface and shock front $\widehat{X}_{\mathrm{a}}$. These deformations obeys a temporal ODE implicitly present in the boundary conditions (3.40)

$$\mathrm{d}_t \widehat{X}_{\mathrm{a}} = \dot{\widehat{X}}_{\mathrm{a}}, \quad \mathrm{a} = \mathrm{es,\ sf}. \tag{4.15}$$

The deformations $\widehat{X}_{\mathrm{a}}$ have to satisfy these equations which needs to be added to the Lagrange functional with two additional Lagrange multipliers ($\widehat{\mu}^{\dagger}_{\mathrm{a}}$, a=es,sf).

If the above mentioned rules are not verified then the Lagrange multipliers are over-, or under-, determined. Lagrange multipliers are recalled in Tab. 4.2. As a consequence, we form the Lagrange functional

Lagrange multipliers	Corresponding constraints	Type
$\widehat{\mathbf{U}}^{\dagger}$	Evolution equation for perturbations	4-vector defined over $[0, \xi_{\mathrm{sf}}] \times [t_0, T]$
$\widehat{\boldsymbol{\nu}}^{\dagger}_{\mathrm{es}}$ and $\widehat{\boldsymbol{\nu}}^{\dagger}_{\mathrm{sf}}$	Hyperbolic subsystem BCs	3-vectors defined over $[t_0, T]$
$\widehat{\eta}^{\dagger}_{\mathrm{es}}$ and $\widehat{\eta}^{\dagger}_{\mathrm{sf}}$	Parabolic subequation BCs	scalars defined over $[t_0, T]$
$\widehat{\mu}^{\dagger}_{\mathrm{es}}$ and $\widehat{\mu}^{\dagger}_{\mathrm{sf}}$	Evolution equation for boundary deformations	scalars defined over $[t_0, T]$
$\widehat{\beta}^{\dagger}_{k}$	Normalization of the initial condition	scalar constants

Table 4.2: Lagrange multipliers used in (4.16).

$$\mathcal{L} = \mathcal{J}(T) - \mathcal{O} - \sum_{\mathrm{a=es,sf}} \left(\mathcal{B}^{h}_{\mathrm{a}} + \mathcal{B}^{p}_{\mathrm{a}} + \mathcal{F}_{\mathrm{a}} \right) - \sum_{k=0}^{p} \mathcal{N}_k, \tag{4.16a}$$

where the different constraints come as follows.

Evolution equation. Equation (3.28) has to be verified at all positions ξ and times t:

$$\mathcal{O} = \int_{t_0,0}^{T,\xi_{\mathrm{sf}}} \widehat{\mathbf{U}}^{\dagger\top} (\partial_t \widehat{\mathbf{U}} - \mathbf{L}\widehat{\mathbf{U}})\, \mathrm{d}\xi\, \mathrm{d}t. \tag{4.16b}$$

Boundary conditions for the hyperbolic subsystem. The part of the state variable corresponding to the hyperbolic subsystem, at the boundary, $\widehat{\mathbf{U}}_{\mathrm{I}}|_{\mathrm{a}}$ has to verify the set point $\widehat{\mathbf{U}}_{\mathrm{I}_{\mathrm{a}}}$, which is a vector function of the deformation $\widehat{X}_{\mathrm{a}}$ and the state variable itself extracted from (3.40). This constraint is projected on the incoming components of the hyperbolic subsystem through the projector $\mathcal{P}^{\mathrm{in}}_{11\mathrm{a}}$. We need to determine as many components of $\widehat{\boldsymbol{\nu}}^{\dagger}_{\mathrm{a}}$ as there are incoming characteristics, i.e. one at a = es and two at a = sf:

$$\mathcal{B}^{h}_{\mathrm{a}} = \int_{t_0}^{T} \widehat{\boldsymbol{\nu}}^{\dagger\top}_{\mathrm{a}} \mathcal{P}^{\mathrm{in}}_{11\mathrm{a}} \left[\widehat{\mathbf{U}}_{\mathrm{I}}|_{\mathrm{a}} - \widehat{\mathbf{U}}_{\mathrm{I}_{\mathrm{a}}}\left(\widehat{\mathbf{U}}|_{\mathrm{a}}, \widehat{X}_{\mathrm{a}}\right)\right] \mathrm{d}t, \tag{4.16c}$$

superscript 'h ' stands for hyperbolic.

Boundary conditions for the parabolic subequation. The boundary conditions for the parabolic subequation corresponds to heat-flux continuity equation (3.39c), expressed in (ξ, t) variables, for a = es, and to the total energy conservation equation in (3.42) for a = sf. Writing these equations $\mathcal{B}^{p}_{\mathrm{a}}$, '$p$ ' for parabolic, the resulting constraint functional reads:

$$\mathcal{B}^{p}_{\mathrm{a}} = \int_{t_0}^{T} \widehat{\eta}^{\dagger}_{\mathrm{a}} \widehat{\mathbf{B}}^{p}_{\mathrm{a}}\left(\widehat{\mathbf{U}}|_{\mathrm{a}}, \widehat{X}_{\mathrm{a}}\right) \mathrm{d}t. \tag{4.16d}$$

Evolution equation for the deformation. The scalar function f_{a} is the kinematic relation (3.39d), expressed in (ξ, t) variables, for a = es, and to the equation on the velocity component in (3.42) for a = sf:

$$\mathcal{F}_{\mathrm{a}} = \int_{t_0}^{T} \widehat{\mu}^{\dagger}_{\mathrm{a}} f_{\mathrm{a}}\left(\widehat{\mathbf{U}}|_{\mathrm{a}}, \widehat{X}_{\mathrm{a}}\right) \mathrm{d}t. \tag{4.16e}$$

Normalization constraint. In the search for a solution to problem (4.14), a diverging initial condition constitutes a trivial solution that we wish to avoid. As a consequence we include some normalization terms:

$$\mathcal{N}_k = \widehat{\beta}^{\dagger}_k \left[\mathcal{I}_k\left(\widehat{\mathbf{U}}|_{t_0}, \widehat{X}_{\mathrm{es}}|_{t_0}, \widehat{X}_{\mathrm{sf}}|_{t_0}\right) - \mathcal{I}^{0}_k\right]. \tag{4.16f}$$

The semi-norms $\mathcal{I}_k$ are chosen to ensure that their kernels are in direct sum in the space of initial conditions $(\widehat{\mathbf{U}}, \widehat{X}_{\mathrm{es}}, \widehat{X}_{\mathrm{sf}})|_{t_0}$. Therefore the normalization embraces the whole space of initial conditions. As the problem is linear, it is sufficient to choose the set points $\mathcal{I}^{0}_k$ so that

$$\sum_{k=0}^{p} \mathcal{I}^{0}_k = 1. \tag{4.17}$$

If the purpose is to compute a gain, i.e. maximizing the ratio

$$\mathcal{G} = \frac{\mathscr{J}(T)}{\mathscr{J}(t_0)}, \tag{4.18}$$

then it is necessary that one of the semi-norms $\mathcal{I}_k$ corresponds to $\mathscr{J}$, e.g. $\mathcal{I}_0 \equiv \mathscr{J}$. In our application we have $p = 1$

and a new parameter r_c, denoting the initial distribution between the $\mathcal{I}_0^0$ and $\mathcal{I}_1^0$, appears

$$\mathcal{I}_0^0 = r_c, \quad \text{and} \quad \mathcal{I}_1^0 = 1 - r_c, \quad 0 \leqslant r_c \leqslant 1. \tag{4.19}$$

This parameter r_c is varied between 0 and 1 so as to span the whole distribution possibilities while constraint (4.17) is fulfilled. If the purpose is to compute a gain (4.18), the value $r_c = 0$ is forbidden.

Remarks:

- In our set of variables, the initial state $(\widehat{\mathbf{U}}, \widehat{X}_{\mathrm{es}}, \widehat{X}_{\mathrm{sf}})|_{t_0}$ plays the role of the *control parameters*, i.e. the variables according to which the optimum is looked for.
- The formulation of the Lagrange functional $\mathcal{L}$ is based on the evolution equation (3.28) with boundary conditions on hyperbolic and parabolic subsystems. Another possibility is to include the penalized evolution equation with the operator $\mathbf{L}_\pi$ (3.53), which already accounts for boundary conditions on the hyperbolic subsystem, and the sole boundary conditions on the parabolic subequation (4.16d). In that case the constraint functional (4.16c) is removed from the Lagrange functional.

  Taking a broader point of view, and keeping in mind that the adjoint problem will finally be integrated in time under a discretized form, there exists multiple possibilities between working with the discretized adjoint of the continuous direct problem (*differentiate then discretize*, our choice) and with the adjoint of the discretized direct problem (*discretize then differentiate*). Arguments presenting the advantages and drawbacks of each option are given in (Gunzburger, 1997).

4.5.2 The adjoint problem

The solution to (4.14) subject to the normalization constraint (4.17) lies in the stationary points of the Lagrange functional $\mathcal{L}$ (Gunzburger, 1997), i.e. the points for which the directional derivative with respect to each of the independent variables vanishes. Namely, we look for points for which the derivative of $\mathcal{L}$ with respect to $\boldsymbol{x}$ in a direction $\boldsymbol{x}'$, given by

$$\nabla_{\boldsymbol{x}}\mathcal{L} \cdot \boldsymbol{x}' = \lim_{\epsilon \to 0} \frac{\mathcal{L}(\boldsymbol{x} + \epsilon \boldsymbol{x}') - \mathcal{L}(\boldsymbol{x})}{\epsilon}, \tag{4.20}$$

vanishes for each independent variable $\boldsymbol{x}$ for a variation in any direction $\boldsymbol{x}'$.

Using the Lagrange multipliers framework amounts to considering that the state variables of the IBVP (3.25), (3.40) are independent. As a consequence the independent variables of $\mathcal{L}$ (4.16) are:

1. The *direct variables*:
   - the perturbation state variables $(\widehat{\mathbf{U}}, \widehat{X}_{\mathrm{es}}, \widehat{X}_{\mathrm{sf}})$, for all $t_0 \leqslant t \leqslant T$ and $0 \leqslant \xi \leqslant \xi_{\mathrm{sf}}$,
   - the boundary values of the perturbation state variables $\widehat{\mathbf{U}}|_{\mathrm{a}}$ and of their spatial derivatives $\partial_\xi \widehat{\mathbf{U}}|_{\mathrm{a}}$, for all $t_0 \leqslant t \leqslant T$ and a = es, sf,
   - and the initial and terminal values of the perturbation state variables, $(\widehat{\mathbf{U}}, \widehat{X}_{\mathrm{es}}, \widehat{X}_{\mathrm{sf}})|_{t_0}$ and $(\widehat{\mathbf{U}}, \widehat{X}_{\mathrm{es}}, \widehat{X}_{\mathrm{sf}})|_T$, for all $0 \leqslant \xi \leqslant \xi_{\mathrm{sf}}$.
2. The *adjoint variables* defined in Tab. 4.2:
   - the adjoint perturbation state $(\widehat{\mathbf{U}}^\dagger, \widehat{\nu}_{\mathrm{a}}^\dagger, \widehat{\eta}_{\mathrm{a}}^\dagger, \widehat{\mu}_{\mathrm{a}}^\dagger)$, for all $t_0 \leqslant t \leqslant T$ and $0 \leqslant \xi \leqslant \xi_{\mathrm{sf}}$,

- the initial and terminal values of the adjoint perturbation state $(\widehat{\mathbf{U}}^\dagger, \widehat{\boldsymbol{\nu}}_{\mathrm{a}}^\dagger, \widehat{\eta}_{\mathrm{a}}^\dagger, \widehat{\mu}_{\mathrm{a}}^\dagger)|_{t_0}$ and $(\widehat{\mathbf{U}}^\dagger, \widehat{\boldsymbol{\nu}}_{\mathrm{a}}^\dagger, \widehat{\eta}_{\mathrm{a}}^\dagger, \widehat{\mu}_{\mathrm{a}}^\dagger)|_T$, for all $0 \leqslant \xi \leqslant \xi_{\mathrm{sf}}$ and a = es, sf,
- and the boundary values of the adjoint perturbation state $\widehat{\mathbf{U}}^\dagger|_{\mathrm{es}}$ and $\widehat{\mathbf{U}}^\dagger|_{\mathrm{sf}}$, for all $t_0 \leqslant t \leqslant T$.

The vanishing of directional derivatives with respect to the adjoint variables gives the direct IBVP (3.28), (3.40), along with boundary conditions, and the vanishing of directional derivatives with respect to the direct variables leads to the *adjoint problem*: evolution equations supplemented by boundary conditions for the adjoint variables. Two *optimality conditions* furnish a relation between the direct and adjoint variables.

Directional derivatives of $\mathcal{L}$ with respect to direct variables are detailed in App. E.1. In what follows, we are using the notations $\mathbf{N}^{\mathrm{a}}$, $\mathbf{M}^{\mathrm{a}}$, $\mathbf{S}^{\mathrm{a},0}$ and $\mathbf{S}^{\mathrm{a},1}$ defined in § 3.2.2 for a = es and sf. The resulting adjoint problem is composed of the following equations:

An adjoint evolution equation, i.e. an evolution equation for $\widehat{\mathbf{U}}^\dagger$, which comes as

$$\partial_t \widehat{\mathbf{U}}^\dagger + \mathbf{A}^\dagger \partial_\xi^2 \widehat{\mathbf{U}}^\dagger + \mathbf{B}^\dagger \partial_\xi \widehat{\mathbf{U}}^\dagger + \mathbf{C}^\dagger \widehat{\mathbf{U}}^\dagger = \mathbf{0} \quad \Leftrightarrow \quad \partial_t \widehat{\mathbf{U}}^\dagger = \mathbf{L}^\dagger \widehat{\mathbf{U}}^\dagger, \tag{4.21a}$$

$$\mathbf{A}^\dagger = -\mathbf{A}^\top, \quad \mathbf{B}^\dagger = (\mathbf{B} - 2\,\partial_\xi \mathbf{A})^\top, \quad \mathbf{C}^\dagger = -\left(\mathbf{C} - \partial_\xi \mathbf{B} + \partial_\xi^2 \mathbf{A}\right)^\top.$$

A terminal condition for $\widehat{\mathbf{U}}^\dagger$,

$$\nabla_{\widehat{\mathbf{U}}|_T} \mathcal{J} - \widehat{\mathbf{U}}^\dagger|_T = 0. \tag{4.21b}$$

Boundary conditions at ξ_{es}, with $(\mathbf{O}^{\mathrm{es}})_i = (\mathbf{M}^{\mathrm{es}})_{2i}$ and $\mathbb{B}_{\mathrm{in}}$ defined as $(\mathbb{B}_{\mathrm{in}})_{ij} = (\mathbf{B}_{11}^{\mathrm{in}^{\mathrm{es}}})_{ji}$, $1 \leqslant i,j \leqslant 3$ and $(\mathbb{B}_{\mathrm{in}})_{4j} = \left(\mathbf{B}_{11}^{\mathrm{in}^{\mathrm{es}}} \mathbf{M}_{11}^{\mathrm{es}\,-1} \mathbf{M}_{12}^{\mathrm{es}}\right)_{\mathrm{j}}$, $1 \leqslant j \leqslant 3$, where $\mathbf{B}_{11}^{\mathrm{in}^{\mathrm{es}}}$ is the matrix of the incoming waves of the hyperbolic subsystem (3.32), come as

$$-\mathbb{B}_{\mathrm{in}} \widehat{\boldsymbol{\nu}}_{\mathrm{es}}^\dagger - \mathbf{M}_{\mathrm{par}}^{\mathrm{es}} \widehat{\eta}_{\mathrm{es}}^\dagger - \mathbf{O}^{\mathrm{es}} \widehat{\mu}_{\mathrm{es}}^\dagger + \left(\mathbf{B}^\top \widehat{\mathbf{U}}^\dagger - \partial_\xi (\mathbf{A}^\top \widehat{\mathbf{U}}^\dagger)\right)\Big|_{\mathrm{es}} = \mathbf{0}, \tag{4.21c}$$

$$\left(\widehat{\mathbf{U}}^{\dagger\top} \mathbf{A}\right)\Big|_{\mathrm{es}} - \widehat{\eta}_{\mathrm{es}}^\dagger \mathbf{N}^{\mathrm{es}} = 0. \tag{4.21d}$$

Boundary conditions at ξ_{sf}, with $(\mathbf{O}^{\mathrm{sf}})_i = (\mathbf{M}^{\mathrm{sf}})_{2i}$ and $\mathbb{B}_{\mathrm{in}}$ defined as $(\mathbb{B}_{\mathrm{in}})_{ij} = (\mathbf{B}_{11}^{\mathrm{in}^{\mathrm{sf}}})_{ji}$, $1 \leqslant i,j \leqslant 3$ and $(\mathbb{B}_{\mathrm{in}})_{4j} = \left(\mathbf{B}_{11}^{\mathrm{in}^{\mathrm{sf}}} \mathbf{M}_{11}^{\mathrm{sf}\,-1} \mathbf{M}_{12}^{\mathrm{sf}}\right)_{\mathrm{j}}$, $1 \leqslant j \leqslant 3$, are given by

$$-\mathbb{B}_{\mathrm{in}} \widehat{\boldsymbol{\nu}}_{\mathrm{sf}}^\dagger - \mathbf{M}_{\mathrm{par}}^{\mathrm{sf}} \widehat{\eta}_{\mathrm{sf}}^\dagger - \mathbf{O}^{\mathrm{sf}} \widehat{\mu}_{\mathrm{sf}}^\dagger - \left(\mathbf{B}^\top \widehat{\mathbf{U}}^\dagger + \partial_\xi (\mathbf{A}^\top \widehat{\mathbf{U}}^\dagger)\right)\Big|_{\mathrm{sf}} = \mathbf{0}, \tag{4.21e}$$

$$-\left(\widehat{\mathbf{U}}^{\dagger\top} \mathbf{A}\right)\Big|_{\mathrm{sf}} - \widehat{\eta}_{\mathrm{sf}}^\dagger \mathbf{N}^{\mathrm{sf}} = 0. \tag{4.21f}$$

Adjoint deformations and **adjoint deformation velocity** are defined for convenience. They correspond to two scalar linear combinations of Lagrange multipliers:

$$\widehat{X}_{\mathrm{a}}^\dagger = \widehat{\boldsymbol{\nu}}_{\mathrm{a}}^{\dagger\,\top} \mathbf{B}_{11}^{\mathrm{in}^{\mathrm{a}}} \mathbf{M}_{11}^{\mathrm{a}\;-1} \mathbf{S}_{\mathrm{I}}^{\mathrm{a},1} + \widehat{\eta}_{\mathrm{a}}^\dagger \mathbf{S}_{\mathrm{II}}^{\mathrm{a},1} + \widehat{\mu}_{\mathrm{a}}^{\dagger\dagger} (\mathbf{S}^{\mathrm{a},1})_2, \quad \text{for a =es, sf,} \tag{4.21g}$$

and

$$\dot{\widehat{X}}_{\mathrm{a}}^{\dagger} = \widehat{\boldsymbol{\nu}}_{\mathrm{a}}^{\dagger\,\top} \mathbf{B}_{11}^{\mathrm{in^a}} \mathbf{M}_{11}^{\mathrm{a}\;-1} \mathbf{S}_{\mathrm{I}}^{\mathrm{a},0} + \widehat{\eta}_{\mathrm{a}}^{\dagger} \mathbf{S}_{\mathrm{II}}^{\mathrm{a},0} + \widehat{\mu}_{\mathrm{a}}^{\dagger} (\mathbf{S}^{\mathrm{a},0})_2, \quad \text{for a =es, sf,} \tag{4.21h}$$

respectively. Their evolution equations are given by

$$\dot{\widehat{X}}_{\mathrm{a}}^{\dagger} - \mathrm{d}_t \widehat{X}_{\mathrm{a}}^{\dagger} = 0, \quad \text{a = es, sf.} \tag{4.21i}$$

Terminal conditions for the adjoint deformations come as

$$\widehat{X}_{\mathrm{a}}^{\dagger}|_T = \nabla_{\widehat{X}_{\mathrm{a}}} \mathcal{J} \Big|_T, \quad \text{a = es, sf.} \tag{4.21j}$$

Optimality conditions closes the system with

$$\widehat{\mathbf{U}}^{\dagger}|_{t_0} - \sum_k \widehat{\beta}_k^{\dagger} \nabla_{\widehat{\mathbf{U}}|_{t_0}} \mathcal{J}_k = \mathbf{0}, \tag{4.21k}$$

$$\widehat{X}_{\mathrm{a}}^{\dagger}|_{t_0} - \sum_k \widehat{\beta}_k^{\dagger} \nabla_{\widehat{X}_{\mathrm{a}}|_{t_0}} \mathcal{J}_k = 0, \quad \text{a = es, sf.} \tag{4.21l}$$

Mathematical properties of the adjoint equation. The adjoint evolution equation (4.21a) appears as a linear reaction-advection-diffusion equation which can be reformulated by means of a decomposition similar that of the direct evolution equation (3.30), namely

$$\partial_t \begin{pmatrix} \widehat{\mathbf{U}}_{\mathrm{I}}^{\dagger} \\ \widehat{\mathbf{U}}_{\mathrm{II}}^{\dagger} \end{pmatrix} + \begin{pmatrix} \mathbf{0} & \mathbf{0} \\ \mathbf{0} & \mathbf{A}_{22}^{\dagger} \end{pmatrix} \partial_{\xi}^2 \begin{pmatrix} \widehat{\mathbf{U}}_{\mathrm{I}}^{\dagger} \\ \widehat{\mathbf{U}}_{\mathrm{II}}^{\dagger} \end{pmatrix} + \begin{pmatrix} \mathbf{B}_{11}^{\dagger} & \mathbf{B}_{12}^{\dagger} \\ \mathbf{B}_{21}^{\dagger} & \mathbf{B}_{22}^{\dagger} \end{pmatrix} \partial_{\xi} \begin{pmatrix} \widehat{\mathbf{U}}_{\mathrm{I}}^{\dagger} \\ \widehat{\mathbf{U}}_{\mathrm{II}}^{\dagger} \end{pmatrix} + \begin{pmatrix} \mathbf{C}_{11}^{\dagger} & \mathbf{C}_{12}^{\dagger} \\ \mathbf{C}_{21}^{\dagger} & \mathbf{C}_{22}^{\dagger} \end{pmatrix} \begin{pmatrix} \widehat{\mathbf{U}}_{\mathrm{I}}^{\dagger} \\ \widehat{\mathbf{U}}_{\mathrm{II}}^{\dagger} \end{pmatrix} = \mathbf{0}, \tag{4.22}$$

with $\widehat{\mathbf{U}}_{\mathrm{I}}^{\dagger} = (\widehat{G}^{\dagger} \quad \widehat{V}_x^{\dagger} \quad \widehat{D}_{\perp}^{\dagger})$ and $\widehat{\mathbf{U}}_{\mathrm{II}}^{\dagger} = \widehat{\Theta}^{\dagger}$. We note from (4.21a) that $\mathbf{B}_{11}^{\dagger} = \mathbf{B}_{11}{}^{\top}$, therefore $\mathbf{B}_{11}^{\dagger}$ is also hyperbolic and shares the same real-valued eigenvalues as $\mathbf{B}_{11}$ and the right eigenvectors of $\mathbf{B}_{11}^{\dagger}$ are the left eigenvectors of $\mathbf{B}_{11}$. From (4.22) it follows that (4.21a) is composed of a parabolic subequation for reverse time

$$\partial_t \widehat{\mathbf{U}}_{\mathrm{II}}^{\dagger} - \mathbf{A}_{22} \partial_{\xi^2}^2 \widehat{\mathbf{U}}_{\mathrm{II}}^{\dagger} = 0, \tag{4.23a}$$

since $\mathbf{A}_{22}^{\dagger} = -\mathbf{A}_{22}$, and a hyperbolic subsystem

$$\partial_t \widehat{\mathbf{U}}_{\mathrm{I}}^{\dagger} + \mathbf{B}_{11}^{\top} \partial_{\xi} \widehat{\mathbf{U}}_{\mathrm{I}}^{\dagger} = 0. \tag{4.23b}$$

4.5.3 Solving the adjoint problem

With the same cautions as those formulated in § 3.2.1, (4.21a) is treated as an incompletely parabolic system. Equation (4.23a) requires that (4.21a) be integrated backward in time from the terminal conditions (4.21b) and (4.21j), unless the system is ill-posed. As (4.23b) is the transposed of (3.32) and because (4.21a) is integrated backward in time, at each boundary, the incoming waves of the hyperbolic part of the adjoint equation (4.23b) correspond to the outgoing waves of the hyperbolic part of the direct equation (3.32) and vice-versa, i.e. the incoming waves of (4.23b) are those of negative velocity (respectively positive) at the external surface (resp. shock front).

For a number of base flows, $\mathbf{B}^{\dagger}$ displays complex-valued eigenvalues in a region close to the external surface. This point raises two problems. Firstly, solutions to (4.21a) may display exponentially growing and decaying modes. Such equations are qualified as *stiff* in (Gear, 1971, § 12). Explicit numerical schemes such as (3.56) are not adapted to deal with this superposition of growing and decaying exponentials. Therefore, solving (4.21a) would require to switch to a fully semi-implicit scheme. Secondly, the characteristics method exposed in § 3.3.3 to deal with subdomain interfaces and the penalty method § 3.3.3 for boundary conditions result to be groundless. Although the physical meaning of the transition between the regions where $\mathbf{B}^\dagger$ is hyperbolic and where $\mathbf{B}^\dagger$ is not hyperbolic is not yet understood, we circumvent this difficulty by an alternative formulation of (4.21a), namely

$$\partial_t \widehat{\mathbf{U}}^\dagger + \partial_\xi^2 \left(\mathbf{A}^\dagger \widehat{\mathbf{U}}^\dagger\right) + \mathbf{B}^\top \partial_\xi \widehat{\mathbf{U}}^\dagger - \left(\mathbf{C} - \partial_\xi \mathbf{B}\right)^\top \widehat{\mathbf{U}}^\dagger = \mathbf{0}, \tag{4.24}$$

where $(\mathbf{A}^\dagger \widehat{\mathbf{U}}^\dagger) = (0 \quad 0 \quad 0 \quad -\mathbf{A}_{22} \widehat{\Theta}^\dagger)^\top$. Using this formulation, (4.24) is integrated using the implicit-explicit RK3 scheme (§ 3.3.3)

$$\widehat{\mathrm{Q}}^{r+1} = \Delta t \, \widehat{\mathbf{F}}^{\dagger^r} - c_{r+1} \widehat{\mathrm{Q}}^r \tag{4.25a}$$

$$\widehat{\mathbf{U}}^{\dagger r+1} = \widehat{\mathbf{U}}^{\dagger r} + a_{r+1} \widehat{\mathrm{Q}}^{r+1} + b_{r+1} \Delta t \left(\widehat{\mathbf{G}}^{\dagger^r} + \widehat{\mathbf{G}}^{\dagger^{r+1}}\right), \tag{4.25b}$$

for $r = 0, 1, 2$, $\widehat{\mathrm{Q}}^0 = \mathbf{0}$ and where $\widehat{\mathbf{U}}^{\dagger r}$ stands for $\widehat{\mathbf{U}}^\dagger(\xi, t^r)$. The operators $\widehat{\mathbf{F}}^\dagger$ and $\widehat{\mathbf{G}}^\dagger$ are defined by

$$\widehat{\mathbf{G}}^\dagger(\xi, t) = -\begin{pmatrix} \mathbf{0} & \mathbf{0} \\ \mathbf{0} & \mathbf{1} \end{pmatrix} \partial_\xi^2 (\mathbf{A}^\dagger \widehat{\mathbf{U}}) + \begin{pmatrix} \mathbf{0} & \mathbf{0} \\ \mathbf{0} & k_\perp^2 C_{44}^\perp / \mathbf{A}_{22}^\dagger \end{pmatrix} \mathbf{A}^\dagger \widehat{\mathbf{U}}, \tag{4.26a}$$

(4.26b)

$$\widehat{\mathbf{F}}^\dagger(\xi, t) = \mathbf{L}_\pi^\dagger \widehat{\mathbf{U}} - \widehat{\mathbf{G}}^\dagger(\xi, t),$$

where $\mathbf{L}_\pi^\dagger$ represents the adjoint evolution equation supplemented by penalty terms enforcing boundary conditions on the hyperbolic subsystem

$$\mathbf{L}_\pi^\dagger(\widehat{\mathbf{U}}^\dagger) = \mathbf{L}^\dagger \widehat{\mathbf{U}}^\dagger + \sum_{\mathrm{a}=\mathrm{es,sf}} \delta_\mathrm{a} \widehat{\mathbf{\Pi}}^{\dagger\,\mathrm{a}} \tag{4.27a}$$

$$\widehat{\mathbf{\Pi}}^{\dagger\,\mathrm{a}} = \tau_\mathrm{a} \mathcal{P}_\mathrm{a}^{\mathrm{in}} \left(\widehat{\mathbf{U}}^\dagger - \widehat{\mathrm{U}}_\mathrm{a}^\dagger(t)\right), \quad \mathrm{a} = \mathrm{es,\ sf}. \tag{4.27b}$$

The operator $\widehat{\mathbf{\Pi}}^{\dagger\,\mathrm{a}}$ is constructed, as for the direct problem, by accounting for the residual error between the set point $\widehat{\mathrm{U}}_\mathrm{a}^\dagger(t)$ determined from (E.11), and $\widehat{\mathbf{U}}^\dagger|_\mathrm{a}$ and projecting it onto the outgoing characteristics of $\mathbf{B}^\top$, since (4.21a) is integrated backward in time. The numerical method used for solving the adjoint problem has been verified on test-cases presented in App. F. Similarly as for the direct problem, the numerical code for the adjoint problem performs computations over each subdomain in parallel using the MPI paradigm with a single process per subdomain.

4.5.4 Optimization methods

Direct-adjoint iteration. Finding the solution to (4.14) amounts to solve (3.28),(3.40) and (4.21) simultaneously. However, integrating (3.28) forward in time and (4.21a) backward in time simultaneously requires to replace the time marching method (3.56),(4.25) by a temporal grid for the time interval $[t_0, T]$, i.e. to choose a set of discrete times t_j and to determine $\widehat{\mathbf{U}}(\xi_i, t_j)$ and $\widehat{\mathbf{U}}^\dagger(\xi_i, t_j)$ simultaneously for all $t_0 \leqslant t_j \leqslant T$ and all $0 \leqslant \xi_i \leqslant \xi_{\mathrm{sf}}$. This

$$\begin{tikzcd}
t = t_0 & & t = T \\
\widehat{\mathbf{U}}(\xi, t_0) \arrow[rr, "(3.28){,}(3.40)"] & & \widehat{\mathbf{U}}(\xi, T) \arrow[d, "(4.21b){,}(4.21j)"] \\
\widehat{\mathbf{U}}^\dagger(\xi, t_0) \arrow[u, "(4.28)"] & & \widehat{\mathbf{U}}^\dagger(\xi, T) \arrow[ll, "(4.21a){,}(4.21i)"']
\end{tikzcd}$$

Figure 4.2: Direct-adjoint iteration.

way of proceeding would lead to solve a linear system whose dimension would be too large to efficiently obtain a solution. An alternative method makes use of direct-adjoint loopings (Gunzburger, 1997). The direct and adjoint problems are solved iteratively with the terminal conditions (4.21b), (4.21j) at the terminal time T (Fig. 4.2). At each iteration, the optimality conditions (4.21k) and (4.21l) provide us with the gradient of the Lagrange functional $\mathcal{L}$ with respect to the control parameters $(\widehat{\mathbf{U}}, \widehat{X}_{\mathrm{es}}, \widehat{X}_{\mathrm{sf}})|_{t_0}$, i.e.

$$\nabla_{\widehat{\mathbf{U}}|_{t_0}} \mathcal{L} = \widehat{\mathbf{U}}^\dagger|_{t_0} - \sum_k \widehat{\beta}_k^\dagger \nabla_{\widehat{\mathbf{U}}|_{t_0}} \mathcal{J}_k, \tag{4.28a}$$

$$\nabla_{\widehat{X}_{\mathrm{a}}|_{t_0}} \mathcal{L} = \widehat{X}_{\mathrm{a}}^\dagger|_{t_0} - \widehat{\beta}_k^\dagger \nabla_{\widehat{X}_{\mathrm{a}}|_{t_0}} \mathcal{J}_k, \quad \mathrm{a} = \mathrm{es}, \mathrm{sf}. \tag{4.28b}$$

At the optimum these gradients vanish.

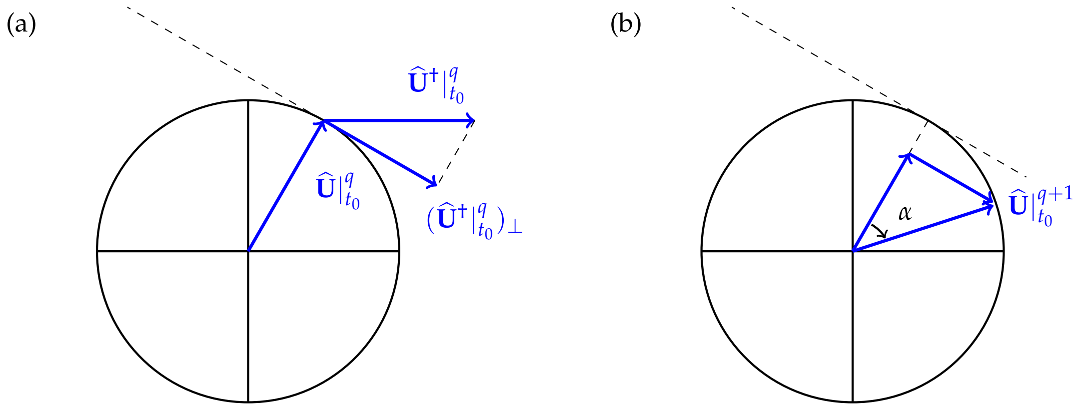

Figure 4.3: Geometrical view of the normalization (adapted from Foures et al., 2013).

Gradient descent methods. Once the gradient of the Lagrange functional with respect to the initial condition (4.28) has been determined at the end of the q-th iteration, a new initial condition is computed $(\widehat{\mathbf{U}}, \widehat{X}_{\mathrm{es}}, \widehat{X}_{\mathrm{sf}})|_{t_0}^{q+1}$ thanks to a gradient descent

$$\widehat{\mathbf{U}}|_{t_0}^{q+1} = \widehat{\mathbf{U}}|_{t_0}^{q} + \epsilon \nabla_{\widehat{\mathbf{U}}|_{t_0}} \mathcal{L}, \quad \text{with} \quad \epsilon \quad \text{the descent step}, \tag{4.29a}$$

$$\widehat{X}_{\mathrm{a}}|_{t_0}^{q+1} = \widehat{X}_{\mathrm{a}}|_{t_0}^{q} + \epsilon \nabla_{\widehat{X}_{\mathrm{a}}|_{t_0}} \mathcal{L}, \quad \text{for a} = \mathrm{es}, \mathrm{sf}. \tag{4.29b}$$

For the sake of clarity we assume that $\mathcal{J}$ is the L_2 norm and as a consequence there is only one normalization subspace. We also display expressions only for $\widehat{\mathbf{U}}$, but it works similarly for the deformations $\widehat{X}_{\mathrm{a}}$. Using (4.28), (4.29) rewrites as

$$\widehat{\mathbf{U}}|_{t_0}^{q+1} = (1 - \epsilon \widehat{\beta}^\dagger) \widehat{\mathbf{U}}|_{t_0}^{q} + \epsilon \widehat{\mathbf{U}}^\dagger|_{t_0}^{q}. \tag{4.30}$$

The standard technique builds on the normalization constraint enforced in (4.16f) to determine, given ϵ, the normalization Lagrange multiplier $\widehat{\beta}^\dagger$ so that $\widehat{\mathbf{U}}|_{t_0}^{q+1}$ fulfils the normalization constraint (4.17). The Lagrange multiplier $\widehat{\beta}^\dagger$ is solution to a second order polynomial in $\widehat{\beta}^\dagger$ whose determinant is

$$\Delta = 4 \int_0^{\xi_{\mathrm{sf}}} \left[(\widehat{\mathbf{U}}^\dagger|_{t_0}^{q} {}^\top \widehat{\mathbf{U}}|_{t_0}^{q})^2 \mathrm{d}\xi + \|\widehat{\mathbf{U}}|_{t_0}^{q}\|^2 (\|\widehat{\mathbf{U}}^\dagger|_{t_0}^{q}\|^2 + \frac{2}{\epsilon} \widehat{\mathbf{U}}^\dagger|_{t_0}^{q} {}^\top \widehat{\mathbf{U}}|_{t_0}^{q}) \right] \mathrm{d}\xi. \tag{4.31}$$

This determinant is positive for a restricted range of values ϵ which may change at each iteration q. This method proves to be very sensitive to the choice of ϵ during numerical tests, as was observed in (Foures et al., 2013), and therefore has not been used to produce the results presented in this thesis dissertation.

The power iteration technique amounts to choose $1 - \epsilon\widehat{\beta}^\dagger = 0$ in (4.30) and to rescale $\widehat{\mathbf{U}}|_{t_0}^{q+1}$ so that (4.17) is fulfilled. In practice the normalization term (4.16f) is omitted and at each iteration we set

$$\widehat{\mathbf{U}}|_{t_0}^{q+1} = \widehat{\mathbf{U}}^\dagger|_{t_0}^{q} \quad \text{and rescale} \quad \widehat{\mathbf{U}}|_{t_0}^{q+1}. \tag{4.32}$$

This method is robust but makes no use of the information contained in $\widehat{\mathbf{U}}|_{t_0}^{q}$.

The true gradient technique omits the normalization term (4.16f) and proposes a geometrical interpretation of the normalization (Douglas et al., 2000; Foures et al., 2013). The initial conditions $\widehat{\mathbf{U}}|_{t_0}$ have to belong to a hypersphere to comply with the normalization constraint. Hence, each new $\widehat{\mathbf{U}}|_{t_0}^{q+1}$ is the result of the rotation of $\widehat{\mathbf{U}}|_{t_0}^{q}$ by an angle c in the plane defined by $\widehat{\mathbf{U}}|_{t_0}^{q}$ and $\nabla_{\widehat{\mathbf{U}}|_{t_0}} \mathcal{L} = \widehat{\mathbf{U}}^\dagger|_{t_0}^{q}$ (Figs. 4.3a and b). To proceed, $\widehat{\mathbf{U}}^\dagger|_{t_0}^{q}$ is projected onto the subspace perpendicular to $\widehat{\mathbf{U}}|_{t_0}^{q}$ (Fig. 4.3a). This projection

$$(\widehat{\mathbf{U}}^\dagger|_{t_0}^{q})_\perp = \widehat{\mathbf{U}}^\dagger|_{t_0}^{q} - \frac{\int_0^{\xi_{\mathrm{sf}}} \widehat{\mathbf{U}}^\dagger|_{t_0}^{q} \widehat{\mathbf{U}}|_{t_0}^{q} \mathrm{d}\xi}{\int_0^{\xi_{\mathrm{sf}}} \|\widehat{\mathbf{U}}|_{t_0}^{q}\|^2 \mathrm{d}\xi} \widehat{\mathbf{U}}|_{t_0}^{q} \tag{4.33}$$

is then normalized and $\widehat{\mathbf{U}}|_{t_0}^{q+1}$ is built as a linear combination of $\widehat{\mathbf{U}}|_{t_0}^{q}$ and the normalized $(\widehat{\mathbf{U}}^\dagger|_{t_0}^{q})_\perp$ (Fig. 4.3b)

$$\widehat{\mathbf{U}}|_{t_0}^{q+1} = \cos(c)\widehat{\mathbf{U}}|_{t_0}^{q} + \sin(c)(\widehat{\mathbf{U}}^\dagger|_{t_0}^{q})_\perp, \quad \text{with} \quad c = \frac{\|(\widehat{\mathbf{U}}^\dagger|_{t_0}^{q})_\perp\|}{\|\widehat{\mathbf{U}}^\dagger|_{t_0}^{q}\|}, \tag{4.34}$$

from (Douglas et al., 2000). The choice of the most adapted method to our problem is not evident. According to Kerswell et al. (2014; 2018), it seems that there is no alternative to confronting each method by numerical experiment. The results presented in this thesis dissertation have been obtained with the *power iteration* method. The *true gradient* method has been tested and behaves similarly.

Initial guess and the potential local maxima. The direct-adjoint procedure requires a first non-zero initial condition at $q = 0$: the *initial guess*. If the objective functional presents local maxima, then two different initial guesses may lead to two different OIP. Three different initial guesses are listed below:

1. An initial condition that approximates the configuration of an ablative Richtmyer–Meshkov instability (ARM) as the deformation of a thin-sheet flow in the large transverse wavelength limit (Clarisse et al., 2016). This configuration corresponds to the perturbation field left by the rippled forerunning shock front formed by a

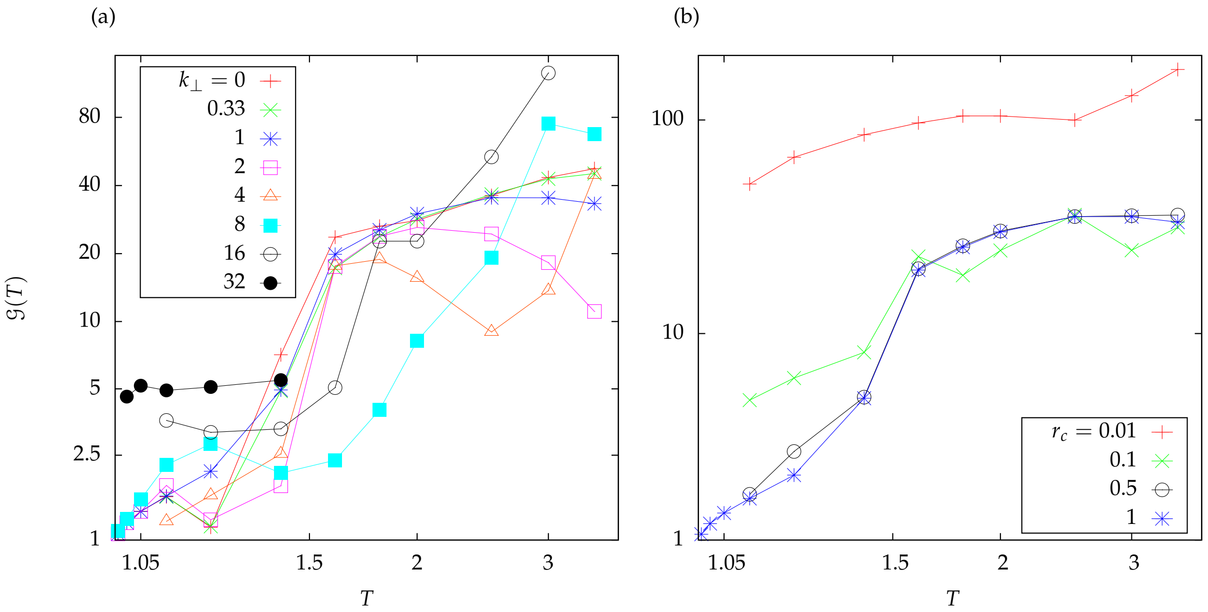

Figure 4.4: Ablation wave RC-1. Gain curves with Chu's energy (Tab. 4.1) in (4.6) for (a) various $k_\perp$ for $r_c = 1$ and (b) various r_c for $k_\perp = 1$. The initial time is $t_0 = 1$.

surface defect of size $\widehat{X}_0$, namely

$$\widehat{\mathbf{U}}|_{t_0} = \widehat{X}_0 \begin{pmatrix} -t^{-\alpha}\bar{G}\mathrm{d}_\xi\bar{G} \\ -t^{-1}\bar{G}\mathrm{d}_\xi\bar{V}_x \\ t^{\alpha-1}k_\perp^2\bar{V}_x|_{\mathrm{sf}}(\xi/\xi_{\mathrm{sf}})^{1-1/\alpha} \\ -t^{\alpha-2}\bar{G}\mathrm{d}_\xi\bar{\Theta} \end{pmatrix}, \tag{4.35a}$$

and

$$\widehat{X}_{\mathrm{es}}|_{t_0} = \widehat{X}_{\mathrm{sf}}|_{t_0} = \widehat{X}_0. \tag{4.35b}$$

This initial condition is a solution to (3.28) only in the case $k_\perp = 0$.

2. The response from a zero perturbation field at $t^- < t_0$ to an external heat-flux perturbation φ_{es} is computed from t^- to t_0. The resulting perturbation field at t_0 is normalized and serves as the initial guess.

3. The initial guess is taken as a uniform perturbation field with non-zero deformations. On the contrary to the choices 1 and 2, this initial guess does not correspond to a solution to (3.28).

These three different initial guesses converge to the same OIP on a test. This test does rule out the possibility that several local maxima exist but means that the use of one or the other initial guess explores the same maximum. For the computations carried out in this thesis we have chosen the ARM initial guess (4.35).

4.6 Optimal perturbation

The optimization procedure presented in § 4.5.1 is used to find the OIPs for the ablation wave RC-1 (§ 3.1). This base flow is preferred to the ablation wave RC-3 for computational issues, although the ablation wave RC-3 is more representative of actual ICF implosion flows due to its supersonic expansion. The computational time required to achieve one direct-adjoint iteration with the ablation wave RC-3 makes the realization of a complete OIP study for this base flow out of reach within the time frame of the present thesis (Tab. 4.3). The determination of an OIP may indeed require several tens of direct-adjoint iterations. However, these computation times are not unattainable with a looser time constraint.

The second obstacle is detailed in § 4.6.6: the time integration of the adjoint problem produces stiffening adjoint solutions in the conduction region, which are as stiff as the base flow is stiff in the ablation flow. This problem is overcome by constructing a grid which is as refined in the conduction region as it is in the ablation front. Although we manage to build a suitable grid for the ablation wave RC-1, we did not manage to do so for the ablation wave RC-3 because of its stiffness (Tab. 3.2).

Base flow	Num. steps $1 \leqslant t \leqslant 3.5$	one direct-adjoint iteration
RC-1	9.8×10^6	3.8 hours
RC-3	1.7×10^8	48 hours

Table 4.3: Computation times of direct-adjoint iterations for the ablation waves RC-1 and RC-3 for $k_\perp = 1$.

We present results for Chu's energy. As explained in § 4.3, Chu's energy bears more physical meaning than the L_2-norm. In addition this functional is positive definite for the state variable $\widehat{\mathbf{U}}$ over the spatial domain $[0, \xi_{\mathrm{sf}}]$, unlike Myers' energy. Chu's energy is supplemented by a complementary functional on the boundary deformations $\mathcal{I}^*$, cf. Tab. 4.1. Ablation layer deformation is given on an indicative basis in Tab. 4.1. Although this objective functional seems interesting for our problem, it suffers from an ill-definition of the integration windows q_{af} and q^*_{af}, especially for $r_c < 1$ (App. E.3).

4.6.1 Parameter variations

The terminal time T, transverse wavenumber $k_\perp$ and initial distribution r_c are varied and the OIP is found in each of these cases.

Parameters	Values
Initial time t_0	1
Terminal time T	$[1.01, 3.5]$
Time duration $D_t = T - t_0$	$[0.01, 2.5]$
Transverse wavenumber $k_\perp$	$[0, 32]$
$k_\perp L_{\mathrm{cond}}$	$[0.53, 52]$
Initial distribution r_c	$[0.01, 1]$
External forcing $(\widehat{\varphi}_{\mathrm{es}}, \widehat{p}_{\mathrm{es}}, \widehat{\mathbf{U}}_u)$	$(0, 0, \mathbf{0})$

Table 4.4: Ablation wave RC-1. Ranges of parameters explored.

Initial time t_0. Due to the singularity of the evolution equations (3.28) at $t = 0$, the initial time t_0 must be strictly positive. We set $t_0 = 1$, which is an arbitrary choice. Because of the similarity, a shift of the initial time would yield the same results if the terminal time T and transverse wavenumber $k_\perp$ are modified appropriately.

Range of terminal times T. The terminal time T is varied in an interval whose upper bound represents the end of the *shock-transit phase* for an actual ICF target design. To determine this bound, we build on the results of

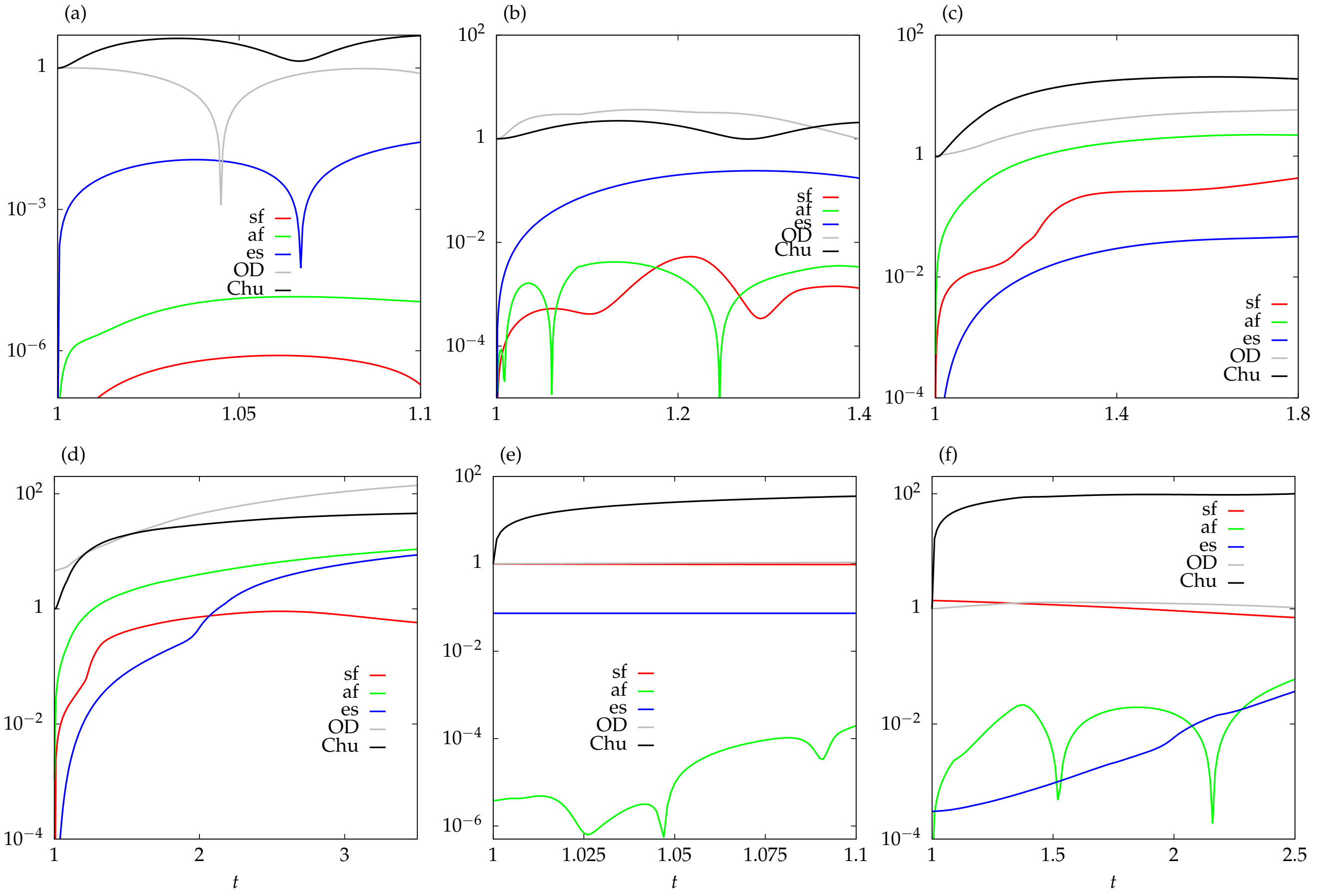

Figure 4.5: Ablation wave RC-1. Deformations of the external surface (es), ablation front (af), and shock front (sf). Gain of Chu's energy ($\mathcal{G}(t)$) and optical depth perturbation (OD). For $r_c = 1$: (a) $(k_\perp, T) = (32, 1.1)$, (b) $(k_\perp, T) = (8, 1.4)$, (c) $(k_\perp, T) = (4, 1.8)$ and (d) $(k_\perp, T) = (0.33, 3.5)$. For $r_c = 0.01$: (e) $(k_\perp, T) = (1, 1.1)$ and (f) $(k_\perp, T) = (1, 2.5)$.

§ 3.5 according to which perturbations propagate close to linear waves in the conduction and compression regions with wave speeds close to the eigenvalues of the advection matrix **B** (3.28c). An external perturbation reaches the ablation layer as a heat-conductivity wave and then initiates a system of reflected isentropic acoustic waves and entropy waves in the compression region (Fig. 3.5).

A simulation of the shock-transit phase for the chosen ICF target design (LMJ target A1040 of Saillard, 2000) with the ICF code FCI2 (Buresi et al., 1986) has allowed us to obtain travel time estimates for a sequence of these waves going back and forth between the ablation front (af) and the shock front (sf). We then identified that over the duration of the shock-transit phase, a forward acoustic wave initially launched from the ablation front can almost accomplish the sequence of trips (af → sf → af → sf → af → sf). From the equivalent travel times in the chosen self-similar ablation wave, the same sequence of trips is observed over the interval $1 < t < 3.69$: Tab. 4.5. We thus conclude that the end of the shock-transit phase for the target corresponds to a time smaller than 3.69 for the self-similar wave. Consequently, we set the upper bound on the terminal time to be $\max T = 3.5$. Over the time laps $1 \leq t \leq 3.5$, the self-similar ablation wave is thus equivalent, in terms of wave trips, to the shock-transit phase of the actual target.

To set the lower bound, we have observed that for most of the $k_\perp$, the gain $\mathcal{G}(T)$ is monotonous for $T \leqslant 1.1$ and $\mathcal{G}(T) \to 1$ as $T \to t_0 = 1$. Therefore by setting $\min\{T\} = 1.01$ we ensure that the lower bound does not belong to a change of regime of the gain $\mathcal{G}(T)$.

Wave type	Ablation layer		Shock front
Forward isentropic acoustic	1.05	→	1.28
Entropy	1.78	←	〃
Forward isentropic acoustic	〃	→	2.18
Entropy	3.02	←	〃
Forward isentropic acoustic	〃	→	3.69
Entropy	5.13	←	〃

Table 4.5: Ablation wave RC-1. Arrival times of characteristic waves at the ablation layer and shock front, from an external perturbation at $t_0 = 1$.

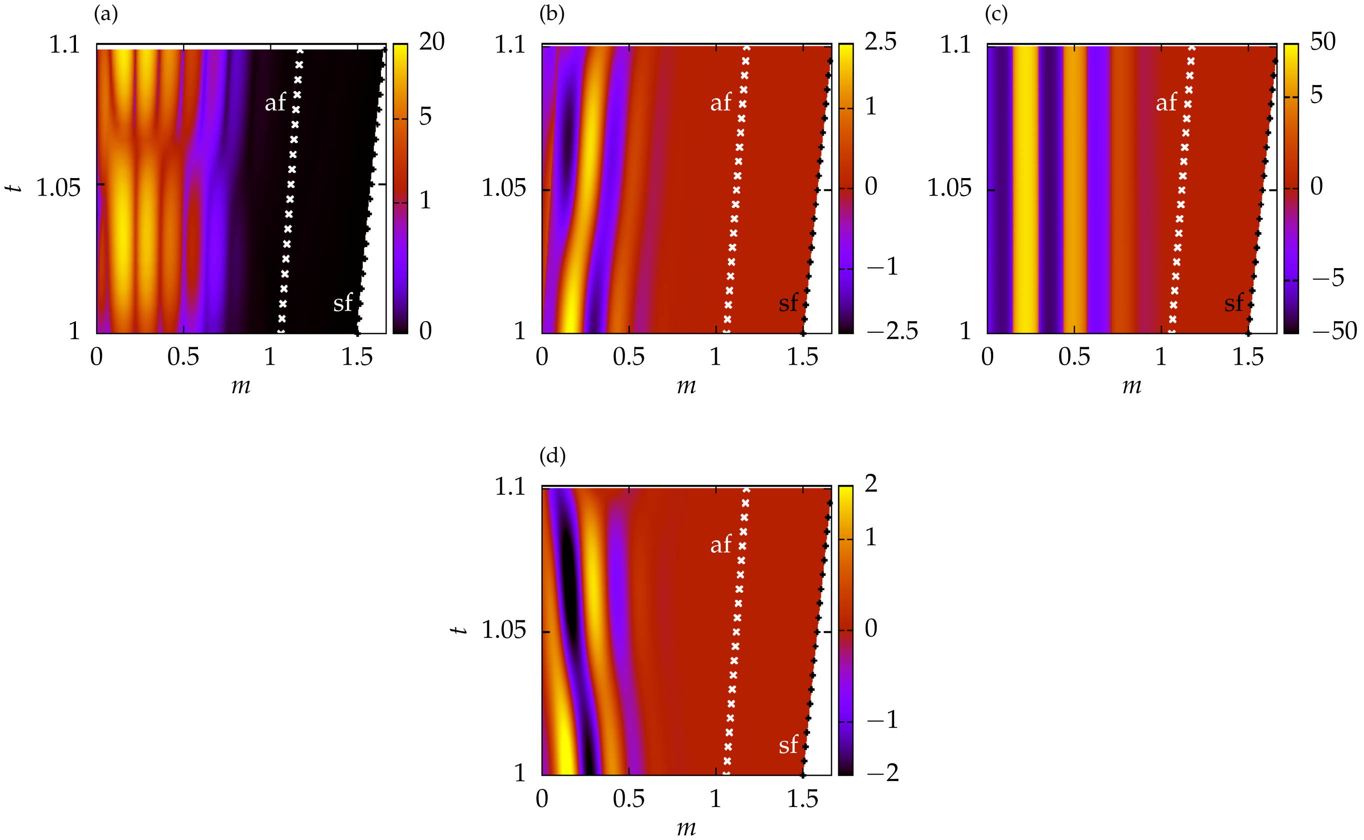

Figure 4.6: Ablation wave RC-1. $(k_\perp, r_c) = (32, 1)$ for $T = 1.1$. (a) Chu's energy density. Projection of the optimal response on the pseudo-characteristic variables: (b) forward acoustics/entropy $\widehat{\mathcal{W}}_2$, (c) vorticity $\widehat{\omega}$, and (d) backward acoustics $\widehat{\mathcal{W}}_4$.

Range of transverse wavenumbers $k_\perp$. The transverse wavenumbers must be chosen so that curvature effects remain negligible in order to remain within the validity of the slab symmetry. A usual criterion is to set the largest transverse wavelength such that

$$\max\{\lambda_\perp\} \leqslant \frac{\text{shell initial outer radius}}{10}, \tag{4.36}$$

which corresponds to a Legendre mode $l = 60$ in spherical symmetry. From t_0 to $\max\{T\}$, the shock front has travelled along a distance d_{sf}. We choose to conserve the dimensionless number

$$\vartheta = \frac{d_{\mathrm{sf}}}{\max\{\lambda_\perp\}} \tag{4.37}$$

between the LMJ target A1040 and the ablation flow RC-1. From the simulation of the LMJ target implosion we get $\vartheta = 1.4$, and from the ablation flow RC-1 $d_{\mathrm{sf}} = 4.4$, yielding the lower bound $\min\{k_\perp\} \approx 2$. However, ICF implosion studies explore a range of Legendre modes lower than 60, typically $10 \leqslant l \leqslant 10^3$ (Haan et al., 2015, Fig. 3). We take this range for our study, which corresponds then to the interval $0.33 \leqslant k_\perp \leqslant 33$. Of course, when transposing these results to the actual geometry of a target, we must keep in mind that curvature effects may modify results for $k_\perp < 2$.

The value $k_\perp = 0$ is added to the set of values explored to address the problem of planar ablation waves with purely longitudinal perturbations. In such a case, the deformations of the interfaces correspond merely to a translation of the interfaces. Although this case is less representative of ICF, hydrodynamic instabilities on planar ablation waves do exist (see Aglitskiy et al., 2010), hence the case $k_\perp = 0$ is of interest.

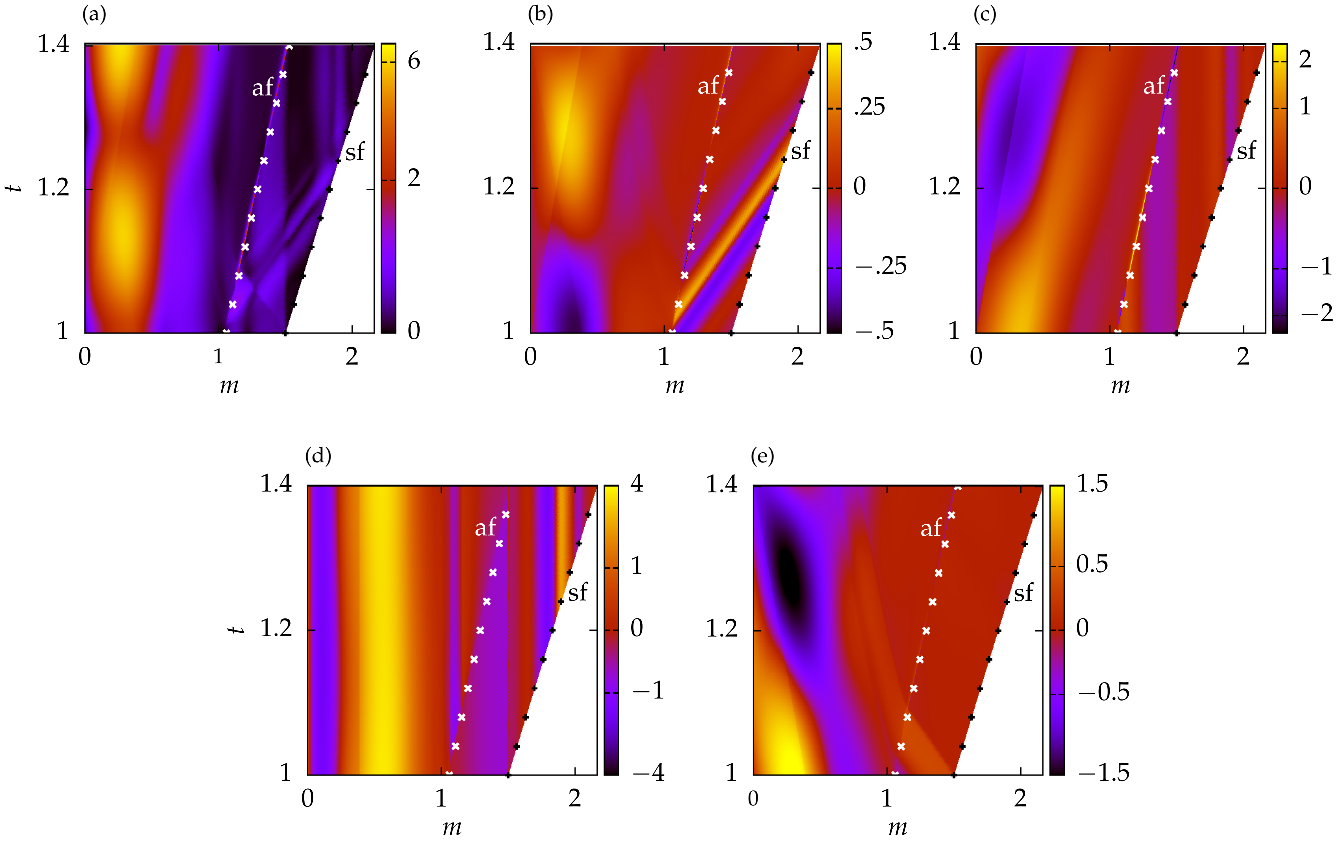

Figure 4.7: Ablation wave RC-1. $(k_\perp, r_c) = (8, 1)$ for $T = 1.4$. (a) Chu's energy density. Projection of the optimal response on the pseudo-characteristic variables: (b) heat-conductivity/forward acoustics $\widehat{\mathcal{W}}_1$, (c) forward acoustics/entropy $\widehat{\mathcal{W}}_2$, (d) vorticity $\widehat{\omega}$, and (e) backward acoustics $\widehat{\mathcal{W}}_4$.

Range of initial distribution r_c. As we are interested into computing a gain, the objective functional at the initial time cannot vanish, which means that r_c has to remain strictly positive. The lower bound of the range is therefore chosen as $r_c = 0.01$. The upper bound is set to $r_c = 1$, so that there is no initial deformation of the external surface and shock front.

4.6.2 Optimal perturbations without initial boundary deformation

Here we explore the case of zero initial deformation of the external surface and shock front: $\mathcal{J}^*(t_0) = 0$ and $\mathcal{J}(t_0) = 1$ in Tab. 4.1, or alternatively $r_c = 1$, for the ranges of parameters listed in Tab. 4.4. We first assess that there is an amplification (i.e. $\mathcal{G} > 1$) for any choice of the parameters $(T, k_\perp, r_c)$ (Figs. 4.4a and b). The ablation flow is therefore prone to amplifying small disturbances for a wide range of transverse wavelengths and characteristic times. The amplification is globally larger for large T or large $k_\perp$. Hence despite the enhanced damping effect of heat diffusion, perturbations of short transverse wavelengths are subject to a strong amplification.

Gain curves are not monotonic but display a series of growths and decreases which may reflect the multiplicity of phenomena at stake. As an example, we note that the arrival time of the first acoustic wave originating from the ablation layer at the shock front (Fig. 4.7b) corresponds to the first maximum in the $(\mathcal{G}(T), T)$ curve for $k_\perp = 8$ at $T = 1.2$ (Fig. 4.4a light blue).

Two distinct optimal growth mechanisms. As T grows and $k_\perp$ decreases, a transformation of the optimal initial perturbation sets up, from a spatially structured signal localized close to the external surface, to a signal localized in the ablation layer and compression region with no well-defined structure. The resulting optimal growth mechanism evolves from local acoustic–vorticity interactions, sketched on Fig. 4.8, to long range interactions coupling the ablation layer and shock front, sketched on Fig. 4.10.

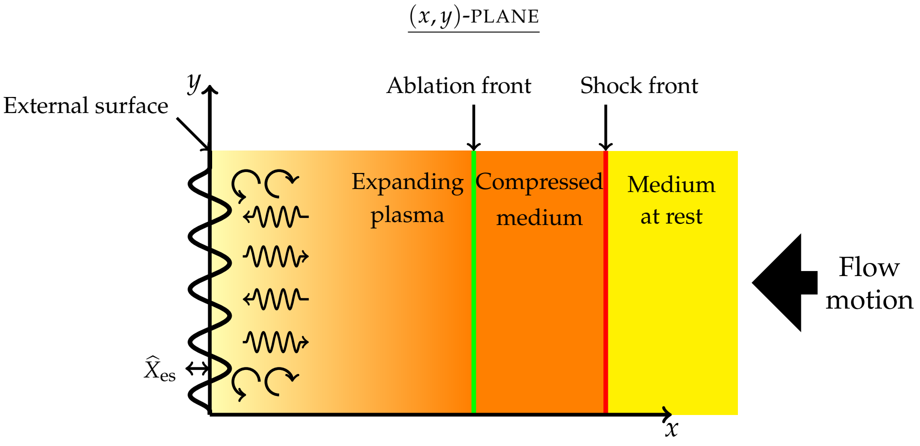

Figure 4.8: Schematic view of the optimal growth mechanism: *acoustic–vorticity interaction*, in the (x, y) plane. Sinusoidal arrows: acoustics; circular arrows: vorticity.

For small terminal times ($T = 1.1$), D_t is shorter than the travel time of acoustic waves between interfaces thus the ablation layer and the shock front play no role in the optimal growth mechanism and their deformations remain negligible (Fig. 4.5a). As the optimal response develops in the vicinity of the external surface, this sole interface is coupled to the perturbation field. The optimal growth mechanism results from local interactions between spatially structured acoustic and vorticity waves located in the vicinity of the external surface, hereafter referred to as *acoustic–vorticity interactions* (Figs. 4.6b-d). This fine spatial structure, and the constructive interaction it induces, are very similar to those emerging from the local study (§ 4.4), acknowledging that a local analysis is meaningful for short terminal times. This spatial structure also makes Chu's energy response strongly fluctuating in space and time (Fig. 4.5a).

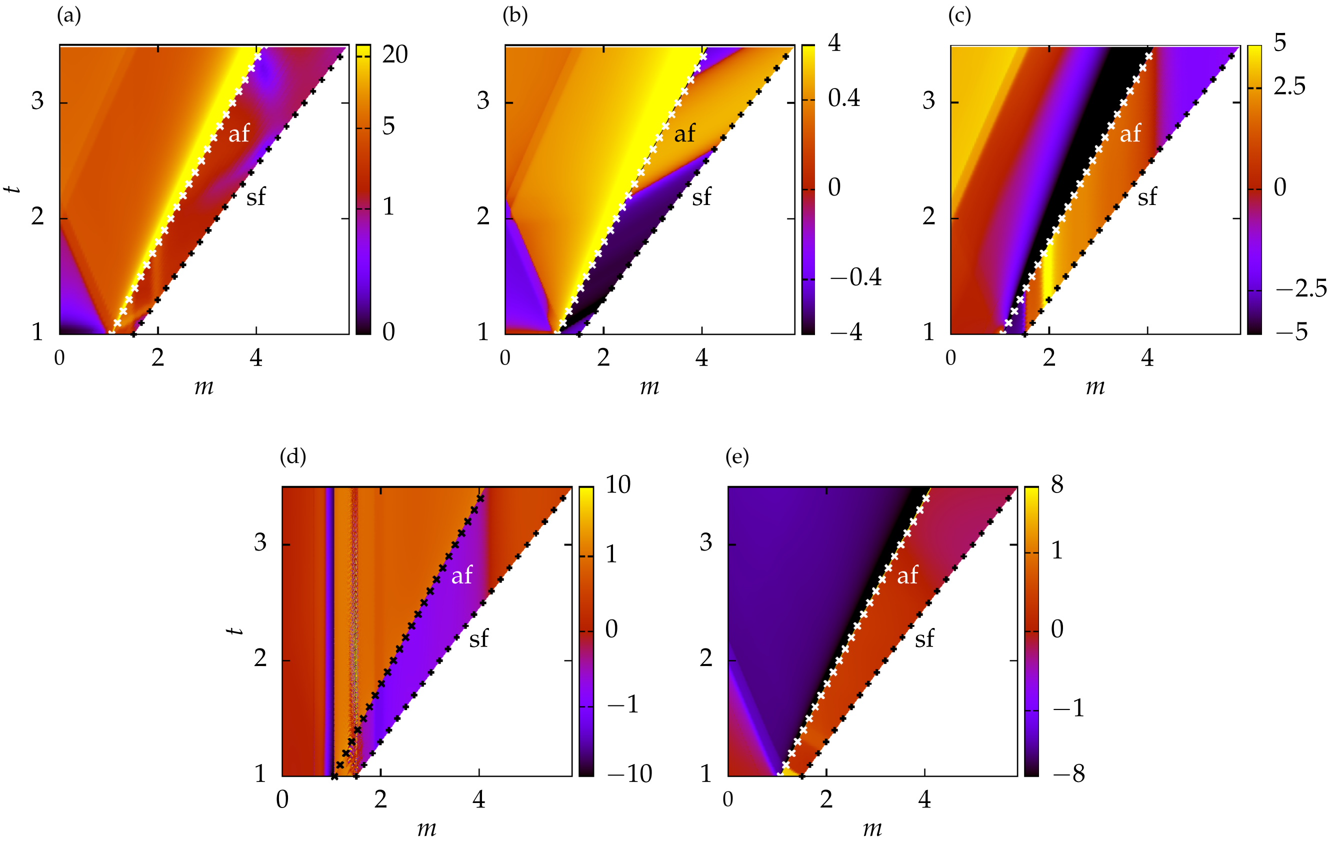

Figure 4.9: Ablation wave RC-1. $(k_\perp, r_c) = (0.33, 1)$ for $T = 3.5$. (a) Chu's energy density. Projection of the optimal response on the pseudo-characteristic variables: (b) heat-conductivity/forward acoustics $\widehat{\mathcal{W}}_1$, (c) forward acoustics/entropy $\widehat{\mathcal{W}}_2$, (d) vorticity $\widehat{\omega}$ and (f) backward acoustics $\widehat{\mathcal{W}}_4$.

As D_t becomes larger than the travel time of acoustic waves between the shock front and the ablation layer ($T = 1.4$), an additional growth mechanism arises in the compression region. Forward acoustic waves travel from the ablation layer up to the shock front which re-emits some vorticity and entropy waves (Figs. 4.7a-d). This is the early stage of the coupling between the ablation layer and the shock front (*af–sf coupling*). Although ablation layer deformation and Chu's energy fluctuations seems to be correlated (Fig. 4.5b), pseudo-characteristic variables in the (m, t) plane show that perturbations reaching the ablation layer come from the shock front and not from the region of high Chu's energy density (Figs. 4.7a, c, e). Chu's energy fluctuations are still mostly due to acoustic–vorticity interactions (Figs. 4.7a, c-e).

Acoustic–vorticity interaction coexists with af–sf coupling at intermediary terminal times, without interacting together (Fig. 4.7a), but disappears before af–sf coupling at large T. For large terminal times corresponding to the end of the shock-transit phase ($T = 3.5$), as D_t equals a few times the travel time of acoustic waves in the compression region, the shock front and ablation layer are strongly coupled and perturbations in the ablation front dominate those contained in the conduction and compression regions.

The resulting optimal growth mechanism evolves from local interactions between acoustic and vorticity waves, without interactions between interfaces, to a regime of coupled shock front and ablation layer where Chu's energy is mostly located in the ablation layer. We interestingly note that heat-conductivity waves, brought to light in § 3.5,

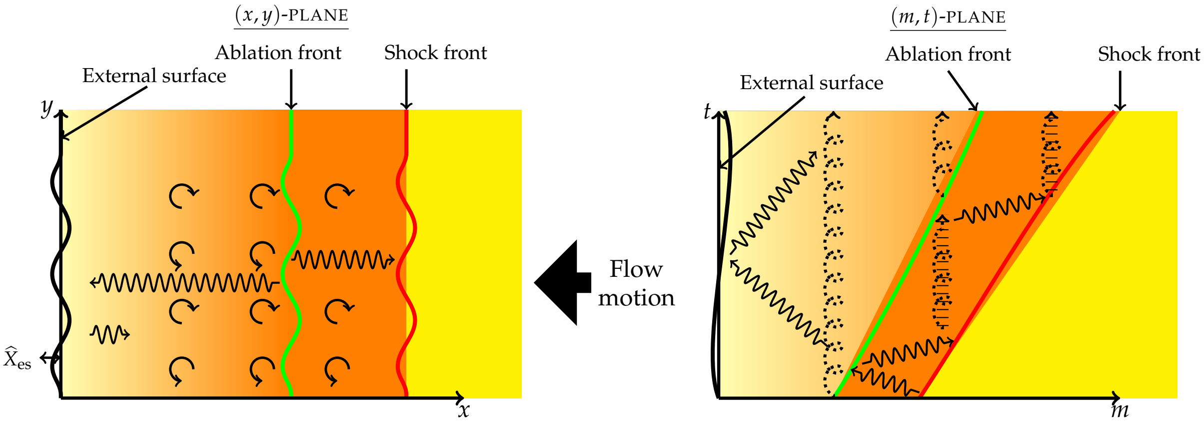

Figure 4.10: Schematic view of the optimal growth mechanism: *af–sf coupling*, in the (x, y) plane (left) and in the (m, t) plane (right). Sinusoidal arrows: acoustics, circular and dashed coil arrows: vorticity, horizontal lines: entropy.

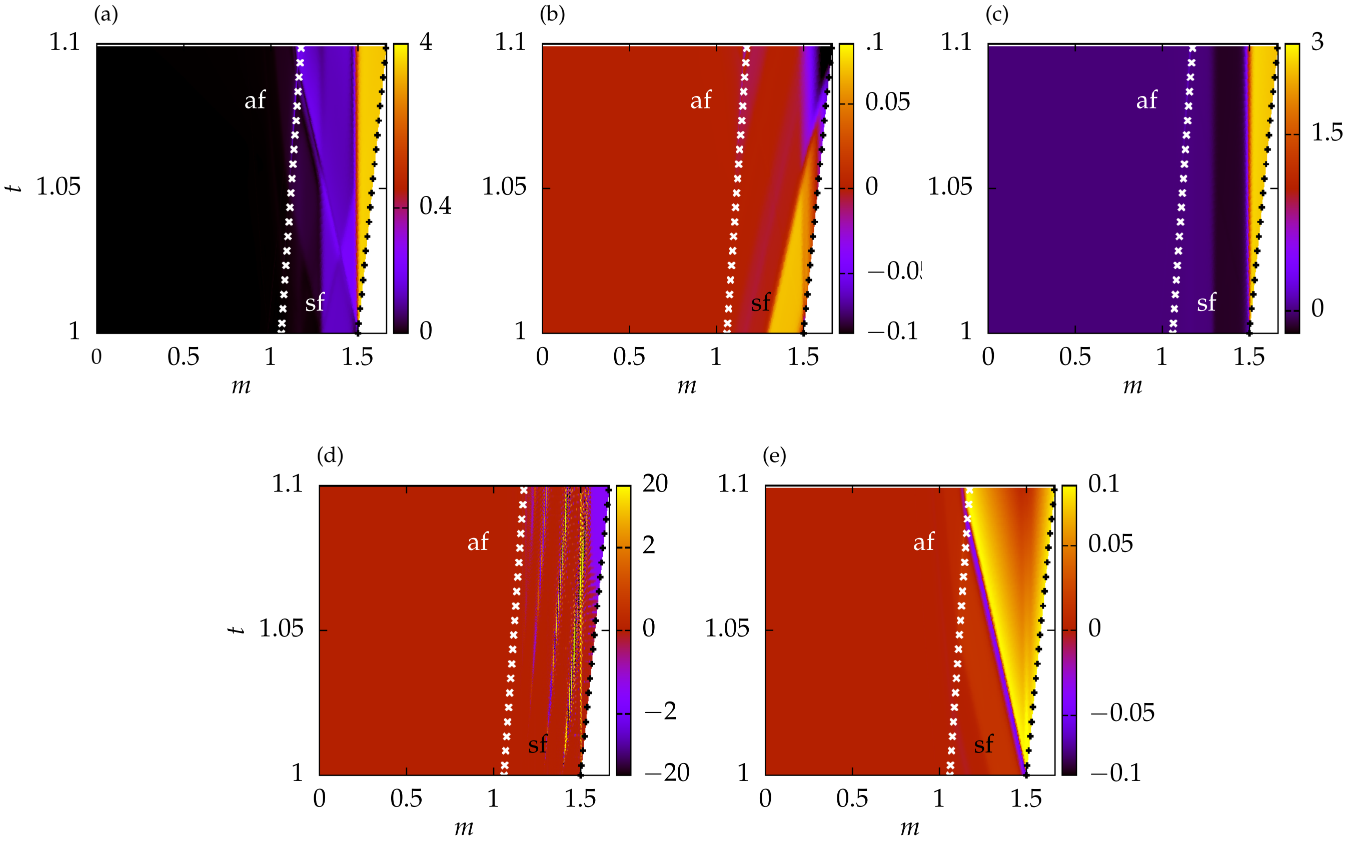

Figure 4.11: Ablation wave RC-1. $(k_\perp, r_c) = (4, 0.01)$ for $T = 1.1$. (a) Chu's energy density. Projection of the optimal response on the pseudo-characteristic variables: (b) heat-conductivity/forward acoustics $\widehat{\mathcal{W}}_1$, (c) forward acoustics/entropy $\widehat{\mathcal{W}}_2$, (d) vorticity $\widehat{\omega}$, and (e) backward acoustics $\widehat{\mathcal{W}}_4$.

turn out to play no role in any the above mentioned growth mechanisms. Furthermore, as the expansion velocity of the ablation wave RC-1 in the conduction region is quasi-sonic (Tab. 3.2), forward acoustic waves arising from the external surface cannot reach the ablation front within the duration $\max(D_t)$ (Tab. 4.4). As a consequence, the external surface is coupled to the ablation front only by means of heat diffusion, which is less efficient than advection in transmitting perturbations.

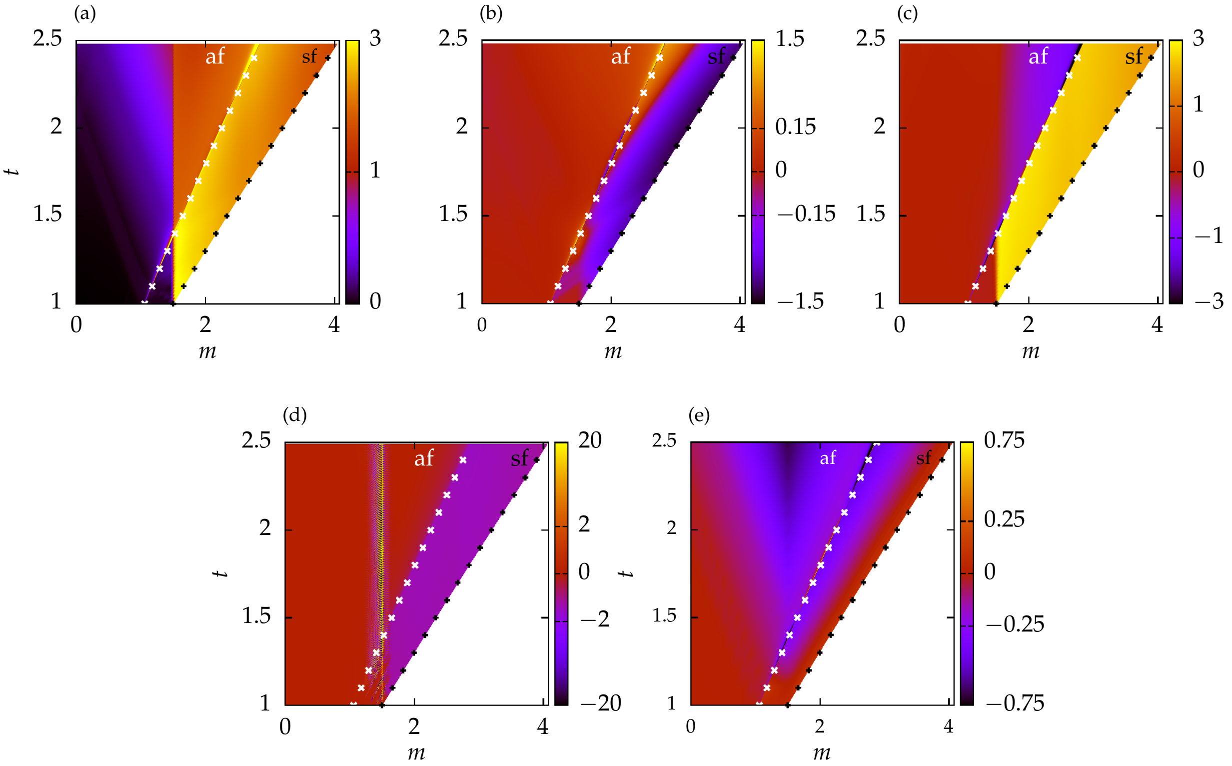

Figure 4.12: Ablation wave RC-1. $(k_\perp, r_c) = (4, 0.01)$ for $T = 2.5$. (a) Chu's energy density. Projection of the optimal response on the pseudo-characteristic variables: (b) heat-conductivity/forward acoustics $\widehat{\mathcal{W}}_1$, (c) forward acoustics/entropy $\widehat{\mathcal{W}}_2$, (d) vorticity $\widehat{\omega}$, and (e) backward acoustics $\widehat{\mathcal{W}}_4$.

4.6.3 Optimal initial deformations of the external surface and shock front

For an initial perturbation concentrated in the deformations rather than over the domain $[0, \xi_{\text{sf}}]$ (case $r_c = 0.01$, i.e. $\mathcal{J}^*(t_0) \gg \mathcal{J}(t_0)$ in Tab. 4.1), the distribution of the initial deformation is a dominant shock front deformation ($\widehat{X}_{\text{sf}}|_{t_0}$) and a negligible external surface deformation ($\widehat{X}_{\text{es}}|_{t_0}$), for both long and short terminal times T (Figs. 4.5e, f). The OIP in the flow consists in a small forward acoustic signal in the vicinity of the shock front (Figs. 4.11b and 4.12b). As the shock front is relatively steady (Fig. 4.5e, f), it produces an entropy and vorticity signal uniform in space and time (Figs. 4.11c, d and 4.12c, d). We do not observe any acoustic retroaction of the ablation layer on the shock front, which is therefore subject to its own dynamics (Figs. 4.11b and 4.12b. The ablation front is stimulated by the entropy and vorticity emitted by the shock front and oscillates. Strictly speaking, there is no af–sf coupling, even for $T = 2.5$ in the case of an initial deformation ($r_c \ll 1$). If the af–sf coupling eventually sets up, it takes a longer time than in the initial perturbation case ($r_c = 1$), which displays a dominant af–sf coupling for $T \geqslant 1.8$. We additionally note that at the shock front, backward acoustics is barely stimulated by incident (acoustic) perturbations which are reflected mostly as entropy and vorticity waves (Figs. 4.9e, G.2d and 4.7e).

4.6.4 Comparison with ablative Richtmyer–Meshkov instability

The interest of a systematic search of the OIP *via* a non-modal analysis, beyond the restricted frame of the ARM-like initial perturbations (4.35), is exemplified on Fig. 4.13. The initial condition (4.35) approximates the perturbation field left by the rippled forerunning shock front formed by a surface defect of size $\widehat{X}_0$, and gives an initial distribution $r_c > 0.99$. The amplification $\mathcal{G}(t)$ of (4.35) is compared to the optimal gain curve $\mathcal{G}(T)$ in the same

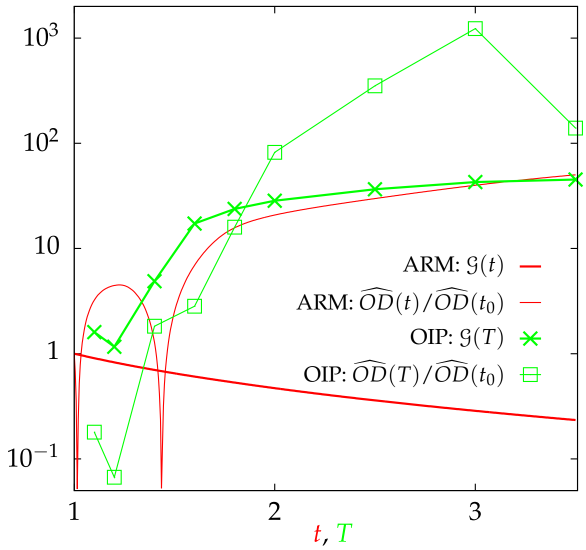

Figure 4.13: Ablation wave RC-1. Amplification $\mathcal{G}(t)$ for an initial ablative Richtmyer–Meshkov instability ARM at $k_\perp = 0.33$, and optimal gain curve $\mathcal{G}(T)$ in the same configuration. For each case, the optical depth amplification is reported, i.e. $\widehat{OD}(t)/\widehat{OD}(t_0)$ for the ARM and $\widehat{OD}(T)/\widehat{OD}(t_0)$ for the OIP.

configuration: $k_\perp = 0.33$, $r_c = 1$ and $1.1 \leqslant T \leqslant 3.5$. It appears that ARM perturbation does not correspond to any of the OIP for the terminal times reported on Fig. 4.13. The comparison between Chu's energy resulting from an initial ARM perturbation and the OIP shows that the ARM instability leads to a weaker amplification at time t than those obtained from the OIPs for terminal times $T = t$. Hence the OIPs display an overamplification of perturbations by comparison with the amplification resulting from an ARM instability. This tends to indicate that some amplification mechanisms of the OIPs are distinct from – and dominant over – the ARM instability during this shock-transit phase and for the relatively long wavelength perturbations presently tested. In terms of optical depth, the OIPs produce weaker signals than the ARM instability over the earlier part of the shock-transit $(t, T < 1.4)$ and significantly stronger levels later on $(t, T > 2)$.

Choosing the initial guess of the direct-adjoint method as the ARM initial perturbation goes along with this conclusion. It enables to quantify the departure of Chu's energy optimal amplification from the ARM instability.

4.6.5 Correlation between Chu's energy, ablation front deformations and optical depth.

At small terminal times, as the acoustic–vorticity interaction mechanism dominates there is no correlation between ablation front deformations and Chu's energy fluctuations (Fig. 4.5a). As T increases, the correlation between $\widehat{X}_{\mathrm{af}}$ and Chu's energy fluctuations is more significant, denoting the fact that af–sf coupling dominates over acoustic–vorticity interaction (Figs. G.1b and 4.5d). The comparison between $\mathcal{J}$ and $\widehat{OD}$ displays three different scenarii: $\widehat{OD}$ decreasing while $\mathcal{J}$ increases (Fig. 4.5a), $\widehat{OD}$ increasing slower than $\mathcal{J}$ (Fig. 4.5c) and $\widehat{OD}$ increasing faster than $\mathcal{J}$ (Fig. 4.5b). From these results it seems that the optical depth cannot furnish information about Chu's energy fluctuations and ablation front deformations.

4.6.6 Obtaining optimal perturbations: computational aspects

The present section presents the conditions under which we have obtained the OIPs. Each point of Figs. 4.4 (a and b) represents the result of an optimization procedure, i.e. a certain number of direct-adjoint iterations. In obtaining

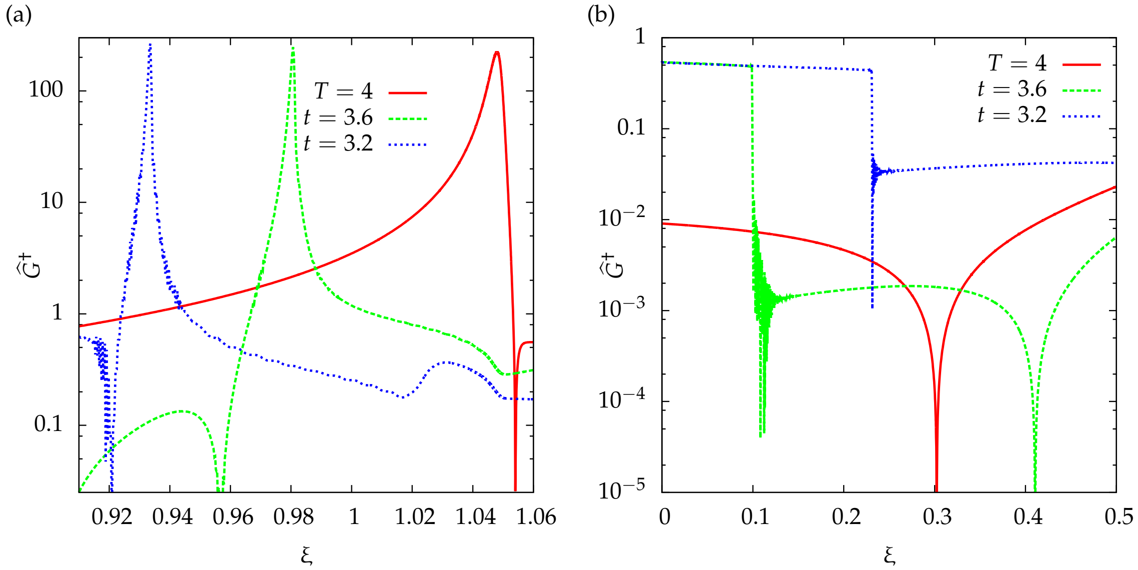

Figure 4.14: Ablation wave RC-1. $k_\perp = 0$, $T = 4$, $r_c = 1$, ill-resolved adjoint density perturbation on a $(N_{\text{cheb}}, N_{\text{dom}}) = (50, 39)$ point grid. (a) Stiffening of the solution while it propagates from the ablation front in the conduction region and (b) step-like wave propagating from the external surface due to the non-consistency of $\widehat{\mathbf{U}}^\dagger|_T$ with $\widehat{X}_{\text{es}}|_T$.

these optimal perturbations, we have faced some computational issues. Three major issues have been identified.

Stiffening of the adjoint solution. The adjoint evolution equation (4.21a) contains an advection term with the matrix $\mathsf{B}^\dagger$ (§ 4.5.2). This matrix is hyperbolic everywhere except in the vicinity of the external surface. We numerically observe that an adjoint perturbation initially located in the ablation layer splits into two waves: one traveling to the shock front and the other to the external surface. The characteristic velocities given by B are such that the velocity of the wave traveling to the external surface decreases, resulting in a stiffening wave propagating in the conduction region. If this signal propagates on a grid whose resolution decreases as it becomes steeper, then the solution is corrupted by spurious high order modes, as shown on Fig. 4.14(a).

To avoid the degradation of the adjoint solution the grid has to be as fine in the conduction region as it is in the ablation layer. This refinement is done by increasing the number of subdomains in the conduction region, which does not lead to a reduction of the critical time step, but increases the number of processors involved in the MPI procedures and the communication time between these processors. For the ablation wave RC-1, the grid corresponds to $(N_{\text{cheb}}, N_{\text{dom}}) = (50, 189)$.

Initially non consistent perturbation field and deformations. The optimization process may lead to an initial perturbation $\widehat{\mathbf{U}}|_{t_0}$ (respectively a terminal adjoint perturbation $\widehat{\mathbf{U}}^\dagger|_T$) that is non consistent with the initial deformations $\widehat{X}_{\text{a}}|_{t_0}$ (resp. terminal adjoint deformations $\widehat{X}_{\text{a}}^\dagger|_T$). This non consistency leads to the advection of step-like waves in the solution domain, as shown on Fig. 4.14(b) for the adjoint density perturbation. As no diffusion is acting on adjoint density, velocity and transverse divergence to smooth these steps, they pollute the solution with high-order modes in a manner comparable to the stiffening of the adjoint solution mentioned above.

To limit the degradation of the solution, the grid has to be refined enough to furnish a rather good description of these step-like waves. The response to this issue is similar to that for the stiffening of the adjoint solution. However, even with a highly refined grid, these steps are responsible for oscillations visible on the vorticity field (Figs. 4.9d, 4.11d and 4.12d). A possible remedy would be to filter the solutions but this has not been tested in the present work.

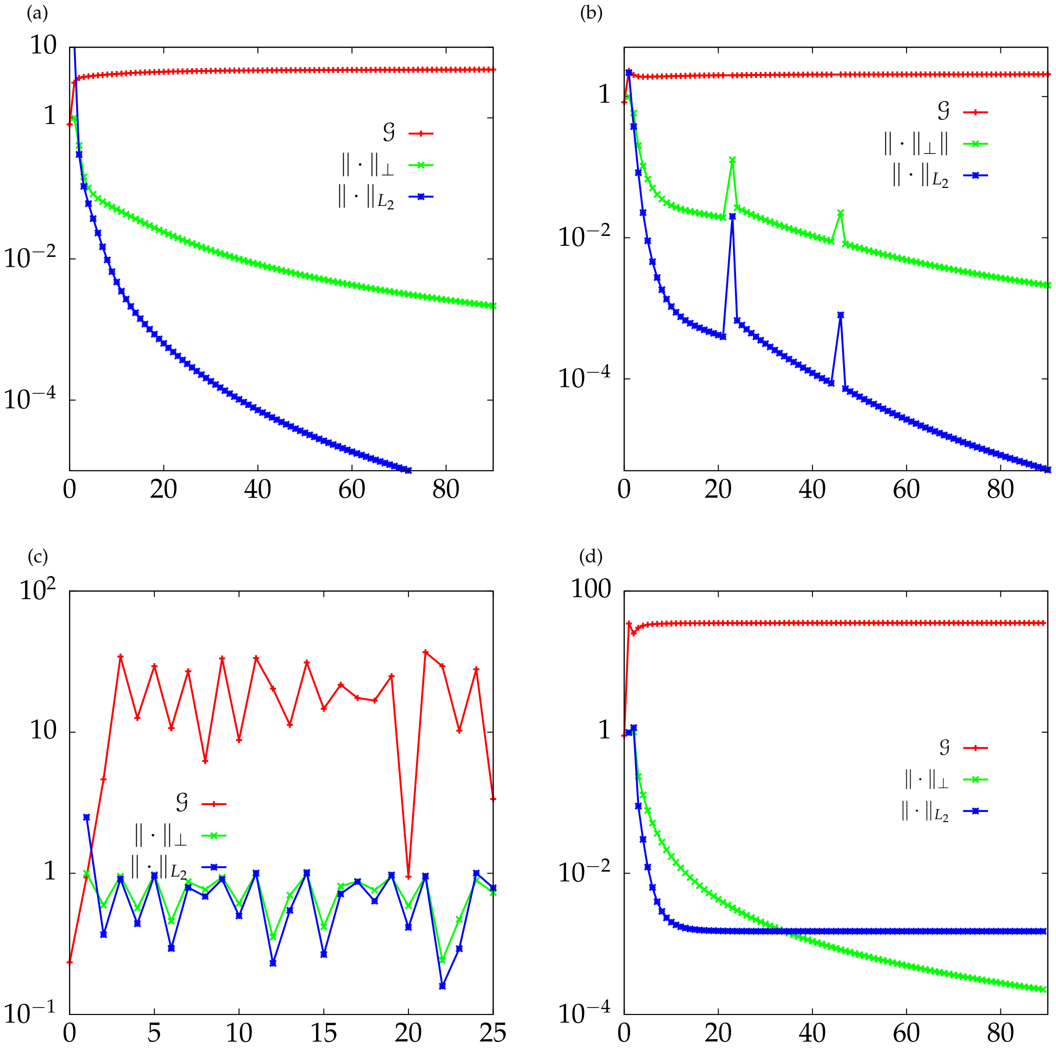

Figure 4.15: Ablation wave RC-1. Gain curves for Chu's energy (Tab. 4.1) and residuals $r_\perp$ and r_{L_2} defined by (4.38) and (4.39). For $r_c = 1$, (a) $(k_\perp, T) = (32, 1.1)$, (b) $(k_\perp, T) = (8, 1.4)$, (c) $(k_\perp, T) = (0.33, 3.5)$ and (d) $r_c = 0.01$ and $(k_\perp, T) = (1, 1.1)$.

Convergence issues for the objective functional. The convergence of the procedure is assessed by two residuals. The first one is based on the 'true gradient' orthogonal projection. From the geometrical perspective (Figs. 4.3a and b) we picture that when convergence is reached the adjoint state $\widehat{\mathbf{U}}^\dagger|_{t_0}$ is colinear to the OIP $\widehat{\mathbf{U}}|_{t_0}$. Therefore the ratio

$$r_\perp = \frac{\left\| (\widehat{\mathbf{U}}, \widehat{X}_{\mathrm{es}}, \widehat{X}_{\mathrm{sf}})|_{t_0 \perp} \right\|}{\left\| (\widehat{\mathbf{U}}, \widehat{X}_{\mathrm{es}}, \widehat{X}_{\mathrm{sf}})|_{t_0} \right\|} \tag{4.38}$$

should vanish. This residual is proposed in (Douglas et al., 2000) and corresponds to the rotation angle c of (4.34), see Fig. 4.3(b). A second residual, more conservative, is based on the L_2-norm of the difference between two subsequent initial perturbations, or

$$r_{L_2} = \frac{\left\| \widehat{\mathbf{U}}|_{t_0}^{q} - \widehat{\mathbf{U}}|_{t_0}^{q+1} \right\|_{L_2}^2 + \left(\widehat{X}_{\mathrm{es}}|_{t_0}^{q} - \widehat{X}_{\mathrm{es}}|_{t_0}^{q+1} \right)^2 + \left(\widehat{X}_{\mathrm{sf}}|_{t_0}^{q} - \widehat{X}_{\mathrm{sf}}|_{t_0}^{q+1} \right)^2}{\left\| \widehat{\mathbf{U}}|_{t_0}^{q+1} \right\|_{L_2}^2 + \left(\widehat{X}_{\mathrm{es}}|_{t_0}^{q+1} \right)^2 + \left(\widehat{X}_{\mathrm{sf}}|_{t_0}^{q+1} \right)^2}. \tag{4.39}$$

Convergence curves of four optimal responses (Figs. 4.6, 4.7, 4.9 and 4.12) are reported in Fig. 4.15. As illustrated in Fig. 4.15(d), the residual r_{L_2} is more conservative than the residual $r_\perp$ as it saturates while $r_\perp$ keeps on decaying. This characteristic comes from the fact that r_{L_2} accounts for any departure of the $(q+1)$-th initial condition with respect to the q-th, while $r_\perp$ is based only on gradient information projected in the tangent subspace. Even when residuals are not saturating (Figs. 4.15a, b), their decay quickly slows down after a few iterations. The case $(k_\perp, T) = (0.33, 3.5)$ (Fig. 4.15c) is the worst situation. Although there is an amplification, the objective functional is oscillating from an iteration to the next one. This ill-performing optimization yields an initial perturbation leading to an amplification, but which cannot be qualified as an *optimal* perturbation. Another kind of ill-performing behavior of the objective functional (not displayed here) is observed for some intermediate terminal times: $\mathcal{G}$ increases up to a value $\mathcal{G}_1 > 1$ and then starts to oscillate with an amplitude $\Delta\mathcal{G} < \mathcal{G}_1/2$ and a period of 20 to 40 iterations. The initial conditions corresponding to $\mathcal{G}_1 + \Delta\mathcal{G}$ and $\mathcal{G}_1 - \Delta\mathcal{G}$ are opposite one to the other.

Both power iteration and true gradient methods display this ill-convergence issue. Although Kerswell et al. (2014; 2018) find no evidence in the superiority of one descent method over the others, Guégan et al. (2006) argue that in their case the use of a conjugate gradient method (Press et al., 1994) has been necessary to ensure the convergence of the procedure. Such a method is being implemented for our problem. In that sense, the *true gradient* descent method is well adapted to the use of conjugate gradient method. Indeed, the normalization is embedded into the geometrical formulation: the new initial condition is normalized whatever the choice of the rotation angle c (4.34). Based on that point, a line maximization is performed on the scalar c with a research interval restricted by its definition within $[0, 2\pi]$.

4.7 Discussion of results

The results presented in this chapter bring to light non-modal effect in ablation waves. Transient amplifications are here first observed on a local analysis and then on a global analysis, which both constitute the first non-modal analysis of ablation waves. A major part of the work done was focused on the implementation of a direct-adjoint method for an ablation flow, with its inherent particularities: compressibility, unsteadiness and stiffness. The optimal initial perturbation (OIP) results for the base flow RC-1 presented in Chap. 4 displays a significant inclination to amplify initial perturbations for a wide range of wavenumbers $0.53 \leqslant k_\perp L_{\text{cond}} \leqslant 52$ and all terminal times T up to the shock-transit time. The amplification is measured by means of Chu's energy norm for perturbations and in the cases of initial conditions given by flow variable perturbations or deformations of the external surface and shock front.

Amplification of stable wavelengths. A well-known instability is the ablative Richtmyer–Meshkov (ARM) mechanism (see 'confinement effect' in § 2.2). In such a case, a surface defect initiates a rippled forerunning shock front and ablation front. In the absence of Darrieus–Landau instability for the range of wavelengths we are considering (Bychkov et al., 2015), wavelengths such that $k_\perp l_{\text{cond}} > 1$ are usually considered as stable (Goncharov et al., 2006; Aglitskiy et al., 2010). However, we have shown that they are also prone to strong amplifications, especially for terminal times being close to the shock-transit time (Fig. 4.4a). This result is of importance as perturbations persisting at the end of the shock-transit phase seed the subsequent acceleration phase, which is strongly favourable to the development of ablative Rayleigh–Taylor instabilities. Therefore, short wavelengths should not be disregarded during the shock-transit phase.

This result also brings to light that the OIP must be searched for outside the scope of the ARM-like perturbations (Fig. 4.13). This point acknowledges the *necessity of non-modal stability analysis for ablation flows, which enables a systematic identification of the most amplified initial perturbation*.

Optimal amplification mechanisms. Two different amplification mechanisms are identified in the absence of initial deformation ($r_c = 1$) of the shock front (sf) and external surface (es), depending on the terminal time. For short terminal times, such that $D_t = T - t_0$ is shorter than the traveling time of an acoustic wave between the shock front and the ablation layer, OIPs correspond to spatially structured acoustic and vorticity waves. Such OIPs are located in the conduction region and amplified by local constructive interactions between these waves, as it was already inferred from a local analysis (§ 4.4). This mechanism makes Chu's energy strongly fluctuating in time and this behavior is hardly detectable on the optical depth perturbation. For larger D_t, up to the shock-transit time, the OIP is amplified via a coupling of the shock front (sf) and the ablation layer (af) by means of forward acoustic waves (af → sf) and entropy/vorticity waves (af ← sf). This optimal growth mechanism concentrates Chu's energy density in the ablation layer, resulting in a correlation of Chu's energy with the ablation front deformation. We also note that in that case the optical depth presents similar variations as Chu's energy.

Sensitivity to defects in the upstream unshocked region. The OIP sought out as a combination of initial deformations ($r_c \ll 1$), $\widehat{X}_{\mathrm{es}}$ and $\widehat{X}_{\mathrm{sf}}$, turns out to be concentrated in $\widehat{X}_{\mathrm{sf}}$. An initial shock front deformation appears more efficient than an external surface deformation to amplify Chu's energy. As explained in § 4.6.2, perturbations arising from the external surface defects reach the ablation front only by means of heat diffusion. By contrast, the initially deformed shock front (non zero $\widehat{X}_{\mathrm{sf}}|_{t_0}$) emits vorticity and entropy waves which stimulate the ablation layer. An initial shock front deformation is therefore more prone to amplifying Chu's energy in the flow domain than an external surface deformation.

This high amplification potential for shock front deformations points out the flow sensitivity to perturbations coming from the upstream unshocked region ($m > m_{\mathrm{sf}}$), such as density inhomogeneities. The present non-modal analysis should be extended to a *sensitivty analysis* of the ablation flow to upstream perturbations. Through such an analysis we could determine the upstream perturbation leading to the most amplified perturbation in terms of Chu's energy, or any other objective functional. The goal being the systematic identification of the most dangerous defect in the ablator material of ICF targets.

Link with actual ICF ablation waves. In the present study, we have determined some optimal perturbations at an 'initial' time $t_0 > 0$ containing non negligible vorticity and acoustic perturbations. The relevance of such initial conditions can be questioned with reason. We argue that the ablation flow has already evolved for $t < t_0$. This previous evolution consists in a forerunning shock front travelling in a potentially inhomogeneous medium, the unshocked upstream ablator. Huete et al. (2012) show that a forerunning shock front in an inhomogeneous medium leaves vorticity and acoustic fields as it passes by. Therefore it is relevant to end up with an OIP consisting of acoustic and vorticity fields, the subsequent question being: *which initial state of the unshocked ablator induces such an OIP ?* A receptivity analysis should be useful to answer this question.

A perfectible computational method. The OIPs computed in the present work result from direct adjoint iterations with a gradient descent step at each iteration. Some of the OIP computations do not display any stabilization of the objective functional, and for the majority of OIP computations convergence is slow.

The use of a conjugate gradient method (Press et al., 1994) is considered, as recommended in (Guégan et al., 2006). Such methods are prescribed in the case of an objective functional displaying ‘narrow valleys’. Although we have no clue of the shape of $\mathcal{J}$, the existence of two optimal growth regimes with their underlying physical mechanisms (heat diffusion, advection, amplification) along with boundary deformations invites us to explore this method. In that sense, the *true gradient* descent (4.34) makes the use of conjugate gradient more straightforward.

We have also mentioned that the three different initial guesses tested (§ 4.5.4) converges to the same optimum. This point does not undermine the existence of other local maxima. In order to broaden the exploration of the objective functional $\mathcal{J}$ and find some potential local maxima, the recourse to a large number of random initial guesses seems a good option. Some issues resulting from such an initial guess method are detailed in (Foures et al., 2013, § 5). In particular, for short terminal times the gradient of the Lagrange functional (4.28) is not smooth since any of the physical processes do not have the time to ‘organize’ the perturbation field. Some other issues may arise from the capabilities of the numerical method (§ 3.3) to handle a random initial condition.

In our opinion, unravelling the above mentioned issues is a prerequisite to the exploration of other objective functionals, such as the ‘ablation layer deformation’, whose definitions over a subinterval of the computational domain will bring additional complications to the optimization problem.

CHAPTER 5

Conclusion and perspectives

The objective of the present work is the identification of optimal initial perturbations (OIPs) in ablation flows. This issue comes after of a series of successive works dedicated to a better understanding of ablation flow instabilities during the shock-transit phase of an ICF implosion, modeled by *self-similar unsteady ablation waves*, and carried out at CEA/DAM. Such instabilities are rooted in the unsteady character of ablation flows and the interactions between the forerunning shock front and the ablation layer. These ablation flow instabilities seed the subsequent acceleration stage of the implosion, during which the ablation layer is strongly accelerated, and therefore highly favourable to ablative Rayleigh–Taylor instabilities.

Self-similar ablation waves stand out from *standard models*, which relay on restrictive flow assumptions such as steadiness, isothermal expansion or isobaric approximations (see Tabs. 2.3, 2.4, 2.5), by an exact description of the hydrodynamics (Abéguilé et al., 2006; Boudesocque-Dubois et al., 2008; Clarisse et al., 2018). When applied to the computation of linear perturbations, this model furnishes the perturbation field in the whole extent of the ablation wave, i.e. from the external surface up to the shock front, and not only shock front and ablation front deformations as most of standard models do. Analyses of linear perturbations of self-similar ablation waves has already provided us with better insights about ablation flow instabilities (Abéguilé et al., 2006; Lombard et al., 2008; Clarisse et al., 2008, 2016). These works have also stressed the importance of short time — and potentially transient — behaviors to the stability of ICF-like ablation flows. Short time horizons are not investigated by stability analyses based on standard models which make use of method of the normal modes. Alternatively, simulations of ICF implosions *via* multiple physics hydrocodes render short time horizons, but it is not conceivable to compute perturbation amplification for a sufficiently large number of initial conditions so as to capture the potential transient behaviors. The framework provided by non-modal, or non-normal, stability analysis is perfectly suited to such an investigation. Building on the self-similar ablation wave model and its joint linear perturbation numerical code, we put the non-modal framework into practice to formulate and solve an optimal initial perturbation (OIP) problem.

In a first attempt, we have assessed the presence of non-modal effects at small scale, i.e. for initial perturbations whose characteristic lengths are much smaller than the characteristic lengths of the base flow. In some regions of the flow believed to be stable, such as the conduction region, the numerical abscissa of the perturbation evolution operator is positive while its eigenspectrum is negative, meaning that initial perturbations are subject to a non-modal transient amplification. The corresponding *optimal initial growth* is recovered by an amplification computation of an initial perturbation localized in the conduction region, which indeed displays transient growth. Fortified by this first insight in non-modal effects in ablation waves, we have performed a global non-modal analysis to identify OIPs for a wide range of transverse wavenumbers, terminal times and initial distributions of the perturbation energy.

Because our problem is unsteady, the OIPs are reached by means of direct-adjoint iterations. The adjoint problem has been derived thanks to the Lagrange multiplier technique. Our configuration, with a compressible fluid, free boundaries and non-homogeneous boundary conditions due to boundary deformations, requires some knowledge we have not identified in the existing literature while building the Lagrange functional. Namely, the Lagrange functional must contain the constraints for the set of boundary conditions that ensure that the direct problem inferred from the Lagrange functional is well-posed. These constraints differ from those given by the sets of physical boundary conditions.

From the observation of gain curves of Chu's energy, a first clear conclusion is that amplification of initial perturbations is effective for all terminal times, transverse wavelengths and initial distributions of the energy, denoting the inclination of ablation flows to significantly amplify a wide variety of perturbations. In particular, short transverse wavelengths, believed to be stable for the ablative Richtmyer–Meshkov instability (ARM), displays strong amplifications. For a given transverse wavelength, the gain curve displays a much larger amplification than the corresponding ARM instability. Searching for OIPs, two *optimal growth mechanisms* have been identified, depending on the terminal time. For short terminal times, the OIP is localized in the conduction region, close to the external surface, and grows thanks to local *acoustic-vorticity interactions*. This OIP has a pronounced spatial structure, as was already inferred from the local non-modal analysis. For larger terminal times, close to the shock-transit time, the OIPs consist in an acoustic signal located in the post-shock region and grows through *ablation layer – shock front coupling*. The transition between these two optimal growth mechanisms is driven by the magnitude of the travel time of acoustic waves between the ablation layer and the shock front, with respect to the time duration of the optimal response (i.e. the difference between terminal time and initial time). These OIPs do not correspond to ARM-type perturbations. This point means that ARM perturbations do not contain the OIP, and that OIPs must be searched for outside of the framework of ARM perturbations. The present work is focused on radiation ablation waves, i.e. with radiation heat conduction, more representative of indirect-drive ICF. However, a similar study can be performed on ablation waves with electron heat conduction, more representative of direct-drive ICF, with no change in our numerical. In this respect, a first of global non-modal analysis performed on an ablation wave with electron heat conduction is presented in App. B. These first results display an inclination to strongly amplify perturbation similar to the case of radiation ablation waves.

To characterize the OIPs and optimal growth mechanisms we have made use of a set of *pseudo-characteristic variables*. This set of variables follows from a numerical investigation of the transmission mechanisms of external perturbations — heat flux and pressure — in an ablation wave. The resulting perturbations turn out to propagate close to linear waves in the conduction and post shock regions. These linear waves provide us with the set of pseudo-characteristics. In the conduction region, one of these families of linear waves corresponds to *heat conductivity waves*, representing a fluctuation of heat-flux perturbations. Heat conductivity linear waves are a direct consequence of nonlinear heat conduction and temperature stratification in the conduction region. Therefore they cannot arise from standard models assuming an isothermal expansion region. Their advection velocity is supersonic. Such waves are effective for perturbations whose longitudinal characteristic length is of the order of — or larger than — the conduction region and transverse wavelengths exceeding this size. In this range of parameters, heat conductivity waves can advect hydrodynamic external perturbations to the ablation layer, through a potential Chapman–Jouguet point. In the context of ICF, the presence of heat conductivity waves means that consequences of acoustic-like events occuring outside the target may not be omitted, even in the case of supersonic expansion flows. Heat conductivity waves constitutes an additional *feedthrough* mechanism besides heat diffusion.

These three contributions: transmission of external perturbations, local model for optimal initial growth and global OIP, constitute the outcomes of the present thesis. Obtaining these results came at the cost of a significant amount of numerical developments. First of all, the existing linear perturbation code inherited from previous works at CEA/DAM has been modified to replace the temporal splitting between gas dynamics and heat conduction by a simultaneous integration of the whole system of equations. This new time integration has enabled a more straightforward formulation of the critical time step for the explicit part of the time integration scheme. Boundary conditions on the hyperbolic susbsystem are now handled *via* a *penalty method*. The resolution of the adjoint problem has also brought its share of numerical difficulties, with an adjoint system being stiff and steep adjoint solutions requiring refined grids. The optimization methods used to find the OIPs may also be improved for more robust ones such as *conjugate gradient*. A more robust optimization method may help to reach convergence in cases for which the current methods — iterate power and true gradient — fail.

Moreover, stronger numerical methods will allow us to address the receptivity of ablation waves to perturbations of the unshocked ablator, i.e. initial inhomogeneities within target materials. Although numerous works have been dedicated to studying the interaction of one — or several — shock waves with a field of perturbations, the above mentioned receptivity problem has never been considered. This receptivity problem is adjacent to the following question: which initial states of the unshocked ablator induce the OIPs of ablation waves that have been identified? Finally, other objective functionals would be worth investigating. In the present work we have used the L_2 norm and Chu's energy. However, some other quantities relevant to ablation wave stability, such as the ablation layer or shock front deformations, can be transformed into suitable objective functionals. The use of such objective functionals, defined over a subregion of the computational domain, would require however more robust numerical methods.

CHAPTER A

Article submitted to *Physical Review E*

Investigation of supersonic heat-conductivity hyperbolic waves in radiative ablation flows, G. Varillon, J.-M. Clarisse, A. Couairon

Investigation of supersonic heat-conductivity hyperbolic waves in radiative ablation flows

G. Varillon,[1, 2, *] J.-M. Clarisse,[1] and A. Couairon[2]
[1] *CEA, DAM, DIF, F-91297 Arpajon, France*
[2] *CPHT, CNRS, École Polytechnique, Institut Polytechnique de Paris, F-91128 Palaiseau, France*
(Dated: December 19, 2019)

We carry out a numerical investigation of three-dimensional linear perturbations in a self-similar ablation wave in slab symmetry, representative of the shock transit phase of a pellet implosion in inertial confienment fusion (ICF). The physics of ablation is modeled by the equation of gas dynamics with a nonlinear heat conduction as an approximation for radiation transport. Linear perturbation responses of the flow, its external surface and shock-wave front, when excited by external pressure or heat-flux perturbation pulses, are computed by fully taking into account the flow compressibility, non-uniformity and unsteadiness. These responses show the effective propagation, at supersonic speeds, of perturbations from the flow external surface through the whole conduction region of the ablation wave, beyond its Chapman–Jouguet point, and up to the ablation front, *after* the birth of the ablation wave. This supersonic forward propagation of perturbations is evidenced by means of a set of appropriate pseudo-characteristic variables and is analyzed to be associated to the ‘heat-conductivity’ waves previously identified in Ref. [1]. Such heat-conductivity linear waves are found to prevail over heat diffusion as a feedthrough mechanism [2] for perturbations of longitudinal characteristic lengths of the order of — or larger than — the conduction region size, and long transverse wavelengths with respect to this region size, and over time scales shorter to much shorter than the shock transit phase duration. This mechanism which results from the dependency of the heat conductivity on temperature and density in conjunction with a flow temperature stratification, is expected to occur for other types of nonlinear heat conductions — e.g. electron heat conduction — as well as to be efficient at transmitting large scale perturbations from the surrounding of an ICF pellet to its inner compressed core at later times of its implosion. Besides, the proposed set of pseudo-characteristic variables are recommended for analyzing perturbation dynamics in an ablation flow as it furnishes additional propagation information over the fundamental linear modes of fluid dynamics [3], especially in the flow conduction region.

I. INTRODUCTION

The hydrodynamic stability of radiation-driven ablation flows is a key issue in inertial confinement fusion (ICF) where a sufficiently symmetric implosion of a spherical pellet is expected to achieve thermonuclear burn. Such flows which originate from exposing the outer shell of a pellet to a growing incident heat flux, present the radial structure of an inward-propagating deflagration, or ablation, wave where a shock front precedes a subsonic heat front that coincides with the leading edge of the heated material expansion wave [4, 5]. Inherently unsteady, these flows are compressible, strongly accelerated and highly nonuniform with a steep heat front, owing to the strong nonlinearity of the heat transport and the intense incident heating.

At the early stage of an ICF implosion, a fore-running converging shock wave compresses and sets into an inward motion the outer pellet shell — the ablator — until it breaks out at the ablator inner surface, during the so-called *shock transit phase.* This shock front is followed by an ablation layer which sets the compressed medium in expansion, resulting in an inward thrusting force that implodes the shell. Hydrodynamic instabilities emerging during the shock transit phase will seed the subsequent *acceleration phase* with perturbations. Many works have shown that perturbations strongly develop during the acceleration stage, resulting in the loss of symmetry of the implosion and eventually inhibiting ignition of fusion reactions (see [6] and references therein). The understanding of hydrodynamic perturbation dynamics during the shock transit phase is therefore of primary importance to ICF.

These perturbation dynamics have been classically analyzed according to two distinct perturbed flow. One corresponds to the ablation by a perturbed incoming heat flux — or illumination asymmetries — of an otherwise unperturbed medium at rest. When the external heat source is a laser light — *laser-driven* ablation — the flow perturbation mechanisms at stake have been designated by the term *laser imprinting* [7]. The other configuration consists in the ablation, by a uniform heat flux, of a uniform medium at rest presenting an initially rippled external surface. The resulting perturbation dynamics, due to the configuration resemblance with that of the Richtmyer–Meshkov instability [8, 9], has been termed *ablative Richtmyer–Meshkov instability* [10]. In both cases the corresponding ablation waves are perturbed over their whole finite spatial extent — i.e. from the fluid external surface up to the fore-running shock front — and this right from their onset.

Theoretical investigations of these perturbation config-

---

[*] gregoire.varillon@polytechnique.edu

urations have exclusively considered laser-driven ablation and have relied mostly on the standard assumptions in practice for the modeling of ICF ablation flows and of their instabilities, namely stationary quasi-isobaric ablation and, in certain instances, discontinuous ablation fronts (e.g. [11]). These investigations along with numerical simulations and dedicated experiments have lead to the conclusion that ablation-front deformations of transverse wavelengths smaller than the thickness, say l_{cond}, of the flow region where heat conduction dominates over advection — *conduction region* — undergo damped oscillations, whereas perturbations of wavelengths much larger than l_{cond} may grow as a result of the ablative Richtmyer–Meshkov instability and, possibly, Darrieus–Landau instability mechanisms [2, 7, 10, 12–19]. A weak acceleration of the ablation front and consequently the dominant influences of the restoring force due to the ablation 'rocket effect' and of the damping provided by mass ablation, in conjunction with the perturbations left behind the oscillating perturbed shock front, are responsible for this damped oscillatory regime. For sufficiently long wavelengths, deformation growth has been found to be roughly linear in time rather than exponential, although, according to theory, exponential growth could occur, under certain conditions, due to the Darrieus–Landau instability [2, 10, 15, 18, 19]. The confinement of the flow by the fore-running shock front and the surface of energy deposition is even more influential in this regime.

Due to the multiplicity of phenomena at stake in ablation waves, the standard modeling of radiation-driven ablation in ICF has relied on simplifying assumptions: i.e. an isothermal expansion, a stationary ablation region, and in certain cases an isobaric approximation for this region [4, 20]. Nowadays, ICF ablation flows are routinely studied by means of multiple-physics simulations which are however computationally more demanding [6].

An intermediate approach between simplified modelings and simulations uses self-similar solutions to the Euler equations with nonlinear heat conduction [21–23]. Such solutions, known since Marshak [24], present the advantage over isobaric, isothermal or stationary solutions of rendering, without further approximations, compressibility, nonuniformity and unsteadiness of ablation waves. They have been exploited to model ICF-type ablation flows [1, 25, 26]. Indeed these self-similar flows present the essential characteristics of an ablation wave as illustrated on Fig. 1 (a): (i) a leading shock front, (ii) a quasi-isentropic compression (post-shock) region, (iii) an ablation layer and (iv) an expansion wave where heat conduction dominates (the *conduction region*). In addition, these self-similar solutions have been used for the computation of linear perturbation responses of ablation waves for configurations of illumination asymmetries and of the ablative Richtmyer–Meshkov instability [21–23, 27]. In addition to the two identified regimes of perturbation growth and damped oscillations for transverse wavelengths, respectively, larger and smaller than the conduction region thickness, these results have pointed out the determining influence of the mean flow unsteadiness on perturbation dynamics at long to moderate wavelengths, including the transition between the two regimes. In particular, for the case of illumination asymmetries, perturbation growth at long wavelengths turns out to be dominated by the mean flow stretching and consequently to be algebraic in time.

In the present work, we aim at gaining insight into the setting up of perturbations in an already existing and unperturbed ablation wave, as a result of a perturbation excitation at the flow external surface. In that respect, this configuration differs from those of illumination asymmetries and ablative Richtmyer–Meshkov instability with the consequences that perturbations will here present short-term dynamics that are absent from such configurations. We analyze the responses of the state variables along with the deformations of the external surface, ablation front and shock front, with the aim of identifying essential physical mechanisms that rule perturbation transmission across the flow. This work goes beyond what was done in Ref. [23], with respect to wave propagation and the analysis of the flow conduction region. Indeed, a local analysis of ablation waves in terms of linear waves propagating in the longitudinal direction reveals that temperature and density stratification in the conduction region, in conjunction with the heat-conductivity nonlinearity, lead to the existence of a family of supersonic forward-propagating waves in this region [1]. Classical description of ablation waves, because of the isothermal assumption, are unable to render such phenomenon, hence the interest of self-similar solutions. Here we extend the analysis of Ref. [1] by considering and numerically solving the exact system of evolution equations for three-dimensional linear perturbations about self-similar ablation waves [21, 22]. The entire deflagration structure of a non-uniform and unsteady ablation wave is described, smoothly, from the fluid external surface where an incoming radiation flux and an external pressure are applied, up to the fore-running shock front. The ablation flow is considered in slab symmetry which is a reasonable approximation insofar as the shock transit phase corresponds to the beginning of a target implosion: curvature effects and convergence effects are actually negligible for sufficiently small perturbation transverse wavelengths. Besides, these solutions assume that the fluid is optically thick, which is an approximation for actual ICF target ablation. We focus on a self-similar ablation flow with a fast expansion of its conduction region (i.e. presenting an isothermal Chapman–Jouguet point) as it presents the main characteristics of the shock transit phase of an ICF pellet implosion [1].

We first (Sec. II) present our model and characterize the chosen ablation flow. Evolution equations are introduced for three-dimensional linear perturbations. The framework of our pseudo-characteristic analysis is presented (Sec. III). Results (Sec. IV) show that the pseudo-characteristic analysis is suitable for understand-

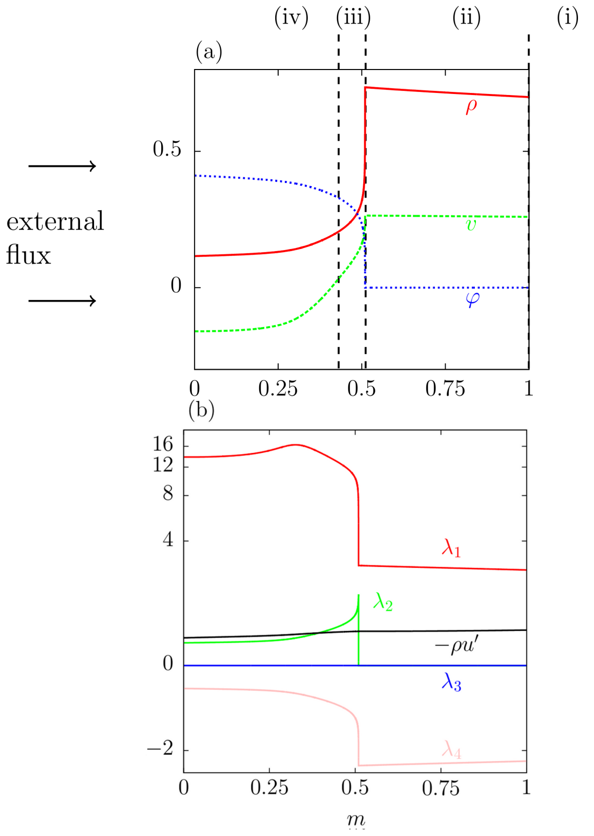

FIG. 1. (a) Base flow profiles in the Lagrangian coordinate m scaled by the function defined by $\mathrm{slog}_1(\cdot) \equiv \mathrm{sgn}(\cdot)\log(1 + |\cdot|)$. Density (red), longitudinal velocity (green) and heat flux (blue). (b) Characteristic wave speeds (Eq. 9) (colored lines) and fluid momentum relatively to the ablation front $-\rho u'$ (black line).

ing the evolution of perturbations. Section IV B presents an important result of this work: we assess quantitatively the ability of supersonic heat-conductivity linear waves to propagate from the external surface beyond the Chapman–Jouguet point. This effect is shown to be due to an advection mechanism which may propagate not only temperature fluctuations, as heat diffusion does, but also density and velocity fluctuations. The efficiency of this propagation is quantified depending on heat diffusion intensity, as well as its impact on ablation front and shock front deformations. Approximate evolution equations are identified in the case of advection dominated and diffusion dominated flow perturbations, couplings in the ablation front layer are then described. In Sec. VI we discuss the implications of our results for analyzing perturbation evolution in actual ICF target implosions.

II. MODEL

In order to investigate the deflagration structure of a non-uniform and unsteady ablation flow, we will consider the evolution of three dimensional linear perturbations of a self-similar ablation flow which exhibits a fast expansion of its conduction region, a situation typical of the shock transit phase of an ICF pellet implosion [20, 25].

A. Governing equations

We consider the motion of a polytropic gas in a semi-infinite slab subject to an irradiation flux and material pressure at its external boundary. The external irradiation flux is sufficiently high so that radiation heat conduction dominates any other diffusive effect (e.g. viscosity). However the fluid temperature is sufficiently low for radiation pressure and radiation energy to be negligible compared to material pressure and internal energy. The material is considered at local thermodynamic equilibrium, allowing us to use a fluid model to describe its motion. Assuming that this motion is along the x direction of a Cartesian system of coordinates (O, x, y, z), the equations of motion are written, in dimensionless form and in the Lagrangian coordinate m, where $\mathrm{d}m = \rho \mathrm{d}x$, as

$$\begin{cases} \partial_t(1/\rho) - \partial_m v = 0, \\ \partial_t v + \partial_m p = 0, \\ \partial_t(e + v^2/2) + \partial_m(pv + \varphi) = 0, \end{cases} \qquad (1)$$

where ρ, v, p , e denote, respectively, the fluid density, velocity, pressure and specific internal energy, and the heat flux φ is related to the fluid density and temperature T through the expression [26]

$$\varphi = -\rho^{-\mu} T^{\nu} \rho \partial_m T \equiv \Psi(\rho, T, \partial_x T), \quad \mu \geq 0, \quad \nu > 1. \qquad (2)$$

This system is closed by the dimensionless equation of state

$$p = \rho T, \quad e = \frac{T}{\gamma - 1},$$

with γ the adiabatic gas exponent. Self-similar reductions of Eq. (1) arise if the time dependence of the incident heat flux and pressure at the external surface follow specific power laws, namely

$$\varphi(0, t) = \mathcal{B}_{\phi} t^{3\alpha - 3}\ , \ p(0, t) = \mathcal{B}_p t^{2\alpha - 2}, \ \text{for } t > 0, \qquad (3)$$
$$\text{with } \alpha = \frac{2\nu - 1}{2\nu - 2},$$

and for an initial state given by $(\rho,\, v,\, T) = (1,\, 0,\, 0)$ for $m \geq 0$ [21, 24]. For certain values of the boundary parameters $(\mathcal{B}_p, \mathcal{B}_{\varphi})$, such solutions present the features of an ablation wave extending from the flow external surface ($m = 0$) through an ablation front up to the fore-running isothermal shock front [1, 26]. This shock front is preceded by an *infinitesimal radiation wavelet* penetrating

TABLE I. Characteristic hydrodynamic numbers of the base flow (defined in [1]): M is the Mach number and Fr the Froude number relatively to the ablation front, completed by the reduced length L_{cond} of the conduction region and the ratio of the minimum of the temperature gradient reduced length L_T to the flow total reduced length L_{tot}.

max M	1.045
$M\vert_{\text{af}}$	0.22
$Fr\vert_{\text{af}}$	80.3
L_{cond}	1.29
L_T/L_{tot}	3.00×10^{-5}

the cold fluid [24]. When values of the heat flux parameter $\mathcal{B}_\phi$ are not too high, this wavelet is negligible and may be combined with the isothermal shock front into a non-isothermal shock front [1, 24, 26]. Solutions to Eq. (1) describe smoothly all features of a radiative ablation wave without any further approximation and notably account for the temperature and density stratification of the conduction region. In the present case, highly accurate solutions to Eqs (1)-(3) are obtained by means of an adaptive multidomain Chebyshev spectral method [28].

In the present work we consider the case of a self-similar ablative wave driven by a sufficiently low external pressure $(\mathcal{B}_\phi, \mathcal{B}_p) = (0.8\,, 0.31)$ with Kramers' fully ionized gas model for radiation conduction ($\mu = 2, \nu = 13/2$) [1, 5]. This ablation flow present the essential features of the shock transit phase of an ICF implosion, namely: a supersonic expansion velocity relatively to the ablation front, and a relatively high ratio of convective to inertial effects — Froude number — at the ablation front (Tab. I).

As a consequence of the self-similarity, lengths evolve as $l(t) = t^\alpha L$, where L denote reduced length functions. The conduction region of length $l_{\text{cond}}(t)$ is the region between the external surface ($m = 0$) and the abation front (af), which is defined as the location of the minimum of the temperature gradient length. This minimum gradient length defines the characteristic thickness of the ablation front $l_T(t)$. The ratio $l_T(t)/l_{\text{tot}}(t)$, where $l_{\text{tot}}(t)$ is the flow total length – i.e. the distance between the external surface and the shock wave front – characterizes the stiffness of the flow (Tab. I).

B. Linear perturbations

Three-dimensional linear perturbations of the above self-similar ablative waves are considered using an Eulerian description in the coordinate system (m, y, z). The resulting system of partial differential equations in physical space is replaced by a one-dimensional system in the yz-Fourier space. With the notation $\widehat{f}$ for the linear perturbation yz-Fourier component of the base flow quantity f with transverse wavenumber $k_\perp = \sqrt{k_x^2 + k_y^2}$, this system reads

$$\partial_t \widehat{\mathbf{U}} = L\widehat{\mathbf{U}} \equiv -\mathsf{A}\partial^2_{m^2}\widehat{\mathbf{U}} - \mathsf{B}\partial_m\widehat{\mathbf{U}} - \mathsf{C}\widehat{\mathbf{U}}\ , \tag{4}$$

with $\widehat{\mathbf{U}} = \left[\widehat{\rho}\,\widehat{v}\,\widehat{d_\perp}\,\widehat{T}\right]^\top$, where $\widehat{d_\perp}$ denotes the Fourier component of the transverse divergence of the transverse velocity, and with the matrices A, B and C defined by

$$\mathsf{A} = \begin{pmatrix} 0 & 0 & 0 & 0 \\ 0 & 0 & 0 & 0 \\ 0 & 0 & 0 & 0 \\ 0 & 0 & 0 & C_v^{-1}\,\rho\,\Psi_{T'} \end{pmatrix}, \mathsf{B} = \begin{pmatrix} 0 & \rho^2 & 0 & 0 \\ T & 0 & 0 & \rho \\ 0 & 0 & 0 & 0 \\ C_v^{-1}\,\Psi_\rho & C_v^{-1}\,p & 0 & \mathsf{B}_{44} \end{pmatrix},$$

$$\mathsf{C} = \begin{pmatrix} \rho\partial_m v & \rho\partial_m\rho & \rho & 0 \\ T\partial_m\rho/\rho & \rho\partial_m v & 0 & \partial_m\rho \\ k_\perp^2 T/\rho & 0 & 0 & -k_\perp^2 \\ \mathsf{C}_{41} & \rho\partial_m T' & C_v^{-1}\,T & \mathsf{C}_{44} \end{pmatrix},$$

$$\begin{aligned} \mathsf{B}_{44} &= C_v^{-1}\left[\partial_m(\rho\Psi_{T'}) + \Psi_T\right], \\ \mathsf{C}_{41} &= C_v^{-1}\left(\partial_m\Psi_\rho - \rho^{-1}\,\partial_m\varphi\right), \\ \mathsf{C}_{44} &= C_v^{-1}\,\left[\rho\partial_m v + \partial_m\Psi_T - k_\perp^2\rho^{-1}\,\Psi_{T'}\right]. \end{aligned}$$

The longitudinal perturbation of the heat flux expands as $\widehat{\varphi}_x = \widehat{\rho}\,\Psi_\rho + \widehat{T}\,\Psi_T + \rho\Psi_{T'}\partial_m\,\widehat{T}$ where Ψ_ρ, Ψ_T and $\Psi_{T'}$ stand for the partial derivatives of Ψ (Eq. 2) with respect to the density, the temperature and the temperature gradient. Similarly, the transverse perturbation of the heat flux expands as $\nabla_\perp \cdot \widehat{\boldsymbol{\varphi}}_\perp = k_\perp^2\,\Psi_{T'}\,\widehat{T}$.

The external surface and shock front are also perturbed and their linear deformations are denoted $\widehat{X}_{\text{es}}(t)$ and $\widehat{X}_{\text{sf}}(t)$, respectively. Perturbed boundary conditions arise from a first order expansion of Eq. (3) between the mean position of the boundary surface and its perturbed position [22]. At the external surface, perturbations in pressure and heat flux are imposed:

$$\widehat{p}_{\text{es}}(t) = \widehat{p}(0,t) + \widehat{X}_{\text{es}}(t)\rho(0,t)\partial_m p|_{m=0}\ , \tag{5a}$$

$$\widehat{\varphi}_{\text{es}}(t) = \widehat{\varphi}(0,t) + \widehat{X}_{\text{es}}(t)\rho(0,t)\partial_m \varphi|_{m=0}\ , \tag{5b}$$

and the following kinematic relation at this material surface applies

$$\widehat{v}_{\text{es}}(t) = \dot{\widehat{X}}_{\text{es}}(t) = v(0,t) + \widehat{X}_{\text{es}}(t)\rho(0,t)\partial_m v|_{m=0}. \tag{5c}$$

At the shock front, Rankine–Hugoniot relations are perturbed to first order and take the form of four linear equations relating flow perturbations downstream to the shock front, $\widehat{\mathbf{U}}_{\text{sf}-}$, to shock front deformation, $\widehat{X}_{\text{sf}}$, shock front deformation velocity, $\dot{\widehat{X}}_{\text{sf}}$, and to the upstream state perturbation $\widehat{\mathbf{U}}_{\text{sf}+}$, say

$$RH\left(\widehat{\mathbf{U}}_{\text{sf}-}, \widehat{X}_{\text{sf}}, \dot{\widehat{X}}_{\text{sf}}, \widehat{\mathbf{U}}_{\text{sf}+}\right) = 0. \tag{6}$$

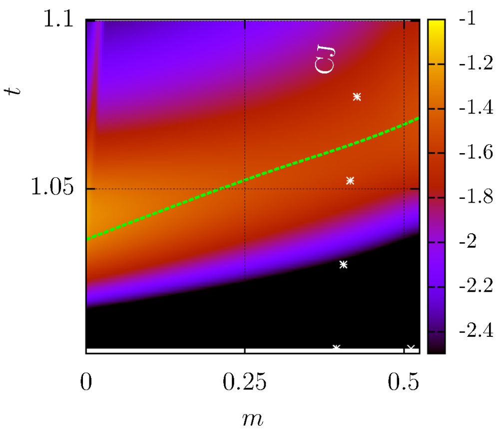

FIG. 2. Projection of the solution to Eq. (4) for a heat flux perturbation $(n, k_\perp) = (4, 1)$ on pseudo-characteristic $\widehat{\mathcal{W}}_1$ in the conduction region in logscale. The green dashed line represents a $\mathcal{C}_1$ characteristics originating from the pulse half height (Eq. 11). Trajectory of the CJ point $(*)$ is also indicated.

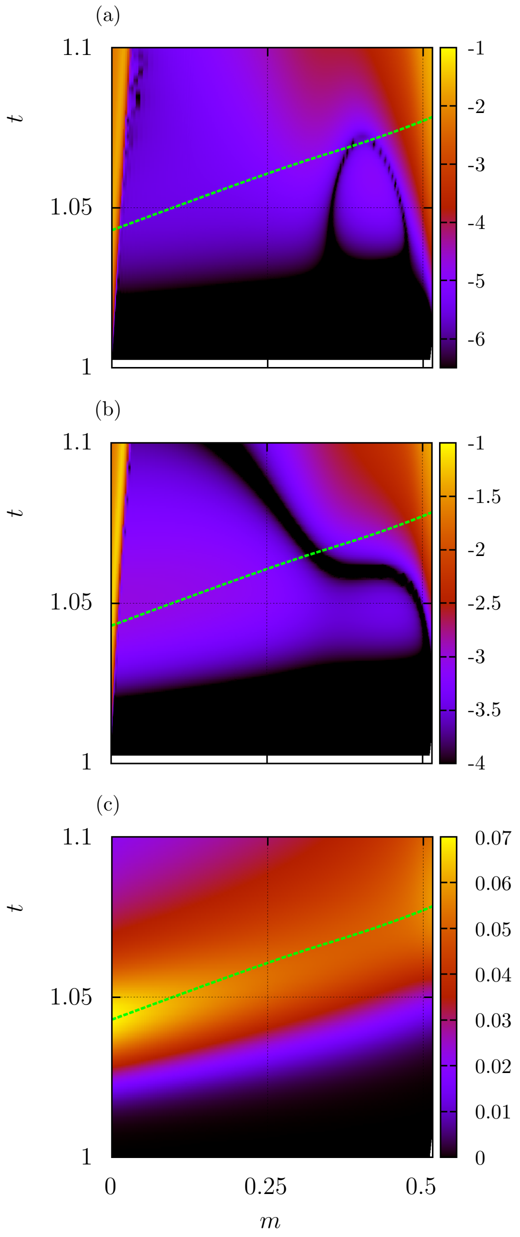

FIG. 3. Perturbation in (a) density in logscale, (b) longitudinal velocity in logscale and (c) temperature in slog_1 scale, for a heat-flux perturbation with $(n, k_\perp) = (4, 0)$.

III. A LOCAL CHARACTERISTIC ANALYSIS

Flow perturbations $\widehat{\mathbf{U}}$ are expressed in a new basis constructed by retaining the sole advection term in Eq. (4). The corresponding first-order system is written as

$$\mathbf{R}^{-1}\partial_t\widehat{\mathbf{U}} + \boldsymbol{\Lambda}(m,t)\mathbf{R}^{-1}\partial_m\widehat{\mathbf{U}} = 0, \tag{7}$$

where

$$\boldsymbol{\Lambda} = \mathrm{diag}(\lambda_i) = \mathbf{R}^{-1}\mathbf{B}\mathbf{R}, \tag{8}$$

with $\mathbf{R}$ the matrix of local right eigenvectors of $\mathbf{B}(m,t)$. The eigenspectrum of $\mathbf{B}$ comprises the null eigenvalue, say $\lambda_3 = 0$, with associated normalized eigenvector given by $\mathbf{R}_3 = [0\,0\,1\,0]^\top$. The remaining eigenvalues, which are determined numerically, turn out to be all real and distinct — say $\lambda_1 > \lambda_2 > \lambda_4$ with $\lambda_4 < 0$ — at any flow location m and time t, thus granting the hyperbolic property to system (Eq. 7). At any point (m,t), this system defines local characteristics as

$$(\mathbf{R}^{-1})_{ij}\mathrm{d}\widehat{\mathbf{U}}_j = 0 \text{ along } \mathcal{C}_i \;:\; \mathrm{d}m/\mathrm{d}t = \lambda_i(m,t), \tag{9}$$

for $i = 1..4$. Eigenvalues and eigenvectors of $\mathbf{B}$ are computed numerically (Fig. 1b) and the identification of the corresponding characteristics as families of propagating waves is given in Tab. II. In the conduction region, sufficiently far from the ablation layer, the characteristics $\mathcal{C}_2$ ($\mathcal{C}_4$) amount to quasi-isothermal acoustic waves propagating in the forward (respectively backward) direction of the flow, while the characteristics $\mathcal{C}_1$ correspond to supersonic forward-propagating waves which advect fluctuations of heat-flux perturbations [1]. These 'heat conductivity' waves are ruled by the dependence of the heat flux function Ψ (Eq. 2) on density and temperature [1]. While crossing the ablation front from the conduction region to the post-shock region, heat conductivity waves $\mathcal{C}_1$ are converted into quasi-isentropic forward acoustic waves, forward quasi-isothermal acoustic waves are transformed into quasi-entropy waves $\mathcal{C}_2$ and backward quasi-isothermal acoustic waves $\mathcal{C}_4$ are similarly converted into quasi-isentropic acoustic waves. The characteristics $\mathcal{C}_3$ represent the advection, at the base flow fluid velocity, of transverse dilatation motions of the fluid, and this regardless of the flow location. The expansion of the conduction region in the present flow (Fig. 1a) is sufficiently strong for the fluid velocity relatively to the ablation front to exceed the local sound speed, thus defining a Chapman–Jouguet (CJ) point: cf. the intersection point, for $m < 0.5$, between the curves for λ_2 and $-\rho u'$ in Fig. 1(b). Acoustic perturbations existing further downstream this CJ point cannot trace back the expansion flow, cross the CJ point and reach the ablation layer. On the contrary, heat conductivity waves propagate beyond this CJ point although the expansion velocity is supersonic, because this wave speed exceeds the expansion velocity (λ_1 on Fig. 1). Within the post-shock region, and at a sufficient distance away from the ablation layer, characteristics $\mathscr{C}_1$ and $\mathscr{C}_4$ come down to quasi-isentropic acoustic waves propagating, respectively, in the forward and backward directions, while characteristics $\mathscr{C}_2$ reduce to quasi-entropy waves moving approximately at the base flow velocity.

System Eq. (4) is then expressed in the pseudo-characteristic variables $\widehat{\mathcal{W}} = \mathsf{R}^{-1}\widehat{\mathbf{U}}$ as

$$\partial_t\widehat{\mathcal{W}} + \mathcal{A}\partial^2_{m^2}\widehat{\mathcal{W}} + \mathbf{\Lambda}\partial_m\widehat{\mathcal{W}} + \mathcal{C}\widehat{\mathcal{W}} + \mathbf{\Delta}\widehat{\mathcal{W}} = \mathbf{0}, \qquad (10a)$$

where

$$\mathcal{A} = \mathsf{R}^{-1}\mathsf{A}\mathsf{R} \quad \text{and} \quad \mathcal{C} = \mathsf{R}^{-1}\mathsf{C}\mathsf{R}, \qquad (10b)$$

and

$$\begin{aligned} \mathbf{\Delta}\widehat{\mathcal{W}} &= \mathsf{R}^{-1}\left[\partial_t\mathsf{R} + \mathsf{A}(\partial^2_{m^2}\mathsf{R}) + \mathsf{B}(\partial_m\mathsf{R})\right]\widehat{\mathcal{W}} \\ &\quad + 2\mathsf{R}^{-1}\mathsf{A}\partial_m\mathsf{R}\partial_m\widehat{\mathcal{W}} \\ &= \mathbf{\Delta}_0\widehat{\mathcal{W}} + \mathbf{\Delta}_1\partial_m\widehat{\mathcal{W}}. \end{aligned} \qquad (10c)$$

In this formulation, the diffusion coefficients of the pseudo-characteristic variables $\widehat{\mathcal{W}}_i$ are given by the diagonal elements $\mathcal{A}_{ii}$ of $\mathcal{A}$ while off-diagonal elements determine the coupling between these different variables through their second-order derivatives or *second derivative coupling*. The *amplification matrix* $\mathcal{C}$ contains both actual (self-)amplification coefficients — the diagonal elements $\mathcal{C}_{ii}$ — and amplitude coupling coefficients — the off-diagonal elements. Advection terms are decoupled by construction. The matrix $\mathbf{\Delta}$ gathers terms originating from time and space dependencies of eigenvectors. Setting $\mathbf{\Delta} = 0$ into Eq. (10a) corresponds to a local decomposition of Eq. (4) in the characteristic basis of Eq. (7), which holds at any point (m, t) but which does not constitute an evolution equation for $\widehat{\mathcal{W}}$ as Eq. (10a) is no longer equivalent to Eq. (4).

IV. RESPONSES TO EXTERNAL PERTURBATIONS

We now investigate how linear perturbations of Eq. (1) propagate, with the help of the pseudo-characteristic basis constructed in Sec. III. Numerical solutions to the system Eqs (4)-(6) are computed, in the Lagrangian variable m, using the same multidomain pseudospectral method as for the base flow and, in time, with a three-step implicit-explicit Runge–Kutta scheme. Boundary conditions are handled using a penalty method while matching conditions at subdomain interfaces are enforced exactly. The numerical code performs computations over each subdomain in parallel using the MPI paradigm with a single process per subdomain. Starting from a zero perturbation initial state ($t_0 = 1$) , the system is perturbed at the external surface with a heat flux or pressure pulse given by

$$\widehat{\varphi}_{\mathrm{es}}(t) = \varphi(0,t)\,\sin^4(\omega_1\,[t - t_0]),$$

with

$$\omega_1 = \frac{2\pi\lambda_1(m = 0, t_0)}{n\,\rho\,l_{\mathrm{cond}}(t_0)}\,, \qquad (11a)$$

or

$$\widehat{p}_{\mathrm{es}}(t) = p(0,t)\,\sin^4(\omega_2\,[t - t_0]),$$

with

$$\omega_2 = \frac{2\pi\lambda_2(m = 0, t_0)}{n\,\rho\,l_{\mathrm{cond}}(t_0)}, \qquad (11b)$$

for $t_0 \leq t \leq t_0 + \pi/\omega_i$ or zero otherwise. The durations of these pulses correspond approximately to the time needed for the corresponding wave ($\mathscr{C}_1$ or $\mathscr{C}_2$) to travel n times the length of the conduction region. The power four on the sine functions ensures a smooth transition at t_0 and $t_0 + \pi/\omega_i$.

Solutions to Eq. (4) are projected on pseudo-characteristic variables $\widehat{\mathcal{W}}_i$ defined in Eq. (7). The various quantities are presented in (m, t) diagrams in which fluid particles move at constant m. On Figs. 2–5, 7 and 10, the mean position of the external surface is $m = 0$ by definition. Similarly, the mean position of the ablation layer (respectively the shock front) is labelled 'af' (resp. 'sf'). The position of the CJ point is labelled 'CJ'. The cold fluid at rest ($m > m_{\mathrm{sf}}(t)$) is free from any source of perturbation. For visualisation purpose we define the function $\mathrm{slog}_a(x) = \mathrm{sgn}(x)\log(1 + a|x|)$ for any real number x and positive parameter a. In addition, colored dashed lines in (m, t) diagrams represent exact characteristics trajectories defined in Eq. (9) originating from pulse half-heights (Eq. 11) at the external surface or from other remarkable points.

Responses to Eq. (4) for an external perturbation tend to propagate close to linear hyperbolic waves. When perturbed with a heat flux pulse $(n, k_\perp) = (4, 1)$, the signal follows, qualitatively, a $\mathscr{C}_1$ characteristics originating from the half height of the heat flux pulse perturbation at the external surface (Fig. 2). The projection of the same solution on the pseudo-characteristic variable $\widehat{\mathcal{W}}_2$ shows no propagation beyond the CJ point (Fig. 4b). In terms of primitive variables (Fig. 3), the only significant signal propagating through the conduction region is a temperature perturbation. This is coherent with the components of $\widehat{\mathcal{W}}_1$ in the basis of primitive variables (Fig. 11).

An external pressure perturbation (Fig. 5b) leads to a spread $\widehat{\mathcal{W}}_1$ signal propagating in the conduction region

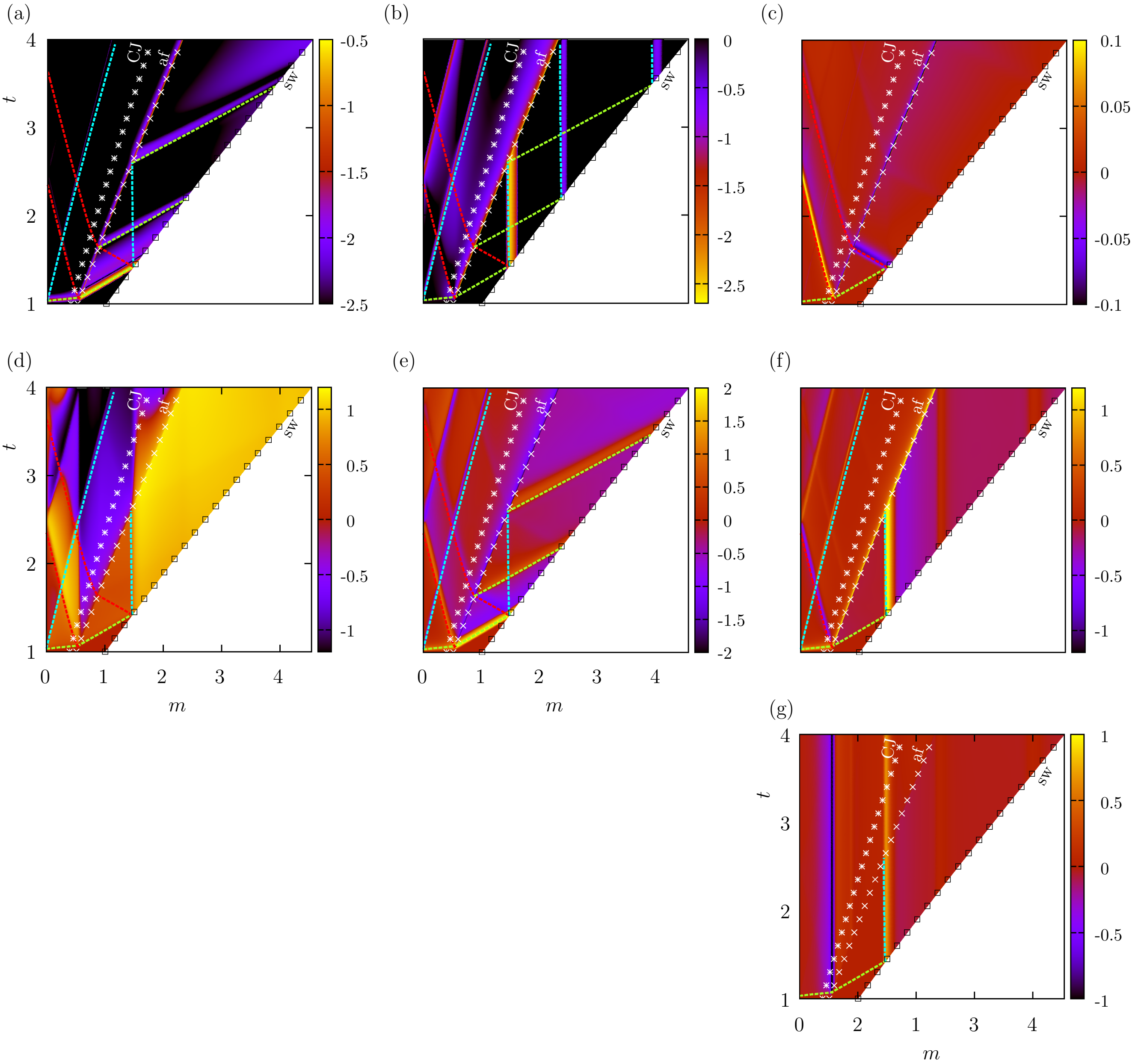

FIG. 4. Response of Eq. (4) to a heat-flux perturbation (Eq. 11b) with $(n, k_\perp) = (4, 1)$ visualized in (m, t) coordinates. Pseudo-characteristic variable: (a) log $|\widehat{\mathcal{W}}_1|$, (b) slog$_{10^3}(\widehat{\mathcal{W}}_2)$, (c) slog$_{10}(\widehat{\mathcal{W}}_4)$, (d) slog$_{10^3}(\widehat{\mathcal{W}}_3)$ and Kovásznay modes: (e) pressure slog$_{10^3}(\widehat{p})$, (f) entropy slog$_{10^3}(\widehat{s})$ and (g) potential vorticity slog$_{10^2}(\widehat{\omega}_\perp/\rho)$ [3]. Trajectories of the mean position of the ablation front (×), CJ point ($*$) and shock front (□). Characteristic trajectories: $\mathcal{C}_1$ (green), $\mathcal{C}_2$ (cyan), $\mathcal{C}_4$ (red), $\mathcal{C}_3$ characteristics are constant m lines. The first $\mathcal{C}_1$ and $\mathcal{C}_2$ characteristics originate from the pulse half-height (Eq. 11a) while the subsequent characteristics originate from the interactions of significant perturbation signals with the shock front, the external surface and the ablation front.

(Fig. 5a). Such a perturbation follows a $\mathcal{C}_1$ characteristics originating from the half height of the pressure perturbation pulse at the external surface.

An external heat-flux perturbation is primarily converted into a heat-conductivity wave perturbation $\widehat{\mathcal{W}}_1$ (Fig 4a) while an external pressure perturbation is primarily converted into a forward quasi-isothermal perturbation $\widehat{\mathcal{W}}_2$ (Fig. 5b). We observe *a posteriori* that response of Eq. (4) to a heat flux or a pressure perturbation follows *a priori* characteristics trajectories $\mathcal{C}_i$ (Eq. 7), either on the projection on pseudo-characteristic variables (Figs. 4-5) or on primitive variables (Fig. 3). The heat-conductivity wave signal ($\widehat{\mathcal{W}}_1$) is the only one able to trace back the expansion flow beyond the CJ point.

TABLE II. Identification of the characteristic waves (Eq. 7) in the conduction region and the post-shock region (adapted from Tab. 6 in [1]).

	Conduction region	Post-shock region
$\mathcal{C}_1$	*Heat conductivity*	*forward quasi-isentropic acoustic*
$\mathcal{C}_2$	*forward quasi-isothermal acoustic*	*Quasi-entropy*
$\mathcal{C}_3$	*Transverse velocity*	*Transverse velocity*
$\mathcal{C}_4$	*backward quasi-isothermal acoustic*	*backward quasi-isentropic acoustic*

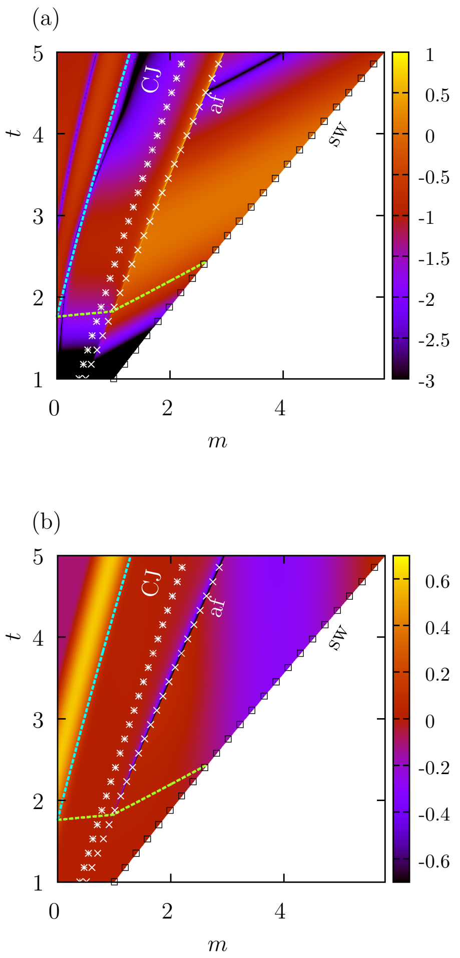

FIG. 5. Response of Eq. (4) to a pressure perturbation (Eq. 11a) with $(n, k_\perp) = (4, 0)$ projected on (a) $\log|\widehat{\mathcal{W}}_1|$ and (b) $\operatorname{slog}_1(\widehat{\mathcal{W}}_2)$. Conventions similar to Fig. 4. The $\mathcal{C}_1$ (green) and $\mathcal{C}_2$ (cyan) characteristics originate from the pulse half maximum (Eq. 11b).

The heat flux perturbation then interacts with the ablation layer where high gradients induce couplings with a reflected backward quasi-isothermal backward acoustic signal ($\widehat{\mathcal{W}_4}$) in the conduction region, and a forward quasi-isentropic acoustic signal ($\widehat{\mathcal{W}_1}$) transmitted to the post-shock region. We observe the formation of a system of reflected traveling waves in the post-shock region, composed of quasi-isothermal acoustic waves and quasi-isentropic waves: see Fig. 6 for a schematic representation. Such reflected waves are unlikely to appear in the conduction region because at the external surface, backward quasi-isothermal acoustic waves are mostly reflected into forward quasi-isothermal acoustic waves unable to propagate beyond the CJ point.

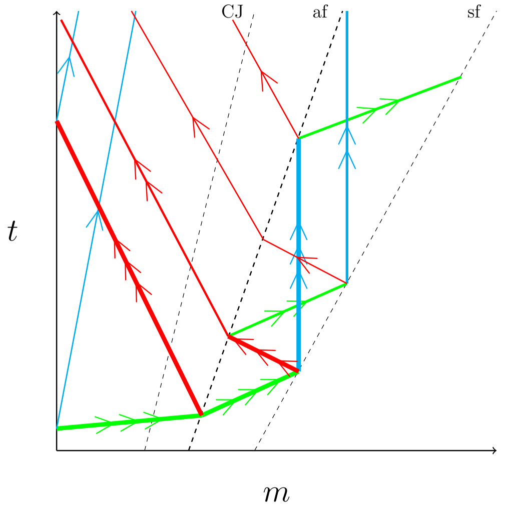

FIG. 6. Schematic representation of perturbation propagation in the (m, t) plane originating from a heat flux perturbation at the external surface. Perturbation trajectories are sketched as colored lines: $\mathcal{C}_1$ (green), $\mathcal{C}_2$ (cyan) and $\mathcal{C}_4$ (red). Arrows indicate the propagation direction. The thickness and number of arrows render the intensity of the corresponding signal. Trajectories of CJ point, ablation front ('af') and shock front ('sf') also indicated.

As mentioned above, while crossing the ablation layer, a perturbation $\widehat{\mathcal{W}_1}$ is partly reflected into the conduction region and partly transmitted to the post-shock region, but a third fraction is trapped into the ablation layer as a perturbation $\widehat{\mathcal{W}}_2$. Such trapping phenomenon is the consequence of the sign reversal of $q = \lambda_2 + \rho u'$. In the conduction region close to the ablation front $q > 0$, therefore no perturbation $\widehat{\mathcal{W}}_2$ originating from the ablation layer can propagate in the conduction region. On the opposite $q < 0$ in the post-shock region. So no perturbation $\widehat{\mathcal{W}}_2$ originating from the ablation layer can propagate into the post-shock region. As a consequence perturbations

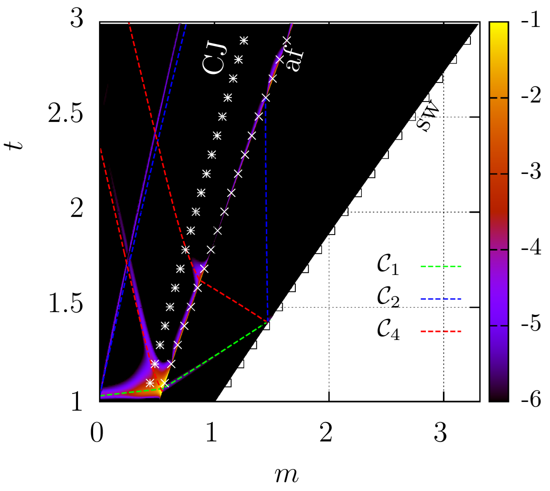

FIG. 7. Baroclinic term (Eq. 12) in logscale for an external heat flux perturbation $(n, k_\perp) = (4, 1)$.

$\widehat{\mathcal{W}}_2$ remain stuck in the ablation layer.

A comparison with a decomposition of perturbations into Kovásznay modes — namely perturbations of pressure, $\widehat{p}$, of entropy, $\widehat{s}$, and of potential transverse vorticity, $\widehat{\omega}_\perp/\rho$, where

$$\widehat{\omega}_\perp = \frac{\rho}{i\,k_\perp}\partial_m \widehat{d}_\perp - i\,k_\perp \widehat{v},$$

highlights the additional information provided by the present pseudo-characteristic variables ($\widehat{\mathcal{W}}_i$) [3]. The decomposition into Kovásznay modes has already been applied to ablation flows and has been found to be relevant in the post-shock region [23]. Indeed, entropy perturbations (Fig. 4f) correspond to $\widehat{\mathcal{W}}_2$ and pressure perturbations (Fig. 4e) appear to result from the superposition of both forward and backward acoustic waves: namely $\widehat{\mathcal{W}}_1$ and $\widehat{\mathcal{W}}_4$ in the post-shock region (Fig. 4a and c). However the propagation direction of acoustic waves cannot be determined from the pressure signal while this information is available from the pseudo-characteristic variables with the distinction between *forward* and *backward* waves. No conclusion could have been deduced from Kovásznay modes into the conduction region. In the conduction region, the pseudo-characteristic variables $\widehat{\mathcal{W}}_1$, $\widehat{\mathcal{W}}_2$, $\widehat{\mathcal{W}}_4$ follow initially the trajectories of the characteristics $\mathcal{C}_1$, $\mathcal{C}_2$ and $\mathcal{C}_4$, respectively, whereas the Kovásznay mode characteristic quantities $\widehat{p}$ and $\widehat{s}$ do not present equivalent features. Indeed, pressure perturbations $\widehat{p}$ (Fig. 4e) coincide mainly with contributions from both pseudo-characteristic variables $\widehat{\mathcal{W}}_2$ and $\widehat{\mathcal{W}}_4$ (Figs. 4b,c) which correspond here to quasi-isothermal acoustic waves (Tab. II). Furthermore, entropy perturbations $\widehat{s}$ (Fig. 4f), in addition to follow also the acoustic wave characteristics, propagate along the characteristics $\mathcal{C}_1$ of the supersonic heat-conductivity waves. Consequently the variables $\widehat{\mathcal{W}}_1$, $\widehat{\mathcal{W}}_2$ and $\widehat{\mathcal{W}}_4$ are more appropriate for describing perturbation evolution in the conduction region than the Kovásznay mode characteristic quantities $\widehat{p}$ and $\widehat{s}$.

Heat conductivity waves $\widehat{\mathcal{W}}_1$ in the conduction region constitute a moving source of transverse divergence for the transverse expansion perturbation $\widehat{d}_\perp$ (Fig. 4d). Transverse expansion perturbations are then conveyed with the fluid (constant m coordinate) but are modified by each acoustic waves crossing the conduction region. By contrast, potential vorticity $\widehat{\omega}_\perp/\rho$ (Fig. 4g) presents clear constant m characteristics in both the conduction and post-shock regions. Therefore potential vorticity constitutes a better characteristic quantity for transverse perturbations than transverse expansion perturbation. The evolution equation for potential vorticity is given by [23]

$$\partial_t\left(\frac{\widehat{\omega}_\perp}{\rho}\right) = i\,\frac{k_\perp}{\rho^2}\left(\widehat{\rho}\partial_m p - \widehat{p}\partial_m \rho\right)\ . \tag{12}$$

Potential vorticity is mostly created at the first interaction of the heat conductivity wave with the ablation layer (Fig. 7), where base flow density and pressure gradients are the largest. Pseudo-characteristic variables $\widehat{\mathcal{W}}_1$, $\widehat{\mathcal{W}}_2$, $\widehat{\mathcal{W}}_4$ and potential vorticity $\widehat{\omega}_\perp/\rho$ are the favored quantities for analyzing the evolution of perturbations in an ablation flow. In particular, the above analysis brings to light the pseudo-characteristic variable $\widehat{\mathcal{W}}_1$ as being the quantity of choice for identifying the propagation of perturbations from the external surface up to the ablation layer in an ablation flow with a supersonic expansion. Implications of this supersonic forward propagation of perturbations are discussed in Sec. V.

A. Transmission of perturbations from the external surface to the ablation front

According to the standard modeling of radiation-driven ablation which assumes an isothermal expansion, isothermal acoustics and heat diffusion are the sole possible mechanisms for perturbation transmission from the flow external surface to the ablation front. In the present section we examine whether or not heat-conductivity waves may contribute to this transmission, in what proportion relatively to heat diffusion, and under which conditions. We do so, by analyzing responses to external pressure and heat-flux perturbations, for various transverse wavenumbers $k_\perp$ and longitudinal characteristic lengths $\lambda_x = n\,l_{\mathrm{cond}}$.

First order deformations of the external surface, the ablation front and the shock front, are shown on Fig. 8 in the case $(n, k_\perp) = (4, 0)$ after normalization to unity according to an energy flux measure

$$E(\widehat{\mathbf{U}}_{\mathrm{es}}) = \left(\int_{t_0}^{T} \widehat{\varphi}_{\mathrm{es}}^2 + (v\widehat{p}_{\mathrm{es}})^2 \mathrm{d}t\right)^{\frac{1}{2}}\ . \tag{13}$$

The case $k_\perp = 0$ is interpreted as the limit of very large transverse wavelength compared to the conduction region. For a given external perturbation energy (Eq. 13),

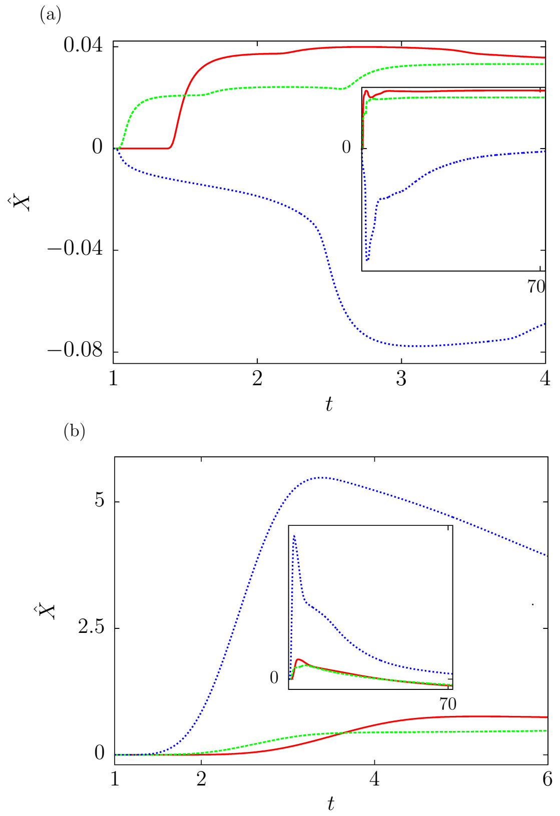

FIG. 8. Deformations of the shock front (red), the ablation front (green) and the external surface (blue) for (a) a longitudinal heat-flux and (b) pressure perturbation $(n, k_\perp) = (4, 0)$, normalized to unity (Eq. 13). These deformations are first order perturbations of mean positions appearing on Fig. 4. The insets illustrate long time behaviours.

a pressure perturbation induces a higher shift than a heat-flux perturbation. In both cases the external surface is immediately shifted: inwardly in the case of a pressure perturbation because of a compression at the external surface, and outwardly in the case of a heat-flux perturbation because of the material expansion due to a temperature increment. The first motion of the ablation front (Fig. 8) corresponds to the arrival of the forerunning heat-conductivity wave identified on Figs. 4 and 5. The same effect is observed at the shock front with a delay corresponding to the acoustic crossing time of the post-shock region. The following motions of the external surface, ablation and shock front correspond to the interactions of the travelling waves observed on Figs. 4 and 5 with the above mentionned interfaces. Consistently with the existing results, a purely longitudinal perturbation $(k_\perp = 0)$ induces a permanent shift of the ablation layer and shock front [13, 22, 27].

To measure the efficiency of perturbation transmission from the external surface to the ablation layer, we consider the ratio

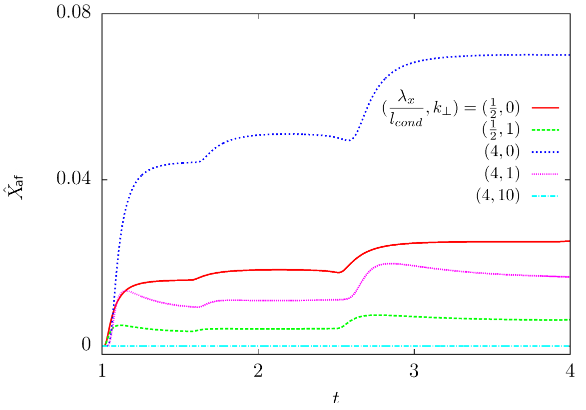

FIG. 9. Deformation of the ablation front at early times for different longitudinal characteristic $\lambda_x / l_{\text{cond}} = \{1/2,\ 4\}$ and transverse wavenumbers $k_\perp = \{0,\ 1,\ 10\}$.

$$r = \frac{\max\limits_t \left\{ \|\widehat{\mathbf{U}}\|_2|_{\text{af}} \right\}}{\max\limits_t \left\{ \|\widehat{\mathbf{U}}\|_2|_{\text{es}} \right\}}, \qquad \text{where } \|\widehat{\mathbf{U}}\|_2 = \sqrt{\sum_{i=1}^{4} \widehat{\mathbf{U}}_i^2}. \qquad (14)$$

This ratio measures the amplification of a signal between the external surface and the ablation layer. The amplification is greater for an external heat-flux perturbation than for a pressure perturbation (Tab. III). This fact corroborates the higher ablation front deformation, relatively to the external surface deformation, in the case of an external heat-flux perturbation than in the case of an external pressure perturbation (Fig. 8). This is again a consequence of the ability of heat-conductivity wave perturbations to trace back the expansion flow, unlike acoustic perturbations.

$\widehat{p}_{\text{es}}$	$\widehat{\varphi}_{\text{es}}$
$2,29 \times 10^3$	$8,41 \times 10^3$

TABLE III. Amplification factor r (Eq. 14) between the external surface and the ablation front, for a heat-flux and external pressure perturbation (Eq. 11a) with $(n, k_\perp) = (4, 0)$.

The effects of diffusion on a heat-flux perturbation are investigated with (i) a shorter longitudinal characteristic length, $n = 0.5$ (Eq. 11), and (ii) a transverse wavenumber increased to 1 and 10. The efficiency of the transmission is reduced but still persists for a longitudinal characteristic length being half of the conduction region size, $n = 0.5$ (Tab. IV). In particular, the ablation front deformation is lowered (Fig. 9 red), but its behaviour is qualitatively similar to the case $n = 4$ (Fig. 9 blue). Therefore, a longitudinal characteristic length being a fraction of the conduction region size does not inhibit the heat conductivity wave that provokes the first shift of the ablation layer and still allows information to be transmitted

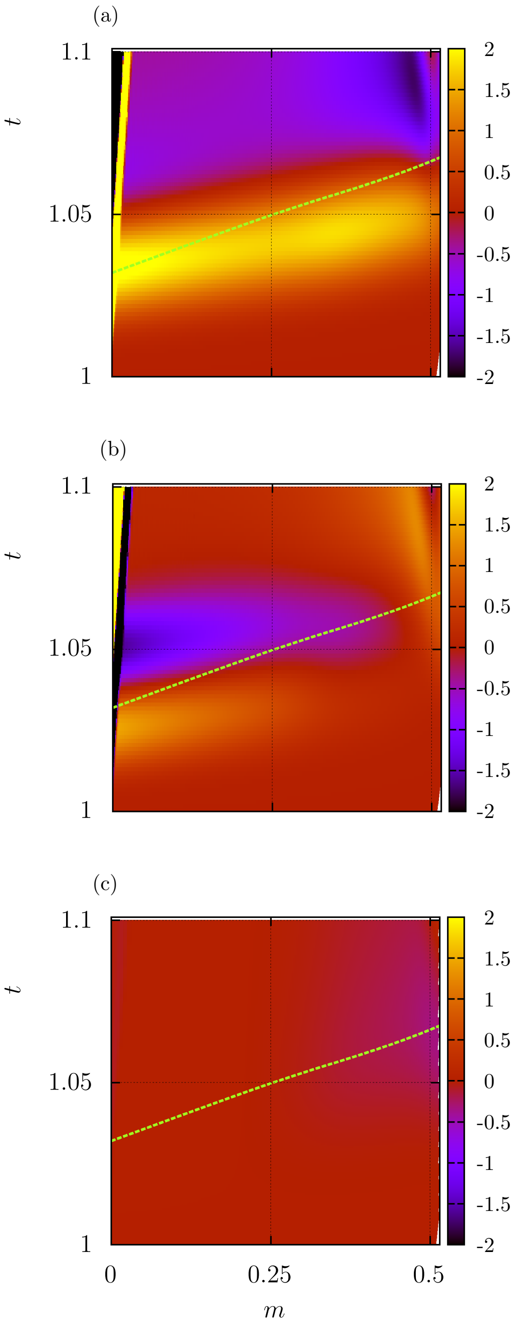

FIG. 10. Contribution from advection, diffusion and remaining terms from Eq. (10a) to the variation rate of $\widehat{\mathcal{W}}_1$ $(n, k_\perp) = (4, 1)$. A $\mathcal{C}_1$ characteristics originating from the top of the heat-flux pulse (Eq. 5).

to the ablation layer from the external surface. Damping effects of transverse diffusion are much stronger than longitudinal diffusion (Tab. IV), as a transverse wavelength of five times the conduction region ($k_\perp = 1$) implies a damping similar to a longitudinal characteristic length of half of the conduction region. Perturbations are efficiently transmitted to the ablation front only for transverse wavelengths that are over several times the conduction region size. Transverse diffusion also implies a transient relaxation after each growth phase (Fig. 9 pink and green). For transverse wavelengths being a fraction of the conduction region or smaller ($k_\perp \geq 10$), the transmission to the ablation layer and the ablation front deformation is negligible. At larger times, and $k_\perp > 0$, we recover the well known shock front oscillations [2, 10, 16, 19, 22, 27].

		$k_\perp$		
		0	*1*	*10*
n	*4*	8.41×10^3	3.68×10^3	1.10×10^{-1}
	0,5	2.9×10^3	1.10×10^3	–

TABLE IV. Amplification factor r (Eq. 14) between the external surface and the ablation front for an external heat-flux perturbation (Eq. 11a) at various n and $k_\perp$.

B. Dominant mechanisms

We have observed earlier (Sec. IV) that perturbations qualitatively follow characteristics trajectories from Eq. (9) in the conduction and the post-shock region. In the present section we carry out a quantitative analysis to discriminate between the main propagation mechanisms: advection or diffusion. Recalling Eq. (10a), the contributions from diffusion, advection and amplification terms, to any of the pseudo-characteristic component variation rate, can be compared at any given flow location and time. The contributions to $\widehat{\mathcal{W}}_1$ in the conduction region for a purely longitudinal heat-flux perturbation (Eq. 11a) are shown on Fig. 10. Diffusion intensity rapidly decays as the signal propagates inside the conduction region. Contributions from amplification terms and non characteristic terms ($\boldsymbol{\Delta}\widehat{\mathcal{W}}$ in Eq. 10a) are negligible even in the ablation layer neighbourhood. Therefore the dominant mechanism enabling heat-conductivity wave perturbations to cross the CJ point is advection, and not diffusion. The existence of supersonic linear heat-conductivity waves is quantitatively confirmed although diffusion exists in this region. This is a direct consequence of base flow stratification in the conduction region. This advection mechanism is able to transmit any hydrodynamic perturbation taking place at the external surface to the ablation layer along a $\mathcal{C}_1$ characteristics, through the CJ point, to the ablation layer.

The quantity $\widehat{\mathcal{W}}_1$ is conserved, in first approximation, along $\mathcal{C}_1$. The composition of a $\mathcal{C}_1$ wave varies across the conduction region but temperature is dominating (Fig. 11). Although the contribution of density in the conserved $\widehat{\mathcal{W}}_1$ wave increases as the wave comes up to the ablation layer, its contribution becomes significant at some location where advection no longer dominates (Fig. 3). Therefore the heat conductivity wave reaching the ablation layer is mostly composed of a temperature perturbation, as observed on Fig. 3 (c).

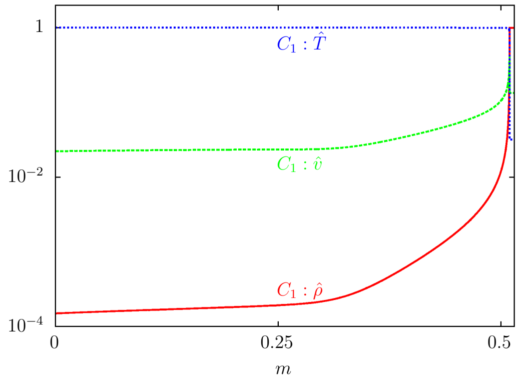

FIG. 11. Contributions of primitive variables ($\widehat{\rho}$, $\widehat{v}_x$, $\widehat{T}$) in a unit heat-conductivity wave quantity ($\widehat{\mathcal{W}}_1$) conserved along $\mathcal{C}_1$ in Eq. (9), no contribution from transverse velocity. Zoom in the conduction region

In the three following sections we broaden this analysis to find out which mechanism dominates depending on the flow location and characteristic length, keeping only dominant terms from Eq. (10a). We are interested in orders of magnitude of the various quantities and not in their actual values.

1. *Dominance of advection*

Advection mechanism dominates where (i) diffusion terms, (ii) amplification terms and (iii) first order coupling terms are sufficiently low. The latter is verified in the conduction region and the post shock region, whatever the wavelength of perturbations. More generally the case of the post-shock region has been extensively studied in [23]. As heat flux is quasi non-existent and the stratification is moderate in this region, advection is the leading mechanisms for perturbations over a wide range of wavelengths.

We have seen previously that pseudo-characteristic variables behave close to linear waves in the conduction region for ($1/2 \leq n \leq 4, 0 \leq k_\perp \leq 1$). Let k_i denote the wavenumber of a linear wave approximating the pseudo-characteristic wave $\widehat{\mathcal{W}}_i$ and ω be the pulsation common to such waves for $i = 1, 2, 4$. The magnitude of spatial derivatives is approximated by

$$|\partial_m^p \widehat{\mathcal{W}}_i| \approx k_i^p |\widehat{\mathcal{W}}_i|, \text{ for } p = 0, 1, 2, \text{ and } i = 1, 2, 4. \tag{15}$$

The pulsation ω is driven by the number of wavelengths n in the conduction region (Eq. 11). In the case of a heat-flux perturbation

$$\omega = k_1 \lambda_1 = \frac{2\pi\lambda_1}{n\,\rho\, l_{\text{cond}}}, \text{ and } k_i = \omega/\lambda_i \text{ for } i = 2, 4.$$

For a given n, $k_{2,4} \gg k_1$ as $\lambda_1 \gg \lambda_{2,4}$ meaning that for a given pulsation quasi-isothermal acoustic waves are sharper than heat-conductivity waves. As a consequence second order derivatives of quasi-isothermal acoustic waves are greatly enhanced compared to those of heat-conductivity waves. Dominating contributions of each pseudo-characteristic variables $\widehat{\mathcal{W}}_j$ to each variation rate $\partial_t \widehat{\mathcal{W}}_i$ through second order derivatives (diff), first order derivatives (adv) and amplification terms (amp), are shown in Fig. 12. These contributions depend on powers of the wavenumber, k_i^p (Eq. 15), and approximate values of $\mathcal{A}_{ij}$, $\mathbf{\Lambda}_{ii}$ and $\mathcal{C}_{ij}$ in the conduction region.

For $1 \lesssim n \lesssim 10$ advection dominates diffusion for heat conductivity and acoustic waves (Fig. 12a). Simplified expressions for the respective variation rates write

$$\begin{aligned}
&\partial_t \widehat{\mathcal{W}}_1 + \lambda_1 \partial_m \widehat{\mathcal{W}}_1 + \sum_{i=2,4} \mathcal{A}_{1i} \partial^2_{m^2} \widehat{\mathcal{W}}_i = 0, \\
&\partial_t \widehat{\mathcal{W}}_2 + \lambda_2 \partial_m \widehat{\mathcal{W}}_2 = 0, \\
&\partial_t \widehat{\mathcal{W}}_4 + \lambda_4 \partial_m \widehat{\mathcal{W}}_4 = 0.
\end{aligned}$$

One first notes that terms $\mathbf{\Delta}_0$ (Eq. 10a), accounting for characteristic basis dependence on base-flow spatial derivatives, are negligible regarding advection and diffusion terms, meaning that the local approximation of Ref. [1] is valid in this region and for this wavelength range. In the scenario of an external heat flux perturbation from an initially unperturbed state, a wave $\widehat{\mathcal{W}}_1$ will be advected along a $\mathcal{C}_1$ characteristics autonomously since the term $\sum_{i=2,4} \mathcal{A}_{1i} \partial^2_{m^2} \widehat{\mathcal{W}}_i$ vanishes. This scenario corresponds to the perturbation history displayed in Figs. 2, 4 & 10. However, as an external heat-flux perturbation perturbs the external surface, a small acoustic perturbation is also emitted (Fig. 9b) which produces a feedback through first and second derivative coupling terms. This coupling explains the very intense tracks following a $\mathcal{C}_2$ characteristics on Figs. 10 (a, b). An external pressure perturbation will be advected along a $\mathcal{C}_2$ characteristics as observed on Figs. 5b. This advected acoustic signal will act as a source moving at velocity λ_2 on the heat conductivity wave ($\widehat{\mathcal{W}}_1$) through second order coupling terms (Fig. 5a). This seeded heat-conductivity wave perturbation will be advected to the ablation front along a $\mathcal{C}_1$ characteristics. Therefore any acoustic perturbation at the external surface may in principle reach the ablation front by a second derivative coupling from acoustic to heat-conductivity waves.

2. *Dominance of diffusion*

As stated in the preceding section, heat flux is quasi non-existent in the post shock region, so diffusion acts only for very short wavelengths. In the ablation layer amplification terms dominate diffusion. For short wavelengths $n \leq 0.1$ second order derivative terms, including diffusion, dominate in the conduction region (Fig. 12)

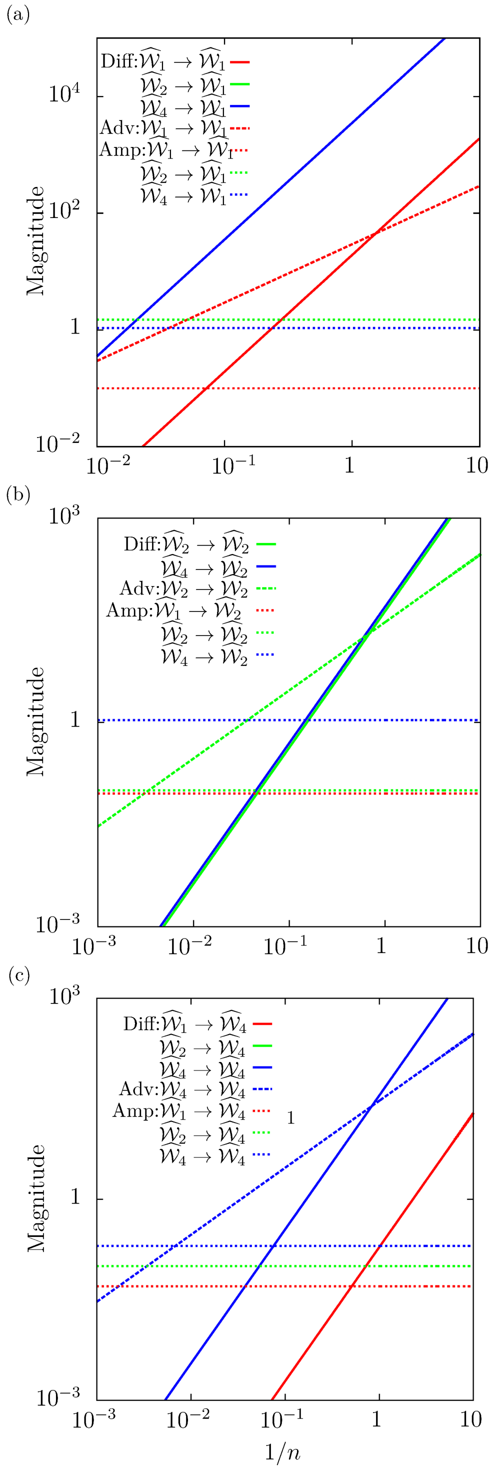

FIG. 12. Dominating terms in Eq. (10a) for (a) $\widehat{\mathcal{W}}_i \to \widehat{\mathcal{W}}_1$, (b) $\widehat{\mathcal{W}}_i \to \widehat{\mathcal{W}}_2$ and (c) $\widehat{\mathcal{W}}_i \to \widehat{\mathcal{W}}_4$, for $1/n$ (Eq. 11) ranging from 10^{-3} to 10 and $m = 0.25$. Contribution from second order derivatives $\mathcal{A}_{ij}\partial_m^2\widehat{\mathcal{W}}_j$ (solid line), first order derivatives $\mathbf{\Lambda}_{ii}\partial_m\widehat{\mathcal{W}}_i$ (dashed line) and amplification terms $(\boldsymbol{\mathcal{C}}_{ij}+\Delta_{ij})\widehat{\mathcal{W}}_j$ (dotted line).

and variation rates may be approximated by

$$\begin{aligned} &\partial_t\widehat{\mathcal{W}}_1 + \mathcal{A}_{11}\partial^2_{m^2}\widehat{\mathcal{W}}_1 + \sum_{i=2,4}\mathcal{A}_{1i}\partial^2_{m^2}\widehat{\mathcal{W}}_i = 0, \\ &\partial_t\widehat{\mathcal{W}}_2 + \mathcal{A}_{22}\partial^2_{m^2}\widehat{\mathcal{W}}_2 + \mathcal{A}_{24}\partial^2_{m^2}\widehat{\mathcal{W}}_4 = 0, \\ &\partial_t\widehat{\mathcal{W}}_4 + \mathcal{A}_{44}\partial^2_{m^2}\widehat{\mathcal{W}}_4 + \mathcal{A}_{42}\partial^2_{m^2}\widehat{\mathcal{W}}_2 = 0. \end{aligned} \tag{16}$$

Heat conductivity waves evolve through diffusion and second derivative couplings with forward and backward quasi-isothermal acoustic waves. The latter evolve as a coupled $\widehat{\mathcal{W}}_2$-$\widehat{\mathcal{W}}_4$ system due do diffusion, therefore the distinction between ‘forward’ and ‘backward’ is no longer appropriate as propagation direction cannot be found where only diffusion acts. The coupling phenomena between heat-conductivity and acoustic waves in the case of the external heat flux and pressure perturbations explained in the preceding section hold, as well as the validity of the local analysis.

3. *Dominance of amplification terms*

In the regions of low base-flow gradients, amplification terms dominate at very long wavelengths, $n \gg 10$ in the conduction region (Fig. 12). The ablation layer is a region of strong base-flow gradients. All amplification terms turn out to dominate other terms due to the stiffness of the base flow (see the ratio of characteristic lengths in Tab. I). In particular it is necessary to take into account terms $\mathbf{\Delta}_0$ (Eq. 10a) accounting for the dependence of the characteristic basis (Eq. 7) on space derivatives, meaning that the local approximation is not valid in this region. As a consequence only amplification terms are retained from Eq. (10a) and the evolution of pseudo-characteristic variables in the ablation front is driven by,

$$\begin{aligned} &\partial_t\widehat{\mathcal{W}}_1 + b_{11}\widehat{\mathcal{W}}_1 + b_{14}\widehat{\mathcal{W}}_4 = 0, \text{ with } b_{11} < 0 \text{ and } b_{14} > 0, \\ &\partial_t\widehat{\mathcal{W}}_2 + b_{21}\widehat{\mathcal{W}}_1 + b_{22}\widehat{\mathcal{W}}_2 + b_{24}\widehat{\mathcal{W}}_4 = 0, \\ &\qquad \text{with } b_{21} > 0 \text{ and } b_{22},\ b_{24} < 0, \\ &\partial_t\widehat{\mathcal{W}}_4 + b_{41}\widehat{\mathcal{W}}_1 + b_{42}\widehat{\mathcal{W}}_2 + b_{44}\widehat{\mathcal{W}}_4 = 0, \end{aligned} \tag{17}$$

where $b_{ij} = \mathcal{C}_{ij} + \mathbf{\Delta}_{0_{ij}}$. (Fig. 13c). As a consequence a heat-conductivity wave is strongly self amplified in the ablation front and does not experience any sign change while crossing the ablation front, as observed on Fig. 4. The quantity $\widehat{\mathcal{W}}_2$ is also self-amplified, additionally to the *trapping* mechanism described in Sec. IV, due to the coefficient b_{22}. Because of the sign of b_{21}, a heat-conductivity wave eventually gives rise to a wave $\widehat{\mathcal{W}}_2$ of opposite sign when it reaches the ablation layer. A backward acoustic wave originating from the post-shock region will also seed a positive reflected forward acoustic wave, consequently maintaining a system of reflected traveling waves between the ablation and shock front. This approximate analysis confirms the observations made on Figs. 4 and 5. No particular driving source term can be identified for the evolution of the quantity $\widehat{\mathcal{W}}_4$ in the ablation layer because none of them dominates and two of them experience a sign change across the ablation layer (Fig. 13c). For a forward propagating perturbation coming from the conduction region

$$b_{41} \sim b_{44} \gg b_{42},$$

so a heat-conductivity wave interacting with the ablation front free from perturbation will seed a backward acoustic wave in the conduction region, as observed on Figs. 4 and 5.

V. DISCUSSION

The present analysis of linear perturbation propagation in an ablation wave has confirmed the existence of heat-conductivity linear waves in the flow conduction region. This existence is the direct consequence of temperature and density stratification in the conduction region and therefore cannot be obtained from the standard modeling of radiation-driven ablation flows which assumes an isothermal expansion region (e.g [4, 20]). Such waves correspond to the propagation of fluctuations of heat-flux perturbations [1](§ 4.2). They are presently found to be an efficient transmission mechanism for perturbations of longitudinal characteristic lengths of the order of — or larger than — the conduction region size and of transverse wavelengths being several times this size. Under these conditions, this transmission by advection prevails over heat diffusion and is, by essence, free of any damping.

Due to their high propagation velocity, heat conductivity waves propagate from the external surface to the ablation layer in a fraction of the acoustic crossing time of the post-shock region, which is itself a fraction of the shock transit phase duration. Therefore, heat conductivity waves may occur for perturbations of the external heat flux and/or pressure over time scales shorter to much shorter than that of the shock transit phase.

Because of second order spatial derivative couplings near the external surface between forward-propagating acoustic and heat-conductivity waves, any hydrodynamic perturbation at the external surface may be partly advected through the conduction region, beyond a potential Chapman–Jouguet point, up to the ablation front. Hence, even fluctuations of the fluid velocity or pressure at the flow external surface may have an impact on the rest of the ablation flow, including the ablation and shock fronts, in the case of a supersonic expansion flow. This transmission process may be effective at any time of an ablation flow provided that the temperature stratification in the conduction region is sufficiently high. This refined analysis of perturbation propagation furnishes a deeper understanding of perturbation feedthrough in ablation flows due to nonlinear heat conduction.

The present results of linear perturbation propagation have been obtained for a particular self-similar ablation wave representative, through its gross hydrodynamic features, of the shock transit phase of an ICF implosion. The present base-flow self-similarity implies that the radiation heat flux as well as the exerted pressure at the flow external surface follow increasing time-power laws

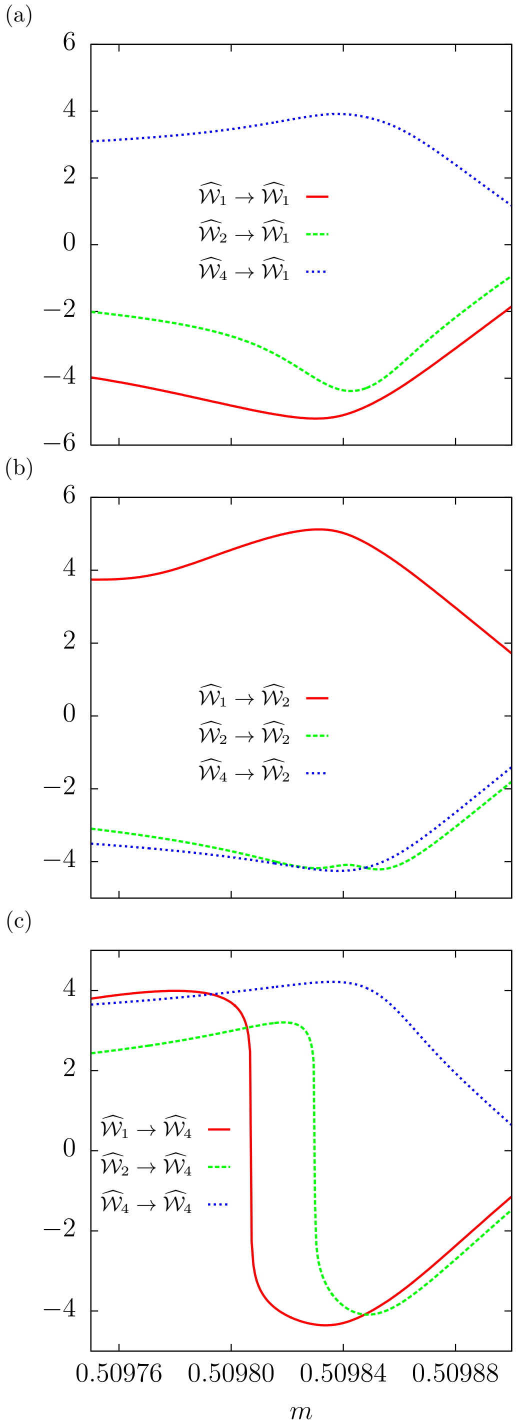

FIG. 13. Magnitude of dominating amplification terms in the ablation layer, (a) $\widehat{\mathcal{W}}_i \to \widehat{\mathcal{W}}_1$, (b) $\widehat{\mathcal{W}}_i \to \widehat{\mathcal{W}}_2$ and (c) $\widehat{\mathcal{W}}_i \to \widehat{\mathcal{W}}_4$.

Eq. (3). These specific behaviors are far from being observed in radiation hydrodynamic simulations of the shock transit phase of an ICF pellet during the foot of the radiation drive. However simulated flow profiles obtained for an actual ICF target design and radiation drive (Figs. 1 and 5 in [**?**]), in the radiation heat-conduction approximation, do not qualitatively differ, for the conduction region, from those of a suitably chosen self-similar ablation wave (Fig. 2 in [1]). Since the properties of heat-conductivity waves are determined by the base-flow temperature and density stratifications in this region, we may expect to also observe forward-propagation of perturbations by supersonic heat-conductivity waves in this particular non self-similar ICF flow. This claim is based on the fact that heat-conductivity waves with supersonic characteristic speeds have been found to occur in self-similar ablation flows presenting very different stratifications of their conduction regions [1]. The presence of such waves thus appears to be related to the high values of the heat-conduction flux in the flow conduction region rather than to the details of the temperature and density stratifications in this region. In that respect, heat-conductivity waves are expected to be present in ablation flows driven by incident heat-flux laws less specific than the time-power laws of Eq. (3). Of course, the velocities and prevailing of these waves depending on the local features of the base flow, a quantitative evaluation of the role played by such waves would require applying the present analysis in pseudo-characteristic variables to the ablation flow under study. Since this analysis is independent of any self-similarity assumption, there is no theoretical obstacle to do so, only the practical complication of dealing with an arbitrary time evolution of the base-flow variables.

Heat-conductivity waves are not restricted to radiation conduction and may occur for other types of nonlinear heat conduction, e.g. electron heat conduction. In this latter case, the linear perturbation analysis proposed in the present work could be applicable to the entire extent of a laser-driven ablative wave, i.e. including the plasma corona expansion, and should be especially relevant in the region between the surface of laser energy deposition and the leading shock front. Such an analysis could even be elaborated and carried out for self-similar solutions of a two-temperature modeling of laser-driven ablation plasmas [29]. In the case of radiation-driven ablation of an ICF pellet, the approximation of radiation heat conduction is justified only for the optically thick part of the ablated material. Therefore the present analysis is relevant to a portion of the ablation wave that starts at some distance donwstream to the ablation layer and extends up to the fore-running shock front. Perturbations, with large transverse wavelengths, of the incoming radiation intensity at the ablator external surface are efficiently transmitted across the optically thin region of the expanding flow, resulting into perturbations of the radiation heat flux at the edge of the conduction region. Since such heat-flux perturbations correspond for a part to the characteristic quantity advected by supersonic heat-conductivity waves, we can still expect to observe the propagation, in addition to the diffusion, of such waves deeper into the conduction region. Obtaining a quantitative assessment of such a process in order to go beyond this conjecture, would require at first to extend the present analysis to the modeling of non-equilibrium radiation diffusion, a task that we leave for future works.

VI. CONCLUSION

The present work provides a numerical investigation of linear perturbations of a realistic self-similar ablation wave in slab symmetry representative of the shock transit phase of an ICF pellet implosion. The perturbation configuration that is treated differs from those of illumination asymmetries and ablative Richtmyer–Meshkov instability since we focus on the setup of perturbations in an already existing and unperturbed ablation flow, under the excitation of heat-flux or pressure perturbations at the flow external surface. The physics of ablation is modeled by the equation of gas dynamics with a nonlinear heat conduction as an approximation for radiation transport. Perturbations of flow variables are three-dimensional without any self-similarity assumption and are computed together with external surface and shock front linear deformations. Linear perturbations of the ablation layer position are provided.

Perturbations are found to behave close to linear waves in the conduction region and the post-shock region. The main result is the observation of supersonic heat conductivity waves advected forward through the supersonic expansion flow, as predicted by Clarisse et al. [1], as a consequence of base flow stratification in the conduction region. This result is allowed by the choice of a modeling derived from first principles and without supplemental simplifying assumptions and could not, for example, have been obtained with the assumptions of an isothermal expansion of the flow conduction region [4, 20]. As a consequence, any hydrodynamic perturbation at the external surface may be advected through the conduction region, beyond a potential Chapman–Jouguet point, up to the ablation front. Although heat diffusion is effective, advection as heat-conductivity waves is found to be the dominant mechanism for longitudinal characteristic lengths being the size of the conduction region (or larger), and remains non-negligible for smaller wavelengths. However, no indication of radiative heat transport instability has been observed because the density fluctuation propagated by the heat-conductivity wave is negligible compared to the temperature fluctuation [30]. Nevertheless, this observation is specific to the ablation flow considered here and heat-conductivity waves carrying higher density fluctuations may arise in other radiative ablation flows.

More generally, the description of the flow perturbations conducted in this paper in terms of longitudinal pseudo-characteristic waves supplemented by the transverse potential vorticity of the velocity field perturbation, has been found to be most appropriate for analyzing perturbation dynamics in both the conduction region and post-shock region of a one-dimensional ablation flow. This description furnishes additional propagation information over the classical fundamental — Kovásznay — modes of fluid dynamics and are more relevant for the density and temperature stratified regions of such flows. The analysis performed by such a description and the companion identification of simplified evolution equations form a methodology that is fully applicable to other ablation flows whether in the context of radiation-driven or laser-driven ablation.

[1] J.-M. Clarisse et al.

[2] Y. Aglitskiy et al. Basic hyrdodynamics of Richtmyer–Meshkov-type growth and oscillations in the inertial confinement fusion-relevant conditions. *Phil. Trans. R. Soc. A*, 368:1739–1768, 2010.

[3] L. S. G. Kovásznay. Turbulence in supersonic flow. *J. Aeronautic. Sci.*, 20(10):657–674, 1953.

[4] S. Atzeni and J. Meyer-ter-Vehn. *The physics of inertial fusion.* Oxford University Press, Oxford, U.K., 2004.

[5] Ya. B. Zel'dovich and Yu. P. Raizer. *Physics of shock waves and high-temperature hydrodynamic phenomena.* Academic Press, New-York, 1967.

[6] J. Lindl, O. Landen, J. Edwards, E. Moses, and NIC Team. Review of the National Ignition Campaign 2009-2012. *Phys. Plasmas*, 21:020501, 2014.

[7] R. J. Taylor et al. Measurement and simulation of laser imprinting and consequent Rayleigh–Taylor growth. *Phys. Rev. Lett.*, 76(10):1643–1646, 1996.

[8] R. D. Richtmyer. Taylor instability in shock acceleration of compressible fluids. *Commun. Pure Appl. Math.*, 13:297–319, 1960.

[9] E. E. Meshkov. Instability of the interface of two gases accelerated by a shock wave. *Soviet Fluid Dynamics*, 4:101–104, 1969.

[10] V. N. Goncharov. Theory of the ablative Richtmyer-Meshkov instability. *Phys. Rev. Lett.*, 82(10):2091–2094, 1999.

[11] H. J. Kull and S. I. Anisimov. Ablative stabilization in the incompressible Rayleigh–Taylor instability. *Phys. Fluids*, 29:2067–2075, 1986.

[12] M. H. Emery et al. Hydrodynamic target response to an induced spatial incoherence-smoothed laser beam. *Phys. Fluids B*, 3(9):2640–2651, 1991.

[13] R. Ishizaki and K. Nishihara. Propagation of a rippled shock wave driven by nonuniform laser ablation. *Phys. Rev. Lett.*, 78(10):1920–1923, 1997.

[14] R. J. Taylor et al. Saturation of laser imprint on ablatively driven plastic targets. *Phys. Rev. Lett.*, 79(10):1861–1864, 1997.

[15] A. L. Velikovich, J. P. Dahlburg, J. H. Gardner, and R. J. Taylor. Saturation of perturbation growth in ablatively driven planar laser targets. *Phys. Plasmas*, 5:1491–1505, 1998.

[16] K. Nishihara, R. Ishizaki, J. G. Wouchuk, Y. Fukuda, and Y. Shimuta. Hydrodynamic perturbation growth in start-up phase in laser implosion. *Phys. Plasmas*, 5(5):1945–1952, 1998.

[17] N. Metzler et al. Reduction of early-time perturbation growth in ablatively driven laser target using tailored density profiles. *Phys. Plasmas*, 6(8):3283–3295, 1999.

[18] V. N. Goncharov et al. A model of laser imprinting. *Phys. Plasmas*, 7(5):2062–2068, 2000.

[19] V. N. Goncharov et al. Early stage of implosion in inertial confinement fusion: Shock timing and perturbation evolution. *Phys. Plasmas*, 13:012702, 2006.

[20] Y. Saillard, P. Arnault, and V. Silvert. Principles of the radiative ablation modeling. *Phys. Plasmas*, 17:123302, 2010.

[21] F. Abéguilé et al. Linear perturbation amplification in self-similar ablation flows of inertial confinement fusion. *Phys. Rev. Lett.*, 97:035002, 2006.

[22] J.-M. Clarisse et al. Linear perturbation response of self-similar ablative flows relevant to inertial confinement fusion. *J. Fluid Mech.*, 609:1–48, 2008.

[23] V. Lombard et al. Kovásznay modes in stability of self-similar ablation flows of ICF. *Europhys. Lett.*, 84:25001, 2008.

[24] R. Marshak. Effect of radiation on shock wave behavior. *Phys. Fluids*, 1(1):24–29, 1958.

[25] J. Sanz et al. Self-similar model for tamped ablation driven by thermal radiation. *Phys. Fluids B*, 4(3):683–692, 1992.

[26] C. Boudesocque-Dubois et al. Self-similar solutions of unsteady ablation flows in inertial confinement fusion. *J. Fluid Mech.*, 603:151–178, 2008.

[27] J.-M. Clarisse et al. Transient effects in unstable ablation fronts and mixing layers in HEDP. *Phys. Scr.*, 91:074005, 2016.

[28] C. Boudesocque-Dubois et al. An adaptive multidomain Chebyshev method for nonlinear eigenvalue problems: Application to self-similar solutions of gas dynamics equations with nonlinear heat conduction. *J. Comput. Phys.*, 235:723–741, 2013.

[29] J. R. Sanmartín and A. Barrero. Self-similar motion of laser half-space plasma. I. Deflagration regime. *Phys. Fluids*, 21(11):1957–1966, 1978.

[30] V. Yu. Bychenkov and W. Rozmus. Radiative heat transport instability in a laser produced inhomogeneous plasma. *Phys. Plasmas*, 22:082705, 2015.

CHAPTER B

Proceedings of the *Congrès Français de Mécanique*

Non-modal hydrodynamic stability analysis of ablation flows relative to inertial confinement fusion, G. Varillon, J.-M. Clarisse, A. Couairon, *Congrès Français de Mécanique, Brest, France, 08/2019*.

Non-modal hydrodynamic stability analysis of ablation flows relative to inertial confinement fusion

Grégoire Varillon[a,b], Jean-Marie Clarisse[a], Arnaud Couairon[b]

a. CEA, DAM, DIF, F-91297 Arpajon, France, jean-marie.clarisse@cea.fr
b. CPHT, CNRS, École polytechnique, IP Paris, F-91128 Palaiseau, France,
gregoire.varillon@polytechnique.edu, arnaud.couairon@polytechnique.edu

Résumé :

The hydrodynamic stability of ablation flows is a key issue in laser-driven inertial confinement fusion (ICF) where a sufficiently symmetric implosion of a spherical pellet is expected to achieve thermonuclear burn. Such flows which originate from exposing the pellet outer shell to a growing incident heat flux, present the radial structure of an inward-propagating deflagration, or 'ablation', wave where a shock wave precedes a subsonic heat front that coindices with the leading edge of the heated material expansion wave. Inherently unsteady, these flows are compressible, strongly accelerated and highly nonuniform with a steep heat front, owing to the strong nonlinearity of the heat transport and the intense incident heating. These features, in addition to non-trivial boundary conditions at the shell external surface and shock front, are sources of non-modal thermo-acoustics effects [1, 2]. However non-modal instability growth in ablation flows relevant to ICF has never been studied so far. The development of instabilities leading to nonlinear phenomena in ablation flows could result into the loss of symmetry of the implosion and could finally inhibit ignition. Transition mechanisms in ablation flows are therefore of primary importance to ICF ignition.

Here we investigate non-modal effects in planar radiative ablation waves by using self-similar ablation solutions to the Euler equations with nonlinear heat conduction, without further approximation, as model base flows representative of the early stage of an ICF pellet implosion [3]. Pseudo-spectra of the local approximation of the perturbation evolution operator reveal a potential for strong transient growth. Because of the base flow unsteadiness, our non-modal linear stability analysis relies on a direct-adjoint method. The flow boundary deformations, at the material external surface and shock front, as well as their adjoint variable counterparts enter this method formulation. Both optimal initial conditions and receptivity to perturbations of the incident heat flux and external surface pressure are considered. Different definitions of objective functionals are investigated, some in relation with experimentally measurable quantities. Optimal response computations are carried out for terminal times and perturbation transverse wavelengths which are determined on the basis of pellet implosion features. Computed optimal responses are physically analysed in terms of diffusion and propagation, with the help of a decomposition into linear hyperbolic waves — corresponding to acoustic, entropy, vorticity and radiation-conductivity waves [3] — for a nonuniform heat-conducting flow.

Abstract :

A non-modal linear hydrodynamic stability analysis of ablation waves is carried out for the first time. This analysis is performed for unsteady self-similar solutions in slab symmetry of the Euler equations with nonlinear heat conduction, using a direct-adjoint method that results from a Lagrangian-based optimization problem. Such solutions are considered in connection with inertial confinement fusion (ICF) experiments where the hydrodynamic stability of ablative flows has been identified as a key issue to the achievement of thermonuclear burn. Inherently unsteady, these flows are compressible, highly nonuniform with a steep heat front, and bounded by a material surface and a shock front — features that are possible sources of non-modal thermo-acoustics effects. Non-modal effects are presently exhibited on a particular ablation wave solution. This finding raises the question of the existence and consequences of such effects in configurations of X-ray driven ablation that are more representative of ICF experiments, which is the object of an ongoing investigation.

Mots clefs : écoulement d'ablation, fusion par confinement inertiel, compressible, conduction non-linéaire de chaleur, effets non-normaux, méthode direct adjoint, perturbations optimales

Introduction

The hydrodynamic stability of laser-driven ablation flows is a key issue in inertial confinement fusion (ICF) where a sufficiently symmetric implosion of a spherical pellet is expected to achieve thermonuclear burn. Such flows which originate from exposing the pellet outer shell to a growing incident heat flux, present the radial structure of an inward-propagating deflagration, or 'ablation', wave: a shock front precedes a subsonic heat front that coincides with the leading edge of the heated material expansion wave [4, chap. 2] [5, vol. 2, chap. 10, §8]. Inherently unsteady, these flows are compressible, strongly accelerated and highly nonuniform with a steep heat front, owing to the strong nonlinearity of the heat transport and the intense incident heating.

At the early stage of an ICF implosion, the hot outer part of the shell is accelerated toward inner colder and denser layers while the forerunning shock front propagates inward through the shell. This 'shock transit phase' is favourable to ablative Richtmyer–Meshkov and ablative Rayleigh–Taylor instabilities [4, chap. 8],[6]. Hydrodynamic instabilities emerging during this phase seed the subsequent stages of the pellet implosion with perturbations. In particular, perturbations seeded at the start of the acceleration phase of an implosion undergo severe growth, as shown by many studies on the subject, possibly leading to unacceptable loss of symmetry and a failure to achieve the condition of thermonuclear burn. The understanding of hydrodynamic perturbation dynamics during the shock transit phase is therefore of primary importance to ICF.

Perturbations may arise from various sources: external pressure or heat flux inhomogeneities, outer surface defects, inhomogeneities inside the shell or roughness at the shell-fuel interface. Due to this multiplicity, experiments and multiple–physics simulations are often focused on isolating a particular perturbation (i.e. outer surface roughness) for a single pattern (e.g. Legendre mode). In such cases simulations have been found to be in good agreement with experiments [7, 8]. However this way of proceeding gives poor results when dealing with 'native roughness' targets [7, 9]. Indeed, in such cases, in which no perturbation initially dominates the others, the isolated mode approach fails to render perturbation growth originating from interaction between different perturbation modes. Furthermore, such growth may occur despite the fact that each of these interacting modes could be decaying in time. Perturbation amplification computations can describe such growth provided that they are started from appropriate initial conditions. However it is not feasible to compute the amplification of a sufficiently large set of eligible initial conditions in order to identify which of them lead to an amplification, and, above all, to the *maximum amplification*. As formalized in [10], the information driving the short time evolution of a dynamical system must be searched in the eigenfunctions of its linearized evolution operator rather than merely in this operator eigenvalues which may only be indicative of the system long time behaviour. The set of method and tools for obtaining this information is known as non-modal ananlysis and has been successfully applied to many linear and nonlinear problems in the field of hydrodynamic stability (see [11] and references therein). Non-modal analysis enables the study of these eigenfunctions and the identification of optimal perturbations leading to the maximum amplification at a given time, or optimal boundary conditions when dealing with a receptivity problem. Non-modal analysis has never been applied to the hydrodynamic stability of ablation flows and the present work aims at changing this fact.

We first (§ 2) present the ablation wave modeling that we are using before introducing base flow and linear perturbation equations. An adjoint problem is then established (§ 3) from the Lagrangian based formulation of a linear perturbation optimization problem. This adjoint problem allows us to set up a direct-adjoint looping procedure in order to reach an optimal inital condition maximizing a functional depending on perturbations. Such a procedure is applied to a particular case of ablation flow (§ 4), exhibiting non-modal effects. These results are finally discussed (§ 5), together with perspectives for radiation driven ablation flows.

Model

Classically in ICF, hydrodynamic instabilities have been investigated either by multiple-physics simulations, either by modal stability analyses of idealized ablation flows (i.e. steady, quasi-isobaric, discontinuous, etc.) [12]. An alternative to these two opposite approaches uses self-similar solutions to the Euler equations with nonlinear heat conduction as base flows [13, 14, 15]. Such solutions, known since [16], present the advantage of rendering exactly nonuniformity and unsteadiness of ablation waves, and have been exploited to model ICF-type ablation flows [17, 18, 3]. Indeed these self-similar flows present the essential characteristics of an ablation wave, namely: (a) a leading shock front, (b) a quasi-isentropic compression ('post-shock') region, (c) an ablation layer and (d) an expansion wave where heat-condution dominates (the 'conduction region'). The present non-modal stability analysis is based on these self-similar solutions which are in slab symmetry. This slab approximation is reasonable insofar as the shock transit phase corresponds to the beginning of a target implosion: curvature effects for sufficiently small perturbation transverse wavelengths and convergence effects are actually negligible.

Governing equations

We consider the motion of a polytropic gas in a semi infinite slab subject to an irradiation flux and material pressure at its external boundary. The external irradiation flux is sufficiently high so that nonlinear heat conduction dominates any other diffusive effect (e.g. viscosity). However the fluid temperature is sufficiently low for radiation pressure and radiation energy to be negligible compared to material pressure and internal energy. The material is considered at local thermodynamic equilibrium, allowing us to use a fluid model to describe its motion. Assuming that this motion is along the x direction of Cartesian system of coordinates (O, x, y, z), the equation of motion are written, in dimensionless form and in the Lagrangian coordinate m, where $\mathrm{d}m = \rho \mathrm{d}x$, as [18]

$$\begin{cases} \partial_t 1/\rho - \partial_m v = 0, \\ \partial_t v + \partial_m p = 0, \\ \partial_t (e + v^2/2) + \partial_m (pv + \varphi) = 0, \end{cases} \tag{1}$$

where ρ, v, p , e denote, respectively, the fluid density, velocity, pressure and specific internal energy, and the heat flux is related to the fluid density and temperature T through the expression

$$\varphi = -\rho^{-\mu} T^{\nu} \rho \partial_m T \equiv \Psi(\rho, T, \partial_x T), \quad -\mu \leq 0, \quad \nu > 0. \tag{2}$$

This system is closed by the dimensionless equation of state

$$p = \rho T,$$
$$e = \frac{T}{\gamma - 1}, \text{ with } \gamma \text{ the adiabatic gas exponent.}$$

Self-similar reductions of (1) arise if the incident heat flux and pressure at the external surface follow specific power laws [16, 13], namely

$$\varphi(0, t) = \mathcal{B}_\phi t^{3\alpha - 3} \text{ , } p(0, t) = \mathcal{B}_p t^{2\alpha - 2}, \text{ for } t > 0, \text{ with } \alpha = \frac{2\nu - 1}{2\nu - 2}, \tag{3}$$

and for an initial state given by $(\rho, v, T) = (1, 0, 0)$ for $m \geq 0$. For certain values of the boundary parameters $(\mathcal{B}_p, \mathcal{B}_\varphi)$, such solutions present the features of an ablation wave extending from the flow external surface ($m = 0$) through an ablation front up to the fore-running shock front [3, 18]. In particular, all the peculiarities of an ablation wave driven by a nonlinear heat conduction are described in a smooth manner, without any further approximation, including the temperature and density stratification of the conduction region. In the present case, highly accurate solutions to (1), (3) are obtained by means of an adaptive multidomain Chebyshev spectral method [20].

Linear perturbations

Three-dimensional linear perturbations of the above self-similar ablative waves are considered using an Eulerian description in the coordinate system (m, y, z). The resulting system of partial differential equations in physical space is replaced by a one-dimensional system in the yz-Fourier space. With the notation $\widehat{f}$ for the yz-Fourier component of the base flow quantity

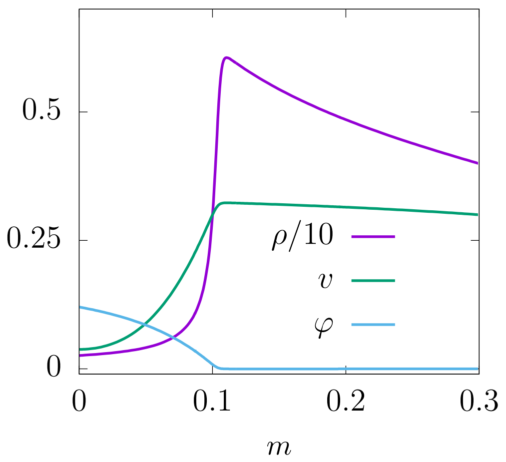

Figure 1: Self-similar ablation wave for the electron heat conduction model of Spitzer [19] $(-\mu = 0, \nu = 5/2)$ and boundary condition parameters $(\mathcal{B}_p, \mathcal{B}_\phi) = (0.124, 0.120)$ of (1). Spatial profiles in the coordinate m at time $t_0 = 1$ of the fluid density ρ, longitudinal velocity v and heat flux φ.

f with transverse wavenumber $k_\perp = \sqrt{k_x^2 + k_y^2}$, this system reads

$$\partial_t \widehat{\mathbf{U}} = L\widehat{\mathbf{U}} \equiv -\mathsf{A}\partial^2_{m^2}\widehat{\mathbf{U}} - \mathsf{B}\partial_m\widehat{\mathbf{U}} - \mathsf{C}\widehat{\mathbf{U}} \,, \tag{4}$$

with $\widehat{\mathbf{U}} = \left[\widehat{\rho}\; \widehat{v}\; \widehat{d}_\perp\; \widehat{T}\right]^\top$, where $\widehat{d}_\perp$ denotes the Fourier component of the transverse divergence of the transverse velocity, and with the matrices A, B and C defined by

$$\mathsf{A} = \begin{pmatrix} 0 & 0 & 0 & 0 \\ 0 & 0 & 0 & 0 \\ 0 & 0 & 0 & 0 \\ 0 & 0 & 0 & C_v^{-1}\,\rho\,\Psi_{T'} \end{pmatrix}, \quad \mathsf{B} = \begin{pmatrix} 0 & \rho^2 & 0 & 0 \\ T & 0 & 0 & \rho \\ 0 & 0 & 0 & 0 \\ C_v^{-1}\,\Psi_\rho & C_v^{-1}\,p & 0 & B_{44} \end{pmatrix},$$

$$\mathsf{C} = \begin{pmatrix} \rho\partial_m v & \rho\partial_m\rho & \rho & 0 \\ T\partial_m\rho/\rho & \rho\partial_m v & 0 & \partial_m\rho \\ k_\perp^2 T/\rho & 0 & 0 & -k_\perp^2 \\ C_{41} & \rho\partial_m T' & C_v^{-1} T & C_{44} \end{pmatrix},$$

$$B_{44} = C_v^{-1}\left[\partial_m(\rho\Psi_{T'}) + \Psi_T\right], \quad C_{41} = C_v^{-1}\left(\partial_m\Psi_\rho - \rho^{-1}\,\partial_m\varphi\right),$$
$$C_{44} = C_v^{-1}\,\left[\rho\partial_m v + \partial_m\Psi_T - k_\perp^2\rho^{-1}\,\Psi_{T'}\right].$$

The longitudinal perturbation of the heat flux expands as $\widehat{\varphi}_x = \widehat{\rho}\,\Psi_\rho + \widehat{T}\,\Psi_T + \rho\Psi_{T'}\partial_m\widehat{T}$ where Ψ_ρ, Ψ_T and $\Psi_{T'}$ stands for the partial derivatives of Ψ (2) with respect to the density, the temperature and the temperature gradient. Similarly, the transverse perturbation of the heat flux expands as $\nabla_\perp \cdot \widehat{\varphi}_\perp = k_\perp^2\,\Psi_{T'}\,\widehat{T}$.

The external surface and shock front are also perturbed and their linear deformations are denoted $\widehat{X}_{\mathrm{es}}(t)$ and $\widehat{X}_{\mathrm{sf}}(t)$, respectively. Perturbed boundary conditions arise from a first order expansion of (3) [14] between the mean position of the boundary surface and its perturbed position. At the external surface, perturbations in density and heat flux are imposed:

$$\widehat{\rho}_{\rm es}(t) = \widehat{\rho}(0,t) + \widehat{X}_{\rm es}(t)\rho(0,t)\partial_m\rho|_{m=0}\,, \tag{5a}$$

$$\widehat{\varphi}_{\rm es}(t) = \widehat{\varphi}(0,t) + \widehat{X}_{\rm es}(t)\rho(0,t)\partial_m\varphi|_{m=0}\,, \tag{5b}$$

and the following kinematic relation at this material surface applies

$$\widehat{v}_{\rm es}(t) = \dot{\widehat{X}}_{\rm es}(t) = v(0,t) + \widehat{X}_{\rm es}(t)\rho(0,t)\partial_m v|_{m=0} \tag{5c}$$

At the shock front, Rankine–Hugoniot relations are perturbed to the first order and take the form of four linear equations relating flow perturbations at the shock front, to shock front deformation $\widehat{X}_{\rm sf}$, shock front deformation velocity $\dot{\widehat{X}}_{\rm sf}$, and to the upstream state perturbation, say

$$RH\left(\widehat{\mathbf{U}}_{\rm sf-}, \widehat{X}_{\rm sf}, \dot{\widehat{X}}_{\rm sf}, \widehat{\mathbf{U}}_{\rm sf+}\right) = 0. \tag{6}$$

System (4) is composed of a parabolic scalar subequation stemming from the total energy conservation, and a hyperbolic subsystem corresponding to the equations of isothermal gas dynamics. Therefore (4) is incompletely parabolic [21] and the problem (4)-(6) is well-posed if at each boundary: one boundary condition is applied on the parabolic subequation and one boundary condition is applied on each of the incoming waves of the hyperbolic subsystem. For $a =$'es' and 'sf', boundary condition operators are formalized as

$$BC_a^h\left(\widehat{U}|_a, \widehat{X}_a\right) = 0,$$
$$BC_a^p\left(\widehat{U}|_a, \widehat{X}_a\right) = 0,$$

where BC_a^p is a scalar operator and the dimension of BC_a^h equals the number of incoming waves at the given boundary.

Optimal perturbations through a Lagrangian

In the present work we are interested in finding the initial states $\{\widehat{\mathbf{U}}(t_0,m), \widehat{X}_{\rm es}(t_0), \widehat{X}_{\rm sf}(t_0)\}$ maximizing an objective functional $\mathcal{J}$ depending only on the final state $\{\widehat{\mathbf{U}}(T,m), \widehat{X}_{\rm es}(T), \widehat{X}_{\rm sf}(T)\}$, where $\{\widehat{\mathbf{U}}, \widehat{X}_{\rm es}, \widehat{X}_{\rm sf}\}$ are solutions of (4)-(6) where $\widehat{\rho}_{\rm es}$ and $\widehat{\varphi}_{\rm es}$ are kept to zero. For this purpose we choose to perform the optimization in an unconstrained space through the definition of a Lagrangian where Lagrange multipliers are introduced to enforce evolution equations, boundary conditions and a constraint on the initial conditions. This Lagrangian reads

$$\begin{aligned}\mathcal{L}(\widehat{\mathbf{U}},\, \widehat{X},\, \widehat{\mathbf{U}}^\dagger,\, \widehat{\boldsymbol{\nu}}^\dagger,\, \widehat{\eta}^\dagger,\, \widehat{\mu}^\dagger,\, \beta^\dagger) = &\\ \mathcal{J} - \int_{m=0,t=t_0}^{m_{\rm sf},T} \widehat{\mathbf{U}}^\dagger \left(\partial_t\widehat{\mathbf{U}} - L(\widehat{\mathbf{U}})\right) {\rm d}t{\rm d}m - \int_{t_0}^{T} \widehat{\boldsymbol{\nu}}_a^\dagger BC_a^h {\rm d}t &\\ - \int_{t_0}^{T} \widehat{\eta}_a^\dagger BC_a^p {\rm d}t - \int_{t_0}^{T} \widehat{\mu}_a^\dagger f_a {\rm d}t - \beta^\dagger\left(\mathcal{I} - K_0\right), &\quad (7)\end{aligned}$$

where subscripts a are summed over boundaries: 'es' and 'sf'. Scalar quantities f_a stand for the evolution equations of $\widehat{X}_a$, taken from (5) and (6), and K_0 is the normalization constant

Lagrange multiplier	Corresponding constraint
$\widehat{\mathbf{U}}^\dagger$	Evolution equation for perturbations
$\widehat{\boldsymbol{\nu}}_{\mathrm{es}}^\dagger$ and $\widehat{\boldsymbol{\nu}}_{\mathrm{sf}}^\dagger$	Hyperbolic boundary conditions at the external surface and shock front
$\widehat{\eta}_{\mathrm{es}}^\dagger$ and $\widehat{\eta}_{\mathrm{sf}}^\dagger$	Parabolic boundary condition at the external condition and shock front
$\widehat{\mu}_{\mathrm{es}}^\dagger$ and $\widehat{\mu}_{\mathrm{sf}}^\dagger$	Evolution equation for boundary deformations
$\beta^\dagger$	Normalization of the initial condition

Table 1: Lagrange multipliers used in (7).

for initial conditions. Lagrange multipliers used in (7) are defined in Tab. 1.

The normalization functional $\mathcal{I}$ depends only on the initial state t_0 and may differ from the objective functional $\mathcal{J}$. The optimum lies in the stationary points of the Lagrangian [22]. Differentiating with respect to the state variables leads to the adjoint problem

$$\partial_t \widehat{\mathbf{U}}^\dagger = L^\dagger \widehat{\mathbf{U}}^\dagger \equiv \mathbf{A}^\top \partial_m^2 \widehat{\mathbf{U}}^\dagger + (2\,\partial_m \mathbf{A} - \mathbf{B})^\top \partial_m \widehat{\mathbf{U}}^\dagger + (\partial_m^2 \mathbf{A} - \partial_m \mathbf{B} + \mathbf{C})^\top \widehat{\mathbf{U}}^\dagger, \tag{8a}$$

$$BC_a^{h\,\dagger} = 0, \quad BC_a^{p\,\dagger} = 0, \tag{8b}$$

$$\mathrm{d}_t \widehat{X}_a^\dagger = \dot{\widehat{X}}_a^\dagger, \tag{8c}$$

where $\dot{\widehat{X}}_a^\dagger$ and $\widehat{X}_a^\dagger$ are scalar linear combinations of $\widehat{\boldsymbol{\nu}}_a^\dagger$, $\widehat{\eta}_a^\dagger$ and $\widehat{\mu}_a^\dagger$. The adjoint problem (8a) is to be integrated backward in time, from a terminal condition, to be well posed. The terminal condition reads

$$\widehat{\mathbf{U}}^\dagger(T, m) = \nabla_{\widehat{\mathbf{U}}|_T} \mathcal{J}, \tag{9a}$$

$$\widehat{X}_a^\dagger(T) = \nabla_{\widehat{X}_a|_T} \mathcal{J}. \tag{9b}$$

Differentiating with respect to the control parameter, $\widehat{\mathbf{U}}(t_0, m), \widehat{X}_a(t_0)$, gives the optimality conditions. Away from an optimum we have

$$\nabla_{\widehat{\mathbf{U}}|_{t_0}} \mathcal{L} = \widehat{\mathbf{U}}^\dagger|_{t_0} - \beta^\dagger \nabla_{\widehat{\mathbf{U}}|_{t_0}} \mathcal{I}, \tag{10a}$$

$$\nabla_{\widehat{X}_a|_{t_0}} \mathcal{L} = \widehat{X}_a^\dagger|_{t_0} - \beta^\dagger \nabla_{\widehat{X}_a|_{t_0}} \mathcal{I}. \tag{10b}$$

At an optimum, the right-hand-sides in (10) vanish. Solving (4) and (8), along with (5) and (10), simultaneously would require a global approximation over the time interval, resulting in a resource intensive procedure. Classically, direct and adjoint problems are solved iteratively, using forward and backward temporal integrations, from a given starting initial condition. Successive initial conditions of the direct problem are found thanks to an iterate power method [23] or a relaxation method [24]. Both methods give similar results. Numerical solutions to the direct system (4)-(6) and to the adjoint system (8), with proper initial conditions, are obtained, in the variable m, using the same multidomain pseudospectral method as for the base flow and, in time, with a three-step implicit-explicit Runge–Kutta scheme. Boundary conditions are handled using a penalty method while matching conditions at subdomain interfaces are enforced exactly. The numerical codes for the direct and adjoint problems perform computations over

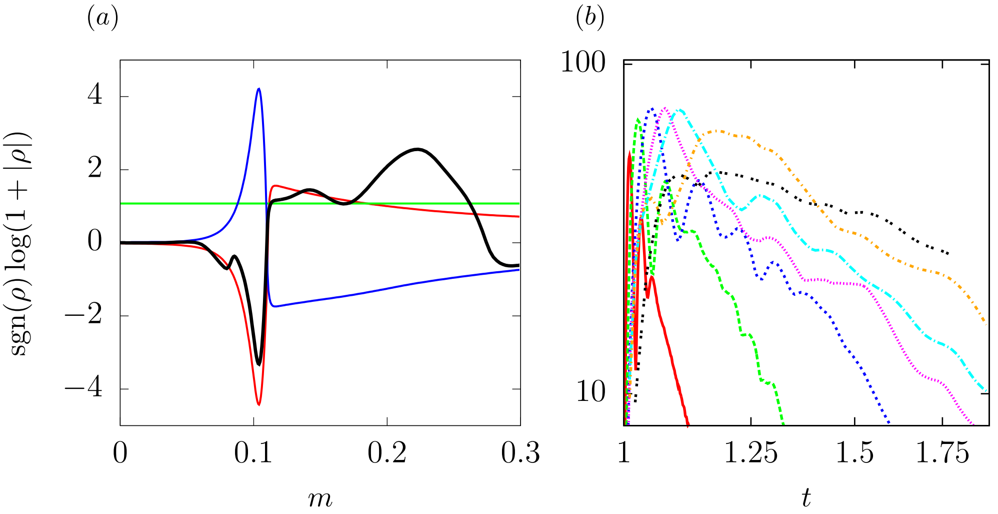

Figure 2: (a) Density perturbation profiles of the starting initial conditions given by (thick lines): a translation of the base flow (red), a uniform perturbed state (green) and a perturbed state resulting from a previous external heat flux perturbation (blue). Common optimal initial density profile (thick black line) for a final time $T = 2$. (b) Objective functional for final times $T = 1.01$, 1.025, 1.05, 1.075, 1.1, 1.2 and 1.6, from bottom to top, for $k_\perp = 0.1$.

each subdomain in parallel using the MPI paradigm with a single process per subdomain.

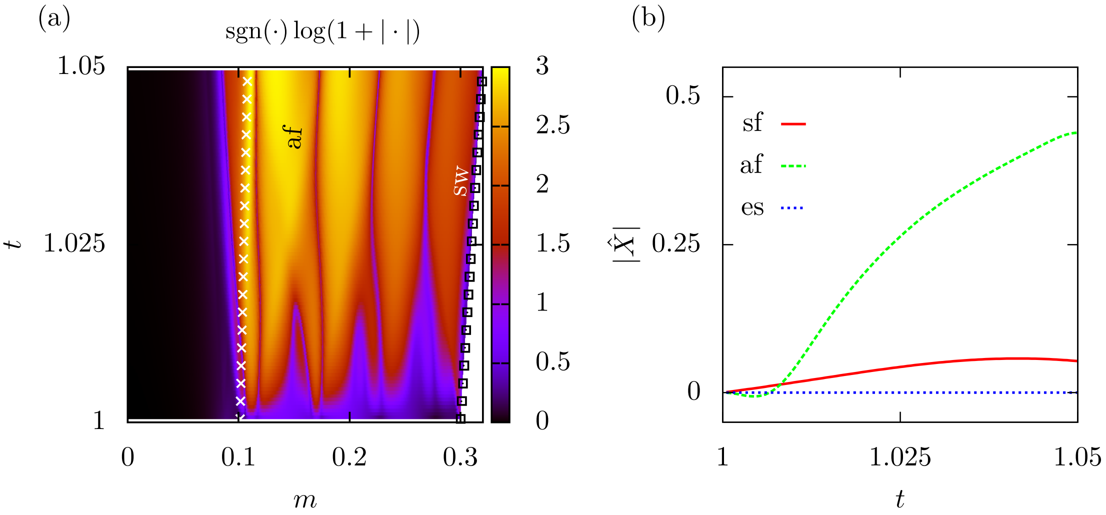

Figure 3: (a) Intensity map in the variables (m, t) of the local Euclidean norm of the solution to (4) with optimal initial condition for final time $T = 1.05$ and $k_\perp = 0.1$. (b) Time evolution of the deformations of the external surface (blue), the ablation front (green) and the shock front (red).

Optimal perturbation of a particular ablation flow

We consider the case of an ablation flow resulting from the direct illumination of the target by a laser. In that case the irradiation flux corresponds to the laser light, propagating in the expanding material up to the critical surface where the density exceeds a critical value. This critical surface corresponds, in our model, to the external surface of the ablation flow where the laser energy is deposited and a material pressure is applied. Heat is transported *via* electron heat conduction [5, chap. VII, §12]. Base flow profiles are shown on Fig. 1. The ablation front is defined as the location of the temperature gradient length minimum. The latter defines the characteristic length of the ablation front, $l_{\mathrm{af}}(t)$. The conduction region, of length $l_{\mathrm{cond}}(t)$, extends from the external surface ($m = 0$) up to the ablation front ($m_{\mathrm{af}} = 0.1013$), and the quasi-isentropic post-shock region extends from the ablation layer up to the shock front ($m_{\mathrm{sf}} = 0.3$). Lengths scale as $l(t) = t^{\alpha} L$ due to self-similarity, where L is a reduced length (Tab. 2).

max M	0.37
$M\|_{\mathrm{af}}$	0.13
$Fr\|_{\mathrm{af}}$	2.07
L_{cond}	$1.013\,10^{-1}$
L_T/L_{tot}	$2.66\,10^{-2}$

Table 2: Main characteristics of the ablation flow of Fig. 1: maximum of the flow Mach number relative to the ablation front, max M, ablation front value of this Mach number, $M|_{\mathrm{af}}$, and of the Froude number, $Fr|_{\mathrm{af}}$, heat conduction region reduced length, L_{cond}, and ratio of the reduced ablation front characteristic length L_T to the ablation wave reduced length L_{tot} (defined in [3]).

Computations have been carried out for various transverse wavenumbers and we present here the results for $k_{\perp} = 0.1$. The objective functional is chosen as the L_2 norm of state variables, namely

$$\mathcal{J} = \frac{1}{2}\int_0^{m_{\mathrm{sf}}} \widehat{\mathbf{U}}^2(T,m)\mathrm{d}m + \frac{1}{2}\left(\widehat{X}_{\mathrm{es}}^2(T) + \widehat{X}_{\mathrm{sf}}^2(T)\right). \tag{11}$$

The convexity of this functional with respect to our set of control parameter is not established. However a numerical experiment shows that initiating the optimization procedure with three different initial conditions leads to the same optimal condition (Fig. 2a). Computations are carried out on a 20 domain grid, each domain containing 50 collocation points. An iteration is composed of the integration of (4) from t_0 to T and (8a) backward, and requires $7\,10^5$ time steps for $T = 4$. Convergence is reached when the L_2 norm of the difference between two successive initial conditions is below a defined threshold (10^{-5}). Reaching convergence requires between 20 and 30 iterations depending on the final time.

At first, optimal initial conditions are obtained for final times ranging from 1.01 to 1.6. The envelope of their L_2 norm across time shows that maximum amplification occurs at $T = 1.05$ (Fig. 2b). It has been observed that perturbations behave like travelling waves, here termed pseudo-characteristic waves, with reflection and coupling at the external surface, the shock front and in the ablation layer. Such pseudo-characteristic waves have been found appropriate for describing perturbations propagating in the conduction region and the post-shock region of ablation flows [3, 25] and their nature is recalled in Tab. 3. Optimal initial conditions and their evolution up to the optimal time are analysed by characterizing them in terms of these longitudinal pseudo-characteristic waves.

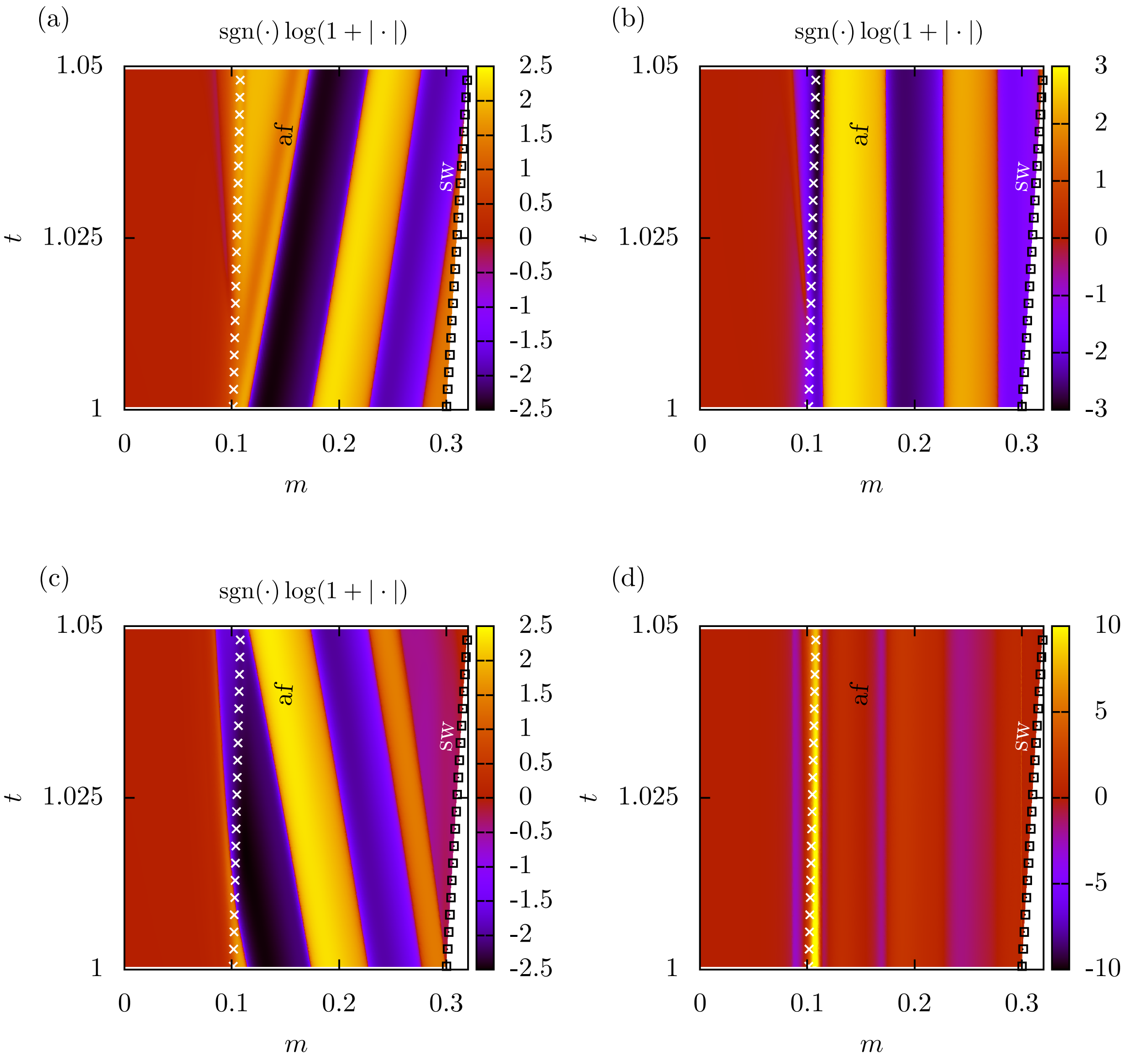

Figure 4: Projection on pseudo-characteristic variables defined in Tab. 3 of the solution to (4), for $T = 1.05$ and $k_\perp = 0.1$, in the variables (m, t): (a) $\widehat{\mathcal{W}}_1$, (b) $\widehat{\mathcal{W}}_2$, (c) $\widehat{\mathcal{W}}_3$ and (d) $\widehat{\omega}/\rho$.

Maximum amplification The optimal initial condition realizing the maximum amplification, at $T = 1.05$, is projected onto the pseudo-characteristic waves described in Tab. 3. This initial condition is very weak in the conduction region, presents a peak in the ablation layer and two oscillations over the post-shock region corresponding to: in phase upstream and downstream propagating acoustic waves, and, in opposite phase, an entropy wave (Fig. 4). Perturbations mainly evolve in the post-shock region and the ablation layer (Fig. 3a). Indeed, the final time is too short, relatively to propagation velocities, for a significant propagation of perturbations. As a result the external surface remains unperturbed while the ablation front and the shock front undergo distortions (Fig. 3b). Moreover, heat diffusion is negligible in the post-shock region and its effects in the ablation layer is much weaker than wave couplings. The present transient growth is therefore mainly due to local constructive interactions between pseudo-characteristic waves (Fig. 4) rather than interactions between the different regions of the flow through such waves. Maximum amplification occurs while the upstream, downstream acoustic and entropy

Wave	*conduction region*	*post-shock region*
$\widehat{\mathcal{W}}_1$	Heat conductivity	quasi-isentropic acoustic
$\widehat{\mathcal{W}}_2$	quasi-isothermal acoustic	quasi-entropy
$\widehat{\mathcal{W}}_3$	Downstream quasi-isothermal acoustic	Downstream quasi-isentropic acoustic
$\widehat{\omega}/\rho$	Vorticity	Vorticity

Table 3: Definition of the pseudo-characteristic waves used for analysing flow perturbations.

waves are superimposed and in phase (Fig. 4a, b and c), in addition to the arrival of the main contribution of vorticity at the ablation front (Fig. 4d).

As noted, maximum amplification occurs at a final time, $T = 1.05$, for which only local effects act and non-local effects do not have time to develop. However, the shock transit phase of an actual ICF target may last much longer than this maximum amplification time. Indeed, during this phase, the external surface, ablation front and shock front may interact several times *via* travelling waves and heat diffusion across the conduction and post-shock regions. Hence, non-local effects should arise in addition to local interactions and it is of interest to determine the optimal initial condition for such a regime.

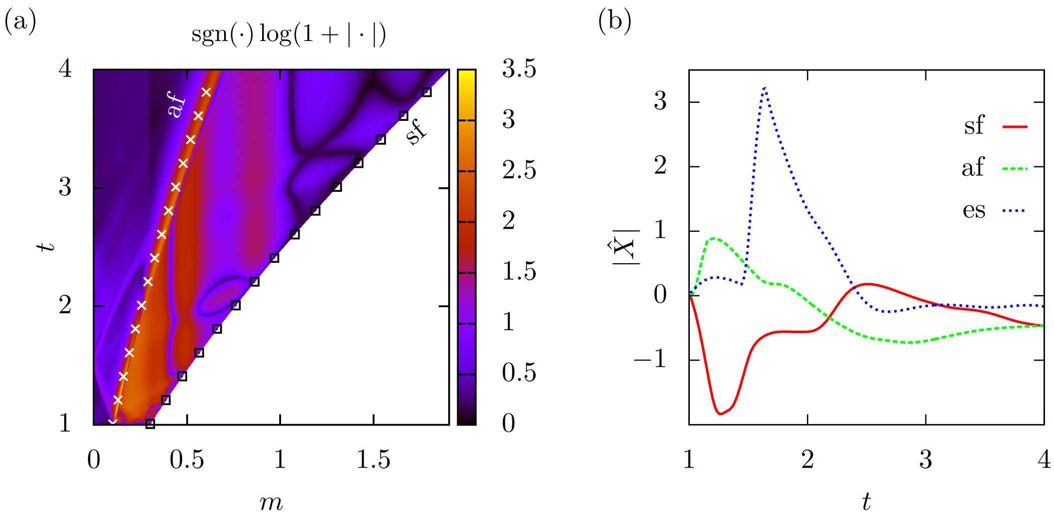

Figure 5: Intensity map in the variables (m, t) of the local Euclidean norm of the solution to (4) with optimal initial condition for final time $T = 4$ and $k_\perp = 0.1$. (b) Time evolution of the deformations of the external surface (blue), the ablation front (green) and the shock front (red).

Amplification at the time horizon of the shock transit phase The terminal time is chosen to be consistent with the duration of a shock transit phase. Simulations have shown that during this phase a few interactions between the shock front and the ablation front occur through acoustic and entropy/vorticity waves. Here, the value of $T = 4$ satifies this condition (Fig. 6a, b and c). As for the maximum amplification case, the present optimal initial condition displays higher levels in the post-shock region than in the conduction region although initial perturbations in this region are no longer negligible. The same arrangement of acoustic and entropy waves is observed in the post-shock region but over a single spatial lobe. In the conduction region, the optimal initial condition is dominated by acoustic waves. External surface and shock front deformations undergo strong transient growth each time travelling waves interact with them, before relaxing to lower absolute values (Fig. 5b). At the final time, much of the contribution to the functional $\mathcal{J}$ lies in the ablation layer and in the entropy perturbations that propagate in the post-shock region (Fig. 5a). Regarding interfaces, most of the contribution comes front the shock front deformation rather than the external surface deformation. We note that the optimal response for $T = 4$ reaches a maximum at a smaller time than the terminal time. The amplification of the ablation front deformation relatively to its initial value is $2.2\,10^2$ at its maximum and $1.1\,10^2$ at the final time. Such final time amplification indicates that the ablation front could remain strongly deformed at the end of the shock transit phase. This would bring a significant seed for ablative Rayleigh–Taylor instabilities to develop during a subsequent acceleration stage of an ICF implosion.

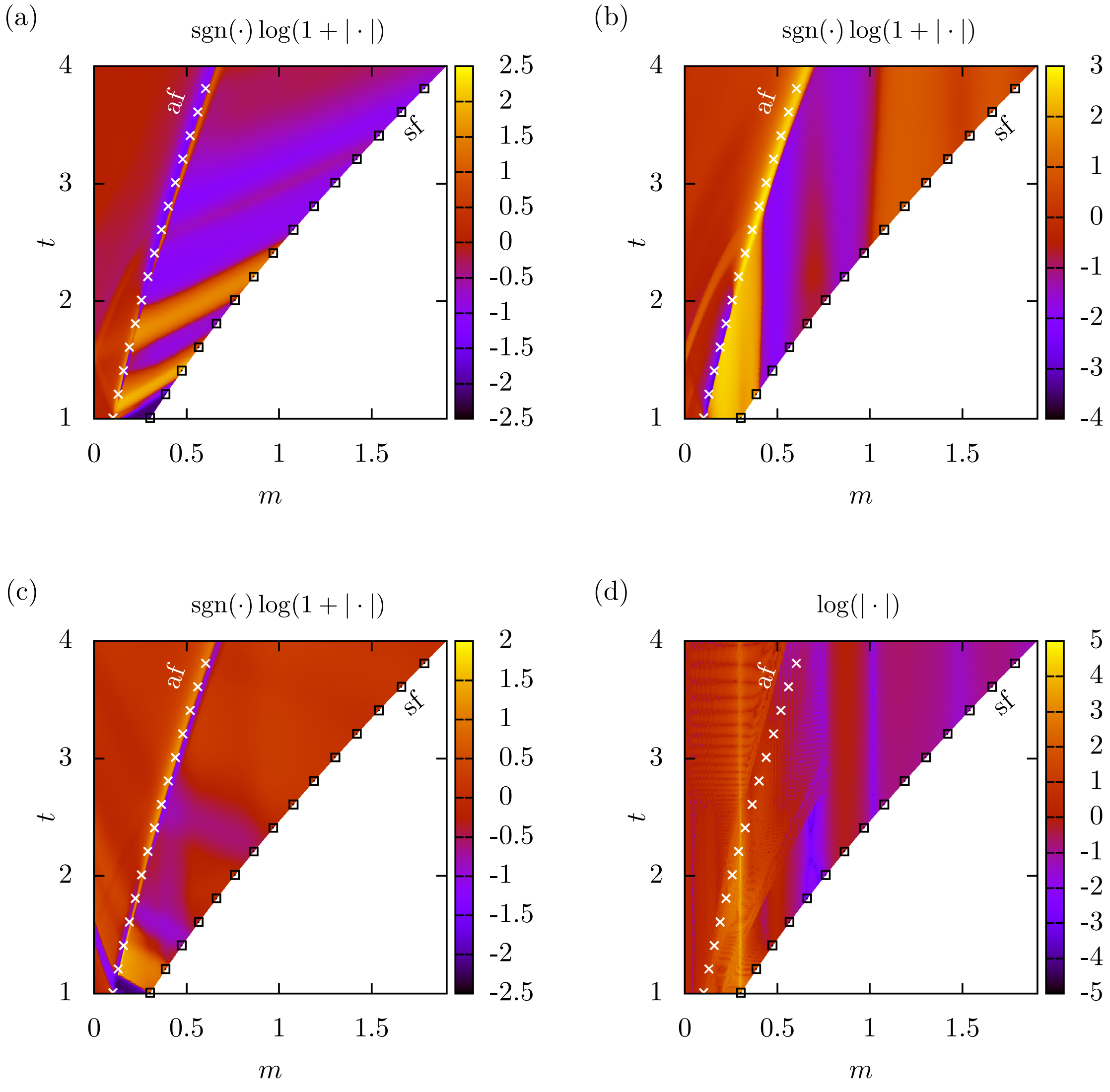

Figure 6: Projection on pseudo-characteristic variables defined in Tab. 3 of the solution to (4), for $T = 4$ and $k_\perp = 0.1$, in the variables (m, t): (a) $\widehat{\mathcal{W}}_1$, (b) $\widehat{\mathcal{W}}_2$, (c) $\widehat{\mathcal{W}}_3$ and (d) $\widehat{\omega}/\rho$.

Discussion and conclusion

In the present work, we carry out the first non-modal stability analysis of an ablation flow. These flows are compressible, non uniform, non stationary and present steep gradients, owing to nonlinear heat conduction, and moving boundaries. A Lagrangian based formulation of the optimization of linear perturbations and boundary deformations is devised. Optimal initial conditions are computed thanks to a direct-adjoint looping. This method is applied to a particular configuration for which we have exhibited significant transient growth for various time horizons. These results prove the existence of non-modal effects in ablation waves, which may be of concern to ICF experiments. They entice us to carry out a systematic non-modal analysis of ICF-like ablation flows driven by X-ray irradiation.

Optimal perturbation computations of radiation driven ablation flows presenting characteristic features of ICF target implosions are ongoing, but they are numerically more demanding. Indeed, such flows present much steeper ablation fronts: as a comparison, their ratio of characteristic lengths (see Tab. 2) range from 10^{-3} to 10^{-5}. This necessarily leads to refined meshes and smaller time steps. As a result, between 10^6 to 10^8 time steps are required for a single direct-adjoint iteration. We believe that, similarly to electron heat conduction results presented in this paper, convergence would be reached within 20 to 30 iterations.

We also expect to find similar local interactions for short-time optimal initial conditions, and non local interactions for optimal initial conditions corresponding to shock transit times of radiation driven ablation flows. Various objective functionals will be tested, corresponding to energy norms (i.e. acoustic, rotational or total energy) or observables (i.e. optical depth or ablation front deformations).

References

[1] K. Wieczorek, C. Sensiau, W. Polifke, and F. Nicoud. Assessing non-normal effects in thermoacoustic systems with mean flow. *Phys. Fluids*, 23, 2011.

[2] F. Nicoud, L. Benoit, C. Sensiau, and T. Poinsot. Acoustic modes in combustors with complex impedances and multidimensional active flames. *AIAA Journal, American Institute of Aeronautics and Astronautics*, 45(2):426–441, 2007.

[3] J.-M. Clarisse, J.-L. Pfister, S. Gauthier, and C Boudesocque-Dubois. A hydrodynamic analysis of self-similar radiative ablation flows. *J. Fluid Mech.*, 848:219–255, 2018.

[4] S. Atzeni and J. Meyer-ter-Vehn. *The physics of inertial fusion.* Oxford University Press, Oxford, U.K., 2004.

[5] Ya. B. Zel'dovich and Yu. P. Raizer. *Physics of shock waves and high-temperature hydrodynamic phenomena.* Academic Press, New-York, 1967.

[6] Y. Aglitskiy, A. L. Velikovich, M. Karasik, N. Metzler, S. T. Zalesak, A. J. Schmitt, L. Phillips, J. H. Gardner, V. Serlin, J. L. Weaver, and S. P. Obenschain. Basic hyrdodynamics of Richtmyer–Meshkov-type growth and oscillations in the inertial confinement fusion-relevant conditions. *Phil. Trans. R. Soc. A*, 368:1739–1768, 2010.

[7] K. S. Raman et al. An in flight radiography platform to measure hydrodynamic instability growth in inertial confinement fusion capsules at the national ignition facility. *Phys. Plasmas*, 21, 2014.

[8] J. L. Peterson, D. T. Casey, O. A. Hurricane, K.S. Raman, H.F. Robey, and V.A. Smalyuk. Validating hydrodynamic growth in national ignition facility implosions. *Phys. Plasmas*, 22, 2015.

[9] V. A. Smalyuk, S. V. Weber, D. T. Casey, D. S. Clark, J. E. Field, S. W. Haan, B. A. Hammel, A. V. Hamza, D. E. Hoover, O. L. Landen, A. Nikroo, H. F. Robey, and C. R. Weber. Hydrodynamic instability growth of three-dimensional, "native-roughness" modulations in x-ray driven, spherical implosions at the National Ignition Facility. *Phys. Plasmas*, 22:072704, 2015.

[10] L. N. Trefethen, A. E. Trefethen, S. C. Reddy, and T. A. Driscoll. Hydrodynamic stability without eigenvalues. *Science*, 261:578–584, 1993.

[11] P. Luchini and A. Bottaro. Adjoint equations in stability analysis. *Annu. Rev. Fluid Mech.*, 46(1):493–517, 2014.

[12] V. Bychkov, M. Modestov, and C. K. Law. Combustion phenomena in modern physics: I. Inertial confinement fusion. *Prog. Energy Combust. Sci.*, 47:32–59, 2015.

[13] F. Abéguilé, C. Boudesocque-Dubois, J.-M. Clarisse, S. Gauthier, and Y. Saillard. Linear perturbation amplification in self-similar ablation flows of inertial confinement fusion. *Phys. Rev. Lett.*, 97:035002, 2006.

[14] J.-M. Clarisse, C. Boudesocque-Dubois, and S. Gauthier. Linear perturbation response of self-similar ablative flows relevant to inertial confinement fusion. *J. Fluid Mech.*, 609:1–48, 2008.

[15] V. Lombard, S. Gauthier, J.-M. Clarisse, and C. Boudesocque-Dubois. Kovásznay modes in stability of self-similar ablation flows of ICF. *Europhys. Lett.*, 84:25001, 2008.

[16] R. Marshak. Effect of radiation on shock wave behavior. *Phys. Fluids*, 1(1):24–29, 1958.

[17] J. Sanz, A. R. Piriz, and F. G. Tomasel. Self-similar model for tamped ablation driven by thermal radiation. *Phys. Fluids B*, 4(3):683–692, 1992.

[18] C. Boudesocque-Dubois, S. Gauthier, and J.-M. Clarisse. Self-similar solutions of unsteady ablation flows in inertial confinement fusion. *J. Fluid Mech.*, 603:151–178, 2008.

[19] J. Duderstadt and G. Moses. *Inertial confinement fusion.* Wiley-Interscience, 1982.

[20] C. Boudesocque-Dubois, V. Lombard, S. Gauthier, and J.-M. Clarisse. An adaptive multidomain Chebyshev method for nonlinear eigenvalue problems: Application to self-similar solutions of gas dynamics equations with nonlinear heat conduction. *J. Comput. Phys.*, 235:723–741, 2013.

[21] J. C. Strikwerda. Initial boundary value problems for incompletely parabolic systems. *Commun. Pure Appl. Math.*, XXX:797–822, 1977.

[22] M. D. Gunzburger. Introduction into mathematical aspect of flow control and optimization. In von Karman Institute for Fluid Dynamics, editor, *Lecture Series 1997-05 on Inverse Design and Optimisation Methods.* April 1997.

[23] P. Corbett and A. Bottaro. Optimal perturbations for boundary layers subject to streamwise pressure gradient. *Phys. Fluids*, 12(1):120–130, 2000.

[24] Y. Duguet, A. Monokrousos, L. Brandt, and D. S. Henningson. Minimal transition thersholds in plane couette flow. *Phys. Fluids*, 25, 2013.

[25] G. Varillon, J.-M. Clarisse, and A. Couairon. Investigation of supersonic heat-conductivity linear waves in ablation flows. In *EPS Plasma Physics Conference*, Prague, Czech Republic, July 2018.

CHAPTER C

Additional information about numerical methods

C.1 Stability of the penalty method for the hyperbolic part of the boundary conditions

Starting from the penalized evolution equation for perturbations (3.53), the objective of the present section is to determine values of the penalty weights τ_{es} and τ_{sf} necessary to ensure that the L_2 norm of the spectral approximation of the solution decays in time. The derivation assumes a steady uniform base flow. The terms resulting from the Fourier transformation in the transverse direction are assumed as already stabilized before the Fourier transform (§ 3.2). Therefore the present derivation focuses on the sole advection term in the longitudinal direction: $\mathbf{B}\partial_\xi \widehat{\mathbf{U}}$. We follow the work of Hesthaven and Gottlieb (1996); Gottlieb and Shu (1996). The penalty method is used to apply boundary conditions only on the explicit step of the time integration, namely

$$\partial_t \widehat{\mathbf{U}} = \widehat{\mathbf{F}},$$

containing only non-conducting terms (3.58). As a consequence we focus on the terms forming $\widehat{\mathbf{F}}$, i.e. without taking into consideration the matrix $\mathbf{A}$ and coefficient $(\mathbf{C})^{\perp}_{44}$ in the evolution operator $\mathbf{L}_\pi$ (3.53). Although there exists no formal proof of stability in the case of unsteady nonuniform base flows, our numerical experiments in such cases do not display signs of numerical instability.

The evolution equation (3.28) is considered in the eigenvector basis of the matrix $\mathbf{B}$ (see 3.37, in which the primitive variable $\widehat{\mathbf{U}}$ is transformed into the characteristic variable $\widehat{\mathcal{W}} = \mathbf{R}^{-1}\widehat{\mathbf{U}}$.

As we are interested in the stability of the spectral approximation of the solution to (3.53), $\widehat{\mathbf{U}}_N$, defined at collocation points ξ_k, the dirac function δ_{es} (respectively δ_{sf}) is approximated by a polynomial of degree lower than N whose value is 1 at ξ_{es} (resp. ξ_{sf}) and zero at the other collocation points. We define the discrete weighted inner product at collocation points ξ_k

$$\langle \boldsymbol{u}_N, \boldsymbol{v}_N \rangle_N = \sum_{k=0}^{N} \boldsymbol{u}_N(\xi_k)^\top \boldsymbol{v}_N(\xi_k)\omega_k, \quad \text{for } \boldsymbol{u}_N \text{ and } \boldsymbol{v}_N \text{ polynomials of order} < N, \tag{C.1}$$

where ω_k are Legendre weights (Canuto et al., 1988), and its associated discrete weighted norm $\|\boldsymbol{u}_N\|_N$. Let us consider $\widehat{\mathcal{W}}_N$ a Legendre spectral approximation of the solution to (3.53) in the characteristic basis of $\mathbf{B}$. Following the reasoning of Hesthaven and Gottlieb (1996) and Gottlieb and Shu (1996), we look for values of τ_a such that $\mathrm{d}_t\|\widehat{\mathcal{W}}_N\|_N^2 \leq 0$ for zero homogeneous conditions. From (3.53) we obtain

$$\frac{\mathrm{d}}{\mathrm{d}t}\left\|\widehat{\mathcal{W}}_N\right\|_N^2 = \left\langle (\mathbf{R}^{-1}\,\mathbf{L}\,\mathbf{R}\widehat{\mathcal{W}})_N, \widehat{\mathcal{W}}_N \right\rangle_N + \left\langle \widehat{\mathcal{W}}_N, (\mathbf{R}^{-1}\,\mathbf{L}\,\mathbf{R}\widehat{\mathcal{W}})_N \right\rangle_N + \mathcal{B}$$

with boundary terms gathered in

$$\mathcal{B} = \omega_0\left(\left\langle \mathbf{R}^{-1}\,\widehat{\mathbf{\Pi}}_N^{\mathrm{es}}, \widehat{\mathcal{W}}_N|_{\mathrm{es}} \right\rangle + \left\langle \widehat{\mathcal{W}}_N|_{\mathrm{es}}, \mathbf{R}^{-1}\,\widehat{\mathbf{\Pi}}_N^{\mathrm{es}} \right\rangle\right) + \omega_N\left(\left\langle \mathbf{R}^{-1}\,\widehat{\mathbf{\Pi}}_N^{\mathrm{sf}}, \widehat{\mathcal{W}}_N|_{\mathrm{sf}} \right\rangle + \left\langle \widehat{\mathcal{W}}_N|_{\mathrm{sf}}, \mathbf{R}^{-1}\,\widehat{\mathbf{\Pi}}_N^{\mathrm{sf}} \right\rangle\right). \tag{C.2}$$

The collocation points $\{\xi_k\}_{0\leq k\leq N}$ are obtained from a coordinate transformation $\xi = h(\zeta)$ (3.49) applied to the set of $N+1$ Gauss-Lobatto points $\{\zeta_k :\ -1 \leqslant \zeta_k \leqslant 1\}$. For the sake of the present derivation the transformation h is assumed to be an affine function. The expression of $\mathbf{R}^{-1}\,\mathbf{L}\,\mathbf{R}$ leads to

$$\begin{aligned}\frac{\mathrm{d}}{\mathrm{d}t}\left\|\widehat{\mathcal{W}}_N\right\|_N^2 = &-\left\langle \left(\frac{1}{h'}\mathbf{D}\partial_\zeta\widehat{\mathcal{W}}\right)_N, \widehat{\mathcal{W}}_N \right\rangle_N \\ &-\left\langle \widehat{\mathcal{W}}_N, \left(\frac{1}{h'}\mathbf{D}\partial_\zeta\widehat{\mathcal{W}}\right)_N \right\rangle_N \\ &+\mathcal{B}.\end{aligned} \tag{C.3}$$

The discrete inner product is now implicitly defined at the collocation point ζ_k, as well as the spectral approximation $\widehat{\mathcal{W}}_N$.

For g_N a Legendre polynomial function of degree lower than N, the quadrature defined by (C.1) is exact (Canuto et al., 1988), i.e.

$$\int_{-1}^{1} g_N(\zeta)\omega d\zeta = \sum_{k=0}^{N} g_N(\zeta_k)\omega_k. \tag{C.4}$$

This property is central to spectral methods. Applying the quadrature rule to (C.3), and performing an integration by parts on the first term in (C.3) gives

$$\begin{aligned}\frac{\mathrm{d}}{\mathrm{d}t}\left\|\widehat{\mathcal{W}}_N\right\|_N^2 = &\int_{-1}^{1}\frac{1}{h'}\left(\widehat{\mathcal{W}}^\top\mathbf{D}^\top\partial_\zeta\widehat{\mathcal{W}}_N - \widehat{\mathcal{W}}^\top\mathbf{D}\partial_\zeta\widehat{\mathcal{W}}\right)_N\mathrm{d}\zeta \\ &-\left[\frac{1}{h'}\left\langle \mathbf{D}\widehat{\mathcal{W}}_N, \widehat{\mathcal{W}}_N \right\rangle\right]_{-1}^{1} \\ &+\mathcal{B}.\end{aligned} \tag{C.5}$$

The first right hand side cancels as $\mathbf{D}$ is diagonal. The expansion of $\mathcal{B}$ gives

$$\begin{aligned}\frac{\mathrm{d}}{\mathrm{d}t}\left\|\widehat{\mathcal{W}}_N\right\|_N^2 = &-\left[\frac{1}{h'}\left\langle \mathbf{D}\widehat{\mathcal{W}}_N, \widehat{\mathcal{W}}_N \right\rangle\right]_{-1}^{1} \\ &+2\omega_0\tau_{\mathrm{es}}\left\langle \mathbf{D}_{\mathrm{es}}^{+}\widehat{\mathcal{W}}_N|_{-1}, \widehat{\mathcal{W}}_N|_{-1} \right\rangle \\ &+2\omega_N\tau_{\mathrm{sf}}\left\langle \mathbf{D}_{\mathrm{sf}}^{-}\widehat{\mathcal{W}}_N|_{1}, \widehat{\mathcal{W}}_N|_{1} \right\rangle.\end{aligned} \tag{C.6}$$

Therefore, the condition $\mathrm{d}_t \|\widehat{\mathcal{W}}_N\|^2 \leq 0$ is fulfilled if

$$\left\langle \left(\frac{1}{h'(-1)} \mathbf{D} + 2\omega_0 \tau_{\mathrm{es}} \mathbf{D}^{+}_{\mathrm{es}} \right) \widehat{\mathcal{W}}_N|_{-1}, \widehat{\mathcal{W}}_N|_{-1} \right\rangle \leq 0, \tag{C.7}$$

and

$$\left\langle \left(\frac{-1}{h'(1)} \mathbf{D} + 2\omega_N \tau_{\mathrm{sf}} \mathbf{D}^{-}_{\mathrm{sf}} \right) \widehat{\mathcal{W}}_N|_{1}, \widehat{\mathcal{W}}_N|_{1} \right\rangle \leq 0, \tag{C.8}$$

or equivalently

$$\tau_{\mathrm{es}} \leq \frac{1}{2\omega_0\, h'(-1)}, \tag{C.9a}$$

$$\tau_{\mathrm{sf}} \geq \frac{1}{2\omega_N\, h'(1)}, \tag{C.9b}$$

so that $\pi_{\mathrm{a}} = 1/(4\,h'(\pm 1))$ in (3.54). If the approximation $\widehat{\mathbf{U}}_N$ is formed of Legendre polynomials, then $\omega_0 = \omega_N = 2/N(N+1)$, and (C.9) corresponds to the results of Hesthaven and Gottlieb (1996).

Penalty method for Chebyshev approximations of ablation flows. Ablation flows considered in the present work are neither uniform nor approximated by Legendre polynomials. Moreover, the coordinate transformation that is used is not an affine function (3.49). However we have found that the bounds for the penalty coefficients in (C.9) are sufficient to stabilize the Chebyshev approximation of acoustic perturbations in a uniform base flow, with the identity transformation for h. The introduction of the penalty terms in (3.53) does not degrade the convergence properties, in space and time, of the approximation.

The same stability features are recovered when dealing with actual ablation flows with a coordinate transformation of the form (3.49). One of the reasons is that, for an optimal grid, the coordinate transformation (3.49) remains close to an affine transformation, combining a shift and a stretching of the subdomain. The stability of the penalty method is observed on numerical experiments with non-uniform base-flows, i.e. for non-zero $\mathbf{C}$. This point is a consequence that close to boundaries, where penalty terms are enforced, the base flow is quite uniform. Therefore contributions are still dominated by the advection terms, stabilized by the penalty method, rather than by the reaction terms of the matrix $\mathbf{C}$.

C.2 Critical time step

As the system (3.28) contains an advective contribution solved explicitly, it is necessary to determine the critical time step that ensures the stability of the discrete time scheme. Section (C.1) gives a sufficient stability condition for the time-continuous and spatially discretized system. In the present section, we investigate stability conditions for the explicit part of the time-discretized system, namely (3.58)

$$\partial_t \widehat{\mathbf{U}} = \widehat{\mathbf{F}}. \tag{C.10}$$

For the derivation, we step back to the evolution equations (3.19) the coordinate system (m, y, z, t). The coordinate transformation $(m, y, z, t) \to (\xi, y, z, t)$ is applied to the system (3.19). Retaining only the terms forming $\widehat{\mathbf{F}}$, i.e.

non-conducting terms, the resulting system is vector shaped and reads

$$\partial_t \tilde{\mathbf{u}} + \mathbf{B}\partial_\xi \tilde{\mathbf{u}} + \mathbf{B}_\perp \partial_\perp \tilde{\mathbf{u}} + \mathbf{C}_\parallel \tilde{\mathbf{u}} = 0, \quad \tilde{\mathbf{u}} = \begin{pmatrix} \tilde{\rho} & \tilde{v}_x & \tilde{v}_\perp & \tilde{T} \end{pmatrix}^\top. \tag{C.11a}$$

with

$$\mathbf{B}_\perp = \begin{pmatrix} 0 & 0 & \bar{G} & 0 \\ 0 & 0 & 0 & 0 \\ t^{2\alpha-2}\dfrac{\bar{\Theta}}{\bar{G}} & 0 & 0 & 1 \\ 0 & 0 & t^{2\alpha-2}C_v^{-1}\bar{\Theta} & 0 \end{pmatrix} \tag{C.11b}$$

We consider an advection mechanism whose wave velocity, advection velocity and spatial step in the direction i are denoted by c_i, v_i and Δ_i, respectively, for $i = \xi$ and $\perp$. Following Courant et al. (1928), we know that a numerical scheme updating an information propagating at finite velocity is stable if the numerical domain of dependence includes the physical domain of dependence. For a two-step finite difference method of second order accuracy, MacCormack (1971) state that the solution is stable if

$$\Delta t \leqslant \alpha_{\mathrm{CFL}} \min_D \frac{1}{\frac{|v_\xi|}{\Delta x} + \frac{|v_\perp|}{\Delta_\perp} + \sqrt{c_\xi^2/\Delta\xi^2 + c_\perp^2/\Delta_\perp^2}}, \tag{C.12}$$

where α_{CFL} is a constant. The criterion (C.12) is adapted to pseudo-spectral discretization (Guillard et al., 1992):

$$\Delta t \leqslant \alpha_{\mathrm{CFL}} \min_D \frac{1}{\frac{|v_\xi|}{K_\xi} + \frac{|v_\perp|}{K_\perp} + \sqrt{(c_\xi/K_\xi)^2 + (c_\perp/K_\perp)^2}}, \tag{C.13}$$

where K_ξ and $K_\perp$ are empirically determined, and account for the dimension in the longitudinal and transverse directions, the degree of polynomial approximation in these dimensions, the discretization scheme and the type of boundary conditions (Dirichlet or Neumann). If a coordinate transformation $\xi = h(\zeta)$ is applied in the longitudinal direction, then:

$$\partial_\xi u = \frac{\partial u}{\partial \zeta}\frac{\mathrm{d}\zeta}{\mathrm{d}\xi} = \frac{\partial u}{\partial \zeta}\frac{1}{h'(\zeta)}. \tag{C.14}$$

The local wave speed and advection velocity are modified by a factor $1/h'(\zeta)$ (Gauthier, 2011).

In our case, the transverse advection velocity is zero and the longitudinal advection velocity is $-\alpha\xi/t$. To adapt the one-dimensional framework presented above to the multidimensional system (C.11), we set the longitudinal and transverse wave speeds to be the largest eigenvalues of $\mathbf{B}$'s and $\mathbf{B}_\perp$, respectively. Following the approach of Guillard et al. (1992), we define a critical time step as

$$\Delta t_c = \min_{ij} \frac{1}{\dfrac{\alpha\xi_i t^{-1}}{|h_i'|K_\xi} + \sqrt{\left(\dfrac{\max \mathrm{sp}\{\mathbf{B}\}_{ij}}{|h_i'|K_\xi}\right)^2 + \left(\dfrac{\max \mathrm{sp}\{\mathbf{B}_\perp\}_{ij}}{K_\perp}\right)^2}}, \tag{C.15}$$

where i and j span the longitudinal and transverse grid, respectively. In what follows the j dependence is omitted as the base flow is uniform in the transverse direction.

Wavespeeds. The eigenvalues of $\mathsf{B}_\perp$ are determined analytically:

$$\mathrm{sp}\{\mathsf{B}_\perp\} = \left\{0, 0, -t^{\alpha-1}\sqrt{\gamma\bar{\Theta}}, t^{\alpha-1}\sqrt{\gamma\bar{\Theta}}\right\}, \quad \text{so that} \quad \max \mathrm{sp}\{\mathsf{B}_\perp\}_i = t^{\alpha-1}\sqrt{\gamma\bar{\Theta}_i} = t^{\alpha-1}c_i. \tag{C.16}$$

The eigenvalues of B (3.28c) are determined numerically.

Transverse Fourier transformation. In the present case (C.11) is Fourier transformed in the transverse direction. The inequality $\lambda_\perp \geqslant 2L_\perp/N_\perp$, with the transverse domain length $L_\perp$ and the number of interpolation points $N_\perp$, must hold for a suitable representation of all transverse wavelengths. As the only wavelength to be represented is $\lambda_\perp = 2\pi/k_\perp$, the most restrictive case is to choose $L_\perp/N_\perp = \pi/k_\perp$. Criterion (C.15) rewrites

$$\Delta t_c = \min_{ij} \frac{1}{\dfrac{\alpha \xi_i t^{-1}}{|h_i'|K_\xi} + t^{\alpha-1}\sqrt{\left(t^{1-\alpha}\dfrac{\max \mathrm{sp}\{\mathsf{B}\}_{ij}}{|h_i'|K_\xi}\right)^2 + \left(c_i \dfrac{k_\perp}{2\pi K_\perp^F}\right)^2}}, \tag{C.17}$$

with $K_\perp^F$ a constant determined latter.

Determination of constants K_ξ and $K_\perp^F$. Stability results are obtained for a time-discretized form of the scalar advection equation

$$\partial_t u + c\partial_\xi u = 0, \quad \text{with } c \text{ a constant}, \tag{C.18}$$

by means of a three-step non degenerate Runge-Kutta explicit scheme. Let $\mathcal{D}$ be the finite dimension approximation of the spatial differential operator $\partial_\xi \cdot$ and λ an eigenvalue of $c\mathcal{D}$. The stability condition for such a scheme is (Boudesocque-Dubois et al., 2003)

$$\left|\sum_{i=0}^{3} \frac{(-\lambda\Delta t)^i}{i!}\right|^2 \leq 1, \quad \text{for all eigenvalues} \quad \lambda. \tag{C.19}$$

- **Fourier discretization**. All eigenvalues are complex in the case of a Fourier differentiation operator (Canuto et al., 1988): $\lambda = i\,c\,k$. Stability condition (C.19) reads

$$\frac{1}{3}\,(k\,c\,\Delta t)^2 - 1 \leq 0 \ \Rightarrow\ \Delta t \leq \frac{\sqrt{3}}{k\,c}\ \forall\, k.$$

  Again, the smallest wavelength possibly represented on the grid is $\lambda_{\min} = 2\,L/N$, so $k_{\max} = \dfrac{2\pi}{\lambda_{\min}} = \dfrac{\pi\,N}{L}$ and

$$\Delta t \leq \frac{\sqrt{3}\,L}{c\,\pi\,N}.$$

  Then, $K_\perp^F$ is defined such that $\Delta t \leq K_\perp^F \dfrac{L}{cN}$, so $K_\perp^F = \dfrac{\sqrt{3}}{2\pi} \approx 0.2757$.

- **Chebychev collocation**. An explicit RK3 scheme has a stability region defined in the complex plane in Peyret (2002). According to Boudesocque-Dubois et al. (2003), if $\lambda\Delta t$ remains in the elliptical region

$$\left(\frac{\Re(\lambda)\,\Delta t}{C_{RK3}^1}\right)^2 + \left(\frac{\Im(\lambda)\,\Delta t}{C_{RK3}^2}\right)^2 \leq 1 \text{ and } \Re(\lambda) \geq 0, \quad \text{with} \quad C_{RK3}^1 \quad \text{and} \quad C_{RK3}^2 \quad \text{two constants},$$

then it fulfils the criterion (C.19). Therefore the stability criterion reads

$$\begin{aligned}
\Delta t \leq & \frac{1}{\sqrt{\left(\frac{\Re(\lambda)}{C^1_{RK3}}\right)^2 + \left(\frac{\Im(\lambda)}{C^2_{RK3}}\right)^2}}, \; \forall\, \lambda \\
\max|\Re(\lambda)| &= |c| \max_j |\Re(d_j)| \\
\max|\Im(\lambda)| &= |c| \max_j |\Im(d_j)|,
\end{aligned}$$

with $\{d_j\}_{j=1,N}$ being eigenvalues of the Chebyshev first-order differential operator penalized for Dirichlet-Dirichlet boundary conditions, or $\mathcal{D}_\pi$, over the domain $[-1;1]$. Values of $\max_j|\Re(d_j)|$ and $\max_j|\Im(d_j)|$ are computed numerically as they depend on the number of points N and the penalty coefficient τ determined in App. C.1. Finally

$$K_\xi = \frac{1}{\sqrt{\left(\frac{\max_j|\Re(d_j)|}{C^1_{RK3}}\right)^2 + \left(\frac{\max_j|\Im(d_j)|}{C^2_{RK3}}\right)^2}}. \tag{C.20}$$

Here the coordinate transformation (3.49) is accounted for in (C.15) and not in the differential operator $\mathcal{D}_\pi$. Therefore the penalty term in $\mathcal{D}_\pi$ must not include the coordinate transformation as $\mathcal{D}$ does not contain the coordinate transformation. An attempt to include the coordinate transform directly in the calculation of K_ξ, i.e. in $\mathcal{D}_\pi$ has been done. It gives similar results, partly because the differential of the coordinate transform $h'(x)$ is quasi-constant on an optimal grid. The choice to work with Chebyshev differential operator $\mathcal{D}_\pi$ over the spectral domain $[-1,1]$ rather than over the physical domain $[0,\xi_{\text{sf}}]$ is motivated by the fact that interior subdomains are thus treated in the same way as the boundary subdomains where penalty terms apply.

CHAPTER D

Verification of the numerical method for the direct equations

D.1 Gas dynamics test-case

The gas dynamics test-case verifies the explicit part of the temporal RK3 scheme (3.58)

$$\partial_t \widehat{\mathbf{U}} = \widehat{\mathbf{F}}, \tag{D.1}$$

which corresponds to the evolution operator of gas dynamics, i.e. (3.28) without heat-conduction. Solutions are sought under the form

$$\widehat{\mathbf{U}}_{\mathrm{sol}} = \widehat{\mathbf{U}}_0 \exp\left[i(\omega t - k_\xi \xi)\right], \tag{D.2}$$

for a stationary and uniform base flow

$$(\bar{G} \quad \bar{V}_x \quad \bar{\Theta}) = (4 \quad 0 \quad 1/3). \tag{D.3}$$

Equation (3.28) with (D.2) boils down to the eigenvalue problem

$$\begin{pmatrix} i\omega & -ik_\xi \bar{G}^2 & \bar{G} & 0 \\ -ik_\xi \bar{\Theta} & i\omega & 0 & -ik_\xi \bar{G} \\ -k_\perp^2 \bar{\Theta}/\bar{G} & 0 & i\omega & -k_\perp^2 \\ 0 & -ik_\xi(\gamma-1)\bar{P} & (\gamma-1)\bar{\Theta} & i\omega \end{pmatrix} \widehat{\mathbf{U}}_0 = \mathbf{0}. \tag{D.4}$$

Non trivial solutions are given by

- $\omega = 0$ of multiplicity two, which yields
  - an entropy mode $\widehat{\mathbf{U}}_{\mathcal{S}} = (-\bar{G} \quad 0 \quad 0 \quad \bar{\Theta})^\top$
  - and a vorticity mode $\widehat{\mathbf{U}}_{\mathcal{V}} = (0 \quad -i \quad \bar{G}k_\xi \quad 0)^\top$,

- and $\omega_{\mathcal{A}+} = c_s\sqrt{k_\xi^2\bar{G}^2 + k_\perp^2} = K_{\mathcal{A}} = -\omega_{\mathcal{A}-}$, with $c_s = \sqrt{\gamma\bar{\Theta}}$, yielding two acoustic modes

$$\widehat{\mathbf{U}}_{\mathcal{A}\pm} = \begin{pmatrix} 1 & \pm\dfrac{k_\xi c_s^2}{K_{\mathcal{A}}} & \mp\dfrac{ic_s^2k_\perp^2}{\bar{G}K_{\mathcal{A}}} & \dfrac{(\gamma-1)\bar{\Theta}}{\bar{G}} \end{pmatrix}^\top . \tag{D.5}$$

A forward acoustic $\widehat{\mathbf{U}}_{\mathcal{A}+}$ signal of wavenumber $k_\xi = 2\pi$ is initiated on a domain $[0,2]$ discretized over 4 subdomains of N points each (N is varied) and evolves over several periods $T = 2\pi/K_{\mathcal{A}}$ with periodic boundary conditions (Fig. D.1 left). As previously noticed (Boudesocque-Dubois et al., 2003), the error increases with the transverse wavenumber $k_\perp$ since $k_\perp$ increases the frequency (Fig. D.1, right). Therefore a finer time step is required to keep the error at the same level for larger $k_\perp$. However, these results acknowledge the fact that the spatial pseudo-spectral scheme combined with the RK3 temporal scheme provide us with a satisfactory description of advection over a large number of periods. The error accumulates steadily with the number of periods. Convergence in space shows that the expected exponential convergence inherent to spectral methods is recovered (Fig. D.2, left). The residual error quickly reaches a lower limit due to the time stepping error. Figure D.2 left shows the efficiency of spectral method as $N_{\text{cheb}} = 16$ points are enough to conveniently describe an acoustic wave with a nine digits accuracy. The third order convergence in time of the RK3 scheme restricted to its purely explicit part is also recovered (Fig. D.2 right).

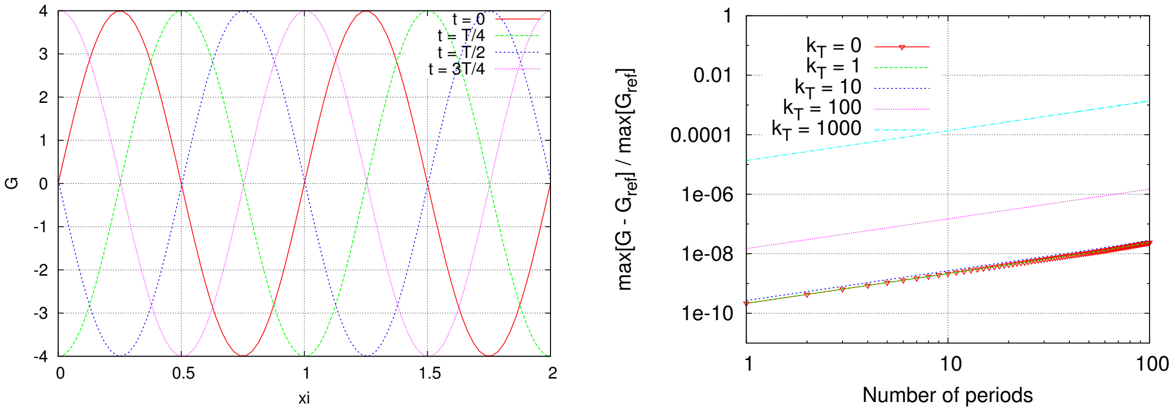

Figure D.1: Gas dynamics. $N_{\text{cheb}} = 32$, time step $\Delta t = 1.62\,10^{-4}$. (left) Density perturbation of the forward acoustic solution (D.2), (right) space maximum relative error in density against the number of periods.

Because boundary conditions are periodic, the above described test-case does not verify the penalty method for boundary conditions on the hyperbolic part. The forward acoustic mode of the form (D.2) can alternatively be enforced at each boundary with the penalty method (§ 3.3.3). The resulting error displays no visible changes compared to the periodic case (Fig. D.3). In particular, the convergence properties in space and time inherent to the pseudo-spectral and RK3 schemes are not altered by the use of the penalty method.

D.2 Heat conduction test-case

The heat conduction test-case verifies the semi-implicit part of the RK3 scheme (3.57). This subequation corresponds to

$$\partial_t\widehat{\Theta} = \lambda_\xi\partial^2_{\xi^2}\widehat{\Theta} + \lambda_\perp\widehat{\Theta}, \quad \text{with} \quad \lambda_\xi = -(\gamma-1)\bar{G}\Psi_{\Theta'} \quad \text{and} \quad \lambda_\perp = (\gamma-1)\frac{k_\perp^2\Psi_{\Theta'}}{\bar{G}}. \tag{D.6}$$

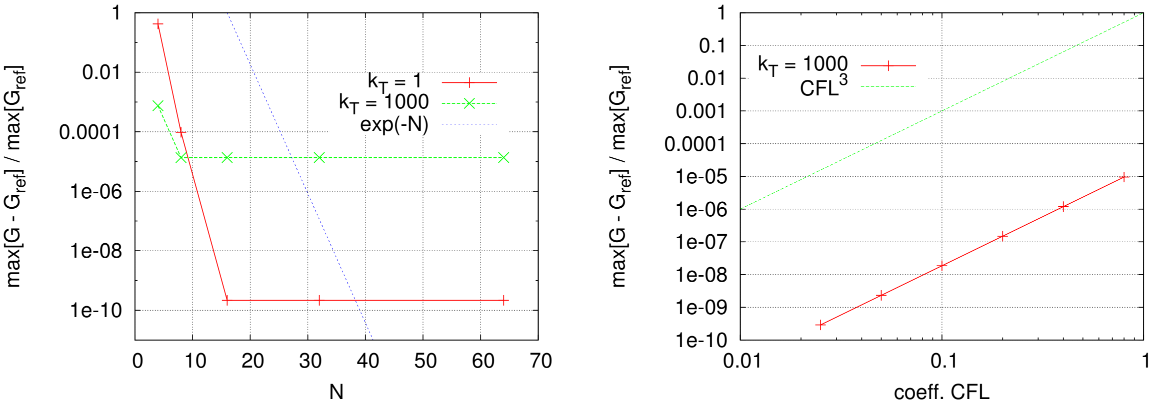

Figure D.2: Gas dynamics. Space maximum relative error in density. (left) Convergence in space for $\Delta t = 5.10^{-5}$, and (right) convergence in time for $N_{\text{cheb}} = 32$ and $\Delta t = CFL \times 5.10^{-5}$.

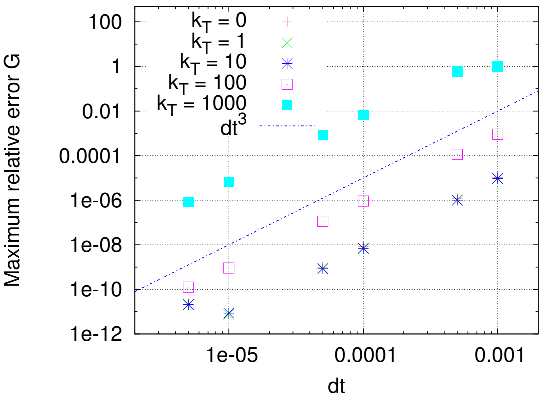

Figure D.3: Gas dynamics. $N_{\text{cheb}} = 32$, convergence in time.

For a stationary and uniform base flow

$$(\bar{G} \quad \bar{V}_x \quad \bar{\Theta}) = (4 \quad 0 \quad 1/3), \tag{D.7}$$

solutions to (D.6) are sought for as separated variable solutions

$$\widehat{\Theta} = f(\xi)g(t) \tag{D.8}$$

with

$$f(\xi) = A\cos(k_\xi \xi) + B\sin(k_\xi \xi) \quad \text{and} \quad k_\xi^2 = -\frac{f''}{f} = \text{const} > 0. \tag{D.9}$$

For Neumann-Neumann homogeneous boundary conditions (i.e. $\partial_\xi \widehat{\Theta} = 0$ at boundaries), non trivial solutions are of the form

$$f(\xi) = B\cos(k_\xi^n \xi), \quad \text{with} \quad (k_\xi^n)^2 = (n + 1/2)\pi/2, \quad \text{for } n \text{ a non zero integer.} \tag{D.10a}$$

Therefore

$$\frac{g'}{g} = \lambda_\xi \frac{f''}{f} + \lambda_\perp = -\lambda_\xi k_\xi^n + \lambda_\perp \tag{D.10b}$$

hence

$$g_n(t) = B_n \exp(-t/\tau_n), \quad \text{with} \quad \tau_n = \frac{1}{\lambda_\xi (n\pi/2)^2 - \lambda_\perp}, \quad n \in \mathbb{N}^*. \tag{D.10c}$$

A solution (D.10) is initiated at $t = 0$ for $n = 1$ on the $[0, 2]$ interval decomposed into 4 subdomains of N points each (Fig. D.4 left). Boundary conditions are enforced at each boundary node. Spatial profiles of the relative error shows that the error remains acceptable for a certain number of characteristic times τ_n. Figures D.5 displays the convergence in space (left) and time (right). With the 'exact' method, the solution is enforced at boundary points (see § 3.3). An implementation of the penalized boundary conditions for the parabolic equation is also tested. However the use of the penalty method strongly alters the performances of the numericals schemes. In particular the convergence in time is not ensured. These poor performances justify our choice to use the 'exact' method to enforce boundary conditions on the parabolic subequation.

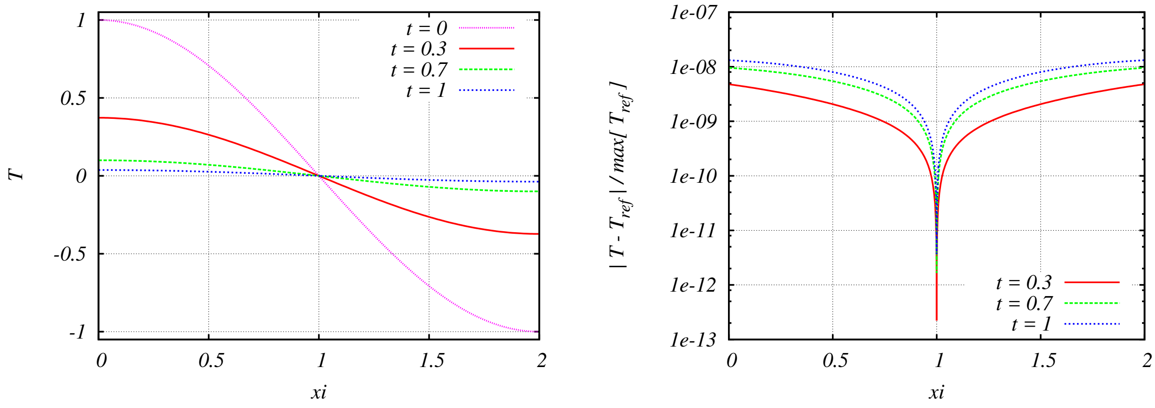

Figure D.4: Heat conduction. $N_{\text{cheb}} = 50$, $\Delta t = 10^{-4}$ and $n = 1$. (left) Evolution of $\widehat{\Theta}$ for $n = 1$ and $k_\perp = 1$ and (right) relative error at different times.

With the 'exact' method, the error converges exponentially in space which is in agreement with the pseudo-spectral scheme. The error converges at order 2 in time, as expected for the semi-implicit part of the RK3 scheme.

D.3 Thermoacoustic test-case

The full RK3 sheme is tested for thermoacoustic solutions of the form

$$\widehat{\mathbf{U}} = \Re\left(\widehat{\mathbf{U}}_0 \exp i \left[\omega t - k_\xi \xi\right]\right), \quad \text{with} \quad k_\xi = 2\pi \quad \text{and } \omega \text{ complex}, \tag{D.11}$$

for a stationary and uniform base flow

$$(\bar{G} \quad \bar{V}_x \quad \bar{\Theta}) = (4 \quad 0 \quad 1/3). \tag{D.12}$$

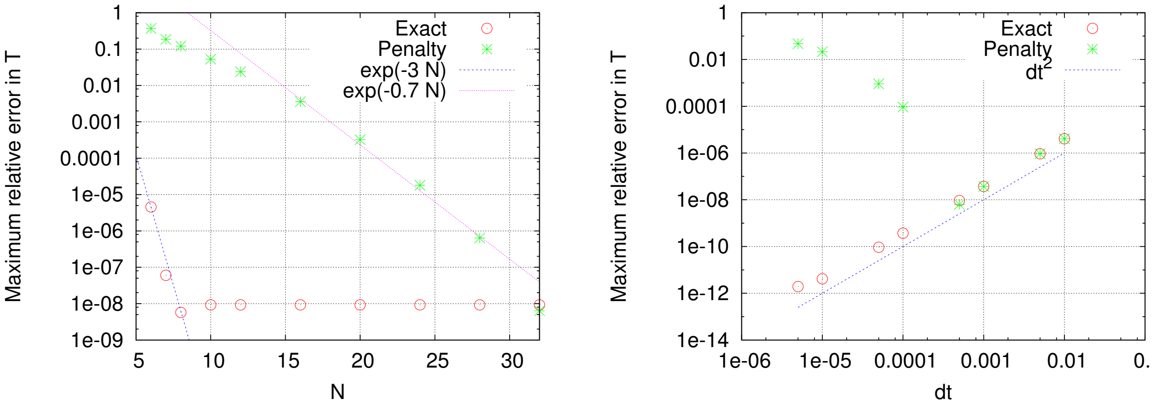

Figure D.5: Heat conduction. Space maximum relative error $n = 1$. (left) Convergence in space for $\Delta t = 5.10^{-4}$ and (right) convergence in time for $N_{\text{cheb}} = 32$.

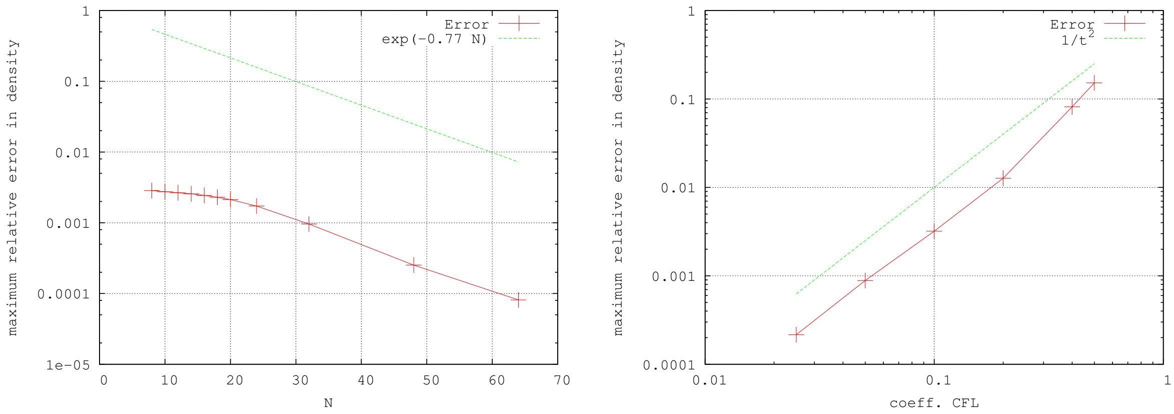

Figure D.6: Thermoacoustic. Maximum relative error in density with $k_\perp = 1$ for the damped forward acoustic perturbation. (left) Convergence in space with $\Delta t = 10^{-5}$ and (right) convergence in time with $N_{\text{cheb}} = 50$.

Equation (3.28) boils down to the eigenvalue problem

$$\begin{pmatrix} i\omega & -ik_\xi \bar{G} & \bar{G} & 0 \\ -ik_\xi \bar{\Theta}/\bar{G} & i\omega & 0 & -ik_\xi \\ -k_\perp^2 \bar{\Theta}/\bar{G} & 0 & i\omega & -k_\perp^2 \\ 0 & -ik_\xi(\gamma-1)\bar{\Theta} & (\gamma-1)\bar{\Theta} & i\omega - (\gamma-1)(k_\xi^2 + k_\perp^2)\Psi_{\Theta'}/\bar{G} \end{pmatrix} \widehat{\mathbf{U}}_0 = \mathbf{0}. \tag{D.13}$$

Eigenvalues and eigenvectors are determined numerically. Non trivial solutions lead to

- two damped acoustic modes, such that $\Re(\omega_{\mathcal{A}+}) > 0$ and $\Re(\omega_{\mathcal{A}-}) < 0$,
- a damped entropy mode, such that $\Re(\omega_S) = 0$,
- and a conserved vorticity mode, such that $\omega_\nu = 0$.

The forward damped acoustic solution ($\Re(\omega_{\mathcal{A}+}) > 0$) is initiated on the interval $[0, 2]$ with periodic boundary conditions, splitted into 4 subdomains of N points each. The exponential convergence in space and second order convergence in time are recovered, as expected for the spatial pseudo-spectral and temporal RK3 schemes, respectively. As for the acoustic test case, errors accumulate faster as the transverse wavenumber $k_\perp$ increases. Indeed,

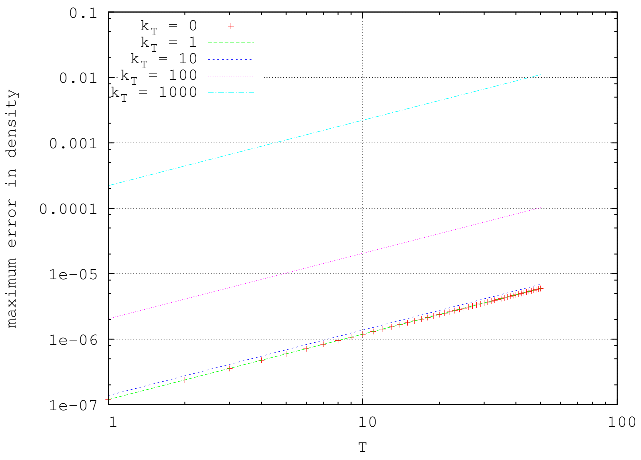

Figure D.7: Thermoacoustic. Maximum error in density for the damped forward acoustic perturbation, with $N_{\text{cheb}} = 50$ and $\Delta t = 10^{-5}$ for various $k_\perp$ against the number of pseudo-period T.

increasing $k_\perp$ reduces the pseudo-period $T = 2\pi/\Re(\omega)$. Therefore, a finer time stepping is required for describing time variations with the same accuracy.

D.4 Munro's rippled shock front

Linearized Rankine–Hugoniot relations (3.42) are verified on the rippled shock problem of Munro (1989). A planar supersonic rippled shock front interact with an upstream perturbed flow, while there is no source of perturbation downstream to the shock front (i.e. in the computational domain).

The flow is assumed to be non-conducting and we consider gas dynamic solutions under the form of (D.2), so that we are addressing the eigenvalue problem (F.4). Similarly, the eigenvalues are

$$\omega = 0, \tag{D.14a}$$

of multiplicity two with eigenvectors detailed in § D.1, and

$$\omega = \omega_{\mathcal{A}\pm} = \pm K_{\mathcal{A}} = \pm c_s \sqrt{k^2_{\xi_{\mathcal{A}}} \bar{G} + k^2_\perp}, \tag{D.14b}$$

yielding upstream and downstream acoustic modes. As the shock front is supersonic and there is no source of perturbation downstream to shock front, the solution is a superposition of an entropy, vorticity and downstream acoustic modes, with wavelengths $k_{\xi_{\mathcal{S}}}$, k_{ξ_ν} and $k_{\xi_{\mathcal{A}}}$, respectively, i.e.

$$\widehat{\mathbf{U}}_0 = \alpha_{\mathcal{S}} \widehat{\mathbf{U}}_{\mathcal{S}} + \alpha_\nu \widehat{\mathbf{U}}_\nu + \alpha_{\mathcal{A}-} \widehat{\mathbf{U}}_{\mathcal{A}-}.$$

Coefficients $\alpha_{\mathcal{S}}$, α_ν and $\alpha_{\mathcal{A}-}$ are determined by applying the linearized Rankine–Hugoniot relation between upstream and downstream perturbation states. The base flow downtream to the shock front is given by

$$\begin{pmatrix} \bar{G} & \bar{V}_x & \bar{\Theta} \end{pmatrix} = \begin{pmatrix} 4 & 0 & 1/3 \end{pmatrix}, \quad \text{corresponding to an upstream state} \quad \begin{pmatrix} \bar{G}^u & \bar{V}^u_x & \bar{\Theta}^u \end{pmatrix} = \begin{pmatrix} 1 & -1 & 0 \end{pmatrix},$$

with an upstream entropy perturbation

$$\left(\widehat{G}^u \quad \widehat{V}_x^u \quad \widehat{D}_\perp^u \quad \widehat{\Theta}\right) = \begin{pmatrix}1 & 0 & 0 & 0\end{pmatrix}.$$

The shock front is located at $m_{\mathrm{sf}} = \bar{G}\bar{U}_x t + m_{\mathrm{sf}}|_{t_0}$, with $\bar{U}_x = \bar{W}_x - \bar{V}_x$ the shock front velocity with respect to downstream fluid velocity and $\bar{W}_x = 1/3$ the shock front velocity in the reference frame. Applying mass conservation at the shock front, i.e. at $m(t) = m_{\mathrm{sf}}$, for all $t > t_0$,

$$k_{\xi_\nu} = k_{\xi_S} = 0 \quad \text{and} \quad \omega_{\mathcal{A}-} + k_{\xi_\mathcal{A}} \bar{G}\bar{U} = 0,$$

where $\omega_{\mathcal{A}-}$ is eliminated with the help of (D.14b),

$$k^2_{\xi_\mathcal{A}} = \frac{-ik_\perp}{\bar{G}\sqrt{1 - \bar{U}^2/c_s^2}}.$$

Therefore the entropy and vorticity perturbations are constant over space and time while the acoustic perturbation is evanescent. From the longitudinal momentum conservation and total energy conservation, it comes that

$$\alpha_S = -2/5, \quad \alpha_\nu = -i \quad \text{and} \quad \alpha_\mathcal{A} = 12/5. \tag{D.15}$$

Shock front deformation is deduced from the transverse momentum conservation

$$\widehat{X}_{\mathrm{sf}} = -\frac{\widehat{d}_\perp}{k_\perp \bar{V}_x^u}. \tag{D.16}$$

The evanescent character of the acoustic solution makes the solution stiffer as time goes on (Fig. D.8 left). At $t = 150$, the solution is ill resolved near the shock front, thus degrading the error on the third domain (Fig.D.8 right) and the error on the shock front deformation (Fig D.9) increase suddenly. Until that time, the dynamics of the shock front is accurately described by perturbed Rankine–Hugoniot relations (3.42) and the evolution equation for the shock front deformation.

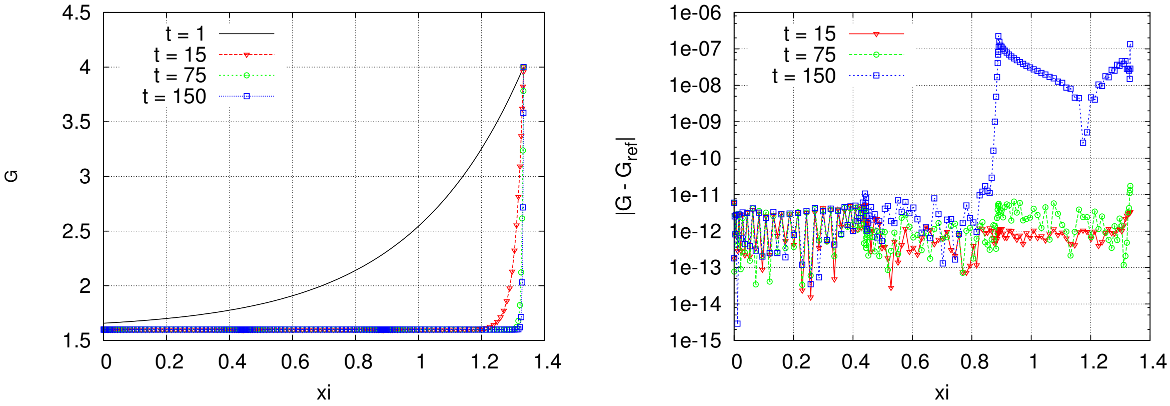

Figure D.8: Munro. (left) Computed density perturbation of Munro's solution and (right) relative error in density in the coordinate $\xi = m/t$. Computation started at $t_0 = 1$ on a grid of 3 subdomains of 50 points each.

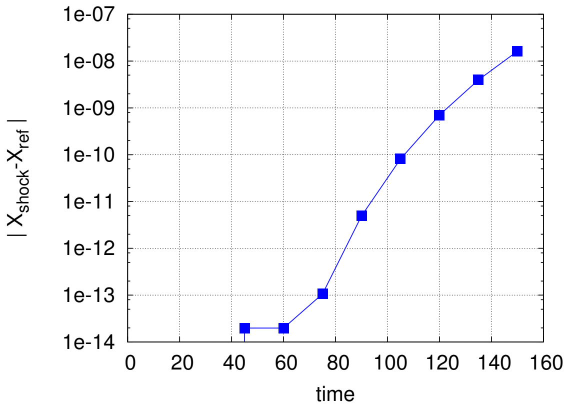

Figure D.9: Munro. Shock front perturbation error. Computation started at $t_0 = 1$ on a grid of 3 subdomains of 50 points each.

D.5 Translation test-case

Evolution equations (3.28) with boundary conditions (3.40) admit an exact solution known as the 'translation solution', defined by (4.35) in the case $k_\perp = 0$ with zero external forcing ($\widehat{\varphi}_{\mathrm{es}} = \widehat{p}_{\mathrm{es}} = 0$ and $\widehat{\mathbf{U}}_u = \mathbf{0}$). According to this solution, state variable perturbations evolve as (4.35) and boundary deformations are steady,

$$\dot{\widehat{X}}_{\mathrm{sf}} = \dot{\widehat{X}}_{\mathrm{es}} = 0. \tag{D.17}$$

Compared to the other test cases, this test verifies the evolution equation for the state variables $\widehat{\mathbf{U}}$ and for the boundary deformations $\widehat{X}_{\mathrm{es}}$ and $\widehat{X}_{\mathrm{sf}}$, on a self-similar ablation wave, i.e. for an unsteady and non-uniform base flow.

The computations are carried out on the ablation wave RC-1, over a grid $(N_{\mathrm{dom}}, N_{\mathrm{cheb}}) = (189, 50)$, and the time step is set by the criterion derived in App. C.2. The time interval is $[1, 3.5]$, corresponding to the largest time interval used for optimization computations of Chap. 4, and represents $9.8\,10^6$ time steps. The present test is challenging for boundary deformations as the exact solution is a zero boundary velocity perturbation. Therefore, any error on the velocity is large relatively to the exact solution. This is what happens with the penalty method. Indeed, this method authorizes a departure of the solution from its set point at boundary nodes. The solution at boundary nodes is used to compute to boundary deformation velocity $\dot{\widehat{X}}_{\mathrm{a}}$. Hence, this departure at boundary nodes pollutes the boundary deformation velocities, which constitutes the right hand side of the evolution equation for boundary deformations (4.15). This inherent error of the penalty scheme is accumulating in the boundary deformations as time steps go on *via* the integration in time of (4.15), and results in an increasing L_2 norm of the error (Fig. D.10).

The use of penalty method for boundary conditions has improved to computation of linear perturbations of ablation wave. However, the accumulation mechanism of the error in the boundary deformations indicates that penalty method, as we have implemented it, may still be improved to deal with these deformations. Two possibilities arise: either modifying the evolution equation for boundary deformations (4.15) to cancel the impact of the penalty method, either computing the boundary deformation velocity from a quantity that is not polluted by the penalty error.

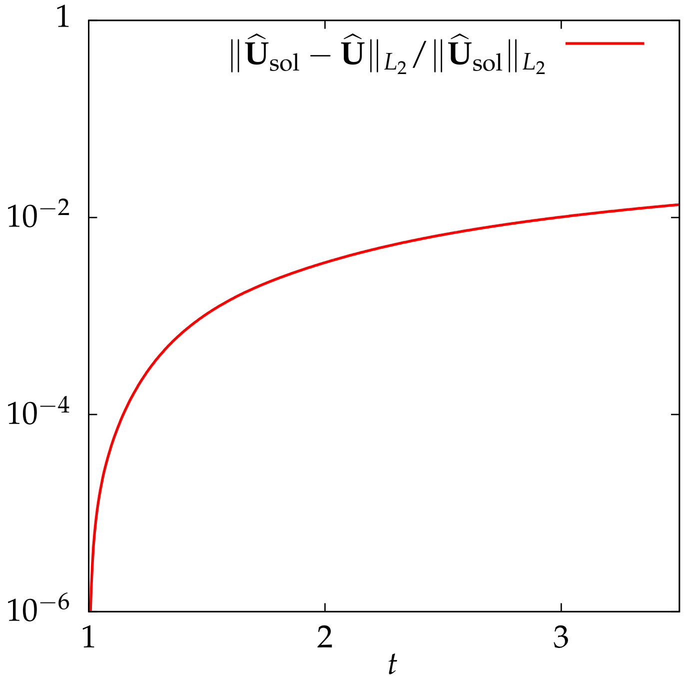

Figure D.10: Translation. Ablation wave RC-1, 189 × 50 points. L_2 norm of the relative error for the 'translation solution' from (4.35).

CHAPTER E

Derivation of the adjoint problem

E.1 Variation of the Lagrange functional

We express the variations of $\mathcal{L}$ (4.16) with respect to the direct variables $(\widehat{\mathbf{U}}, \widehat{X}_{\mathrm{es}}, \widehat{X}_{\mathrm{sf}})$ in the directions $(\delta\widehat{\mathbf{U}}, \delta\widehat{X}_{\mathrm{es}}, \delta\widehat{X}_{\mathrm{sf}})$. The main manipulations consist in replacing operators for boundary conditions and evolution equations by their expressions and performing integrations by part. The successive vanishing of the variations with respect to each of the independent variables yields the adjoint problem (4.21). The definition of an *adjoint deformation* (4.21h) and an *adjoint deformation velocity* (4.21g) naturally stem from this derivation. Finally, we give some details about the implementation of boundary conditions for the adjoint problem.

Variation with respect to $\widehat{\mathbf{U}}$. We have from (4.16),

$$\begin{aligned}\nabla_{\widehat{\mathbf{U}}}\mathcal{L}\cdot\delta\widehat{\mathbf{U}} =& \nabla_{\widehat{\mathbf{U}}|_T}\mathcal{J}\cdot\delta\widehat{\mathbf{U}}|_T - \int_{t_0,0}^{T,\xi_{\mathrm{sf}}} \widehat{\mathbf{U}}^{\dagger^\top}\left(\partial_t\delta\widehat{\mathbf{U}} - \mathbf{L}\delta\widehat{\mathbf{U}}\right)\mathrm{d}t\mathrm{d}\xi \\ &- \int_{t_0}^{T}\widehat{\boldsymbol{\nu}}_{\mathrm{a}}^{\dagger^\top}\mathcal{P}_{\mathrm{a}}^{\mathrm{in}}\left[\delta\widehat{\mathbf{U}}_{\mathrm{I}}|_{\mathrm{a}} - \widehat{\mathbf{U}}_{\mathrm{a\,I}}\left(\delta\widehat{\mathbf{U}}|_{\mathrm{a}}, \widehat{X}_{\mathrm{a}}\right)\right]\mathrm{d}t - \int_{t_0}^{T}\widehat{\eta}_{\mathrm{a}}^{\dagger}\widehat{\mathbf{B}}_{\mathrm{a}}^{p}\left(\delta\widehat{\mathbf{U}}|_{\mathrm{a}}, \widehat{X}_{\mathrm{a}}\right)\mathrm{d}t \\ &- \int_{t_0}^{T}\widehat{\mu}_{\mathrm{a}}^{\dagger}f_{\mathrm{a}}\left(\delta\widehat{\mathbf{U}}|_{\mathrm{a}}, \widehat{X}_{\mathrm{a}}\right)\mathrm{d}t - \nabla_{\widehat{\mathbf{U}}|_{t_0}}\sum_{k=0}^{1}\widehat{\beta}_k^{\dagger}\mathcal{I}_k\left(\delta\widehat{\mathbf{U}}|_{t_0}\right). \end{aligned} \tag{E.1}$$

Operators $\mathcal{P}_{\mathrm{a}}^{\mathrm{in}}$, $\widehat{\mathbf{B}}_{\mathrm{a}}^{p}$ and f_{a} are replaced by their expressions from (3.40) and (3.42). After some integrations by parts and some algebra, it follows that

$$\begin{aligned}
\nabla_{\widehat{\mathbf{U}}}\mathcal{L}\cdot\delta\widehat{\mathbf{U}} = & \nabla_{\widehat{\mathbf{U}}|_T}\mathcal{J}\cdot\delta\widehat{\mathbf{U}}|_T + \int_{t_0,0}^{T,\xi_{\mathrm{sf}}}\left(\partial_t\widehat{\mathbf{U}}^\dagger - \mathbf{L}^\dagger\widehat{\mathbf{U}}^\dagger)\right)^\top\delta\widehat{\mathbf{U}}\mathrm{d}t\mathrm{d}\xi - \int_0^{\xi_{\mathrm{sf}}}\left[\widehat{\mathbf{U}}^{\dagger\top}\delta\widehat{\mathbf{U}}\right]_{t_0}^{T}\mathrm{d}\xi \\
& - \int_{t_0}^{T}\left[\widehat{\mathbf{U}}^{\dagger^\top}\mathbf{A}\delta\partial_\xi\widehat{\mathbf{U}} - \left(\partial_\xi(\widehat{\mathbf{U}}^{\dagger^\top}\mathbf{A}) - \widehat{\mathbf{U}}^{\dagger^\top}\mathbf{B}\right)\delta\widehat{\mathbf{U}}\right]_0^{\xi_{\mathrm{sf}}}\mathrm{d}t \\
& - \int_{t_0}^{T}\widehat{\nu}_{\mathrm{es}}^{\dagger\ \top}\mathbf{B}_{11}^{\mathrm{in}}\left[\delta\widehat{\mathbf{U}}_{\mathrm{I}}|_{\mathrm{es}} - \mathbf{M}_{11}^{\mathrm{es}\ -1}\left(E_3\delta\widehat{D}_\perp|_{\mathrm{es}} - \mathbf{M}_{12}^{\mathrm{es}}\delta\widehat{\mathbf{U}}_{\mathrm{II}}|_{\mathrm{es}}\right]\mathrm{d}t - \int_{t_0}^{T}\widehat{\nu}_{\mathrm{sf}}^{\dagger\ \top}\mathbf{B}_{11}^{\mathrm{in}}\left[\delta\widehat{\mathbf{U}}_{\mathrm{I}}|_{\mathrm{sf}} - \mathbf{M}_{\mathrm{I}}^{\mathrm{sf}-1}\left(\mathbf{M}_{\mathrm{II}}^{\mathrm{sf}}\delta\widehat{\mathbf{U}}_{\mathrm{II}}|_{\mathrm{sf}}\right)\right]\mathrm{d}t \\
& - \int_{t_0}^{T}\widehat{\eta}_{\mathrm{es}}^{\dagger}\left(\mathbf{N}_{22}^{\mathrm{es}}\delta\partial_\xi\widehat{\mathbf{U}}_{\mathrm{II}}|_{\mathrm{es}} + \mathbf{M}_{\mathrm{par}}^{\mathrm{es}}\delta\widehat{\mathbf{U}}|_{\mathrm{es}}\right)\mathrm{d}t - \int_{t_0}^{T}\widehat{\eta}_{\mathrm{sf}}^{\dagger}\left(\mathbf{N}_{22}^{\mathrm{sf}}\delta\partial_\xi\widehat{\mathbf{U}}_{\mathrm{II}}|_{\mathrm{sf}} + \mathbf{M}_{\mathrm{par}}^{\mathrm{sf}}\delta\widehat{\mathbf{U}}|_{\mathrm{sf}}\right)\mathrm{d}t \\
& - \int_{t_0}^{T}\widehat{\mu}_{\mathrm{es}}^{\dagger}\left(\boldsymbol{O}^{\mathrm{es}}\delta\widehat{\mathbf{U}}\right)\mathrm{d}t - \int_{t_0}^{T}\widehat{\mu}_{\mathrm{sf}}^{\dagger}\left(\boldsymbol{O}^{\mathrm{sf}}\delta\widehat{\mathbf{U}}\right)\mathrm{d}t \\
& - \sum_{k=0}^{1}\widehat{\beta}_k^\dagger\mathcal{J}_k\left(\delta\widehat{\mathbf{U}}|_{t_0}\right),
\end{aligned} \tag{E.2}$$

where $E_3 = (0 \quad 0 \quad 1)^\top$.

- Cancelling variations $\delta\widehat{\mathbf{U}}$ for all $0 \leqslant \xi \leqslant \xi_{\mathrm{sf}}$ and $t_0 \leqslant t \leqslant T$, yields the adjoint equation

  $$\partial_t\widehat{\mathbf{U}}^\dagger = \mathbf{L}^\dagger\widehat{\mathbf{U}}^\dagger \Leftrightarrow \partial_t\widehat{\mathbf{U}}^\dagger - \mathbf{A}^\top\partial_\xi^2\widehat{\mathbf{U}}^\dagger + \left(\mathbf{B}^\top - 2\,\partial_\xi\mathbf{A}^\top\right)\partial_\xi\widehat{\mathbf{U}}^\dagger - \left(\mathbf{C}^\top - \partial_\xi\mathbf{B}^\top + \partial_\xi^2\mathbf{A}^\top\right)\widehat{\mathbf{U}}^\dagger = 0, \tag{E.3a}$$

  and the definitions

  $$\mathbf{A}^\dagger = -\mathbf{A}^\top, \quad \mathbf{B}^\dagger = (\mathbf{B} - 2\partial_\xi\mathbf{A})^\top \quad \text{and} \quad \mathbf{C}^\dagger = -\left(\mathbf{C} - \partial_\xi\mathbf{B}^\top + \partial_{\xi^2}^2\mathbf{C}\right)^\top. \tag{E.3b}$$

- Cancelling variations $\delta\widehat{\mathbf{U}}$ at t_0 and T yields the optimality condition (4.21k) and terminal condition (4.21b).

- Cancelling variations $\delta\widehat{\mathbf{U}}|_{\mathrm{es}}$ and $\delta\widehat{\mathbf{U}}|_{\mathrm{sf}}$ yields boundary conditions (4.21c) and (4.21e).

- Cancelling variations $\delta\partial_\xi\widehat{\mathbf{U}}|_{\mathrm{es}}$ and $\delta\partial_\xi\widehat{\mathbf{U}}|_{\mathrm{sf}}$ yields boundary conditions (4.21d) and (4.21f).

Variation with respect to $\widehat{X}_{\mathrm{a}}$. From (4.16), we obtain that

$$
\begin{aligned}
\nabla_{\widehat{X}_{\mathrm{a}}}\mathcal{L}\cdot\delta\widehat{X}_{\mathrm{a}} =& \nabla_{\widehat{X}_{\mathrm{a}}}\mathcal{J}\cdot\delta\widehat{X}_{\mathrm{a}}|_T + \int_{t_0}^{T} \widehat{\boldsymbol{\nu}}_{\mathrm{a}}^{\dagger^\top}\mathcal{P}_{\mathrm{a}}^{\mathrm{in}}\widehat{\mathbf{U}}_{\mathrm{a\,I}}\left(\widehat{\mathbf{U}}|_{\mathrm{a}},\delta\widehat{X}_{\mathrm{a}}\right)\mathrm{d}t \\
&- \int_{t_0}^{T} \widehat{\eta}_{\mathrm{a}}^{\dagger}\mathbf{B}_{\mathrm{a}}^{p}\left(\widehat{\mathbf{U}}|_{\mathrm{a}},\delta\widehat{X}_{\mathrm{a}}\right)\mathrm{d}t - \int_{t_0}^{T} \widehat{\mu}_{\mathrm{a}}^{\dagger}f_{\mathrm{a}}\left(\widehat{\mathbf{U}}|_{\mathrm{a}},\delta\widehat{X}_{\mathrm{a}}\right)\mathrm{d}t \\
&- \nabla_{\widehat{X}_{\mathrm{a}}|_{t_0}}\sum_{k=0}^{1}\widehat{\beta}_k^{\dagger}\mathcal{I}_k\left(\delta\widehat{X}_{\mathrm{es}}|_{t_0},\delta\widehat{X}_{\mathrm{sf}}|_{t_0}\right).
\end{aligned}
\tag{E.4}
$$

Similarly, after an integration by part and some algebra it follows

$$
\begin{aligned}
\nabla_{\widehat{X}_{\mathrm{a}}}\mathcal{L}\cdot\delta\widehat{X}_{\mathrm{a}} =& \nabla_{\widehat{X}_{\mathrm{a}}}\mathcal{J}\cdot\delta\widehat{X}_{\mathrm{a}}|_T \\
&- \int_{t_0}^{T} \widehat{\boldsymbol{\nu}}_{\mathrm{a}}^{\dagger\top}\mathbf{B}_{11}^{\mathrm{in}}{\mathbf{M}_{11}^{\mathrm{a}}}^{-1}\left(\mathbf{S}_{\mathrm{I}}^{\mathrm{a},0}\delta\widehat{X}_{\mathrm{a}} + \mathbf{S}_{\mathrm{I}}^{\mathrm{a},1}\delta\dot{\widehat{X}}_{\mathrm{a}}\right)\mathrm{d}t - \int_{t_0}^{T} \widehat{\eta}_{\mathrm{a}}^{\dagger}\left(\mathbf{N}_{22}^{\mathrm{a}}\mathbf{S}_{\mathrm{II}}^{\mathrm{a},0}\delta\widehat{X}_{\mathrm{a}} + \mathbf{S}_{\mathrm{II}}^{\mathrm{a},1}\delta\dot{\widehat{X}}_{\mathrm{a}}\right)\mathrm{d}t \\
&- \int_{t_0}^{T} \widehat{\mu}_{\mathrm{a}}^{\dagger}\left((\mathbf{S}^{\mathrm{a},0})_2\delta\widehat{X}_{\mathrm{a}} + (\mathbf{S}^{\mathrm{a},1})_2\delta\dot{\widehat{X}}_{\mathrm{a}}\right)\mathrm{d}t - \sum_{k=0}^{1}\widehat{\beta}_k^{\dagger}\mathcal{I}_k\left(\delta\widehat{X}_{\mathrm{a}}|_{t_0},\delta\widehat{X}_{\mathrm{sf}}|_{t_0}\right).
\end{aligned}
\tag{E.5}
$$

- Cancelling variations $\delta\widehat{X}_{\mathrm{a}}$ yields

$$
\mathrm{d}_t\left(\widehat{\boldsymbol{\nu}}_{\mathrm{a}}^{\dagger\top}\mathbf{B}_{11}^{\mathrm{in}}{\mathbf{M}_{11}^{\mathrm{a}}}^{-1}\mathbf{S}_{\mathrm{I}}^{\mathrm{a},1} + \widehat{\eta}_{\mathrm{a}}^{\dagger}\mathbf{S}_{\mathrm{II}}^{\mathrm{a}\,1} + \widehat{\mu}_{\mathrm{a}}^{\dagger}(\mathbf{S}^{\mathrm{a},1})_2\right) = \widehat{\boldsymbol{\nu}}_{\mathrm{a}}^{\dagger\top}\mathbf{B}_{11}^{\mathrm{in}}{\mathbf{M}_{11}^{\mathrm{a}}}^{-1}\mathbf{S}_{\mathrm{I}}^{\mathrm{a},0} + \widehat{\eta}_{\mathrm{a}}^{\dagger}\mathbf{S}_{\mathrm{II}}^{\mathrm{a}\,0} + \widehat{\mu}_{\mathrm{a}}^{\dagger}(\mathbf{S}^{\mathrm{a},0})_2
\tag{E.6}
$$

  and we define the *adjoint deformation* and *adjoint deformation velocity*

$$
\widehat{X}_{\mathrm{a}}^{\dagger} = \widehat{\boldsymbol{\nu}}_{\mathrm{a}}^{\dagger\top}\mathbf{B}_{11}^{\mathrm{in}}{\mathbf{M}_{11}^{\mathrm{a}}}^{-1}\mathbf{S}_{\mathrm{I}}^{\mathrm{a},1} + \widehat{\eta}_{\mathrm{a}}^{\dagger}\mathbf{S}_{\mathrm{II}}^{\mathrm{a}\,1} + \widehat{\mu}_{\mathrm{a}}^{\dagger}(\mathbf{S}^{\mathrm{a},1})_2
\tag{E.7}
$$

$$
\dot{\widehat{X}}_{\mathrm{a}}^{\dagger} = \widehat{\boldsymbol{\nu}}_{\mathrm{a}}^{\dagger\top}\mathbf{B}_{11}^{\mathrm{in}}{\mathbf{M}_{11}^{\mathrm{a}}}^{-1}\mathbf{S}_{\mathrm{I}}^{\mathrm{a},0} + \widehat{\eta}_{\mathrm{a}}^{\dagger}\mathbf{S}_{\mathrm{II}}^{\mathrm{a}\,0} + \widehat{\mu}_{\mathrm{a}}^{\dagger}(\mathbf{S}^{\mathrm{a},0})_2.
\tag{E.8}
$$

E.2 Implementation of the adjoint boundary conditions

Here we give some details about the implementation of (4.21c)–(4.21f). At $\xi = \xi_{\mathrm{a}}$, $\mathbb{B}_{\mathrm{in}}^{(4,4)} = {\mathbf{B}_{11}^{+}}^{\top}$ and ${\mathbf{B}_{11}^{\dagger}}^{\mathrm{in}} = {\mathbf{B}_{11}^{-}}^{\top}$. Therefore boundary conditions for the hyperbolic subsystem write

$$
\mathbf{B}_{11}^{\top}\widehat{\mathbf{U}}_{\mathrm{I}}^{\dagger} = -\mathbf{B}_{21}^{\top}\widehat{\mathbf{U}}_{\mathrm{II}}^{\dagger} + {\mathbf{B}_{11}^{+}}^{\top}\widehat{\boldsymbol{\nu}}_{\mathrm{a}}^{\dagger} + {\mathbf{M}_{21}^{\mathrm{a}}}^{\top}\widehat{\eta}_{\mathrm{a}}^{\dagger} + \boldsymbol{O}^{\mathrm{a}}\widehat{\mu}_{\mathrm{a}}^{\dagger}.
\tag{E.9}
$$

Multiplying on the left by $\mathbf{R}_{11}^{\top}$ gives

$$
\mathbf{D}_{11}\widehat{\mathcal{W}}_{\mathrm{I}}^{\dagger} = \mathbf{D}_{11}^{+}\mathbf{R}_{11}^{\top}\widehat{\boldsymbol{\nu}}_{\mathrm{a}}^{\dagger} + \mathbf{R}_{11}^{\top}\left(-\mathbf{B}_{21}^{\top}\widehat{\mathbf{U}}_{\mathrm{II}}^{\dagger} + {\mathbf{M}_{21}^{\mathrm{a}}}^{\top}\widehat{\eta}_{\mathrm{a}}^{\dagger} + \boldsymbol{O}^{\mathrm{a}}\widehat{\mu}_{\mathrm{a}}^{\dagger}\right),
\tag{E.10}
$$

where $\widehat{\mathcal{W}}_{\mathrm{I}}^{\dagger} = \mathbf{R}^{\top}\widehat{\mathbf{U}}_{\mathrm{I}}^{\dagger}$ denotes the characteristic adjoint variable. The incoming information on hyperbolic components of the adjoint problem is

$$
\mathbf{D}_{11}^{-}\widehat{\mathcal{W}}_{\mathrm{I}}^{\dagger} = {\mathbf{R}_{11}^{-}}^{\top}\left(-\mathbf{B}_{21}^{\top}\widehat{\mathbf{U}}_{\mathrm{II}}^{\dagger} + {\mathbf{M}_{21}^{\mathrm{es}}}^{\top}\widehat{\eta}_{\mathrm{es}}^{\dagger} + \boldsymbol{O}^{\mathrm{a}}\widehat{\mu}_{\mathrm{es}}^{\dagger}\right), \quad \text{at a = es} \quad \text{and}
\tag{E.11a}
$$

$$
\mathbf{D}_{11}^{+}\widehat{\mathcal{W}}_{\mathrm{I}}^{\dagger} = {\mathbf{R}_{11}^{+}}^{\top}\left(-\mathbf{B}_{21}^{\top}\widehat{\mathbf{U}}_{\mathrm{II}}^{\dagger} + {\mathbf{M}_{21}^{\mathrm{sf}}}^{\top}\widehat{\eta}_{\mathrm{sf}}^{\dagger} + \boldsymbol{O}^{\mathrm{sf}}\widehat{\mu}_{\mathrm{sf}}^{\dagger}\right), \quad \text{at a = sf,}
\tag{E.11b}
$$

whereas the outgoing information is

$$\mathbf{D}_{11}^{\pm}\widehat{\mathcal{W}}_{\mathrm{I}}^{\dagger} = \mathbf{D}_{11}^{\pm}\mathbf{R}_{11}^{\top}\widehat{\boldsymbol{\nu}}_{\mathrm{a}}^{\dagger} + \mathbf{R}_{11}^{\pm\;\top}\left(-\mathbf{B}_{21}^{\top}\widehat{\mathbf{U}}_{\mathrm{II}}^{\dagger} + \mathbf{M}_{21}^{\mathrm{a}\;\top}\widehat{\eta}_{\mathrm{a}}^{\dagger} + O^{\mathrm{a}}\widehat{\mu}_{\mathrm{a}}^{\dagger}\right), \tag{E.12}$$

with $+$ at a = es and $-$ at a = sf. Matrix $\mathbf{R}_{11}^{-\;\top}$ (respectively $\mathbf{R}_{11}^{+\;\top}$) is defined as $\mathbf{R}_{11}^{\top}$ with zeros on the rows corresponding to the negative (resp. positive) eigenvalues of $\mathbf{D}$. We use (4.21d) to replace $\widehat{\eta}_{\mathrm{a}}^{\dagger}$ by $\widehat{\mathbf{U}}_{\mathrm{II}}^{\dagger}$

$$\mathbf{A}_{22}\widehat{\mathbf{U}}_{\mathrm{II}}^{\dagger} - \mathbf{N}_{22}^{\mathrm{a}}\widehat{\eta}_{\mathrm{a}}^{\dagger} = 0. \tag{E.13}$$

The following quantities have to be determined

$$\lambda_i(\mathbf{R}_{11}^{\top})_{ij}\widehat{\boldsymbol{\nu}}_{\mathrm{a}j}^{\dagger}, \quad \text{for} \quad \lambda_i \quad \text{positive (respectively negative) eigenvalues at } \xi = 0 \text{ (resp. } \xi = \xi_{\mathrm{sf}})$$

and

$$\widehat{\mu}_{\mathrm{a}}^{\dagger},$$

using the knowledge of $\widehat{X}_{\mathrm{a}}$, $\widehat{\mathbf{U}}_{\mathrm{II}}$ and $\mathbf{D}_{11}^{\pm}\widehat{\mathcal{W}}_{\mathrm{I}}^{\dagger}$. For this purpose we proceed as follows:

1. knowing $\mathbf{D}_{\pm}\widehat{\mathcal{W}}_{\mathrm{I}}^{\dagger}$ (E.12) and $\widehat{X}_{\mathrm{a}}$, the unknowns $\mathbf{D}_{11}^{\mp}\widehat{\mathcal{W}}_{\mathrm{I}}^{\dagger}$ and $\widehat{\mu}_{\mathrm{a}}^{\dagger}$ are computed simultaneously from the system formed by (4.21h) and (E.11),
2. $\dot{\widehat{X}}_{\mathrm{a}}^{\dagger}$ is computed from (4.21g) and the adjoint deformation is integrated in time.

E.3 Integration window q_{af}

The function $q_{\mathrm{af}}(\xi)$ is an integration mask function over $[\xi_{\mathrm{af}}^{-}, \xi_{\mathrm{af}}^{+}]$ encompassing the maximum of the specific total energy variation rate $\bar{q}_0$

$$\begin{aligned} q_{\mathrm{af}}(\xi) &= 0, \quad \text{for} \quad \xi \leqslant \xi_{\mathrm{af}}^{-} \quad \text{or} \quad \xi \geqslant \xi_{\mathrm{af}}^{+}, \\ q_{\mathrm{af}}(\xi) &= \tanh(\tan(\pi\theta)) \quad \text{for} \quad \xi_{\mathrm{af}}^{-} \leqslant \xi \leqslant \xi_{\mathrm{af}}^{+}, \end{aligned} \tag{E.14}$$

with

$$\theta = \frac{\xi - \xi^{-}}{\xi_{\max} - \xi_{\mathrm{af}}^{-}} - \frac{1}{2}, \quad \text{if} \quad \xi_{\mathrm{af}}^{-} \leqslant \xi \leqslant \xi_{\max}, \quad \text{or} \quad \frac{1}{2} - \frac{\xi - \xi_{\max}}{\xi_{\mathrm{af}}^{+} - \xi_{\max}}, \quad \text{if} \quad \xi_{\max} \leqslant \xi \leqslant \xi_{\mathrm{af}}^{+},$$

and

$$\xi_{\max} = \arg\left\{\max(\bar{q}_0)\right\}, \quad \bar{q}_0 = |\partial_{\xi}(\bar{P}\bar{V}_x + \bar{\Phi}_x)|,$$

and

$$\left\{\xi_{\mathrm{af}}^{-}, \xi_{\mathrm{af}}^{+}\right\} = \arg\left\{\max(\bar{q}_0) - 0.9(\max(\bar{q}_0) - \min(\bar{q}_0))\right\}. \tag{E.15}$$

The interval $\left[\xi_{\mathrm{af}}^{-}, \xi_{\mathrm{af}}^{+}\right]$ comprises the steep gradients of the ablation layer and (E.14) ensures a smooth matching at ξ_{af}^{-} and ξ_{af}^{+}.

CHAPTER F

Verification of the numerical method for the adjoint equations

The time integration of the adjoint equation (4.21a) is verified on analytical test-cases as for the direct equation (App. D).

F.1 Hyperbolic test-case

This first test-case verifies the explicit part of the temporal RK3 scheme (4.25)

$$\partial_t \widehat{\mathbf{U}}^\dagger = \widehat{\mathbf{F}}^\dagger, \tag{F.1}$$

which corresponds purely to advection and amplification terms. Solutions are sought under the form

$$\widehat{\mathbf{U}}^\dagger_{\mathrm{sol}} = \widehat{\mathbf{U}}^\dagger_0 \exp\left[i(\omega t - k_\xi \xi)\right], \tag{F.2}$$

for a stationary and uniform base flow

$$(\bar{G} \quad \bar{V}_x \quad \bar{\Theta}) = (4 \quad 0 \quad 1/3). \tag{F.3}$$

Equation (4.21a) with (F.2) boils down to the eigenvalue problem

$$\begin{pmatrix} i\omega & -ik_\xi \bar{G}^2 & -\bar{G} & 0 \\ -ik_\xi \bar{\Theta} & i\omega & 0 & -ik_\xi \bar{G} \\ k_\perp^2 \bar{\Theta}/\bar{G} & 0 & i\omega & k_\perp^2 \\ 0 & -ik_\xi(\gamma-1)\bar{P} & -(\gamma-1)\bar{\Theta} & i\omega \end{pmatrix}^\top \widehat{\mathbf{U}}^\dagger_0 = \mathbf{0}. \tag{F.4}$$

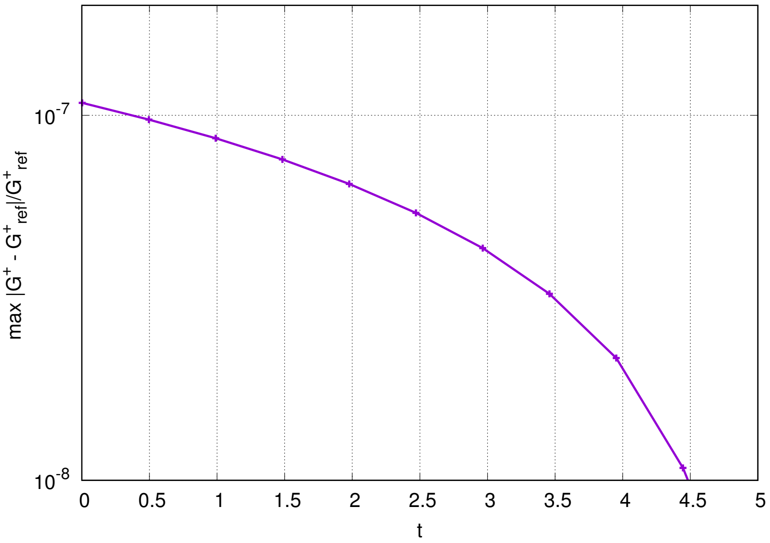

Figure F.1: $(\Delta t, N_{\text{dom}} \times N_{\text{cheb}}) = (1.62\,10^{-4}, 4 \times 32)$ and $k_\perp = 1$. Space maximum relative error in adjoint density against time.

A non-trivial solution with positive velocity is given by $\omega_{\mathcal{A}} = c_s\sqrt{k_\xi^2 \bar{G}^2 + k_\perp^2} = K_{\mathcal{A}}$, with $c_s = \sqrt{\gamma\bar{\Theta}}$, yielding the eigenvector

$$\widehat{\mathbf{U}}^\dagger_{\mathcal{A}} = \begin{pmatrix} \dfrac{\bar{\Theta}}{\bar{G}} & \dfrac{k_\xi c_s^2 \bar{G}}{\omega_{\mathcal{A}}} & -\dfrac{i c_s^2}{\omega_{\mathcal{A}}} & 1 \end{pmatrix}^\top . \tag{F.5}$$

A difference with the acoustic test-case (F.4) is that the adjoint transverse divergence of the transverse velocity $\widehat{D}^\dagger_\perp$ is non-zero even for $k_\perp = 0$.

A signal of wavenumber $k_\xi = 2\pi$ is initiated on a domain $[0, 2]$ discretized over 4 subdomains. This initial condition is integrated in time over 15 periods $T = 2\pi/\omega_{\mathcal{A}}$, from $t = 5$ to $t = 0$. Boundary conditions are periodic. The error steadily accumulates with time (Fig. F.1) but remains low.

F.2 Parabolic test-case

The parabolic test-case verifies the semi-implicit part of the RK3 scheme (4.25), which corresponds to the equation

$$\partial_t \widehat{\Theta}^\dagger = \lambda_\xi \partial^2_{\xi^\dagger} \widehat{\Theta}^\dagger + \lambda_\perp \widehat{\Theta}^\dagger, \quad \text{with} \quad \lambda_\xi = (\gamma - 1)\bar{G}\Psi_{\Theta'} \quad \text{and} \quad \lambda_\perp = -k_\perp^2 \frac{\Psi_{\Theta'}}{\bar{G}}. \tag{F.6}$$

For a stationary and uniform base flow

$$\begin{pmatrix} \bar{G} & \bar{V}_x & \bar{\Theta} \end{pmatrix} = \begin{pmatrix} 4 & 0 & 1/3 \end{pmatrix}, \tag{F.7}$$

solutions are sought for as separated variable functions

$$\widehat{\Theta}^\dagger = f(\xi) g(t). \tag{F.8}$$

Similarily to the direct case, solutions are of the form

$$\widehat{\Theta}^\dagger_n(\xi, t) = B_n \exp(t/\tau_n)\sin(k_\xi^n), \quad \text{with} \quad k_\xi^n = n\pi/2 \quad \text{and} \quad 1/\tau_n = -(k_\xi^n)^2 \lambda_\zeta + \lambda_\perp, \tag{F.9}$$

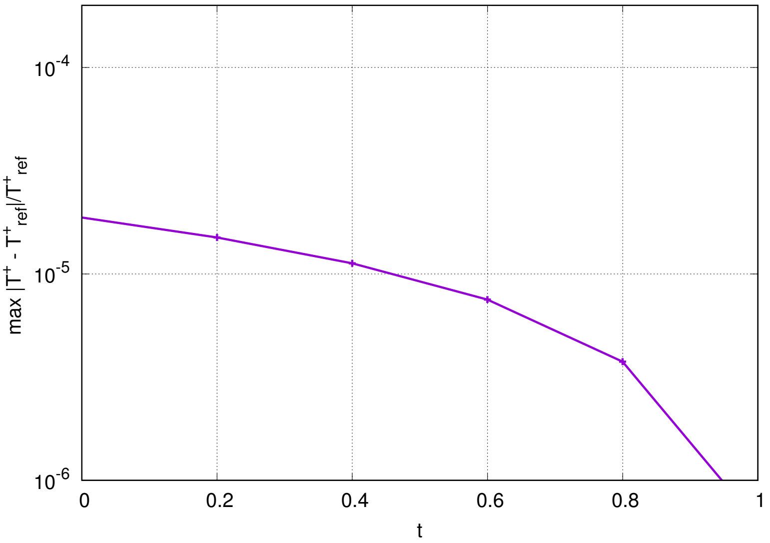

Figure F.2: $(\Delta t, N_{\mathrm{dom}} \times N_{\mathrm{cheb}}) = (10^{-4}, 4 \times 50)$ and $k_\perp = 1$. Space maximum relative error on the adjoint temperature against time.

with n an integer, for homogeneous Dirichlet boundary conditions.

A solution is initiated on a domain $[0, 2]$ for $n = 1$ and $k_\perp = 1$ at $t = 1$ and integrated in time up to $t = 0$ (Fig. F.2). The error is higher than in the heat conduction test-case in the direct case (heat-conduction test-case, Fig. D.4). This is explained by the fact that in the heat-condution test-case boundary conditions are Neumann type, whereas in the present parabolic test-case, boundary conditions are Dirichlet type. For $n = 1$, the solution is steeper in the Dirichlet case than in the Neumann case. The steepness of the solution in the present test-case would be obtained with $n = 2$ in the direct heat-conduction test-case.

F.3 Full adjoint equation

The combination of the explicit part and semi-implicit part of the RK3 scheme (4.25) are verified in this test-case. Solutions are sought for under the form

$$\widehat{\mathbf{U}}^\dagger = \Re\left(\widehat{\mathbf{U}}_0^\dagger \exp i\left[\omega t - k_\xi \xi\right]\right), \quad \text{with} \quad k_\xi = 2\pi \quad \text{and } \omega \text{ complex}, \tag{F.10}$$

for a stationary and uniform base flow

$$(\bar{G} \quad \bar{V}_x \quad \bar{\Theta}) = (4 \quad 0 \quad 1/3). \tag{F.11}$$

Equation (4.21a) boils down to the eigenvalue problem

$$\begin{pmatrix} i\omega & -ik_\xi \bar{G} & -\bar{G} & 0 \\ -ik_\xi \bar{\Theta}/\bar{G} & i\omega & 0 & -ik_\xi \\ k_\perp^2 \bar{\Theta}/\bar{G} & 0 & i\omega & k_\perp^2 \\ 0 & -ik_\xi(\gamma-1)\bar{\Theta} & -(\gamma-1)\bar{\Theta} & i\omega + (\gamma-1)(k_\xi^2 + k_\perp^2)\Psi_{\Theta'}/\bar{G} \end{pmatrix}^\top \widehat{\mathbf{U}}_0^\dagger = \mathbf{0}. \tag{F.12}$$

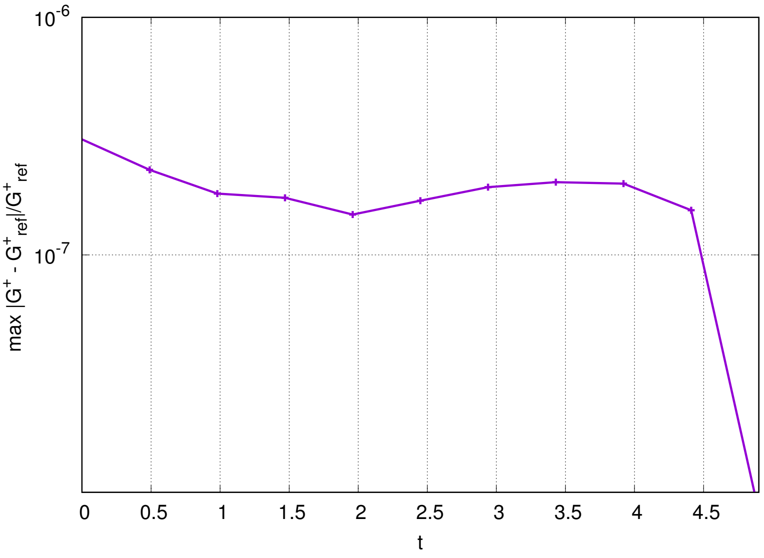

Figure F.3: $(\Delta t, N_{\mathrm{dom}} \times N_{\mathrm{cheb}}) = (10^{-4}, 4 \times 50)$ and $k_\perp = 1$. Space maximum relative error in adjoint density against time.

Similarly to the direct case (§ D.3), there exists four nontrivial solutions determined numerically. Here we focus on the only one corresponding to $\Re(\omega) > 0$. Such a solution is initiated on an interval $[0, 2]$ divided into four subdomains, with periodic boundary conditions. The solution is integrated in time from $t = 5$ to $t = 0$, which corresponds to approximately 5 pseudo-periods. The space maximum relative error in adjoint density (Fig. F.3) remains at a level which is similar to the thermoacoustic test-case of the direct equation (§ D.3).

CHAPTER G

Optimal responses

G.1 Additional optimal responses

In the present appendix we present the optimal growth corresponding to $(k_\perp, T) = (4, 1.8)$ for $r_c = 1$. Although this result present no additional information compared to those of § 4.6, it reinforces our conclusions.

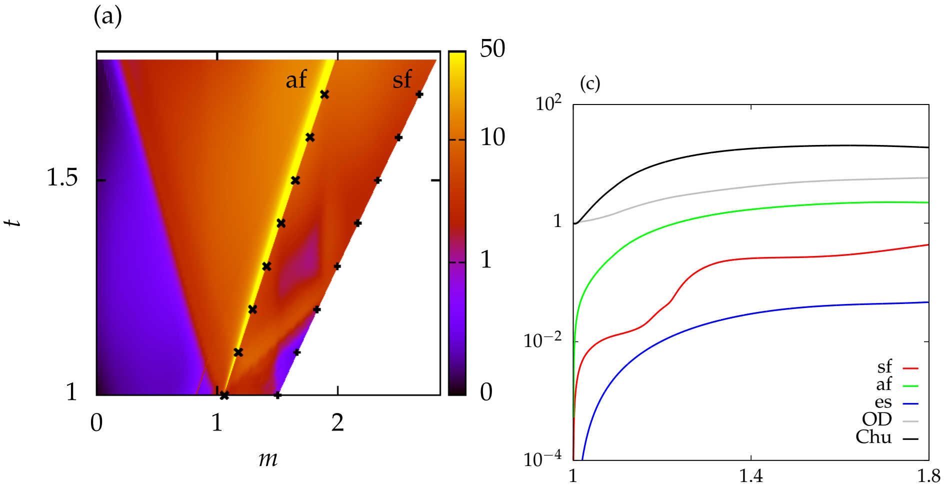

Figure G.1: Ablation wave RC-1. $(k_\perp, r_c) = (4, 1)$ for $T = 1.8$. (a) Chu's energy density and (b) deformations of the external surface, ablation front and shock front with Chu's energy and the optical depth perturbation.

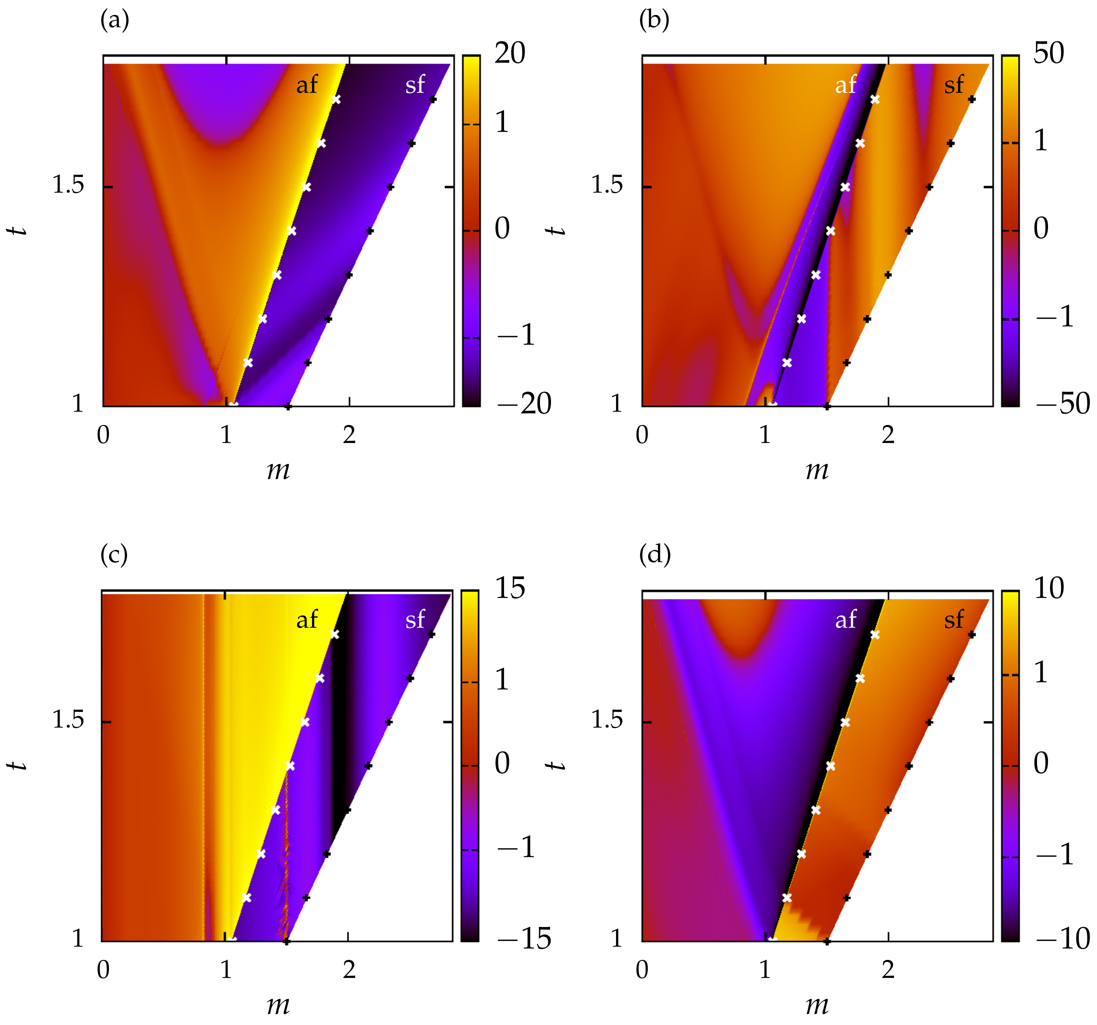

Figure G.2: Ablation wave RC-1. $(k_\perp, r_c) = (4, 1)$ for $T = 1.8$. Projection of the optimal response on the pseudo-characteristic variables: (a) heat-conductivity/forward acoustics $\widehat{\mathcal{W}}_1$, (b) forward acoustics/entropy $\widehat{\mathcal{W}}_2$, (c) vorticity $\widehat{\omega}$, and (d) backward acoustics $\widehat{\mathcal{W}}_4$.

List of communications

Posters

- Investigation of supersonic heat-conductivity linear waves in the conduction region, *G. Varillon, J.-M. Clarisse, A. Couairon*, Journée des Doctorants de la DIF, 06/2018, Bruyères-le-Châtel, France
- Investigation of supersonic heat-conductivity linear waves in ablation flows, *G. Varillon, J.-M. Clarisse, A. Couairon*, 46th EPS Plasma physics, 07/2018, Prague, Czech Republic
- Investigation of supersonic heat-conductivity linear waves in ablation flows, *G. Varillon, J.-M. Clarisse, A. Couairon*, International school on low temperature plasma physics, 10/2018, Bad Honnef, Germany
- Non-modal linear stability analysis of ablation flows relative to inertial confinement fusion, *G. Varillon, J.-M. Clarisse, A. Couairon*, IUTAM transition, 09/2019, London, UK

Oral talks

- Non-modal hydrodynamic stability analysis of ablation flows relative to ICF, *G. Varillon, J.-M. Clarisse, A. Couairon*, Journée des thèses du CPHT, 02/2018, Palaiseau, France
- Non-modal hydrodynamic stability analysis of ablation flows relative to ICF, *G. Varillon, J.-M. Clarisse, A. Couairon*, Journées scientifiques de l'Ecole Doctorale Ondes et Matière, 02/2018, Palaiseau, France
- Non-modal linear stability analysis of ablation flows relative to inertial confinement fusion, *G. Varillon, J.-M. Clarisse, A. Couairon*, Journée des thèses du CPHT, 11/2018, Palaiseau, France
- Non-modal linear stability analysis of ablation flows relative to inertial confinement fusion, *G. Varillon, J.-M. Clarisse, A. Couairon*, Journées de la Dynamique des Fluides du Plateau, 01/2019, Gif-sur-Yvette, France
- Analyse non-normale de stabilité hydrodynamique des écoulements d'ablation en fusion par confinement inertiel, *G. Varillon, J.-M. Clarisse, A. Couairon*, Journée des Doctorants de la DIF, 06/2019, Bruyères-le-Châtel, France

- Analyse non-normale de stabilité hydrodynamique des écoulements d'ablation en fusion par confinement inertiel, *G. Varillon, J.-M. Clarisse, A. Couairon*, 24^{e} Congrès Français de Mécanique, 06/2019, Brest, France

Articles

- Investigation of supersonic heat-conductivity linear waves in ablation flows, *G. Varillon, J.-M. Clarisse, A. Couairon*, Proc. 46th EPS Plasma physics, 07/2018, Prague, Czech Republic
- Non-modal linear stability analysis of ablation flows relative to inertial confinement fusion, *G. Varillon, J.-M. Clarisse, A. Couairon*, Proc. 24^{e} Congrès Français de Mécanique, 06/2019, Brest, France
- Non-modal linear stability analysis of ablation flows relative to inertial confinement fusion, *G. Varillon, J.-M. Clarisse, A. Couairon*, Proc. IUTAM transition, 09/2019, London, UK
- *submitted to Phys. Rev. E*: Investigation of supersonic heat-conductivity hyperbolic waves in radiative ablation flows, *G. Varillon, J.-M. Clarisse, A. Couairon*
- *prepared for Phys. Rev. Lett.*: Stability of ablation flow in inertial confinement fusion: non-modal growth, *G. Varillon, J.-M. Clarisse, A. Couairon*

List of Figures

List of Tables

Extended summary in French

La fusion par confinement inertiel (FCI) vise à initier des réactions de fusion thermonucléaire par l'implosion de cavités sphériques millimétriques remplies de noyaux fusibles légers (Atzeni and Meyer-ter-Vehn, 2004). Ces implosions se produisent sous l'action d'un flux d'irradiation externe conçu pour induire une déflagration, ou onde d'ablation, qui pousse vers l'intérieur l'enveloppe extérieure de la cavité – l'ablateur – choisie pour être opaque à l'irradiation incidente. L'écoulement résultant consiste en une onde thermique subsonique, ou front d'ablation, qui coïncide avec la tête de l'onde de détente du matériau chauffé, qui pénètre dans l'ablateur. Ce front d'ablation est précédé d'une onde de choc qui comprime l'ablateur au repos. Par nature instables, ces écoulements d'ablation sont compressibles et stratifiés avec un front thermique abrupt, en raison de la forte non-linéarité du transport de chaleur et de l'intensité du chauffage incident. Le succès de la FCI dépend de la capacité à atteindre et maintenir pendant un temps suffisamment long des températures et densités suffisamment élevées dans le fusible, qui sont nécessaires pour déclencher des réactions thermonucléaires.

La stabilité hydrodynamique des écoulements d'ablation a été étudiée en de manière théorique à partir d'hypothèses simplificatrices d'écoulements moyens qui ne sont pas nécessairement respectées dans les cas réels : stationnarité de l'écoulement moyen, approximation bas Mach, domaines (semi-)infinis, front d'ablation discontinu, uniformité de certaines régions de l'écoulement. En outre, ces travaux se sont exclusivement appuyés sur la méthode des modes normaux, en se concentrant sur les fonctions propres de l'écoulement les plus instables. Cette méthode ne donne que des résultats de stabilité asymptotiques – i.e. en temps long – et omet les éventuels phénomènes de croissance transitoire propres aux opérateurs non normaux. De plus, la non-stationnarité des écoulements d'ablation induit des régimes d'évolution des perturbations de durée finie, soulevant ainsi logiquement la question de la dynamique des perturbations à court terme (Clarisse et al., 2016). Des configurations plus réalistes sont étudiées classiquement au moyen de simulations numériques multidimensionnelles avec des codes d'hydrodynamique FCI qui intègrent les phénomènes physiques les plus pertinents. Ces simulations "full physics", qui pallient les insuffisances ci-dessus, consistent à calculer des amplifications de perturbation à partir de conditions initiales ou limites perturbées particulières qui sont considérées comme les plus dangereuses pour un écoulement moyen donné. Outre le coût de calcul de ces simulations, cette façon de procéder se heurte à une difficulté majeure lors d'implosions FCI réelles, à savoir des sources de perturbations multiples dont les contributions restent, pour certaines d'entre elles, insuffisamment connues et maîtrisées.

Dans ce contexte, les méthodes d'analyse de stabilité non-normale (Schmid, 2007), capables d'identifier les perturbations les plus dangereuses dans des écoulements dépendant du temps et de durée finie, sont non seulement les plus appropriées mais semblent aussi être une nécessité. Puisque le coût actuel des simulations physiques complètes interdit la mise en œuvre de telles méthodes avec les codes de simulation FCI "full-physics" existants, nous avons recours, pour ce travail, à une modélisation simplifiée des ondes d'ablation instationnaires. Cette modélisation est fournie par des solutions auto-semblables des équations d'Euler avec une conduction non linéaire de chaleur en symétrie plane. Certaines de ces solutions sont représentatives de la première étape d'une implosion d'une cavité, ou *phase de transit de choc*, durant laquelle l'onde de choc est en train de traverser l'épaisseur de l'ablateur (Boudesocque-Dubois et al., 2008). En particulier, ces écoulements auto-semblables représentent la structure complète d'une onde d'ablation : un front de choc avant, une région comprimée, une couche d'ablation et une zone d'expansion.

Dans ce travail, nous effectuons la première analyse de stabilité non-normale réalisée sur un écoulement d'ablation. Qui plus est, cet écoulement est pertinent pour la FCI. Dans le cas d'un écoulement moyen instationnaire, les perturbations initiales optimales sont obtenues au moyen d'itérations direct-adjoint. Le problème adjoint est établi via la méthode des multiplicateurs de Lagrange Gunzburger (1997). Ce faisant, nous obtenons pour la première fois, à notre connaissance, une formulation correcte d'une fonctionnelle de Lagrange dans le cas d'un système d'équations d'évolution parabolique incomplet avec des frontières dynamiques perturbées.

L'optimisation des perturbations initiales montre une amplification des perturbations à court terme pour tous les nombres d'ondes transverses couvrant le spectre de perturbation classiquement considéré pour les cibles FCI, et pour tous les temps terminaux intermédiaires, inférieurs ou égaux à la durée de la phase de transit de choc. Ces résultats contrastent avec les résultats existants basés sur l'analyse en mode normaux, les simulations et les expériences dédiées de configurations de perturbations particulières, pour lesquelles seules les grandes longueurs d'onde engendrent une amplification possible alors que les petites longueurs d'onde sont amorties. Ce résultat souligne la nécessité d'une analyse non modale pour les écoulements d'ablation dans le contexte de la FCI. Les mécanismes de croissance optimale consistent en des *interactions d'ondes acoustiques et de vorticité* pour des temps terminaux court vis-à-vis de la phase de transit de choc, et un *couplage front d'ablation – onde de choc* à des temps terminaux proche de la fin de la phase de transit. Une analyse physique des perturbations optimales montre que celles-ci diffèrent fortement de la configuration de perturbation de l'instabilité de Richtmyer–Meshkov ablative (Goncharov, 1999) habituellement considérée comme l'une des plus dangereuses en FCI.

Ce travail illustre la nécessité d'une analyse non-normale dans le contexte de la FCI et ouvre la voie à une analyse de la réceptivité des écoulements d'ablation aux défauts de l'ablateur, ainsi que, à plus long terme, au *design opimal* des cibles de FCI.

Bibliography

Abéguilé, F., Boudesocque-Dubois, C., Clarisse, J.-M., Gauthier, S., and Saillard, Y. (2006). Linear perturbation amplification in self-similar ablation flows of inertial confinement fusion. *Phys. Rev. Lett.*, 97:035002.

Aglitskiy, Y., Velikovich, A. L., Karasik, M., Metzler, N., Zalesak, S. T., Schmitt, A. J., Phillips, L., Gardner, J. H., Serlin, V., Weaver, J. L., and Obenschain, S. P. (2010). Basic hyrdodynamics of Richtmyer–Meshkov-type growth and oscillations in the inertial confinement fusion-relevant conditions. *Phil. Trans. R. Soc. A*, 368:1739–1768.

Atzeni, S. (1987). The physical basis for numerical fluid simulations in laser fusion. *Plasma Phys. Control. Fusion*, 29.

Atzeni, S. and Meyer-ter-Vehn, J. (2004). *The physics of inertial fusion*. Oxford University Press, Oxford, U.K.

Bajac, J. (1973). Etude d'une classe de solutions des écoulements plan compressibles avec transfert radiatif. Technical Report CEA-R-4482, Commissariat à l'Energie Atomique.

Baker, L. (1978). Stability of ablation and combustion fronts. *Phys. Fluids*, 21(2):295–297.

Barenblatt, G. I. (1979). *Similarity, self-similarity, and intermediate asymptotics*. Consultants Bureau, New-York.

Barrero, A. and Sanmartín, J. R. (1977). Self-similar motion of laser fusion plasma. Absorption in an unbounded plasma. *Phys. Fluids*, 20(7):1155–1163.

Bayliss, A. and Turkel, E. (1992). Mappings and accuracy fo Chebyshev pseudo-spectral approximations. *J. Comput. Phys.*, 101:349–358.

Betti, R., Goncharov, V. N., McCrory, R. L., and Verdon, C. P. (1998). Growth rates of the ablative Rayleigh–Taylor instability in inertial confinement fusion. *Phys. Plasmas*, 5(5):1446–1454.

Blumenthal, R. S., Tangirala, A. K., Sujith, R. I., and Polifke, W. (2017). A systems perspective on non-normality in low-order thermoacoustic models: Full norms, semi-norms and transient growth. *Int. J. Spray Comb. Dyna.*, 9(1):19–43.

Bodner, S. E. (1974). Rayleigh–Taylor instability and laser-pellet fusion. *Phys. Rev. Lett.*, 33(13):761–764.

Boudesocque-Dubois, C. (2000). *Perturbations linéaires d'une solution autosemblable de l'hydrodynamique avec conduction non linéaire*. Thèse de doctorat, Université de Paris 6.

Boudesocque-Dubois, C., Clarisse, J.-M., and Gauthier, S. (2001). Hydrodynamic stability of ablation fronts: linear perturbation of a self-similar solution. In M. Kálal and K. Rohlena and M. Šiňor, editor, *ECLIM 2000: 26th European Conference on Laser Interaction with Matter*, volume 4424 of *Proceedings of SPIE*, pages 220–223. SPIE.

Boudesocque-Dubois, C., Clarisse, J.-M., and Gauthier, S. (2003). A spectral Chebyshev method for linear stability analysis of one-dimensional exact solutions of gas dynamics. *J. Comput. Phys.*, 184:592–618.

Boudesocque-Dubois, C., Gauthier, S., and Clarisse, J.-M. (2008). Self-similar solutions of unsteady ablation flows in inertial confinement fusion. *J. Fluid Mech.*, 603:151–178.

Boudesocque-Dubois, C., Lombard, V., Gauthier, S., and Clarisse, J.-M. (2013). An adaptive multidomain Chebyshev method for nonlinear eigenvalue problems: Application to self-similar solutions of gas dynamics equations with nonlinear heat conduction. *J. Comput. Phys.*, 235:723–741.

Buresi, E., Coutant, J., Dautray, R., Decroisette, M., Duborgel, B., Guillaneux, P., Launspach, J., Nelson, P., Patou, C., Reisse, J.-M., and Watteau, J.-P. (1986). Laser program development at CEL-V: overview of recent experimental results. *Laser Part. Beams*, 4:531.

Bychkov, V., Modestov, M., and Law, C. K. (2015). Combustion phenomena in modern physics: I. Inertial confinement fusion. *Prog. Energy Combust. Sci.*, 47:32–59.

Bychkov, V. V., Golberg, S. M., and Liberman, M. A. (1991). Growth rate of the Rayleigh–Taylor instability instability in an ablatively accelerated inhomogeneous plasma. *Sov. Phys. JETP*, 73(4):642–653.

Bychkov, V. V., Golberg, S. M., and Liberman, M. A. (1994). Self-consistent model of the Rayleigh–Taylor instability in ablatively accelerated laser plasma. *Phys. Plasmas*, 1(9):2976–2986.

Cantrell, R. H. and Hart, R. W. (1964). Interaction between sound and flow in acoustic cavities: mass, momentum, and energy considerations. 36(4):697–706.

Canuto, C., Hussaini, M. Y., Quarteroni, A., and Zang, T. A. (1988). *Spectral methods in fluid dynamics*. Springer Verlag.

Canuto, V. M., Goldman, I., and Chasnov, J. (1987). A model for fully developped turbulence. *Phys. Fluids*, 30(11):3391–3418.

Chandrasekhar, S. (1961). *Hydrodynamic and hydromagnetic stability*. Oxford University Press.

Chu, B.-T. (1965). On the energy transfer to small disturbances in fluid flow (parti i). *Acta Mechanica*, 1:215–234.

Chu, B.-T. and Kovásznay, L. S. G. (1958). Non-linear interactions in a viscous heat-conducting compressible gas. *J. Fluid Mech.*, 3:494–514.

Clarisse, J.-M., Boudesocque-Dubois, C., and Gauthier, S. (2008). Linear perturbation response of self-similar ablative flows relevant to inertial confinement fusion. *J. Fluid Mech.*, 609:1–48.

Clarisse, J.-M., Gauthier, S., Dastugue, L., Vallet, A., and Schneider, N. (2016). Transient effects in unstable ablation fronts and mixing layers in HEDP. *Phys. Scr.*, 91:074005.

Clarisse, J.-M., Pfister, J.-L., Gauthier, S., and Boudesocque-Dubois, C. (2018). A hydrodynamic analysis of self-similar radiative ablation flows. *J. Fluid Mech.*, 848:219–255.

Clavin, P. and Masse, L. (2004). Instabilities of ablation fronts in inertial confinement fusion: A comparison with flames. *Phys. Plasmas*, 11(2):690–705.

Corbett, P. and Bottaro, A. (2001). Optimal linear growth in swept boundary layers. *J. Fluid Mech.*, 435:1–23.

Cossu, C. (2014). An introduction to optimal control. 66(2):024801.

Courant, R., Friedrichs, K., and Lewy, H. (1928). On the partial difference equations of mathematical physics. *Mathematische Annalen*, 100:32–74.

Dastugue, L. (2013). *Contributions à l'étude de la stabilité d'écoulements autosemblables d'onde thermique pour la fusion par confinement inertiel*. Thèse de doctorat, Université Pierre et Marie Curie/Paris 6.

Dastugue, L., Clarisse, J.-M., and Gauthier, S. (2012). Hydrodynamic stability of self-similar supersonic heat waves related to inertial confinement fusion. In Ratynskaya, S., Blomberg, L., and Fasoli, A., editors, *39th EPS Conference & 16th Int. Congress on Plasma Pysics*, volume 36F of *Europhysics Conference Abstracts*. EPS.

Douglas, S. C., Amari, S., and Kung, S.-Y. (2000). On gradient adaptation with unit-norm constraints. 48(6):1843–1847.

Drazin, P. G. and Reid, W. H. (1981). *Hydrodynamic stability*. Cambridge University Press, Cambridge, U.K.

Foures, D. P. G., Caulfield, C. P., and Schmid, P. J. (2012). Variational framework for flow optimization using seminorm constraints. *Phys. Rev. E*, 86(2):026306.

Foures, D. P. G., Caulfield, C. P., and Schmid, P. J. (2013). Localization of flow structures using ∞-norm optimization. *J. Fluid Mech.*, 729:672–701.

Funaro, D., Quarteroni, A., and Zanolli, P. (1988). An iterative procedure with interface relaxation for domain decomposition methods. *SIAM J. Numer. Anal.*, 25(6):1213–1236.

Gardner, J. H., Bodner, S., and Dahlburg, J. P. (1991). Numerical simulation of ablative Rayleigh–Taylor instability. *Phys. Fluids*, B 3(4):1070–1074.

Gauthier, S. (2011). Critères de stabilité temporelle pour des discrétisations spectrales - document de travail. *unpublished*.

Gauthier, S., Le Creurer, B., Abéguilé, F., Boudesocque-Dubois, C., and Clarisse, J.-M. (2005). A self-adaptive domain decomposition method with Chebyshev method. *Int. J. Pure Appl. Math.*, 24:553–577.

Gear, C. (1971). *Numerical initial value problems in ordinary differential equations*. Prentice-Hall.

George, K. J. and Sujith, R. I. (2012). Disturbance energy norms: A critical analysis. *J. Sound Vib.*, 331(7):1552–1566.

Giles, M. and Pierce, N. (1997). Adjoint equations in cfd - duality, boundary conditions and solution behaviour. In *13th Computational Fluid Dynamics Conference*.

Giles, M. and Pierce, N. (2000). An introduction to the adjoint approach to design. *Flow Turb. Combust.*, 65:393–415.

Goncharov, V. N. (1999). Theory of the ablative Richtmyer-Meshkov instability. *Phys. Rev. Lett.*, 82(10):2091–2094.

Goncharov, V. N., Betti, R., and McCrory, R. L. (1996a). Self-consistent stability analysis of ablation fronts with small Froude numbers. *Phys. Plasmas*, 3(12):4665–4676.

Goncharov, V. N., Betti, R., McCrory, R. L., Sorotokin, P., and Verdon, C. P. (1996b). Self-consistent stability analysis of ablation fronts with large Froude numbers. *Phys. Plasmas*, 3(4):1402–1414.

Goncharov, V. N., Gotchev, O. V., Vianello, E., Boehly, T. R., Knauer, J. P., McKenty, P. W., Radha, P. B., Regan, S. P., Sangster, T. C., Skupsky, S., Smalyuk, V. A., Betti, R., McCrory, R. L., Meyerhofer, D. D., and Cherfils-Clérouin, C. (2006). Early stage of implosion in inertial confinement fusion: Shock timing and perturbation evolution. *Phys. Plasmas*, 13:012702.

Goncharov, V. N., McKenty, P., Skupsky, S., Betti, R., McCrory, R. L., and Cherfils-Clérouin, C. (2000). Modeling hydrodynamic instabilities in inertial confinement fusion targets. *Phys. Plasmas*, 7(12):5118–5139.

Gottlieb, D. and Shu, C.-W. (1996). On the Gibbs phenomenon III: Recovering exponential accuracy in a subinterval from a spectral partial sum of a piecewise analytic function. *SIAM J. Numer. Anal.*, 33:280–290.

Gu, J. F., Ge, F. J., Zou, S. Y., Dai, Z. S., Huang, T., Pu, Y., Song, P., Wu, C., Li, C., Kang, D., Ye, W. H., Zheng, W., Jiang, W., Chen, T., Chen, Z., Yan, J., Zhang, X., Yu, B., Chen, J., Song, Z., Tang, Q., Deng, B., Wang, F., Yang, J., Jiang, S., Ding, Y., and Zhu, S. P. (2018). Investigation of the yield degradation of the first shaped-pulse implosion experiments on the SG-III laser facility. *Phys. Plasmas*, 25(12):122706.

Guégan, A., Schmid, P. J., and Huerre, P. (2006). Optimal energy growth and optimal control in swept Hiemenz flow. *J. Fluid Mech.*, 566:11–45.

Guillard, H., Malé, J.-M., and Peyret, R. (1992). Adaptive spectral methods with application to mixing layer computations. *J. Comput. Phys.*, 102(1):114–127.

Gunzburger, M. D. (1997). Introduction into mathematical aspect of flow control and optimization. In von Karman Institute for Fluid Dynamics, editor, *Lecture Series 1997-05 on Inverse Design and Optimisation Methods*.

Gustafsson, B. and Sundström, A. (1978). Incompletely parabolic problems in fluid dynamics. *SIAM J. Appl. Math.*, 35(2):343–357.

Haan, S. W., Huang, H., Johnson, M. A., Stadermann, M., Baxamusa, S., Bhandarkar, S., Clark, D. S., Smalyuk, V., and Robey, H. F. (2015). Instability growth seeded by oxygen in CH shells on the National Ignition Facility. *Phys. Plasmas*, 22(3):032708.

Hanifi, A., Schmid, J., and Henningson, D. S. (1996). Transient growth in compressible boundary layer flow. *Phys. Fluids*, 8(3):826–837.

Hatchett, S. (1991). Ablation gas dynamics of low-z materials illuminated by soft x-rays. Report UCRL-JC-108348. Lawrence Livermore National Laboratory, Livermore, CA.

Henrici, P. (1962). Bounds for iterates, inverses, spectral variation and fields of values of non-normalmatrices. *Numerische Mathematik*, 4(24).

Hesthaven, J. S. and Gottlieb, D. (1996). A stable spectral penalty methods for navier-stokes equations. part i. (3):579–612.

Hirsch, C. (1988). *Numerical computation of internal and external flows*. Wiley, Chichester.

Horn, R. and Johnson, C. R. (1990). *Matrix Analysis*. Cambridge University Press.

Huete, C., Wouchuk, J. G., Canaud, B., and Velikovich, A. L. (2012). Analytical linear theory for the shock and re-shock density inhomogeneities. *J. Fluid Mech.*, 700:214–245.

Jameson, A. (1988). Aerodynamic design via control theory. *J. Sci. Comput.*, 3.

Jameson, A. (1995). *Computational Fluid Dynamics Review*, chapter Optimum aerodynamic design using the control theory, pages 495–528. World Scientific.

Kerswell, R. R. (2018). Nonlinear nonmodal stability theory. *Annu. Rev. Fluid Mech.*, pages 319–346.

Kerswell, R. R. et al. (2014). An optimization approach for analysing nonlinear stability with transition to turbulence in fluids as an exemplar. *Reports on Progress in Physics*, 77.

Kopriva, D. A. (1986). A spectral multidomain method for the solution of hyperbolic systems. *Appl. Num. Math.*, 2:221–241.

Kreiss, H.-O. (1970). Initial boundary value problems for hyperbolic systems. *Commun. Pure Appl. Math.*, 23:277–298.

Kull, H. J. (1989). Incompressible description of Rayleigh–Taylor instabilities in laser-ablated plasmas. *Phys. Fluids B*, 1:170–182.

Kull, H. J. and Anisimov, S. I. (1986). Ablative stabilization in the incompressible Rayleigh–Taylor instability. *Phys. Fluids*, 29:2067–2075.

Le Métayer, O. and Saurel, R. (2006). Compressible exact solutions for one-dimensional laser ablation fronts. *J. Fluid Mech.*, 561:465–475.

Lemke, M., Reiss, J., and Sesterhenn, J. (2014). Compressible flow, reactive flow, adjoint equations. *Combust. Flame*, 161(10):2552–2564.

Lindl, J. (1995). Development of the indirect[U+2010]drive approach to inertial confinement fusion and the target physics basis for ignition and gain. *Phys. Plasmas*, 2(11):3933–4024.

Lindl, J., Amendt, P., Berger, R., Glendinning, S., Glenzer, S., Haan, S., Kauffman, R., Landen, O., and Suter, L. (2004). The physics basis for ignition using indirect-drive targets on the National Ignition Facility. *Phys. Plasmas*, 11(2):339–491.

Lindl, J., Landen, O., Edwards, J., Moses, E., and Team, N. (2014). Review of the National Ignition Campaign 2009-2012. *Phys. Plasmas*, 21:020501.

Lindl, J. D. and Mead, W. C. (1975). Two-dimensional simulation of fluid instability in laser-fusion pellets. *Phys. Rev. Lett.*, 34(20):1273–1276.

Lombard, V. (2008). *Modes de Kovásznay pour l'étude de la stabilité linéaire d'écoulements d'ablation autosemblables*. Thèse de doctorat, Université de Paris 6.

Lombard, V., Gauthier, S., Clarisse, J.-M., and Boudesocque-Dubois, C. (2008). Kovásznay modes in stability of self-similar ablation flows of ICF. *Europhys. Lett.*, 84:25001.

Luchini, P. and Bottaro, A. (1998). Gortler vortices: a backward-in-time approach to the receptivity problem. *J. Fluid Mech.*, 363:47–65.

Luchini, P. and Bottaro, A. (2014). Adjoint equations in stability analysis. *Annu. Rev. Fluid Mech.*, 46(1):493–517.

M. G. Macaraeg, C. L. S. (1986). Improvement in spectral collocation discretization through multiple domain technique. *Applied Numerical Mathematics*, (2):95–108.

MacCormack, R. (1971). Numerical solution of a shock wave with a laminar boundary layer. In *Lecture Notes in Physics*, volume 8, pages 151–163. Springer Berlin/Heidelberg.

Manheimer, W. M. and Colombant, D. G. (1984). Slab model for Rayleigh–Taylor stabilization by vortex shedding, compressibility, thermal conduction, and ablation. *Phys. Fluids*, 27(4):983–993.

Marshak, R. (1958). Effect of radiation on shock wave behavior. *Phys. Fluids*, 1(1):24–29.

Meshkov, E. E. (1969). Instability of the interface of two gases accelerated by a shock wave. *Soviet Fluid Dynamics*, 4:101–104.

Mihalas, D. and Mihalas, B. W. (1984). *Foundations of radiation hydrodynamics*. Oxford University Press, Oxford.

Miquel, J.-L. (2016). LMJ & PETAL status and first experiments. *Journal of Physics: Conference Series*, 717:012084.

Munro, D. H. (1989). Rippled shock front solutions for testing hydrodynamic stability simulations. *Phys. Fluids B*, 1(1):134–141.

Myers, M. K. (1991). Transport of energy by disturbances in arbitrary steady flows. *J. Fluid Mech.*, 226:383–400.

Nicoud, F., Benoit, L., Sensiau, C., and Poinsot, T. (2007). Acoustic modes in combustors with complex impedances and multidimensional active flames. *AIAA Journal, American Institute of Aeronautics and Astronautics*, 45(2):426–441.

Nishihara, K. (1982). Scaling laws of plasma ablation by thermal radiation. *Jpn. J. Appl. Phys.*, 21:L571–L573.

Nishihara, K., Ishizaki, R., Wouchuk, J. G., Fukuda, Y., and Shimuta, Y. (1998). Hydrodynamic perturbation growth in start-up phase in laser implosion. *Phys. Plasmas*, 5(5):1945–1952.

Nozaki, K. and Nishihara, K. (1980). Deflagration waves supported by thermal radiation. *J. Phys. Soc. Jpn.*, 48(3):993–997.

Nuckolls, J., Wood, L., Thiessen, A., and Zimmerman, G. (1972). Laser compression of matter to super-high densities: thermonuclear (CTR) applications. *Nature*, 239:139–142.

Orszag, S. (1980). Spectral methods for problems in complex geometries. *J. Comput. Phys.*, 37:70–92.

Perron, N. (2015). Parallélisation d'un code de stabilité hydrodynamique pour la fusion par confinement inertiel. Rapport de stage, CEA, DAM, DIF.

Peterson, J. L. et al. (2015). Validating hydrodynamic growth in national ignition facility implosions. *Phys. Plasmas*, 22(5).

Peyret, R. (2002). *Spectral Methods for Incompressible Viscous Flow*. Springer.

Piriz, A. R. (2001). Compressibility effects on the Rayleigh–Taylor instability of an ablation front. *Phys. Plasmas*, 8(12):5268–5276.

Piriz, A. R., Sanz, J., and Ibañez, L. F. (1997). Rayleigh–Taylor instability of steady ablation fronts: The discontinuity model revisited. *Phys. Plasmas*, 4(4):1117–1126.

Press, W. H., Teukolsky, S. A., Vetterling, W. T., and Flannery, B. P. (1994). *Numerical recipes*. Cambridge University Press, Cambridge, UK, 2 edition.

Pulicani, J. P. (1988). A spectral multi-domain method for the solution of 1-D-Helmholtz ans Stokes-type equations. *Comput. Fluids*, 16(2):207–215.

Raman, K. S., Smalyuk, V. A., Casey, D. T., Haan, S. W., Hoover, D. E., Hurricane, O. A., Kroll, J. J., Nikroo, A., Peterson, J. L., Remington, B. A., Robey, H. F., Clark, D. S., Hammel, B. A., Landen, O. L., Marinak, M. M., Munro, D. H., Peterson, K. J., and Salmonson, J. (2014). An in-flight radiography platform to measure hydrodynamic instability growth in inertial confinement fusion capsules at the National Ignition Facility. *Phys. Plasmas*, 21:072710.

Reddy, S. C., Schmid, P. J., and Henningson, D. S. (1993). Pseudospectra of the Orr-Sommerfeld operator. *SIAM Applied Mathematics*, 53(1):15–47.

Reinicke, P. and Meyer-ter-Vehn, J. (1991). The point explosion with heat conduction. *Phys. Fluids A*, 3:1807–1818.

Renaud, F. (1996). *Méthode spectrale de décomposition dynamique de domaines : application aux écoulements compressibles de Rayleigh-Bénard et Kelvin-Helmholtz*. Thèse de doctorat, Université de Nice-Sofia antipolis.

Renaud, F. and Gauthier, S. (1997). A dynamical pseudo-spectral domain decomposition technique: Application to viscous compressible flows. *J. Comput. Phys.*, 131:89–108.

Richtmyer, R. D. (1960). Taylor instability in shock acceleration of compressible fluids. *Commun. Pure Appl. Math.*, 13:297–319.

Saillard, Y. (2000). Hydrodynamique de l'implosion d'une cible FCI. *C. R. Acad. Sc. Paris*, t. 1, Série IV:705–718.

Saillard, Y., Arnault, P., and Silvert, V. (2010). Principles of the radiative ablation modeling. *Phys. Plasmas*, 17:123302.

Sakagami, H. and Nishihara, K. (1990). Rayleigh–Taylor instability on the pusher-fuel contact surface of stagnating targets. *Phys. Fluids B*, 2(11):2715–2730.

Sanmartín, J. R. and Barrero, A. (1978). Self-similar motion of laser half-space plasma. I. Deflagration regime. *Phys. Fluids*, 21(11):1957–1966.

Sanz, J. (1996). Self-consistent analytical model of the Rayleigh–Taylor instability in inertial confinement fusion. *Phys. Rev. E*, 53(4):4026–4045.

Sanz, J. et al. (1992). Self-similar model for tamped ablation driven by thermal radiation. *Phys. Fluids B*, 4(3):683–692.

Sanz, J., Masse, L., and Clavin, P. (2006). The linear Darrieus–Landau and Rayleigh–Taylor instabilities in inertial confinement fusion revisited. *Phys. Plasmas*, 13:102702.

Schmid, P. J. (2007). Nonmodal stability theory. *Annu. Rev. Fluid Mech.*, 39:129–162.

Schmid, P. J. and Henningson, D. S. (2001). *Stability and transition in shear flows*. Springer.

Smalyuk, V. A. et al. (2015). Hydrodynamic instability growth of three-dimensional, "native-roughness" modulations in x-ray driven, spherical implosions at the National Ignition Facility. *Phys. Plasmas*, 22:072704.

Smalyuk, V. A. et al. (2017). Hydrodynamic instability growth of three-dimensional modulations in radiation-driven implosions with "low-foot" and "high-foot" drives at the National Ignition Facility. *Phys. Plasmas*, 24:042706.

Strikwerda, J. C. (1977). Initial boundary value problems for incompletely parabolic systems. *Commun. Pure Appl. Math.*, XXX:797–822.

Takabe, H., Mima, K., Montierth, L., and Morse, R. L. (1985). Self-consistent growth rate of the Rayleigh–Taylor instability in an ablatively accelerating plasma. *Phys. Fluids*, 28(12):3676–3682.

Takabe, H., Nishihara, K., and Taniuti, T. (1978). Deflagration waves in laser compression. i. *J. Phys. Soc. Jpn.*, 45(6):2001–2008.

Thompson, K. (1987). Time dependent boundary conditions for hyperbolic systems. *J. Comput. Phys.*, 68:1–24.

Thompson, K. (1990). Time-dependent boundary conditions for hyperbolic systems, II. *J. Comput. Phys.*, 89:439–461.

Trefethen, L. N. (1999). Computation of Pseudospectra. *Acta Numerica*, pages 247–295.

Trefethen, L. N. et al. (1993). Hydrodynamic stability without eigenvalues. *Science*, 261:578–584.

Velikovich, A. L., Dahlburg, J. P., Gardner, J. H., and Taylor, R. J. (1998). Saturation of perturbation growth in ablatively driven planar laser targets. *Phys. Plasmas*, 5:1491–1505.

Volkov, O., Protas, B., Liao, W., and Glander, D. W. (2009). Adjoint-based optimization of thermo-fluid phenomena in welding processes. *J. Eng. Math.*, 65:201–220.

Wieczorek, K. et al. (2011). Assessing non-normal effects in thermoacoustic systems with mean flow. *Phys. Fluids*, 23(10):107103.

Wilkinson, J. P. and Jacobs, J. W. (2007). Experimental study of the single-mode three-dimensional rayleigh-taylor instability. *Physics of Fluids*, 19(12):124102.

Williamson, J. H. (1980). Low-storage Runge–Kutta schemes. *J. Comput. Phys.*, 35(1):48–56.

Wouchuk, J. G. (2001a). Growth rate of the linear Richtmyer-Meshkov instability when a rarefaction is reflected. *Phys. Fluids*, 8(6):2890–2907.

Wouchuk, J. G. (2001b). Growth rate of the linear Richtmyer-Meshkov instability when a shock is reflected. *Phys. Rev. E*, 63(056303):1–13.

Zel'dovich, Y. B. and Raizer, Y. P. (1967). *Physics of shock waves and high-temperature hydrodynamic phenomena*. Academic Press, New-York.

université
PARIS-SACLAY

ÉCOLE DOCTORALE
Ondes et Matière
(EDOM)

Titre : Analyse non-normale de stabilité hydrodynamique d'écoulements d'ablation en fusion par confinement inertiel

Mots clés : HED, front d'ablation, perturbations optimales, méthodes spectrales, direct–adjoint, compressible

Résumé : Un écoulement d'ablation se forme lorsqu'un matériau dense est soudainement exposé à un flux énergétique intense. Une onde de choc se propage alors dans ce matériau, suivi d'un front d'ablation correspondant à la superposition d'un front thermique et de la tête d'une onde de détente. Leur forte stratification et leur caractère accéléré rendent les écoulements d'ablation particulièrement sensibles aux instabilités hydrodynamiques.

On rencontre les écoulements d'ablation en fusion par confinement inertiel (FCI) où ils jouent un rôle majeur pour la compression d'une cible de fusion sphérique. Le succès de la FCI repose, entre autres, sur une compression suffisamment symétrique de la cible, ce qui requiert un contrôle des instabilités de front d'ablation. Cependant, la multiplicité des sources de perturbations rend difficile l'identification des défauts initiaux les plus dangereux pour la stabilité du front d'ablation. Pour répondre à cette question, ce travail propose une première analyse non-normale de stabilité linéaire d'un écoulement d'ablation radiative. Le modèle d'écoulement autosemblable utilisé prend en compte la compressibilité, l'instationnarité et la conduction de chaleur non-linéaire caractéristiques des écoulements d'ablation (Abéguilé et al., 2006; Clarisse et al., 2018). Les perturbations initiales optimales sont identifiées pour différents horizons temporels et longueurs d'onde et caractérisées en fonction de leur nature (acoustique, entropie, vorticité, déformation des interfaces). Deux mécanismes de croissance optimales sont identifiés. Ils diffèrent notamment de l'instabilité de Richtmyer–Meshkov ablative.

Ces perturbations optimales sont obtenues *via* une résolution itérative direct–adjoint. Le problème adjoint est formulé à partir du formalisme des multiplicateurs de Lagrange. Une attention particulière est donnée à l'inclusion des contraintes sur les conditions limites et les équations d'évolution pour les déformations dans le lagrangien. Ces travaux ouvrent la voie à une identification *systématique* des défauts initiaux dans l'ablateur des cibles FCI les plus dangereux vis-à-vis du processus d'implosion.

Title : Non-modal hydrodynamic stability analysis of ablation flows relative to inertial confinement fusion

Keywords : HEDP, ablation fronts, optimal perturbations, spectral methods, direct–adjoint, compressible, ICF

Abstract : Ablation waves form when a dense medium is suddenly exposed to a strong irradiation flux. A forerunning shock front propagates inside the dense medium, followed by an ablation front which corresponds to the superposition of the foot of a heat front and the leading edge of a rarefaction wave. Ablation waves are highly sensitive to hydrodynamic instabilities due to their strong stratification and inherent acceleration.

Ablation waves arise during the implosion of inertial confinement fusion (ICF) targets, for which they are critical regarding the compression of a spherical fusion target. Achieving ICF ignition requires a sufficiently symmetrical implosion, which is possible if ablation front instabilities are controlled. However, the identification of the most dangerous initial defect regarding ablation front stability is difficult due to the multiplicity of perturbation sources.

To address this issue, we carried out the first non-modal linear stability analysis of a radiation driven ablation wave. We make use of a self-similar flow model that renders the compressibility, unsteadiness and nonlinear heat conduction proper to ablation flows (Abéguilé et al., 2006; Clarisse et al., 2018). Initial optimal perturbations are identified for various terminal times and wavelengths and characterized according to their nature (acoustic, entropic, vorticity or boundary deformation). Two distinct optimal growth mechanisms are identified. They notably differ from the ablative Richtmyer–Meshkov instability.

Initial optimal perturbations are obtained by means of direct–adjoint iterations. The adjoint problem is derived from the Lagrange multipliers technique. Particular attention is drawn to constraints on boundary conditions and free surface evolution equations while building the Lagrange functional. This work paves the way to a *systematic* identification of the most dangerous initial defects in the ablator of ICF targets regarding the implosion process.

Université Paris-Saclay
Espace Technologique / Immeuble Discovery
Route de l'Orme aux Merisiers RD 128 / 91190 Saint-Aubin, France